The Role of Casting Defects in the Fatigue Behavior of Notched Cast Aluminum Alloys

by

Ashraf A. Dabayeh

A thesis
Presented to the University of Waterloo
in fulfillment of the
thesis requirement for the degree of
Doctor of Philosophy

in

Civil Engineering

Waterloo, Ontario, Canada, 1998
© Ashraf A. Dabayeh 1998

National Library of Canada
Acquisitions and Bibliographic Services
395 Wellington Street
Ottawa ON K1A 0N4
Canada

Bibliothèque nationale du Canada
Acquisitions et services bibliographiques
395, rue Wellington
Ottawa ON K1A 0N4
Canada

Your file Votre référence

Our file Notre référence

The author has granted a non-exclusive licence allowing the National Library of Canada to reproduce, loan, distribute or sell copies of this thesis in microform, paper or electronic formats.

L'auteur a accordé une licence non exclusive permettant à la Bibliothèque nationale du Canada de reproduire, prêter, distribuer ou vendre des copies de cette thèse sous la forme de microfiche/film, de reproduction sur papier ou sur format électronique.

The author retains ownership of the copyright in this thesis. Neither the thesis nor substantial extracts from it may be printed or otherwise reproduced without the author's permission.

L'auteur conserve la propriété du droit d'auteur qui protège cette thèse. Ni la thèse ni des extraits substantiels de celle-ci ne doivent être imprimés ou autrement reproduits sans son autorisation.

0-612-32821-X

Canada

The University of Waterloo requires the signatures of all persons using or photocopying this thesis. Please sign below and give address and date.

ABSTRACT

In this investigation, a number of fatigue problems related to the presence of a flaw at a notch root have been addressed. The region in front of the notch root in which the defect affects fatigue crack growth has been determined. The reductions in smooth specimen fatigue strength for constant amplitude loading, intermittent underload block loading, and for a SAE service load history caused by a flaw at notch root were determined by fatigue tests. The fatigue test data were generated on three cast aluminum materials, including Al 206, Al 319, and Al 390. The cast Al 319 material was tested in the as cast and hipped conditions. Hipping is a process in which the material is subjected to a high pressure at high temperature and then slowly cooled to eliminate or close internal flaws. Smooth specimens, notched specimens, and notched specimens with an artificial or natural flaw at a notch root were fatigue tested. The smooth specimens fatigue test results showed that the block loading history, which consisted of underloads followed by constant amplitude smaller cycles, reduced the crack opening stress so that the constant amplitude cycles were fully effective. The smooth specimens results also showed that the hipping process increased the constant amplitude fatigue strength by 62.5% for the 319 cast aluminum alloy. The notched and notched with artificial or natural flaw at a notch root results, obtained under the constant amplitude loading and under the block loading history, showed that natural flaws in the as cast 319 aluminum alloy can be modeled by an equivalent drilled hole of the same size. Fatigue test results obtained under the service load history were used to study the fatigue strength reductions from the notched specimens, caused by a defect at notch root. The results showed that the fatigue lives of the 3.0 mm and 1.5 mm radius notched specimens with a 0.6 mm diameter flaw at the notch root were 40% and 38% shorter than the notched specimen fatigue lives, respectively.

The fatigue life of smooth specimens, notched specimens, and notched specimens with a flaw at the notch root subjected to constant amplitude loading, intermittent underload block loading, and a SAE service load history was predicted using a crack growth model. The crack growth model calculations were based on elastic and plastic notch strain calculations based on Neuber's formula, crack opening stress calculations, and a reference crack growth rate curve obtained during closure-free crack growth. Fatigue life predictions were in good agreement with the experimental results.

The crack growth model was used to study the effect of the variation in the flaw size and flaw position at the notch root on fatigue life. The fatigue life predictions revealed that the fatigue life of notched specimens having a small notch radius, of a size comparable to the flaw size, is more affected by a given variation in flaw size and flaw position than notched specimens having a large notch radius. The model predictions matched the observed fatigue lives. Fatigue life predictions for specimens with a flaw at a notch root using the crack growth model were compared with those obtained using conventional methods of strain-life and effective strain-life analyses. Results obtained showed that the conventional methods for fatigue life prediction using the fatigue notch factor, K_f, do not account for the decrease in concentration factor as the crack advances and cannot describe the fatigue behavior of notches with a high K_t value that decays rapidly, such as a notch with a flaw at the notch root.

In the absence of sufficient experimental data or finite element results to calibrate a model describing the variation in crack opening stress, a conservative assumption has sometimes been made that the crack opening stress throughout fatigue loading remains at the level it would have following the largest cycle. This assumption, while shown in earlier studies to be conservative, was reasonable for the materials and histories examined. It was shown in this study that this assumption is more conservative for the cast aluminum material used. The more conservativness was caused by the crack opening stress which requires fewer cycles, after the application of an underload or an overload, to reach the steady state crack opening stress than that for the materials studied earlier (1045 Steel and 2024-T351 aluminum). The analytical crack growth model was used to determine the frequency of the cycle in the SAE GKN Grapple-Skidder history that had a crack opening stress, which when used as a constant level gives the correct fatigue life.

ACKNOWLEDGMENTS

I wish to express my sincere gratitude to my supervisor, Professor Tim Topper, for his expertise, guidance, patience and understanding. I would like to thank Dr. Ahmad Varvani-Farahani for his help with the materials' microstructural analysis, Mr. Tom Lam for his discussions and help with the computer work, and Mr. Andy Barber for his technical expertise.

I would like to thank my father, mother, and sister for their moral support. I am particularly indebted to my wife, Rania, who has lovingly encouraged me throughout this work, enlightened me with bright ideas, and has waited patiently for this day. I would also like to thank Dr. Hussein Abdel-Raouf for his help and especially for his valuable advice.

Finally, I gratefully acknowledge the National Sciences and Engineering Research Council of Canada and the University of Waterloo for their financial support.

TO RANIA AND OUR NEW BABY

"OMAR"

TABLE OF CONTENTS

LIST OF TABLES

Chapter 3

Chapter 4

Chapter 5

LIST OF FIGURES

Chapter 1

Chapter 2

Chapter 3

Chapter 4

Chapter 5

NOMENCLATURE

$\frac{da}{dN}$	Crack growth rate per cycle
ΔK	Stress intensity factor range
C, m	Crack growth rate material constants
N_f	Number of fatigue cycles to failure
$2N_f$	Number of fatigue reversals to failure
l_i, l_f	Initial and final crack lengths
ΔK_{th}	Threshold stress intensity factor range
ΔK_i	Intrinsic threshold stress intensity factor range
L_1	Crack length which separates between microstructurally and physically short crack regimes
L_2	Crack length which separates between physically short crack regime and long crack regime
K_t	Theoretical surface stress concentration factor
a	Crack length
ΔK_{eff}	Effective stress intensity factor range
K_{max}, K_{min}	Maximum and minimum stress intensity factors
K_{open}	Stress intensity factor at the crack opening stress level
K_c	Fracture toughness
$\Delta\sigma_f, \Delta\sigma_{th}$	Fatigue limit stress range at R=-1
K_σ, K_ε	Stress and strain concentration factors
S, σ	Nominal and local stresses
e, ε	Nominal and local strains
E	Elastic Young's Modulus
K_p	Elastic stress concentration factor for a crack in a notch or a crack in a flaw at the notch root
K'	Cyclic strength coefficient
n'	Cyclic strain hardening exponent
S_{op}	Instantaneous crack opening stress

S_{opss}	Steady state crack opening stress
S_{opul}	Crack opening stress after the underload cycle
ρ	Radius of curvature
Q_ϵ	Surface strain concentration factor
N	Number of cycles
K_f	Fatigue notch factor
S_{max}, S_{min}	Maximum and minimum nominal stresses
$\sigma_{max}, \sigma_{min}$	Maximum and minimum local stresses
HG	High-Gas
LG	Low-Gas
C.A.	Constant amplitude
V.A.	Variable amplitude

CHAPTER 1

FATIGUE BEHAVIOR OF CAST METALS

1.1 Introduction

Discontinuities in metallic components give rise to stress concentrations at which fatigue cracks initiate. The presence of a flaw at a geometric stress concentration, such as a notch root, will further increase the local stresses and strains and reduce the component's fatigue strength. The main thrust of this investigation is to study the fatigue behavior of a component having a flaw at a notch root. Another aim of this thesis is to provide a model which describes the growth of a flaw from a notch root and which predicts fatigue lives for a variety of fatigue loading histories.

In this investigation the effect of the variation of the flaw size and flaw position in a notch root and the relative size of the flaw to the notch size on fatigue strength is studied. The reductions in fatigue strength from that of a notched specimen due to the presence of a defect at the notch root are examined, and a model for predicting the fatigue life behavior of notched components containing defects in their stress concentration regions is introduced.

1.2 Fabrication of Metals

Metal fabrication is the method by which materials (i.e. metals or alloys) are manufactured or formed into useful products. Metal fabrication techniques include extrusion, forging, rolling, casting, welding, etc. The method or methods chosen depend on many factors, the most important of which are the required properties of the component and the cost. Some of the numerous metal fabrication techniques are listed schematically in Figure 1.1.

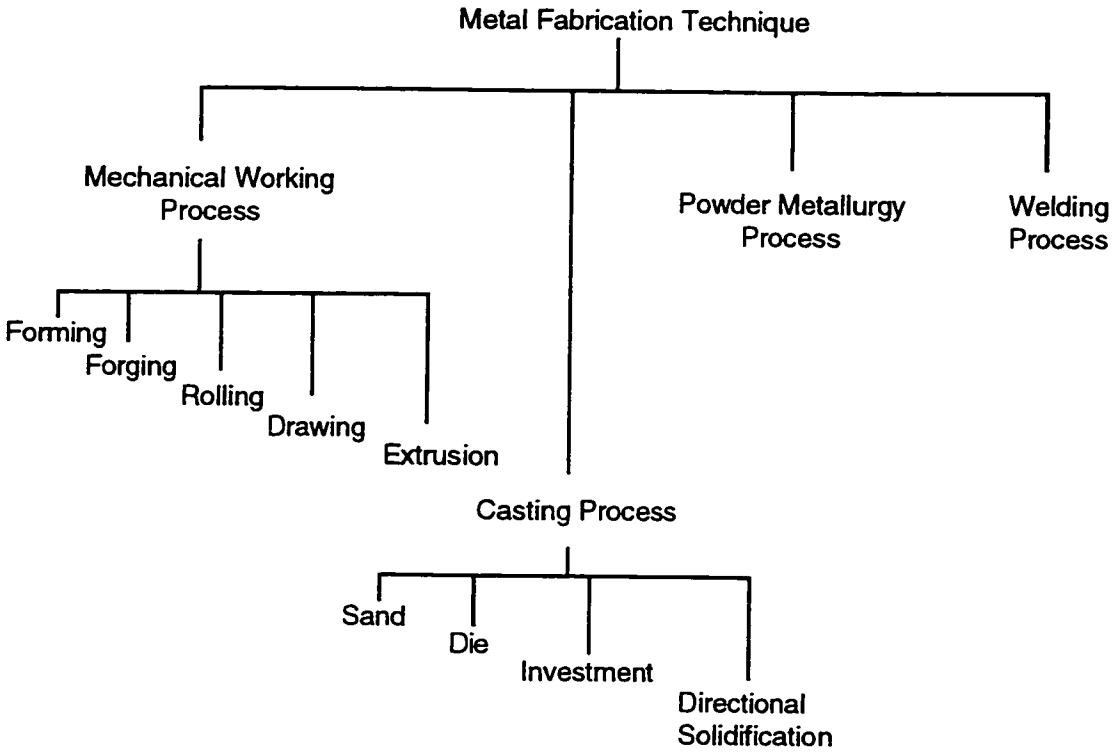

Figure 1.1 Most popular metal fabrication techniques

The casting process is the oldest known metal fabrication technique. Casting consists of pouring a totally molten metal into a mold cavity which has the desired shape. Upon solidification, the metal will take the shape of the mold but acquires some shrinkage cavities or pores. Casting does not give as high a strength as other processes, but it is an economic solution for parts having complicated shapes. Casting techniques are employed when

a- The particular alloy used is so low in ductility that other forming process cannot be used.

b- The existence of internal defects is acceptable.

c- Casting is less expensive than other techniques.

The amount of gases in solutions increases with increasing temperature and with time at an elevated temperature. Therefore, casting is usually done at the lowest possible temperature, and with the least possible delay, to decrease defect size. If, during cooling and solidification, evolving gases are trapped at the solid-liquid interface, dendretic arms and gas pores are formed which weaken the cast metal.

The distribution of defects in cast metals on a microscopic scale is usually considered to be random. However, some researchers, such as Turkdogan and Grange [1], have illustrated that, for given initial levels of silicon, manganese, and oxygen in cast steel, there is a carbon level above which gas pores occur due to ebullition of carbon mono-oxide. This leads to non uniform dispersions. In general, the number, size, and distribution of defects may differ for different alloys and different casting techniques.

Aluminum alloys are characterized by their relatively low density (2.7 g/cm^3 as compared to 7.9 g/cm^3 for steel) and their resistance to corrosion. Their mechanical properties can be enhanced and improved by cold working and by alloying; however, this enhancement tends to affect their corrosion resistance. Common applications of aluminum alloys are aircraft industry components and automotive industry components (i.e. car bodies, engine blocks, etc.). The materials used in this study are cast aluminum alloys which are used mainly in automotive engine blocks.

1.3 Fatigue of Metals

Almost all types of engineering structures are subjected to fatigue. In some of them, such as aircraft, design against fatigue is as important as design against yielding or conventional fracture.

In fatigue we are concerned with a type of failure in which fracture occurs under an alternating stress in which the peak stress would be safe if applied once unidirectionally. Fatigue fracture involves material softening and/or hardening, crack nucleation, crack growth, and final fracture. Crack nucleation can occur even when a structure is elastically stressed. A nucleated crack will then grow slowly at first and then at an increasing rate under cyclic loading or stressing. When the crack reaches a critical length, fast fracture occurs. During the period of crack advance the structure can still carry the applied loads. A schematic illustration of the various fatigue stages is shown in Figure 1.2.

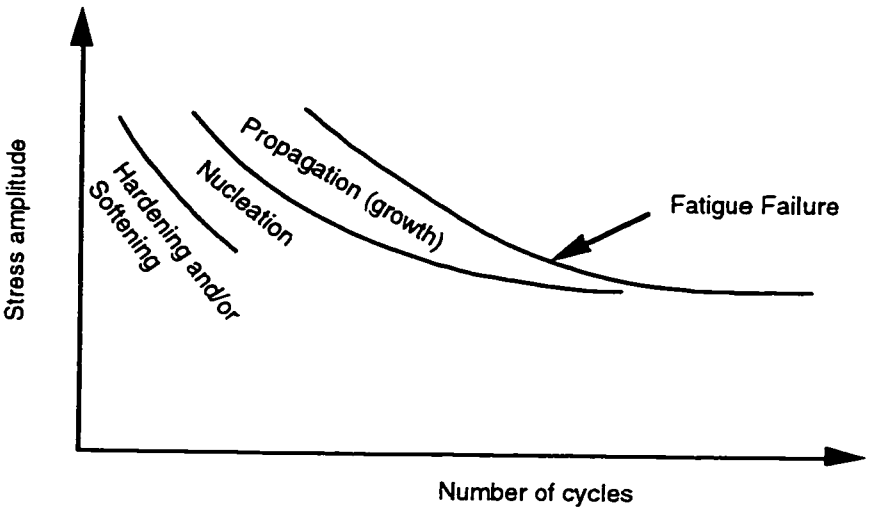

Figure 1.2 A schematic for various fatigue stages

The fatigue life of structural components can be estimated by an integration of crack growth rates. Rates are usually correlated with the stress intensity factor K, using a fracture mechanics approach, following the equation proposed by Paris and Erdogan [2]:

$$\frac{da}{dN} = C(\Delta K)^m \qquad 1.1$$

where a is the crack length, N is the number of cycles, and C and m are material constants

Fatigue lives for components subjected to alternating stress levels are predicted by an integration of equation 1.1 to give

$$N_f = \int_{l_i}^{l_f} \frac{da}{C(\Delta K)^m} \qquad 1.2$$

where l_i and l_f are the initial and final crack lengths, respectively.

1.4 Effect of Casting Defects on Fatigue Behavior

Extensive work on the fatigue resistance of cast steels by De Kazinczy [3-8] was reported by Mitchell [9]. De Kazinczy [3] investigated defects at the origin of fatigue cracks of several medium carbon steels in order to evaluate their effect on fatigue strength. He found that microshrinkage cavities extending from 0.004 to 0.008 inch below the specimen surface were the origin of failure in 77 percent of the tests, slag layers and sulphide inclusions accounted for 17 percent while fractures due to spherical inclusions accounted for 6 percent. Defect size is known to have an important effect on fatigue strength. Evans *et al.* [10] studied the effect of casting section size on fatigue strength. They found that the lower fatigue limit for specimens taken from the center of a large casting compared to specimens taken from the surface was due to an increase in the size of microshrinkage cavities. The increased section size led to decreased solidification rates which in turn gave larger defect sizes. De Kazinczy [5] in research on 2000 A° thick Nbc precipitates showed that microshrinkage cavities were the initiation sites for fatigue fracture in every sample he tested. Briggs *et al.* [11] concluded from their research that the fatigue limit of specimens having drilled holes was approximately equal to that for cast specimens having pores of the same maximum size.

Mitchell [12] studied the effects of graphite morphology on the fatigue resistance of gray cast iron. He found that the introduction of coarse graphite flakes in a homogenous steel matrix, as in cast iron, caused a decrease in fatigue resistance of more than a factor of 3 in strain upon extrapolation to 10^8 reversals (0.0005 as compared to 0.018). He added that, in the hardness ranges investigated, the matrix structure is of less importance than the graphite size and matrix hardness in controlling the fatigue resistance of cast iron. In conclusion, he reported that the best fatigue resistances in his investigation were from fine graphite and soft matrices.

Later, Heuler *et al.* [13] studied manufacturing defects in the near surface region of 2.25% Cr 1% Mo castings. The defects examined were micropores, pinholes, slag, oxide layers, inclusions, hot tears and small microcracks in welds. They found that the largest defects were hot tears having a mean surface area of 11 mm^2, and only inclusions and blowholes have large notch radii which range from 400 to 500 μm. Surface defects such as pinholes (piping), slag inclusions, and small surface defects

in welded areas proved to be the most effective crack initiators while internal defects such as hot tears and micropores (although they were large) served as crack initiators in less than 40 percent of the cases. They concluded that surface and near surface defects initiate cracks sooner than defects embedded in the specimen. Defects having small notch radii such as surface cracks at welds, pinholes, slag, and oxide layers initiate cracks more frequently than, for example, hot tears, inclusions, blowholes, and micropores.

Thus it can be seen that cracks initiate from larger defects rather than smaller ones but they initiate sooner from those on or near the surface even if they have smaller radii. The surface texture has an effect on fatigue crack initiation. Günger and Edwards [14] found that small cracks nucleated from defects on both as-cast and polished surfaces in squeeze-cast 6082 aluminum alloy. However, the large (~ 90 μm in diameter) surface defects on the as-cast surface caused an approximate 20 percent reduction in fatigue life when compared to polished surfaces where cracks initiated from smaller (~ 12 μm in diameter) microporosity. When they measured the crack growth rate of small cracks, they found that both the as-cast and polished specimen data fell within the same scatter band. This result means that the effect on fatigue performance was due to crack initiation rather than propagation. This result was also assured when they found that the life fraction spent for a crack to grow to 100 μm (which is about the size of the as-cast surface defect) was 35 to 65 percent of the total life for polished specimens, whereas, it was about 2 to 10 percent of the life for specimens with an as-cast surface.

Couper *et al.* [15] studied the fatigue behavior of a Strontium-modified heat-treatable Al-7Si-0.4Mg cast aluminum alloy. Their shrinkage pores were up to 140 μm in diameter and again they found that in nearly all samples tested, the interdendritic pores close to or at the specimen surface were the site of crack initiation. Evidence of classical crack initiation from persistent slip bands was also seen but such cracks, being less severe than casting defects, never caused failure. Also their results suggest that in practical fatigue applications it is better to minimize the pore size rather then the volume fraction of porosity. They fatigue tested their aluminum material for five different heat treatments and they found that the S-N behavior was insensitive to heat-treatment. This behavior is a result of the fact that fatigue crack initiation occurs from casting defects, notably, shrinkage porosity. DuQuesnay *et al.* [16], after studying the fatigue of a nodular cast iron automobile

suspension knuckle, found that cracks always initiated from casting surface defects and that the fatigue life could be extended significantly by machining away the as-cast surface in the fatigue sensitive locations.

Fatigue strength with different degrees of porosity was studied by Sonsino and Ziese [17]. They reported the influence of porosity on constant- and variable-amplitude fatigue of an age-hardened alloy G-Al-7Si-0.6Mg and a non-age-hardened alloy G-Al-11Si-Mg-Sr. They found that if the degree of porosity (ρ) is increased from 0 to 4 % and from 0 to 8 %, fatigue strength is reduced by about 11 percent and 17 percent, respectively, for both alloys in the unnotched condition. This decrease was distinctly lower in the notched condition for the age-hardened alloy. With ρ=4 there was hardly any decrease and with ρ=8 there was a drop of 7 percent from which they concluded that, in the presence of external notches, pores have hardly any influence on the fatigue strength of axially stressed components. However, in the notched condition of the non-age-hardened alloy, there was a drop of 20 percent because of the low material yield stress.

Stanzl-Tschegg *et al.* [18] showed in their work on AlSi11 cast aluminum alloy that it is mainly the cast voids that determine the fatigue properties and that these material inhomogeneities reduce the fatigue strength and lead to early fractures. The origin of almost all of their cracks was a void at or close to the specimen surface. They concluded that voids mainly influence crack initiation while other material characteristics like ductility, alloying, and crack closure determine the fatigue crack growth properties. Liu *et al.* [19] investigated the effect of inclusions in rail steel on fatigue crack initiation. Their results revealed that crack initiation occurs at elongated inclusions rather than round ones. They explained that the elongated inclusions acted as stress raisers for crack initiation. They concluded that inclusions are harmful to fatigue properties and those which are brittle are significantly more harmful than those which deform plastically. Khalifa [20] studied fatigue crack initiation associated with inclusions in a low carbon steel. His examination of the fracture surfaces indicated that crack initiation occasionally occurred at inclusion sites. He stated that relatively large inclusions in steels and aluminum alloys are more likely to act as focal points for fatigue crack initiation. Skallerud *et al.* [21] measured the fatigue life of cylindrical aluminum specimens containing shrinkage cavities. They observed that fatigue cracks almost always initiated from shrinkage pores at or close to the specimen surface. They concluded that a typical crack

initiated around pores at or near the specimen surface and one reason for this was a high stress concentration due to shrinkage pores.

In summary, it can be concluded that in cast metals

1- Almost all cracks initiate from material defects.

2- Fatigue cracks initiate from larger defects rather smaller ones but initiate sooner from surface or near surface defects than from interior defects.

3- The as-cast surface causes a significant reduction in fatigue life when compared to polished surfaces.

1.5 Influence of Porosity and Casting Defects on Fatigue Crack Growth

1.5.1 Short Cracks

It is well documented that, for a given stress intensity, short fatigue crack growth rates are higher than long crack growth rates. The first reported observations of this phenomenon was by Pearson [22] who examined the effect of crack size on propagation rates in a precipitation hardened aluminum alloy. He found that short flaws, 0.006 to 0.5 mm deep, grew up to 100 times faster than longer flaws, tens of millimeters in size, which were subjected to the same nominal stress intensity. Other studies like Lankford [23] who examined 7075 aluminum alloy, and Tanaka *et al.* [24], who tested silicon iron, reported transient acceleration and retardation characteristics associated with the growth of short fatigue cracks. It is also significant that some studies have observed initially higher fatigue crack propagation rates for notched specimens than the rates for a central crack. This difference continually reduces and eventually disappears with increasing crack length [25, 26]. A further observation of interest by El-Haddad *et al.* [25] is that while cracks in specimens having large radius circular notches have continuously increasing crack growth rates, the cracks in small radius circular and elliptical notched specimens exhibited a crack growth rate that initially decreases, reaches a minimum and thereafter increases. Smith, Miller and Hammunda [27, 28] predicted this trend based on the argument that initiation and early growth of a crack is controlled by the plastic strain field of the notch which diminishes rapidly. They

explained the latter increase in crack growth in terms of the increasing stress intensity with crack length.

Gerard *et al.* [29] studied the influence of pore microstructure on short crack growth during low cycle fatigue by testing powder-processed titanium material. They found that the presence of porosity enhances short crack propagation adjacent to the pores as a result of localized pore-induced plasticity. Their observations showed that, once the crack extends beyond the plastic zone of an isolated pore, it decelerates to propagation rates similar to those observed for fully dense material. For low levels of porosity in which the pores are isolated, they observed that the overall short crack growth rates are not significantly affected because most of the crack growth occurs outside the pore-induced plastic zone. For the interconnected pores they observed higher crack growth rates than for cracks of the same size in a fully dense material. They finally concluded that for metals containing less than or equal to 6 percent isolated porosity, the pores should accelerate the short crack growth adjacent to the pore only in a region which scales with the pore size.

Güngör and Edwards [14], while studying the effect of surface texture on fatigue life in a squeeze-cast Al-Mg-Si alloy, measured crack growth rates for short cracks emanating from the as-cast and the polished surfaces. Cracks that nucleated at large surface defects on the as-cast surface showed a deceleration during their early growth. It was concluded that the growth rate deceleration arose from the "stress concentrating" effect of the particle. However, small cracks on the polished surfaces showed very irregular growth patterns after initiation. They suggested that the reason for these irregularities in crack growth rates (decelerations and accelerations) was the interaction of the crack with microstructural features such as grain boundaries and inclusions. They mentioned that the majority of the microporosity occurs at grain boundaries and that all the pores that initiated cracks lay on grain boundaries so that the initial crack growth was predominantly intergranular. In addition, they also observed crack arrest at particles which explains some of the irregularities in crack growth rates.

1.5.2 Long Cracks

Ogawa and Kobayashi [30] studied near-threshold crack growth and crack closure in nodular cast iron. The cast iron defects were in the form of spheroidal graphites which under cyclic loading were crushed to form a powder. The graphite powder accumulated within the crack and enhanced crack closure. The schematic illustration of graphite-induced crack closure is shown in Figure 1.3.

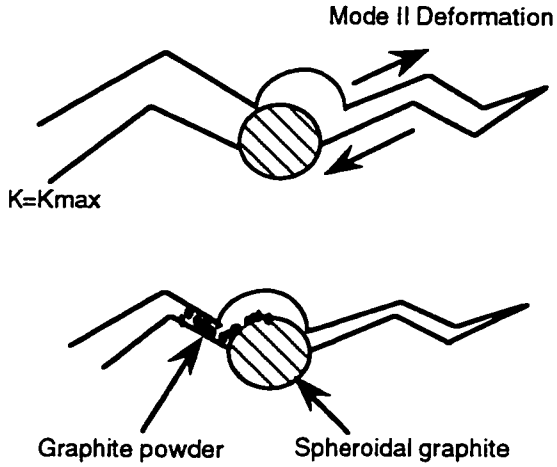

Figure 1.3 A schematic illustration of graphite-induced surface closure [30]

They concluded that the contribution of graphite-induced crack closure increases with increasing R and ΔK similar to oxide-induced crack closure. Therefore, the marked influence of stress ratio on the near-threshold crack growth in a nodular cast iron is controlled by graphite-induced crack closure.

In a study by Heuler *et al.* [13] on steel castings containing near-surface defects, the crack growth rate of cracks emanating from hot tears in $2\frac{1}{4}\%$ Cr 1% Mo castings was measured. Hot tears are intergranular material separations of varying depths and they have a dendretic structure. They noticed that cracks initiate at the very lowest points of the hot tears. They also found that the local crack growth rate can vary considerably for hot tears that are open, partially closed, or completely closed. In some cases they found crack growth to be faster or slower than in specimens without hot tears. However, the mean rate of crack growth corresponds to that of the sound material.

Thus it can be concluded that the crack growth rate for short cracks emanating from defects is higher than long crack growth rates, but the difference between crack growth rates reduces and eventually disappears with increasing crack length. This

deceleration corresponds to the decrease in the stress concentrating effect of the defect with distance from the defect. The deceleration can also be attributed to the crack closure phenomenon. Short cracks have lower closure than long cracks and the crack closure builds up as the crack advances, which decelerates the crack growth rate. Long crack growth rates are in some cases faster and in others slower than for sound material, but the mean rate corresponds to the rate for sound material. Tokaji *et al.* [31] studied fatigue crack propagation and crack closure in spheroidal-graphite cast irons with different microstructures: ferrite, pearlite, bull's eye and bainite. They found that the fatigue crack propagation rates plotted against the stress intensity factor range showed a microstructure dependence due to differing contributions of crack closure. However, they also found that the effect of these microstructures tended to disappear when the fatigue crack propagation data were plotted in terms of the effective stress intensity factor range, ΔK_{eff}, indicating that the microstructure affected crack closure behavior, but not the intrinsic fatigue crack propagation resistance. In terms of the effective stress intensity, the fatigue crack propagation was the same for all the microstructures they studied. They remarked that, in fatigue crack propagation, coarser microstructures would result in more remarkable deflections in the crack path which would lead to a rougher fracture surface, and enhanced crack closure. As a consequence, such microstructures should give an excellent fatigue crack propagation resistance in terms of ΔK.

1.6 Non Damaging Defects in Fatigue

It is generally accepted by most investigators that the fatigue strength of a material which contains inclusions or defects is lower than that which is defect-free. However, a specimen may include a defect and have the same fatigue limit as a defect-free specimen. In other words, material that is called defective is defective from the fatigue strength standpoint of view, only if the defect is able to induce a propagating crack that causes failure. It is known that the size of non damaging defects in fatigue decreases with increasing strength of material. The effect of small defects on fatigue strength was studied by Murakami and Endo [32]. They drilled small artificial holes, the diameter of which varied from 40 to 200 μm, in a low carbon and medium carbon steels. They observed non-propagating cracks of 100

μm in low carbon steel and 50 μm in medium carbon steel on plain specimens which were subjected to the fatigue limit stress. The critical diameters obtained from their fatigue tests using drilled artificial holes were 70 μm and 55 μm for the low and medium carbon steels, respectively, which were comparable to what they observed in plain specimens. They concluded that, it is expected that a steel specimen having initial defects in its matrix, the sizes of which are smaller than the critical size (L_O) of the crack found at fatigue limit, will not show the characteristics of a defective material (i.e. marked decrease of fatigue strength). L_O is a material constant and in general is greater than grain size. They explained that this critical length occurs because many cracks first initiate along slip bands in grains or on grain boundaries and afterward some of them propagate beyond grain boundaries and then cease to propagate. They added that after a crack initiates in a grain, the stress in the grain is released and the grain may be equivalently regarded as a traction free defect.

A unified method for the quantitative evaluation of the effect in fatigue of various defects of different irregularities in shape, size, directions, and locations was made possible by Murakami and Endo [33] who introduced a geometrical parameter which controls the fatigue strength of materials containing small defects. The geometrical parameter as a representative dimension is the square root of the area ($\sqrt{area}$) of a defect projected in the direction of the maximum tensile stress. Fatigue limits of defected materials were then described in terms of an equation and non damaging defects were described in terms of a critical value of this projected area as follows:

$$\sigma_w^{n_1}\sqrt{area} = C_1 \qquad 1.3$$

$$\tau_w^{n_2}\sqrt{area} = C_2 \qquad 1.4$$

where σ_w is the fatigue strength in bending or tension-compression fatigue; τ_w is the torsional fatigue strength; n_1, n_2, C_1, C_2 are material constants. When the $\sqrt{area}$ is smaller than the critical value (L_O), the fatigue strength, σ_w, of the specimen containing the defect becomes equal to that of the plain specimen.

1.7 Fatigue Crack Shapes and Stress Intensity Factors

Due to the irregularities of defects shapes, directions, and configuration, it is very complicated and almost impossible to analyze stress concentration and stress distribution in the vicinity of defects, especially when it is a three dimensional defect. However, irregular planar defects were studied [34] and were found to have locally maximum and minimum stress intensity factors, respectively, at convex and concave corners on their fronts as shown in Figure 1.4.

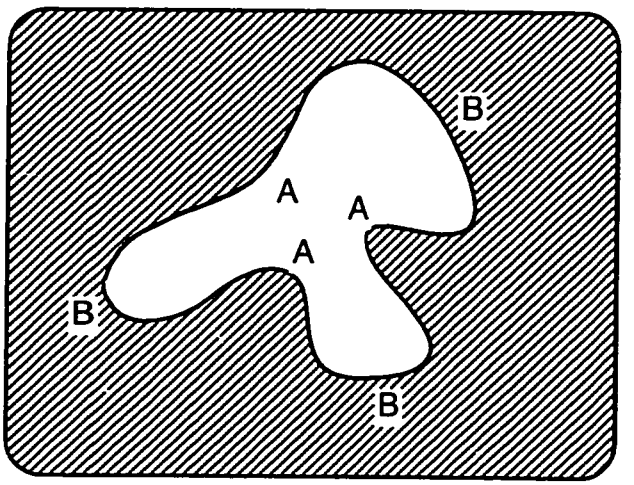

Figure 1.4 Internal defect with convex (A) and concave (B) aspects [34]

The growth increments of points such as A are high, and points such as B are low, and the protrusion rapidly becomes smoothened-out by the advance of the surrounding crack. It has been also found that if an irregular defect is allowed to grow indefinitely, it will attain a regular shape such that the stress intensity factor is approximately constant around its front. BS PD 6493 and ASME X1 codes of practice recharactarize surface and surface breaking irregular defects as either ellipses or semi-ellipses.

Gilchrist and Smith [34] in their study showed that, for an internal near-surface elliptical defect, the initial defect growth prior to breakout is quite small and during stages succeeding the breakout, the crack growth rate along the external surface is significantly higher than at other points on the crack front. They added that this crack growth becomes stable as the defect assumes a thumbnail profile growing in a

self-similar manner having an equal stress intensity factor around its front as shown in Figure 1.5.

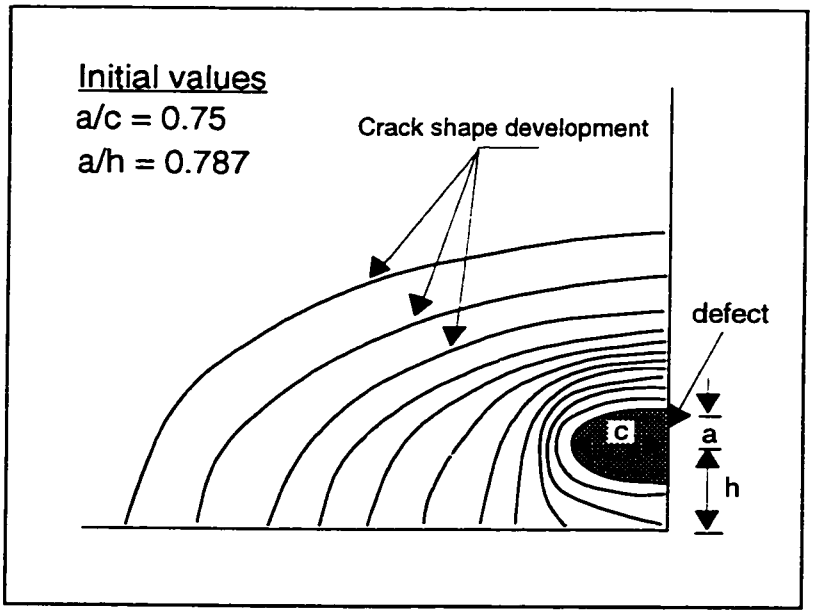

Figure 1.5 A schematic of shape development of an internally initiated elliptical defect subjected to tension fatigue [34]

The stress intensity factor is the key ingredient in fatigue failure predictions. It should be determined for the particular geometry and loading in question at various stages of crack growth. Springfield and Jung [35] examined the stress intensity distributions for circular surface flaws in the roots of fillets in rods loaded by remote tension. Nord [36] presented the stress intensity factor solution for hyperbolic cracks in threaded rods. Shivakumar and Neuman [37] presented the stress intensity factor solutions for semi-elliptical and quarter-elliptical corner cracks emanating from a semi-circular notch in a tension specimen. All previous work has been done for two dimensional flaws located at a stress concentration region such as fillets or notches. Other than this, there appears to be no work done for three dimensional flaws.

1.8 Fatigue Life Prediction Models

1.8.1 Fatigue Crack Initiation

For many years, it was assumed in design that most of the fatigue life of initially uncracked components was spent in "initiating a crack of engineering size". This size was variously taken as the crack length at which a small fatigue specimen failed or as some observable size. In terms of our current understanding of the progress of fatigue processes, this initiation phase consists of the following:

1- Cyclic slip band formation

2- Crack initiation in a slip band

3- Growth of the initiated microcrack to the defined "initiation size".

Not included in the "initiation phase' are the subsequent growth of the initiated microcrack and the final fracture.

It has been suggested that cyclic slip and crack initiation phases are short enough to be ignored for service loading, and the fatigue life can be represented by the propagation of a small crack from the size of a slip band crack to the size at which fracture occurs. This section reports some of the studies concerned with the early stages of fatigue.

Sato and Shimada [38] investigated local strain at the notch root and its effect on fatigue crack initiation in four metals, which were a low carbon steel (S45C), an aluminum alloy (5052), a stainless steel (SUS304), and brass (Cu-Zn). They proposed an evaluation method for fatigue crack initiation. This method assumes that the measured maximum strain behavior at the region local to the notch root during fatigue tests could systematically explain the crack initiation mechanism. They used a real time, fine-grid method for measuring their local strain. In this method they engraved cross-line grids with a pitch of 25.4 μm by electroplating the specimen to about 2 μm in depth. They took photographs of the grid near the notch root continuously through an optical microscope, and the strains at the notch root were obtained by measuring the deformation of the grid on the negative film. They presented the relationship for the local maximum strain, ε_{max}, versus fatigue cycles, N, as shown in Figure 1.6. The relationship showed that for the different materials the maximum strain value at the first cycle of the fatigue test decreases rapidly and then increases gradually and monotonically with number of cycles. After this

process, the presence of a small crack was confirmed at the notch root. They found that for the four materials studied, the maximum local strain value at the first cycle of the fatigue test coincided with that at crack initiation. The maximum strain defined from the cyclic strain changes at the notch root was proposed then as one possible parameter for estimating fatigue crack initiation life. The crack initiation point was determined by two methods. One was the confirmation of an initiated small crack which had propagated 10-15 μm from the notch root by using microscopic observation. The second used the "crooked point" on the curve of maximum strain versus number of cycles, as shown in Figure 1.6. Liu *et al.* [19] evaluated fatigue crack initiation at inclusions in fully pearlitic steels. They used acoustic emission to detect the onset of crack initiation during fatigue testing. Results revealed that crack initiation occurred at elongated inclusions. They observed three different mechanisms for fatigue crack initiation:

1- Microcrack initiation in a local deformation band ahead of the inclusion.

2- Interfacial surface decoherence.

3- An inclusion breaks and acts as a crack.

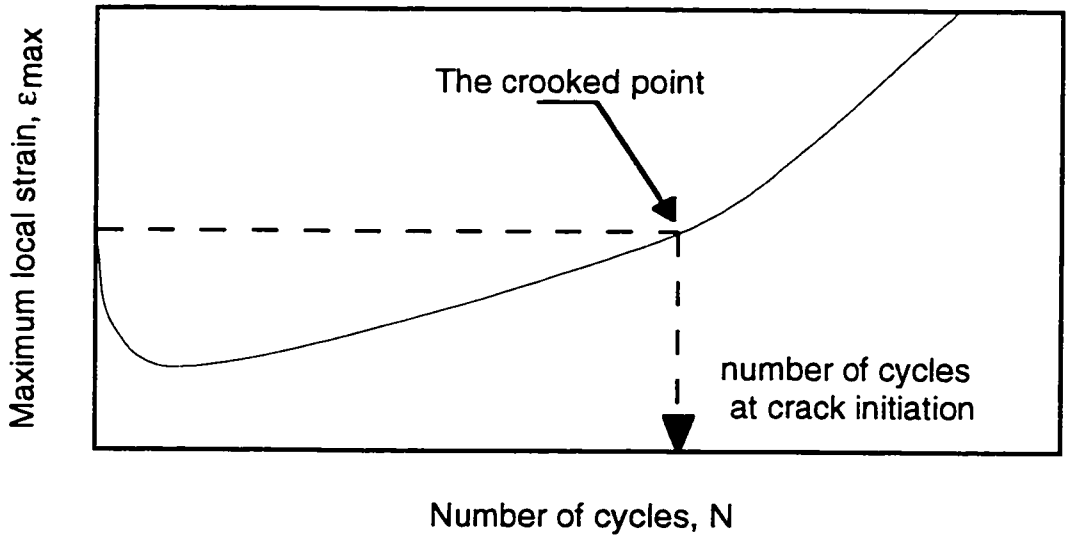

Figure 1.6 The relation between maximum strain and number of cycles [38]

Although most engineering structures and components are designed such that nominal loads remain elastic, stress concentrations often cause plastic strains to develop in the vicinity of notches. Because of the constraint imposed by the elastically stressed material surrounding the plastic zone, deformation at the notch

root is considered to be strain controlled. The local strain-life approach has gained acceptance as a useful method of evaluating the fatigue life of a notched component. Early fatigue research showed that damage is dependent on plastic deformation or strain. In the strain-life approach, the plastic strain or deformation is directly measured and quantified. Failure of the component is assumed to occur when the "equally stressed volume of material" fails, see Figure 1.7 [39]. Because of this, strain-life methods are often considered "initiation" life estimates. The strain-life approach was initially developed in response to the need to analyse fatigue problems involving fairly short fatigue lives. Subsequently it became clear that service loadings of many machines, vehicles, and structures include occasional severe events that can best be evaluated using a strain-based approach. One example include loadings on aircraft due to gusts of wind in storms, and also loads due to combat maneuvers of fighter aircraft. Fatigue life prediction using a strain-life approach is discussed in chapter 5.

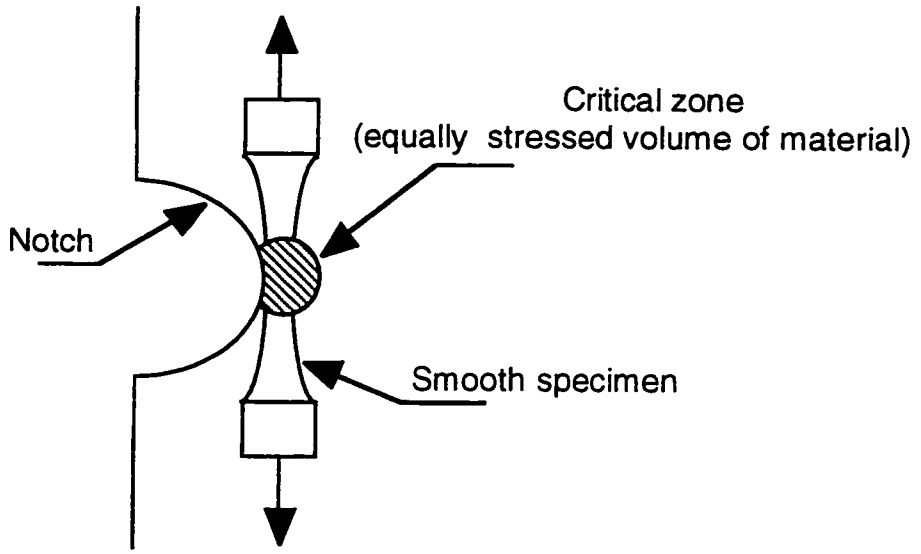

Figure 1.7 Equally stressed volume of material [39]

1.8.2 Fatigue Crack Propagation

Fatigue crack propagation can be divided into three phases:

1- *The growth of a microcrack, (short fatigue crack growth).* This phase includes microstructurally and physically small crack growth. A schematic plot for the threshold stress, for fully reversed constant-amplitude loading crack growth, on

logarithmic co-ordinates of threshold stress versus crack length, is shown in Figure 1.8. The Figure shows the regimes of short and long crack growth.

In the microstructurally short crack regime, cracks may grow temporarily at stress levels below the fatigue limit but will stop at barriers. The interaction of a small fatigue crack with a microstructural barrier, such as a grain boundary or a secondary phase, causes the following:

a- When a small crack approaches a microstructural barrier it will decelerate or arrest due to the barrier and will grow quickly once it overcomes the barrier.

b- The major retardation effect of the microstructural barrier to small fatigue crack growth is within the first few grains. As the crack propagates, the microstructural barrier effect becomes less.

c- The influence of the microstructural barrier on the growth of a small fatigue crack is greatest when the stress range is close to the fatigue limit stress range. As the stress range becomes larger, the effect of barriers rapidly reduces as does the fraction of the fatigue life spent in the short crack regime.

In the physically short crack regime, the threshold stress increases as the crack length becomes shorter but falls further below the value associated with LEFM, as shown in Figure 1.8, until, at the end of the regime, it reaches the fatigue limit for the material. In other words, these cracks can propagate at fatigue threshold stresses below both the fatigue limit and the long crack threshold stress given by ΔK_{th}. Taylor [40], using criteria for the validity of LEFM, suggested that L_2 shown in Figure 1.8 be defined by the greater of 10 times the metallurgical barrier spacing or 10 times the grain size. On the other hand, Kendall *et al.* [41] and Blom *et al.* [42] found that for steels and high strength aluminum alloys, experimental evidence indicated that LEFM analysis was adequate if closure was taken into account. The emphasis on LEFM applicability is not very important since a strain-based intensity factor [43] which becomes identical to the LEFM for elastic strains and identical to J at inelastic strain levels adequately correlated crack growth in the physically short crack regime with that of long cracks.

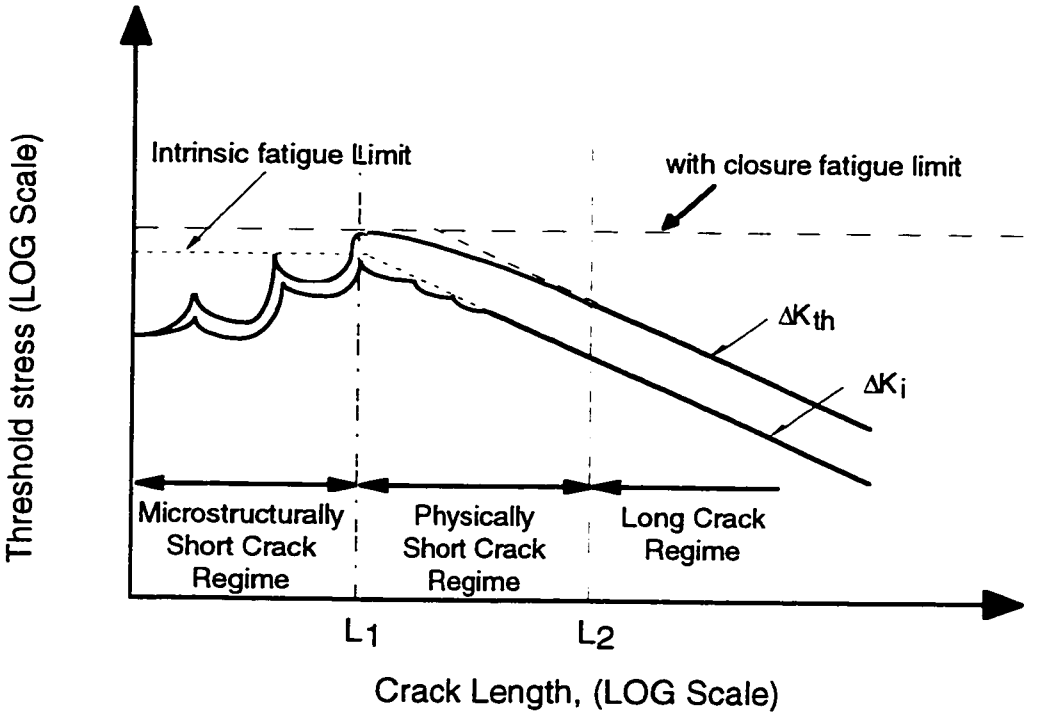

Figure 1.8 Variation of threshold stress with crack length

Blom *et al.* [42], Kendall *et al.* [41], and Soniak and Remy [44] all found that measurable crack closure began at L_1 and showed an initially steep build up that tapered off to a steady state value for long cracks at L_2, Figure 1.9. When these closure measurements were used to deduce effective stress intensities for short cracks, data for long and short cracks fell together on the intrinsic curve for long cracks. These authors suggested that once closure was accounted for, the long crack regime could be considered to begin at L_1. The fraction of the fatigue life spent propagating a crack through the metallurgically short crack regime represents almost all the fatigue life at the fatigue limit but rapidly decreases to a negligible fraction as the strain amplitude increases [45]. Figure 1.10 [46] illustrates this trend for a low carbon steel. Topper *et al.* [45] noted that this feature of short crack growth becomes important in variable-amplitude fatigue in which the first few large load cycles will provide enough local cyclic plasticity to rapidly advance a crack through the metallurgically short crack regime. They added that, the fact that the period spent in the metallurgically short crack regime (Zone 1) in many practical applications does not represent a significant fraction of fatigue life allows simplified fracture mechanics models applicable to post-Zone 1 fatigue behavior to be extended to this regime without serious errors in fatigue life prediction. A strain-

based short-crack fracture mechanics model by El-Haddad *et al.* [47], which uses the strain-based intensity factor mentioned earlier, is one of such models.

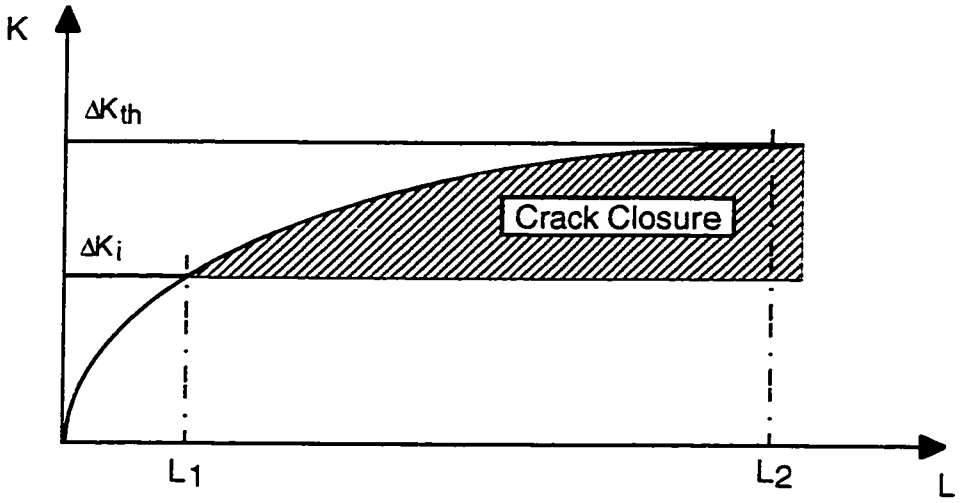

Figure 1.9 Variation of threshold stress intensity factor with crack length [45]

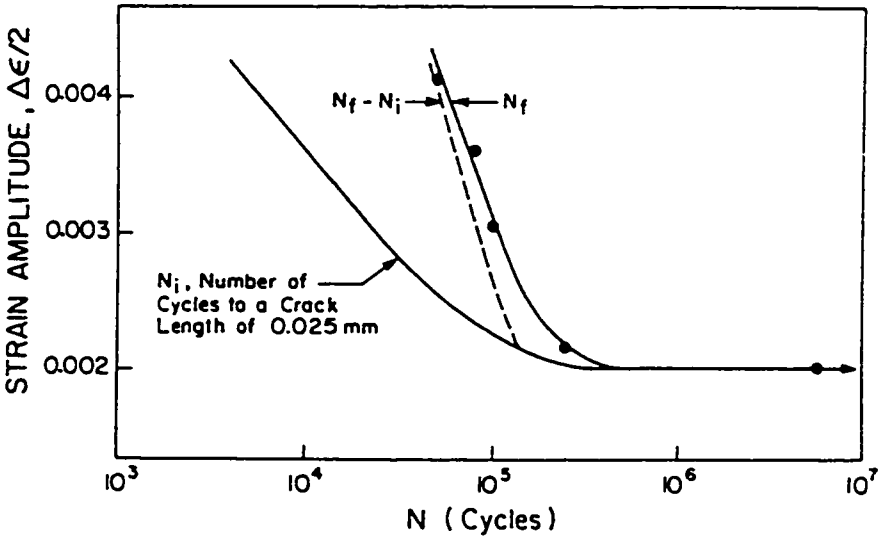

Figure 1.10 Typical strain-life diagram for a low carbon steel [46]

Topper *et al.* [45], in explaining the crack propagation of short cracks from notches, noted that the propagation of a crack through the length, L_1, requires that the stress in a constant-amplitude test be equal to the fatigue limit up to that length. They also added that if a notch is blunt, so that the stress concentration of a crack in a notch at a length L_1 is little different than K_t, a fatigue limit stress in the notch approximately equal to the material fatigue limit divided by K_t will be adequate to propagate the crack. If, on the other hand, the notch depth becomes very small then a much higher stress will be required since the stress will decrease significantly over the distance L_1, otherwise crack propagation will stop when the crack tip stress reaches the fatigue limit. They explained that a crack may also arrest in the physically short crack regime in which the threshold stress intensity is increasing with crack closure, if at some point the applied ΔK becomes less than ΔK_{th}. These conditions are shown in Figure 1.11. At ΔS_2, the stress level is high enough to drive a crack through the microstructurally short crack regime, but the crack is arrested as increasing crack closure in the physically short crack regime increases the threshold stress intensity above the applied ΔK. The minimum stress for continuous crack propagation, ΔS_1, gives a ΔK versus L curve that becomes tangent to, but does not fall below, the threshold curve.

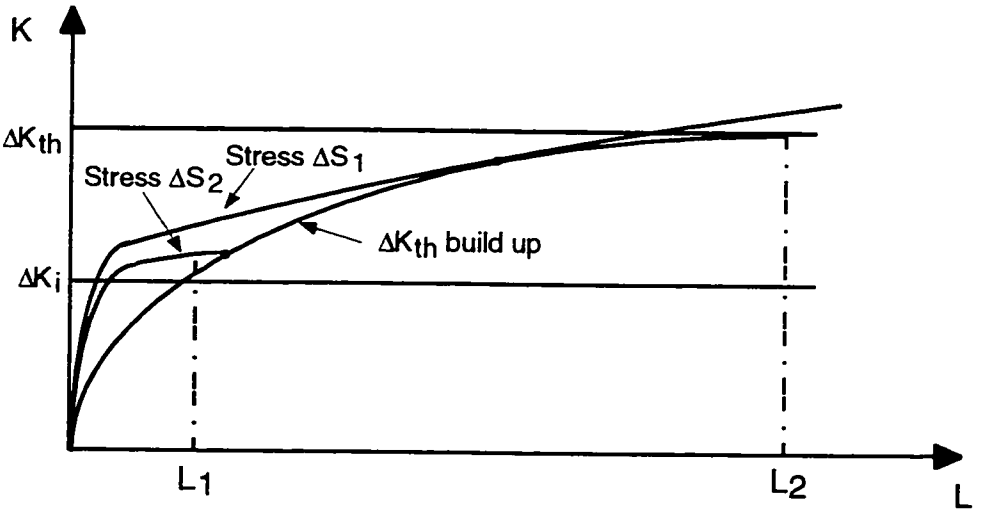

Figure 1.11 Variation of stress intensity factor with crack length for a crack in a notch [45]

2- *The growth of a macrocrack, (long fatigue crack growth).* This phase includes the growth of a long fatigue crack using Linear Elastic Fracture Mechanics (LEFM) principles. These principles are used to relate the stress magnitude and distribution near the crack tip to the following:

a- The remote stress applied to the cracked component

b- The crack size and shape

c- The material properties of the cracked component.

The stress intensity factor K was introduced to define the magnitude of the local stresses around the crack tip and takes the general form given by

$$K = f(g)\sigma\sqrt{\pi a} \qquad 1.5$$

where σ is the remote stress applied, a is the crack length, and $f(g)$ is a correction factor that depends on specimen and crack geometry. Stress intensity factor solutions have been obtained for a variety of problems and published in handbook form [48-50]. For a given material and set of test conditions, the crack growth behavior can be described by the relationship between cyclic crack growth rate da / dN and stress intensity range ΔK as given in equation 1.1. A schematic for the crack growth curve plotted on a log-log scale is shown in Figure 1.12. At low growth rates, the curve generally becomes steep and approaches the fatigue crack growth threshold ΔK_{th}. The applied stress ratio, R, can have a significant effect on the crack growth rate. In general, for a constant ΔK, the more positive the stress ratio, R, the higher the crack growth rate until a closure free fully effective stress cycle is reached at which the crack growth rate is a maximum. Crack closure arguments are often used to explain the stress ratio effect of crack growth rates as well as environmental effects on ΔK_{th}. In addition, crack closure theories are very important in variable-amplitude fatigue crack growth predictions, which are discussed in chapter 5. Elber [51] observed that the surfaces of fatigue cracks close when the remotely applied load is still tensile and do not open again until a sufficiently high tensile load is obtained on the next loading cycle. He proposed that crack closure occurs as a result of crack-tip plasticity. As the crack grows, a wake of plastically deformed material is developed while the surrounding body remains elastic. Elber proposed that, as the component is unloaded, the

plastically "stretched" material causes the crack surfaces to contact each other before zero load is reached, Figure 1.13. Elber further introduced the idea of a crack opening stress which is defined as the value of applied stress at which the crack is just fully open, S_{op}. He suggested that the crack must be fully open for fatigue crack growth to occur:

$$\Delta K_{eff} = K_{max} - K_{open} \qquad 1.6$$

$$\Delta K = K_{max} - K_{min} \qquad 1.7$$

consequently,

$$\Delta K > \Delta K_{eff} \qquad 1.8$$

Therefore an effective stress intensity factor range, ΔK_{eff}, which is smaller than ΔK, should be used in fatigue crack growth predictions. Elber also proposed that ΔK_{eff} accounts for the R effect on growth rates. At higher values of R, less crack closure results and ΔK_{eff} becomes closer to ΔK because K_{open} approaches K_{min}.

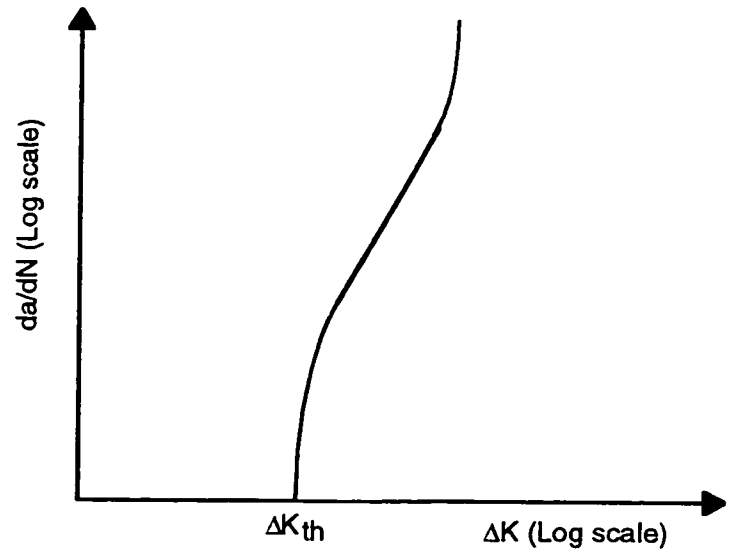

Figure 1.12 Schematic for fatigue crack growth rate versus stress intensity factor range

3- *Final failure.*

As the stress intensity factor reaches a critical value, K_c, unstable fracture occurs. This critical value of the stress intensity factor is known as the fracture toughness of the material. The fracture toughness can be considered as the limiting value of the stress intensity.

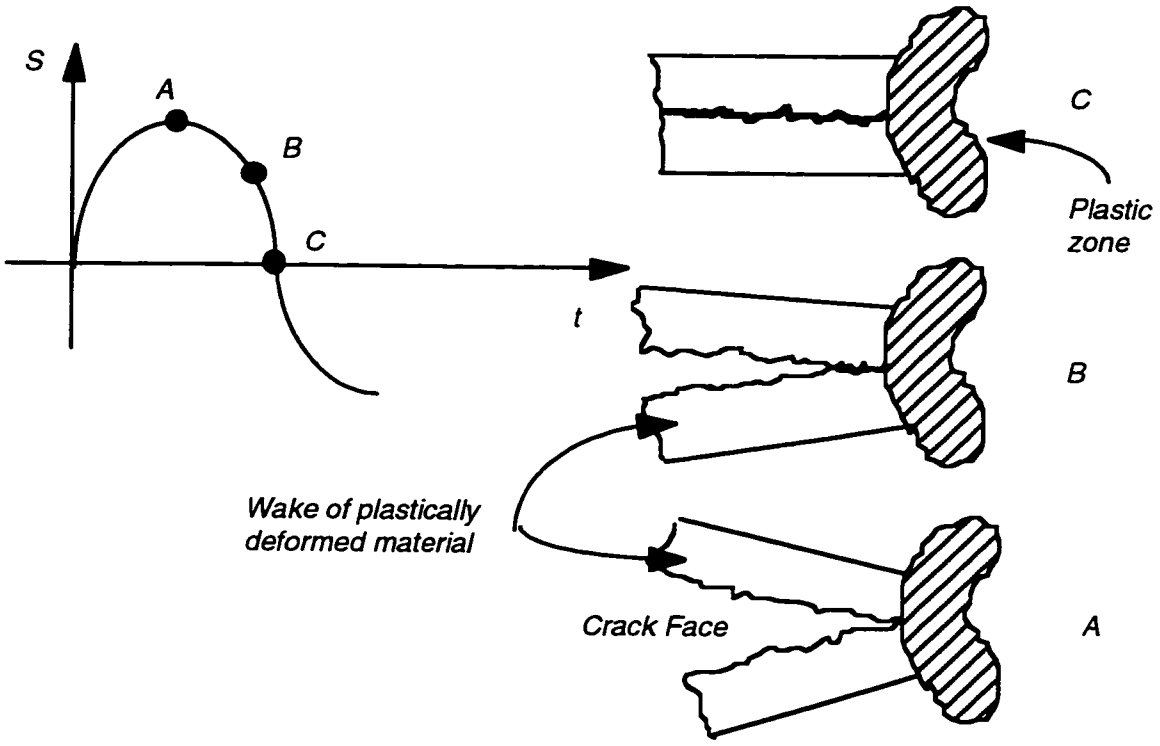

Figure 1.13 Crack closure phenomenon

Analytical predictions of fatigue crack propagation can be divided into two broad categories. The first category includes those methods or models proposed to describe crack propagation under constant-amplitude loading. The second category includes more complex models that take into account load sequence effects on crack growth, such as crack retardation, arrest and crack growth acceleration. The second category is needed to simulate real histories because, in practice, stresses or strains fluctuate randomly. The following section presents fatigue crack growth models for different materials under constant and variable-amplitude loadings.

Zhu [52] proposed a model for small fatigue crack growth based on the assumption that normalized Kitagawa-Takahashi diagrams (Figure 1.14) for different materials are similar. He stated that if the threshold stress range is normalized with respect to the material's fatigue limit, and the crack length is normalized with respect to the material's microstructural barrier spacing, then variations between the Kitagawa-Takahashi diagrams for different materials are very small, so that it is reasonable to assume that the normalized Kitagawa-Takahashi diagram is the same for different materials. The model simulates the stress-sensitive blocking effect of

microstructural barriers to small fatigue crack growth and describes the behavior of microstructurally small fatigue crack and physically small fatigue crack growth rates.

The model suggested in Zhu's study is expressed in the following form:

$$\frac{dc}{dN} = Af(\Delta K)^2 \qquad 1.9$$

where

$$f = (1-(\frac{\Delta\sigma_f}{\Delta\sigma_t})10^s)^2 \qquad 1.10$$

and

$$s = n\left(1-\sqrt{1+\left(\frac{\log(2c/D)}{m}\right)^2}\right) \qquad 1.11$$

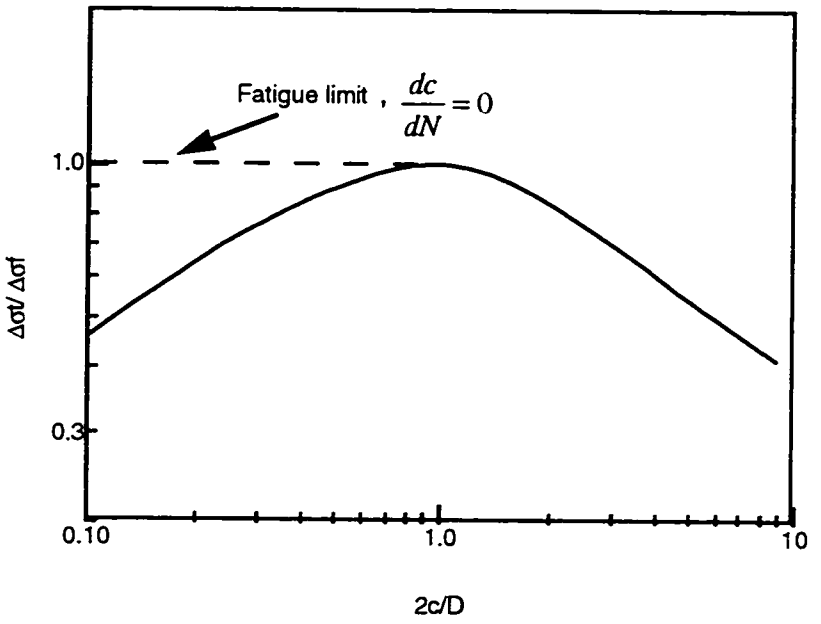

Figure 1.14 The normalized Kitagawa-Takahashi diagram [52]

where ΔK is the stress intensity factor range in MPa $\sqrt{m}$

$\frac{dc}{dN}$ is the crack growth rate in m/cycle

f is the barrier blocking factor

$\Delta\sigma_t$ is the applied stress range

$\Delta\sigma_f$ is the fatigue limit stress range

D is the spacing between barriers

c is half surface crack length

A, m, n are constants

To obtain the threshold stress for any crack length in the small crack regime, equations 1.10 and 1.11 are substituted into equation 1.9, and then equating dc/dN in equation 1.9 to zero gives

$$\log\left(\frac{\Delta\sigma_t}{\Delta\sigma_f}\right) = n\left(1-\sqrt{1+\left(\frac{\log(2c/D)}{m}\right)^2}\right) \qquad 1.12$$

This is the formula used to plot the Kitagawa-Takahashi diagram in the small crack regime. The parameters m and n are constant for different materials and the fatigue limit can be obtained from a conventional fatigue test, so it is only parameters A and D which have to be determined by fitting equation 1.9 to some small crack experimental data. Others [53-56] have established similar kinds of models for small fatigue crack growth. This model is distinguished from the other models in that it incorporates the material's fatigue limit.

1.8.2.1 Fatigue Life Prediction using Effective Strain Intensity Factors

El Haddad *et al.* [57] used an elastic-plastic fracture mechanics solution for short fatigue cracks to predict the fatigue life of smooth and notched specimens under constant-amplitude loading. The model they used admits plasticity by replacing the conventional stress term in the ΔK equation by a strain term, and accounts for the propagation of very short cracks by introducing an effective crack length which is equal to the actual crack length increased by a fictitious length l_o. The length l_o is a material constant and is calculated from the smooth specimen fatigue limit and the long crack threshold stress intensity as follows:

$$l_o = \frac{1}{\pi}\left(\frac{\Delta K_{th}}{F\Delta\sigma_f}\right)^2 \qquad 1.13$$

The length l_o constitutes an increasing fraction of the effective length for short crack lengths until, for the limiting case of an uncracked surface, it represents the

effective crack length at which the fatigue limit stress will just propagate a crack into the interior of the specimen. They concluded that strain-based intensity factor solutions successfully correlated data for the growth of short cracks in plastically strained notches with elastic, long crack results. Their predicted propagation life for smooth and notched specimens was within 50 % of the actual fatigue lives for all cases.

Gerald and Menegazzi [58] proposed a relatively general model to simulate crack propagation under variable-amplitude loading. The model describes the cycle-by-cycle progression of the crack. They used a Paris law model for propagation, and transient effects were introduced through the concept of an effective stress intensity factor range. The model was tried for different types of block loading histories in which the stress intensity factor range varies. The calculated results obtained with the model were very close to the experimental results. They concluded that, the transient effect predictions which the model provides are soundly corroborated by the most sophisticated experimental results available, which calls for a continuation of this model.

1.8.2.2 Fatigue Life Prediction for Materials containing Defects

Fatigue life has also been predicted and assessed for materials with casting defects. The models proposed tried to simulate the behavior of the material when casting defects of irregular shape (gas pores and shrinkage cavities) or of different nature than the matrix (inclusions) were present. Ting and Lawrence [59] modeled the effect of casting defects on the fatigue life of as-cast and smooth specimens of a AA319 cast aluminum alloy. The fatigue life was assumed to be the sum of a crack nucleation life and a crack propagation life, including the growth of short and long cracks. They quantified the fatigue initiating defect depth "D" by measuring the square root of its projected area, T, onto the plane normal to the applied stress direction. The defect depth was then estimated based on the known T and the aspect ratio AR which is defined as the crack depth divided by half-crack length on the surface as follows:

$$D = T\sqrt{AR} \qquad 1.14$$

The model then assumed a pore to be a notch having a diameter equal to D. They estimated the crack initiation life for a crack initiating at a notch using the local-strain approach. They also estimated the crack propagation life by integrating Paris power law expression from a specified nucleated crack length, l_t, as defined by Dowling [60], (see Figure 1.15 [61]), to a final crack length at failure. Dowling defined the crack length l_t which separates long cracks from short cracks to be in the range of 0.1ρ to 0.2ρ, where ρ is the notch-tip radius, and is given by

$$l_t = \frac{c}{\left(1.12\frac{K_t}{F}\right)^2 - 1} \qquad 1.15$$

where c is the notch radius
K_t is the elastic stress concentration factor
F is the crack shape factor

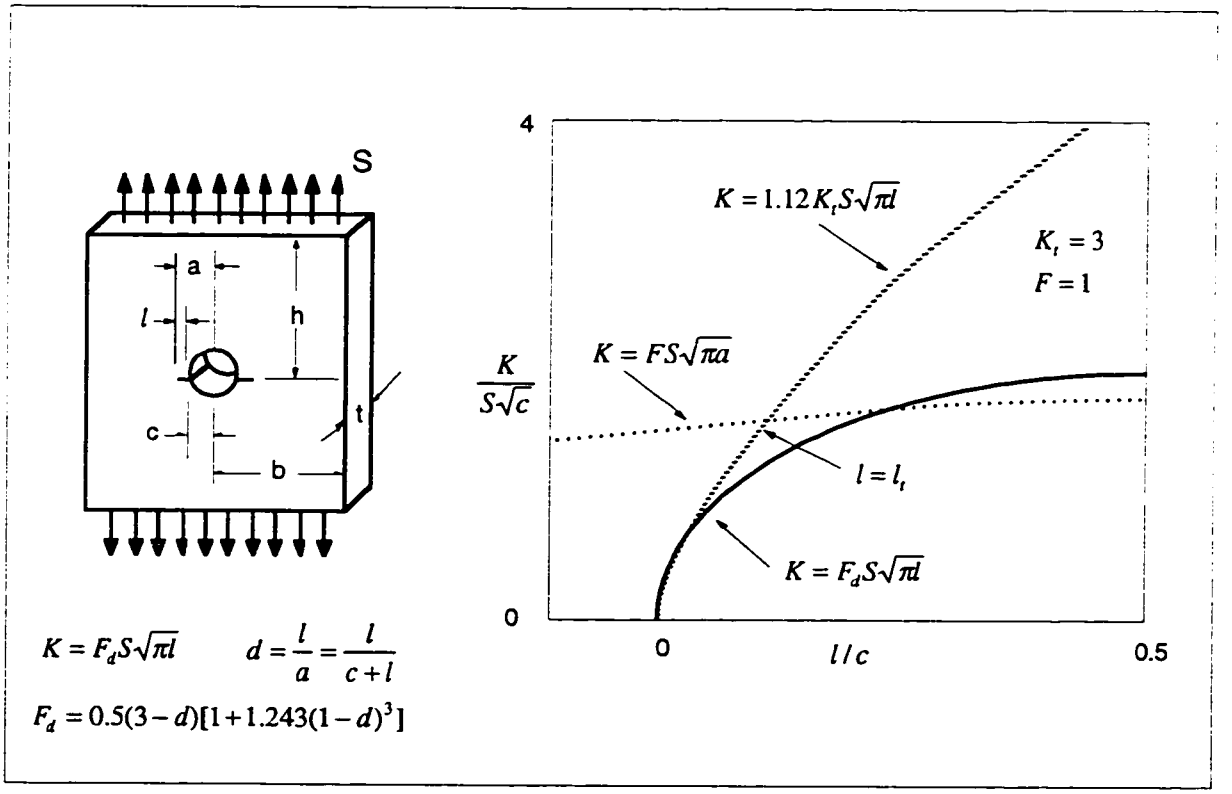

Figure 1.15 Stress intensities for a pair of cracks growing from a circular hole in a remotely loaded, wide plate [61] a<<b,h

Ting and Lawrence's model results indicated that the nucleation period for a crack emanating from a casting defect was negligible and that the effect of defect size on fatigue life was more severe for low stress ranges than for high stress ranges. Skalleurd *et al.* [21] assessed the fatigue life of aluminum alloys with casting defects. They found that gas pores with a maximum diameter larger than 0.2 mm resulted in a significant reduction of their fatigue life. They carried out numerical calculations to predict crack growth and fatigue life taking closure and short crack effects into account. In their model they simplified the irregular shape of surface shrinkage cavities into simple semi-circular or semi-elliptical shapes for two dimensional modeling and into a spherical shape for three dimensional modeling. This simplification was based on fractography which showed that the defects quickly develop into the simplified shapes as a crack grows. They suggested that the deviation of their predicted results from the experimental results was due to the non-linearity of the $da/dN - \Delta K_{eff}$ curve, especially near the fatigue threshold, which was not taken into account in the analysis. They suggested that the assumption of a linear crack growth relationship may be over simplified and the damage accumulation model based on ΔK_{eff} as the damage parameter should be improved. They concluded that cavities in components of cast Al-7Si-0.4Mg alloys have a significant effect on fatigue life and that when those pores are present the initiation period is very short. In their study they showed that a relatively simple fatigue crack growth model performed well in the analysis of cracks from casting defects.

Larson *et al.* [62] studied the fatigue life of hourglass shaped specimens of a hardened spring steel. They formulated a model for the probability of fatigue failure of the hourglass specimens. In that model, inclusions in the steel were assumed to be spherical in shape. Their work was based on the concept that microcracks initiate at the interface of inclusions with the matrix. The microcracks grow a small distance away from the interface until the notch effect dissipates or a microstructural barrier to propagation is encountered. In their model, which is based on linear elastic fracture mechanics, they assume that cracks are only open for positive loads so that the effective stress is equal to the difference between the maximum stress and the greater of the minimum stress and zero. They studied two different criteria for crack arrest at inclusions. In the first, it was assumed that cracks at inclusions could be represented by penny shaped cracks of the same diameter as the inclusion. In the second, a more realistic crack arrest criterion was suggested in which the stress

intensity of an annular crack at a spherical pore was considered. They added that the high rate of early propagation of cracks from inclusions might be due to the influence of the residual stresses around the inclusion resulting from different shrinkage rates of the inclusion and matrix during cooling after heat treatment. They also found that the presence of any defect (whether an inclusion or a pore) shortens the initiation fatigue life but this shortening is a negligible portion of the total fatigue life.

1.9 Purpose and Objectives of this Investigation

1.9.1 The General Problem

Most studies to date have examined the fatigue behavior of cast materials under constant- and variable-amplitude loading. The results of these studies led to the conclusion that the fatigue life of a material containing defects is shorter than a defect free material. The main thrust of this investigation is to study the fatigue behavior of a component having a flaw at a notch root. Another aim of this thesis is to provide a model which describes the growth of a flaw from a notch root and which predicts fatigue lives for a variety of fatigue loading histories.

Discontinuities give rise to stress concentrations at which fatigue cracks initiate. The presence of a flaw at a geometric stress concentration, such as a notch root, will further increase the local stresses and strains and reduce the fatigue strength. The fatigue strength reduction, in a notched specimen fatigue strength, due to a defect at notch root, and the effect of the ratio of the notch size to flaw size on these reductions will be investigated. The region in front of a notch root in which a defect affects fatigue crack growth will be determined. The reductions in fatigue strength from that for smooth and notched specimens due to the existence of a flaw at a notch root will be evaluated for different loading histories. The histories studied include constant-amplitude loading, an intermittent underload block loading history, and a SAE service load history. The hipping process and its usefulness in eliminating or closing a material's internal flaws and improving its fatigue life will also be evaluated.

A strain-based intensity factor crack growth model will be presented and will be used to predict the fatigue life of smooth specimens, notched specimens, and notched specimens with flaws at a notch root. The model will be used to study the effect of a variation in the flaw size and flaw position at the notch root on the fatigue life. The usefulness and accuracy of the model will also be evaluated by comparing its fatigue life predictions for smooth specimens, notched specimens, and notched specimens with a flaw at the notch root with the predictions obtained using conventional strain-life and effective strain-life methods, and fatigue data.

1.9.2 Objectives

The objectives for this investigation are the following:

1) Examine the effect of the variation of the flaw size and flaw position in a notch root and the relative size of the flaw to the notch size on fatigue strength.

2) Show to what extent a hipping process, which decreases the size of the casting defects, improves fatigue strength for constant- and variable-amplitude fatigue.

3) Examine reductions in fatigue strength from that of a notched specimen due to the presence of a defect at the notch root and to determine the effect of the ratio of notch size to flaw size on these reductions.

4) Model the fatigue life behavior of notched components containing defects in their stress concentration regions.

5) Predict, for 3 types of cast aluminum alloys; (Al 319, Al 390, and Al 206), their fatigue life under different types of load histories using a fracture mechanics crack growth model.

6) Examine the applicability of a fracture mechanics crack growth model to predicting fatigue life by comparing its results and those of conventional methods to experimentally measured data.

1.9.3 Outline

Chapter 2 provides the fatigue crack growth model used to predict the fatigue life of the cast aluminum materials examined in this study. An approximate stress intensity factor solution for a crack emanating from a flaw at a notch root is presented. The case of a crack emanating from a flaw at a distance away from the notch root is also dealt with.

In Chapter 3, the materials used in this study and their mechanical properties are presented, the experimental programs are described, and the different test techniques are explained. The experimental methodology which includes a new technique for producing closure free crack growth data and a new technique for measuring changes in crack opening stresses under a variable-amplitude loading history is explained.

Chapter 4 examines the fatigue behavior of smooth specimens, notched specimens, and notched specimens with a flaw at the notch root. Fatigue test results for hipped specimens with an artificial flaw at a notch root are compared with fatigue test results for as-cast specimens with a natural flaw at a notch root. This chapter also gives fatigue life predictions using a crack growth model presented in chapter 2. The effect of variations in flaw size and flaw position at the notch root on fatigue life are examined by predicting the fatigue life using the crack growth model.

Chapter 5 gives fatigue test results for smooth specimens, notched specimens, and notched specimens with a flaw at the notch root when a SAE loading history, corresponding to the torsion channel of the SAE GKN Grapple-Skidder history is applied. The fatigue strength reductions from those of a notched specimen due to the presence of a defect at notch root are determined. A comparison of the fatigue life predictions obtained using the conventional strain-life approach, the effective strain-life approach, and the crack growth model are presented.

Chapter 6 gives the general conclusions of this investigation.

CHAPTER 2

ANALYTICAL MODELING

2.1 Introduction

One of the main objectives of this research is to observe and model the fatigue behavior of notched cast aluminum components having cast inhomogeneities or flaws near or at the notch root. Some previous studies, reported in chapter 1, examined smooth cast metal specimens under constant- and variable-amplitude loading. However, it appears that the problem of flaws at notches has not been given much attention.

The study of the fatigue behavior of cast aluminum alloys for constant- and variable-amplitude loading which is presented in this thesis involved the following:

1- Fatigue tests of smooth specimens of cast and hipped metals.

2- Fatigue tests of notched specimens of cast and hipped metals.

3- Fatigue tests of notched specimens of cast and hipped metals when a flaw is located near or at the notch root.

It is the purpose of this chapter to model analytically the above mentioned fatigue behavior of smooth, notched, and notched with a flaw near or at notch root components under constant- and variable-amplitude loading.

2.2 The Fatigue Crack Growth Model Components

The fatigue crack growth model is based on a fracture mechanics approach for short and long cracks. It includes the following:

a- Closure-free stress intensity factor versus crack growth rate data.

b- Steady state and transient crack opening stress models.

c- Metal cyclic stress-strain data.

d- A strain-based intensity factor

e- Elastic and plastic notch strain relationships (Neuber's rule is used)

f- A Rainflow cycle counting technique.

The model calculates the fatigue life of a specimen or a component by numerical integration of crack growth on a cycle-by-cycle basis.

The steps in the use of the model are as follows:

1- Read, in no particular order, the input data, which includes

a- The specimen geometry in terms of the notch size, the flaw size, and the flaw distance from the notch root.

b- The material cyclic stress-strain data, Young's Modulus, yield strength, and fracture toughness(K_c).

c- Crack growth rate data obtained during closure-free crack growth.

d- Crack opening stress formulas and the material constants which will be used in the steady state and the transient crack opening stress formulas.

e- The stress or strain intensity factor solution for the given specimen geometry. (i.e. smooth, notched, or flaw near or at notch root).

2- Following the applied load history, reversal by reversal, the model calculates the local stresses and strains based on Neuber's formula, and the stress or strain intensity factor solutions for the specimen geometry.

3- A rainflow cycle counting technique is used to determine closed stress-strain loops. Once each cycle is closed damage calculations are made.

4- For each closed cycle, crack opening stress and strain is calculated based on the steady state and transient crack opening stress formulas.

5- The effective stresses and strains of each cycle are calculated by subtracting the crack opening stress or strain from the total stress or strain values of each closed cycle. The effective strains are used together with a surface strain concentration factor, that accounts for the increase of local strain experienced by short cracks, to calculate the effective strain intensity factor range (ΔK_{eff}).

6- The ΔK_{eff} value is used to enter the plot of the closure free crack growth rate versus effective stress intensity factor and read the value of the crack growth rate. The crack growth increment, ΔL, due to one cycle is then calculated and added to the total crack length.

7- The maximum stress intensity is compared with the fracture toughness, and the crack length is compared with one half the specimen width. If either the fracture toughness or one half the specimen width is exceeded, the calculation is stopped; otherwise the model continues with the next reversal as in step 2.

8- In case of a flaw at a notch root, the crack growth is calculated in the specimen width and length directions until the crack reaches the specimen edges; then the crack is considered to be a through crack growing in the length direction until fracture.

The algorithm for the model used is shown in Figure 2.1. The components of the model are described below.

2.2.1 Local Stresses and Strains

Local stresses and strains throughout the region in which the fatigue crack grows are inputs to the fatigue life prediction program. Semi-circular edge notched components, with and without a flaw at the notch root, were used in this research. Their local stresses and strains were calculated using Neuber's rule.

$$K_t = \sqrt{K_\sigma K_\varepsilon} \qquad 2.1$$

where $K_\sigma = \frac{\sigma}{S}$ is the stress concentration factor

$K_\varepsilon = \frac{\varepsilon}{e}$ is the strain concentration factor

K_t is the theoretical surface stress concentration factor

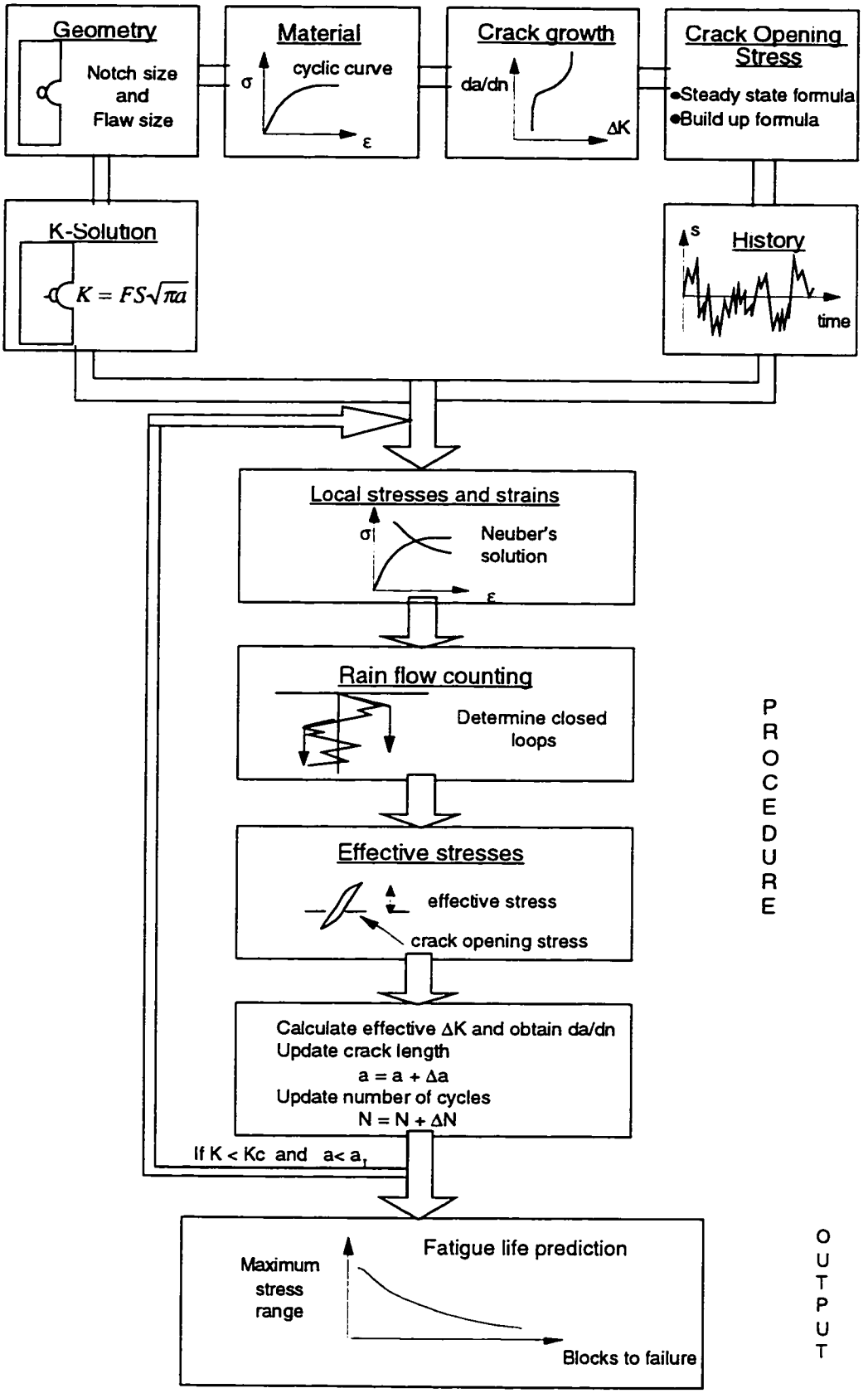

Figure 2.1 Algorithm for the fatigue life prediction crack growth model

Equation 2.1 can be applied for both nominally elastic and plastic stresses and strains. For nominally plastic stresses and strains it becomes as follows:

$$K_t^2 = \frac{\sigma}{S}\frac{\varepsilon}{e} \qquad 2.2$$

$$K_t^2 Se = \sigma\varepsilon \qquad 2.3$$

and for nominally elastic stresses and strains it becomes

$$K_t^2 = \frac{\sigma}{S}\frac{\varepsilon}{S/E} \qquad 2.4$$

$$K_t S = \sqrt{E\sigma\varepsilon} \qquad 2.5$$

and for locally elastic stresses and strains it becomes

$$K_t^2 S^2 = \sigma^2 \qquad 2.6$$

$$K_t S = \sigma \qquad 2.7$$

However, since we are dealing with a crack emanating from a notch or from a flaw at a notch root, the theoretical stress concentration factor, K_t, for the notch root is replaced by the elastic stress concentration factor, K_p, for a crack in a notch or a crack in a flaw at the notch root. The elastic stress concentration factor, K_p, accounts for the increase in crack tip stress due to a notch or a flaw in a notch. It can be calculated from the following formula if the stress intensity factor range, ΔK, is known:

$$K_p = \frac{\Delta K}{F\Delta S\sqrt{\pi l}} \qquad 2.8$$

where ΔK is the stress intensity factor range

F is a geometric factor that accounts for crack front shape and finite specimen size

K_p is the elastic stress concentration factor

ΔS is the nominal stress range, and

l is the crack length.

A stress intensity factor solution proposed by Topper and El-Haddad [63] was used for cracks emanating from a notch, while an approximate stress intensity factor solution [64] for the specimens with a defect at a notch root, which will be discussed later in section 2.2.5, has been calculated using the stress intensity factor solution for a circular crack emanating from a spherical cavity by Murakami *et al.* [65] in combination with the stress intensity factor solution for embedded semi-elliptical cracks in finite notched plates under tension by Newman [66]. The K_p was then used together with the cyclic stress-strain curve equation in Neuber's rule to obtain the local stresses and strains in the vicinity of the crack tip for inelastic conditions. Local strains were used to calculate the strain intensity factor for inelastic local strains as will be explained in section 2.2.5. The procedure for calculating the local stresses and strains is as follows:

a- Neuber's rule is used to derive the relation between local and nominal stresses and strains

$$K_p^{\,2} = K_\sigma K_\varepsilon \qquad 2.9$$

$$K_p^{\,2} = \frac{\Delta\sigma}{\Delta S}\frac{\Delta\varepsilon}{\Delta e} \qquad 2.10$$

$$K_p^{\,2}\Delta S\Delta e = \Delta\sigma\Delta\varepsilon \qquad 2.11$$

$$K_p\sqrt{\Delta S\Delta e} = \sqrt{\Delta\sigma\Delta\varepsilon} \qquad 2.12$$

b- The material's cyclic stress-strain equation, which can be described by the following formula,

$$\varepsilon = \frac{\sigma}{E} + \left(\frac{\sigma}{K'}\right)^{1/n'} \qquad 2.13$$

where K' is the cyclic strength coefficient
n' is the cyclic strain hardening exponent,

is used to derive and plot the relation between $\sqrt{\Delta\sigma\Delta\varepsilon}$ and $\Delta\varepsilon$ as shown, for a 319 cast aluminum alloy material, in Figure 2.2.

c- Local strains in the vicinity of the crack tip are obtained by entering the value of $K_p\sqrt{\Delta S\Delta e}$ in Figure 2.2, and reading the value of $\Delta\varepsilon$.

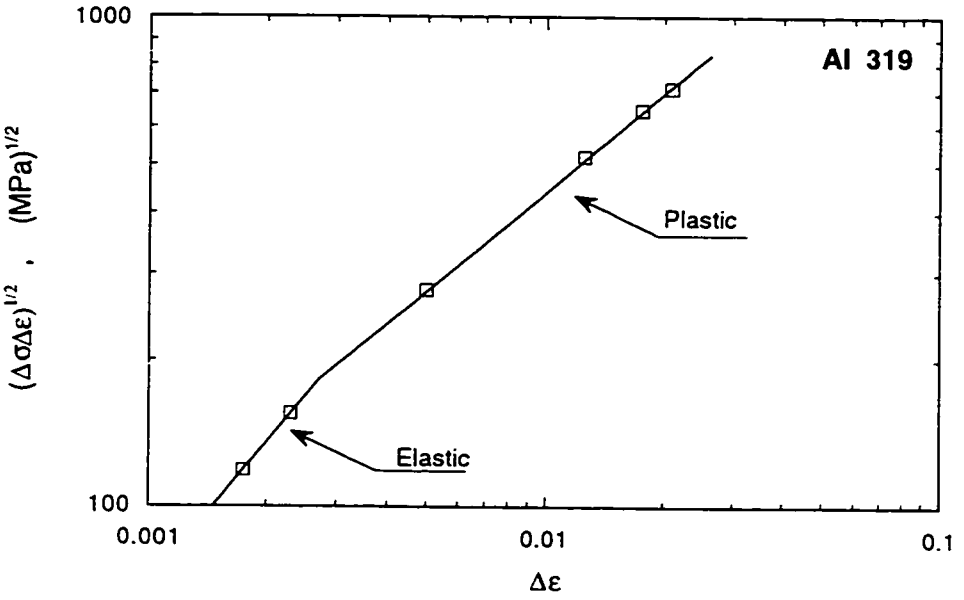

Figure 2.2 The relation between $\sqrt{\Delta\sigma\Delta\varepsilon}$ and $\Delta\varepsilon$ for a 319 cast aluminum alloy material

2.2.2 Cycle Counting

The complexity of variable-amplitude histories is reduced by changing the history into a number of events which can be compared to the available constant-amplitude test data [39]. This process of reducing a complex load history into a number of constant-amplitude events is called cycle counting. Early attempts at cycle counting involved a variety of procedures such as "level crossing counting", "peak counting", and "simple range counting". None of these procedures takes into account the closing of stress-strain loops and all of them result in breaking loops into smaller cycles. The rainflow counting technique [67], which takes the closing of stress-strain loops into account, was used to reduce the history applied in this investigation to closed stress-strain loops and to determine simultaneously the maximum and minimum stresses in each loop.

2.2.3 Crack Opening Stress Calculation Under Constant- and Variable-amplitude Loading

The crack growth model uses an effective strain intensity factor, in which only the effective portion of the applied stresses or strains (the portion of the cycle during which the crack is open) is considered in calculations. For a constant-amplitude loading history, a steady state crack opening stress formula is used. For a variable-amplitude history, both the steady state crack opening stress formula and a formula for transient changes in the crack opening stress are used to follow the changes in crack opening stress levels during the history.

2.2.3.1 The Steady State Crack Opening Stress Formula

An empirical model, proposed by DuQuesnay [68], for the steady-state crack opening stress under constant-amplitude loading, calibrated with experimental data, was used. The model, which has two experimentally determined constants, θ and φ, takes the following form,

$$S_{op} = \theta\sigma_{max}\left[1-\left(\frac{\sigma_{max}}{\sigma_y}\right)^2\right]+\varphi\sigma_{min} \qquad 2.14$$

where σ_{max} and σ_{min} are the local maximum and minimum notch root stresses in notched specimens, or the nominal maximum and minimum stresses in smooth specimens, and σ_y is the cyclic yield stress. In this study, crack opening stress measurements were performed using a high magnification microscope (900X) and values of θ=0.55 and of φ =0.2 were obtained. The crack opening stress measurements are described in chapter 4.

2.2.3.2 The Transient Crack Opening Stress Formula

For variable-amplitude loading, the crack opening stress level is not constant, but changes form cycle to cycle. It was found in an earlier study by the author and colleagues [69] that the crack opening stress drops immediately after the application of a compressive underload or a tensile overload, and then gradually increases at a decreasing rate with subsequent constant-amplitude cycling, as can be seen in Figure 2.3. It was also observed that the number of cycles needed for the crack

opening stress to recover to its steady state level after a compressive underload or a tensile overload depends on the "recovered stress range" (the stress difference between the post-underload or overload crack opening stress and the steady state crack opening stress). The greater the recovered stress range the larger the number of cycles needed. An empirical crack opening stress build-up formula was proposed to describe the crack opening stress behavior. The formula takes the following form,

$$\frac{(S_{op} - S_{opul})}{(S_{opss} - S_{opul})} = 1 - \psi Exp(-b(N / N_{0.8})^{a}) \qquad 2.15$$

where

ψ, **b** and **a** are material constants derived from curve fitting

S_{op} is the instantaneous crack opening stress

S_{opul} is the post-underload crack opening stress

S_{opss} is the steady state crack opening stress of the cycles following the underload

N is the number of cycles following the underload or overload.

$N_{0.8}$ is the number of cycles following the underload or overload at which the normalized recovered stress $(S_{op} - S_{opul})/(S_{opss} - S_{opul})$ reaches 80% of its steady state level

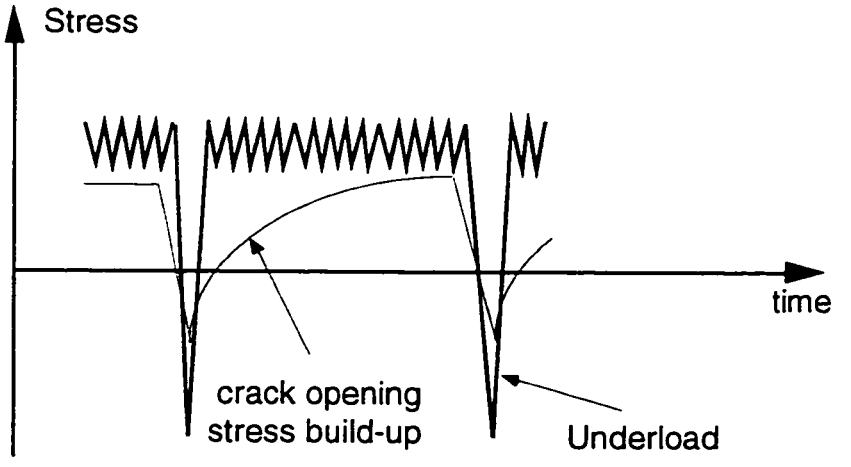

Figure 2.3 A schematic for crack opening stress build-up after underloads

Equation 2.14 was used with Equation 2.15 to calculate the crack opening stress levels for variable-amplitude loading histories. The variable-amplitude histories

used in this study are block loading histories and service load histories. In the block loading history, each block consisted of an underload followed by number of smaller constant-amplitude cycles. The number, amplitude, and stress ratio of the small cycles were changed from test to test.

2.2.4 Closure Free Crack Growth Rate

Paris and Erdogan [2] first proposed the fatigue crack propagation law,

$$\frac{da}{dN} = C(\Delta K)^m \qquad 2.16$$

where

da/dN is the fatigue crack growth rate per cycle
C and m are material constants which depend on environment, load ratio, and crack closure.

Subsequent investigators [70] have studied the effect of changes in load ratio and the accompanying changes in crack closure on fatigue crack growth. They found that the crack growth curves for various positive R ratios are normalized to a single curve by accounting for crack closure. This means that the crack driving force depends mainly on the effective portion of the fatigue cycle. Then equation 2.16 changes to

$$\frac{da}{dN} = C(\Delta K_{eff})^m \qquad 2.17$$

A variable-amplitude block loading history that gave fully open stress cycles was used to obtain a crack growth versus effective stress intensity curve. The loading block consisted of an underload cycle followed by a number of constant-amplitude small cycles at a high R ratio ($R > 0.75$). The procedure for the test will be described in chapter 3. The closure-free crack growth curve was used in the fatigue crack propagation model.

2.2.5 Strain Intensity Factor Solutions

In a fractographic examination, it was observed that the defects in the cast aluminum alloys were either gas pores or shrinkage cavities. Gas pores are almost spherical while shrinkage cavities are irregular in shape. A previous fractographic investigation by Skallerud *et al.* [21] on a cast aluminum alloy showed that cracks growing from irregular defects, of a given type, quickly approached a circular or elliptical shape. A finite element method (FEM) approach for calculating K and da/dN in irregularly shaped cracks investigated by Smith and Cooper [71] and Soboyejo *et al.* [72] also supported these simplified shapes. To account for the worst possible position of a defect from the point of view of fatigue, the defect was assumed to be at the surface of the specimen. The irregular shape of a shrinkage cavity was simplified to a spherical cavity which enclosed the gas pore as shown in Figure 2.4.

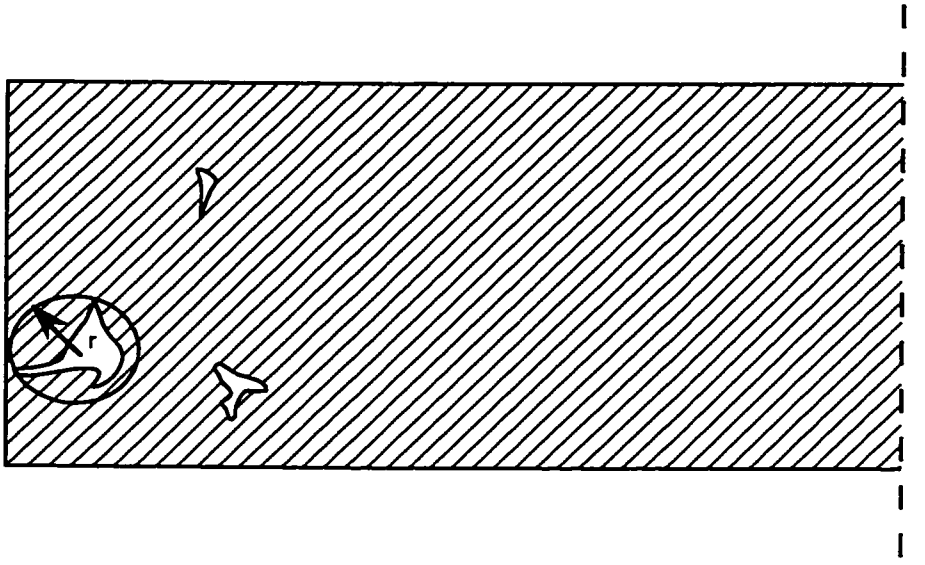

Figure 2.4 Defect geometry and its simplification

Flaws of the cast aluminum alloy in smooth specimens are modeled as edge notches having the same radius as that of the simplified defect or flaw. The elastic stress concentration factor, K_p, for a crack emanating from a notch was based on the equation proposed by Topper and El-Haddad [63]:

$$K_p = \sqrt{\frac{c}{2(\rho/2+l)}}\left(1+\frac{\rho}{2(\rho/2+l)}\right)\left(1+\frac{1}{2}\sqrt{\frac{\rho}{c}}\right) \qquad 2.18$$

where c is the notch radius

ρ is the radius curvature , which is equal to c in case of circular shapes

l is the crack length measured from the edge of the notch.

For a circular notch the term $(1+\frac{1}{2}\sqrt{\frac{\rho}{c}})$ is constant and can be substituted by $\frac{K_t}{2}$ while ρ can be substituted by c. Then equation 2.18 takes the following form,

$$K_p = \frac{K_t}{2}\sqrt{\frac{c/2}{c/2+l}}(1+\frac{c/2}{c/2+l}) \qquad 2.19$$

For large cracks, equation 2.19 should be replaced by $\sqrt{\frac{l+c}{l}}$ which assumes that the effective length of a crack is equal to the actual crack length, l, plus the notch depth.

Exact solutions for the elastic stress concentration factor solution, K_p, for a flaw in a notch are not available. An approximate stress intensity factor solution for a defect at the notch root has been calculated using available stress intensity factor solutions for individual notches and spherical cavities. The stress intensity factor solution , F_I, for a circular crack emanating from a spherical cavity by Murakami *et al.* [65] was used in combination with the stress intensity factor solution for embedded semi-elliptical cracks in finite notched plates under tension by Newman [66].

The dimensionless stress intensity factor solution, F_I, for a circular crack emanating from a spherical cavity given by Murakami *et al.* [65] is

$$F_I = \frac{K_I}{1.1215\eta\sigma\sqrt{\pi\lambda}} \qquad 2.20$$

in which λ is the crack length, and for spherical cavities $\eta = \frac{27}{14}$. This solution is shown in Figure 2.5. In the problem under study the cavity occurs at a notch root as shown in Figure 2.6. It is assumed that the stress, σ, applied to the flaw at the notch root is equal to a uniform stress, σ_{uf}, instead of the non linear notch stress field. This assumption is made because the stress intensity factor solution for a crack emanating from a flaw, by Murakami *et al.* [65], is for a uniform remote

applied stress. The uniform stress, σ_{uf}, is obtained by dividing the area, A, under the notch stress field by the crack length as shown in Figure 2.7. To check the accuracy of the uniform stress assumption, σ_{uf}, a simple case for a semi-elliptical surface crack in a smooth finite width plate was tested. The stress intensity factor at the deepest point of the semi-elliptical surface crack was calculated using a weight function (see Appendix A). The calculation was done first using a non linear notch stress field and then repeated using the uniform stress field assumption explained earlier. The results showed that the difference between the two solutions varies with the crack aspect ratio and that the uniform stress solution is smaller by 7 to 15 %, as shown in Figure 2.8. The uniform stress solution used was multiplied by a factor of 10% to represent the average of the difference between the solutions.

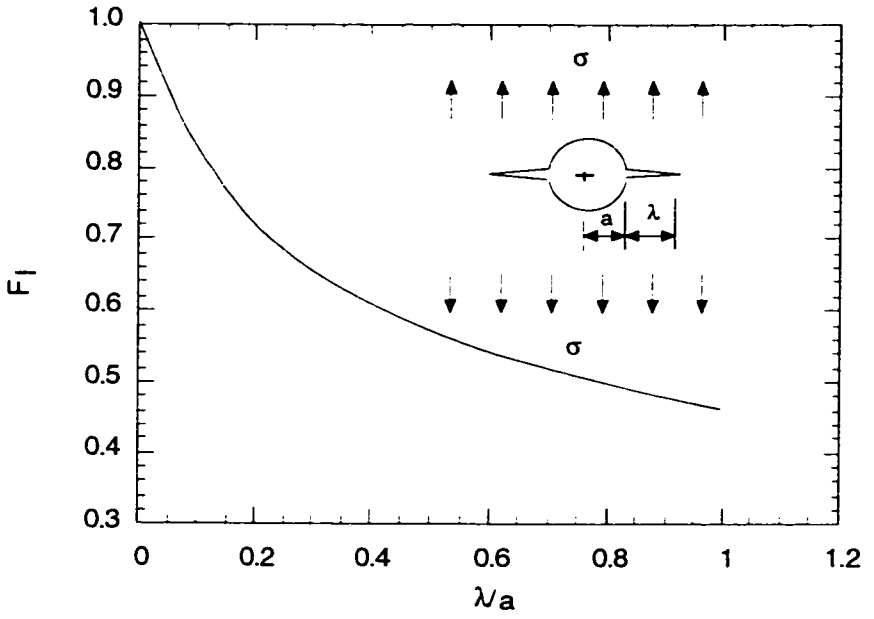

Figure 2.5 Dimensionless stress intensity factor for a circular crack emanating from a spherical cavity in an infinite solid body

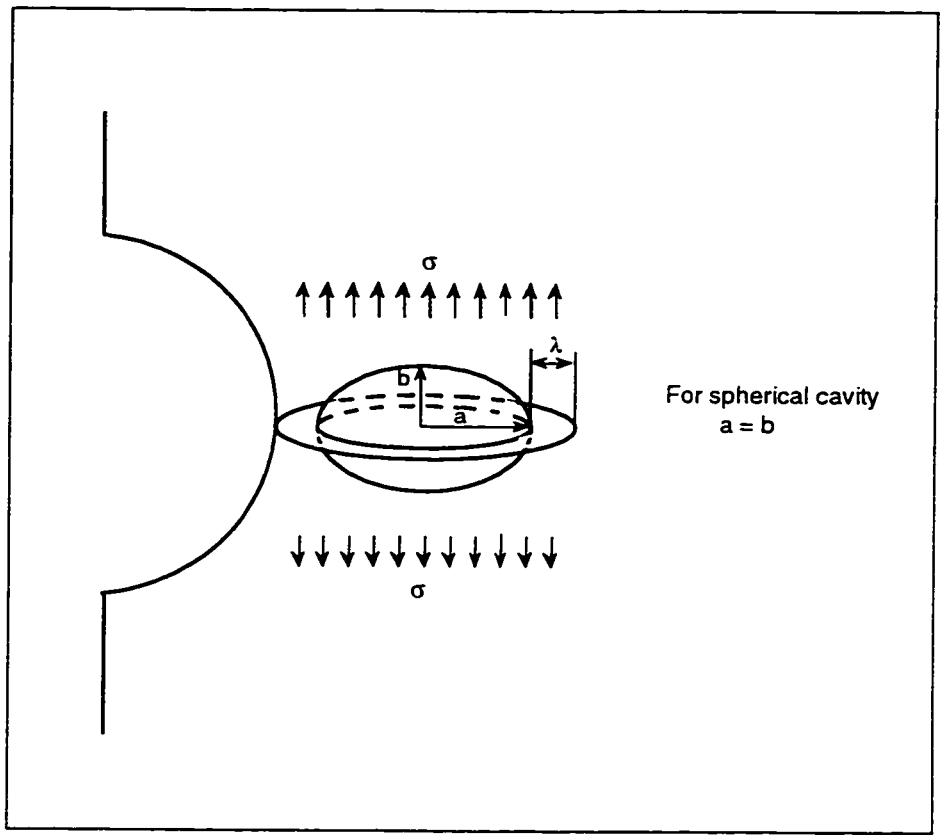

Figure 2.6 The position of the cavity at the notch root

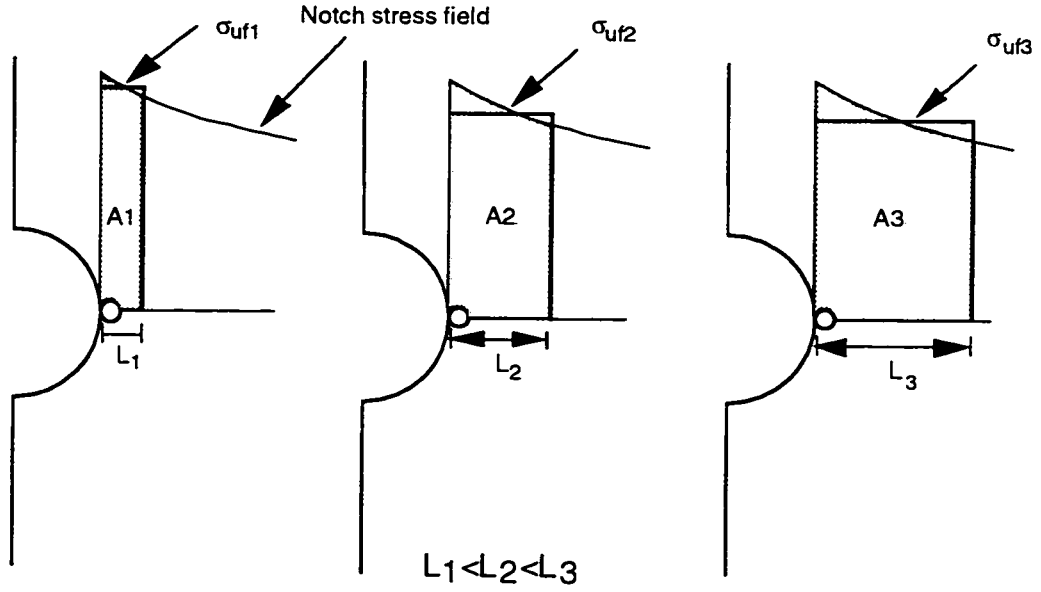

Figure 2.7 Schematic illustration for the determination of σ_{uf}

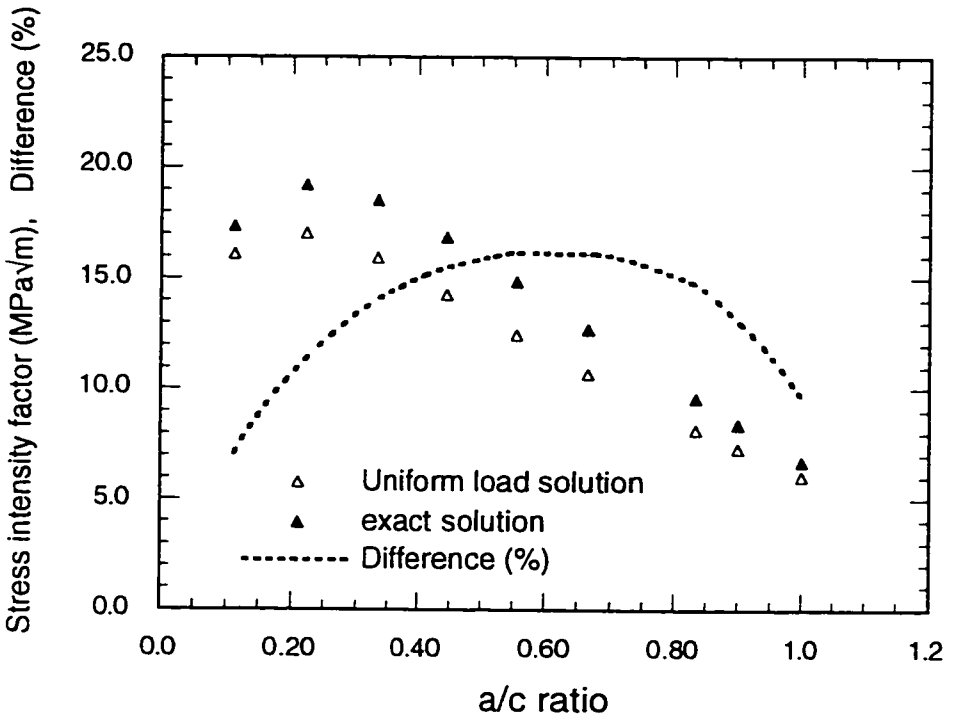

Figure 2.8 Difference between the uniform stress solution and the exact solution

After the crack had grown out of the stress field of the cavity, a notch stress field using a Newman [66] stress intensity factor solution for a semi-elliptical surface crack located at the center of a semi-circular edge notch was assumed. This stress intensity factor solution is given by the following equation:

$$K = S\sqrt{\frac{\pi a}{\Omega}}F\left(\frac{a}{c},\frac{a}{t},\frac{c}{r},\frac{c}{w},\frac{r}{t},\frac{r}{w},\phi\right) \qquad 2.21$$

where F is the boundary correction factor. The variables used in equations 2.21 to 2.42 are shown in Figure 2.9.

The shape factor Ω in equation 2.21 is given by

$$\Omega = 1+1.464(a/c)^{1.65} \qquad \text{for } a/c \le 1 \qquad 2.22$$

$$\Omega = 1+1.464(c/a)^{1.65} \qquad \text{for } a/c > 1 \qquad 2.23$$

The boundary correction factor equation for a semi-elliptical surface crack located at the center of a semi-circular edge notch subjected to remote uniform stress or uniform displacement is

$$F = [M_1 + M_2(a/t)^2 + M_3(a/t)^4]g_1g_2g_3g_4g_5f_\phi f_w \quad 2.24$$

$$M_1 = 1 \quad 2.25$$

$$M_2 = 0.05/[0.11 + (a/c)^{3/2}] \quad 2.26$$

$$M_3 = 0.29/[0.23 + (a/c)^{3/2}] \quad 2.27$$

$$g_1 = 1 - [(a/t)^4(2.6 - 2a/t)^{1/2}/(1 + 4a/c)]\cos\phi \quad 2.28$$

$$g_2 = [1 + 0.358\lambda + 1.425\lambda^2 - 1.578\lambda^3 + 2.156\lambda^4]/(1 + 0.08\lambda^2) \quad 2.29$$

$$\lambda = 1/[1 + (c/r)\cos(0.9\phi)] \quad 2.30$$

$$g_3 = 1 + 0.1(1 - \cos\phi)^2(1 - a/t)^{10} \quad 2.31$$

$$g_4 = K_t[0.36 - 0.032/(1 + c/r)^{1/2}] \quad 2.32$$

where K_t is the theoretical surface stress concentration factor.

$$g_5 = 1 + (a/c)^{1/2}[0.003(r/t)^2 + 0.035(r/t)(1 - \cos\phi)^3] - 0.35(a/t)^2(1 - 0.5a/c)^3\cos\phi \quad 2.33$$

$$f_w = 1 - 0.2\gamma + 9.4\gamma^2 - 19.4\gamma^3 + 27.1\gamma^4 \quad 2.34$$

$$\gamma = (a/t)^{1/2}(c + r)/w \quad 2.35$$

$$f_\phi = [(a/c)^2\cos^2\phi + \sin^2\phi]^{1/4} \quad 2.36$$

For a/c > 1

$$M_1 = (c/a)^{1/2}(1.04 - 0.04c/a) \quad 2.37$$

$$f_\phi = [(c/a)^2\sin^2\phi + \cos^2\phi]^{1/4} \quad 2.38$$

When the surface-crack length, 2a, reaches the sheet thickness, 2t, the stress intensity factors for a through crack emanating from a semi-circular notch subjected to remote uniform stress or uniform displacement is:

$$K = S\sqrt{\pi c}F_n(\frac{c}{w},\frac{c}{r},\frac{r}{w}) \qquad 2.39$$

The boundary correction factor F_n is:

$$F_n = f_1 g_4 f_w \qquad 2.40$$

where g_4 and f_w are as given before. The function f_1 is given by

$$f_1 = 1 + 0.358\lambda + 1.425\lambda^2 - 1.578\lambda^3 + 2.156\lambda^4 \qquad 2.41$$

$$\lambda = 1/(1 + c/r) \qquad 2.42$$

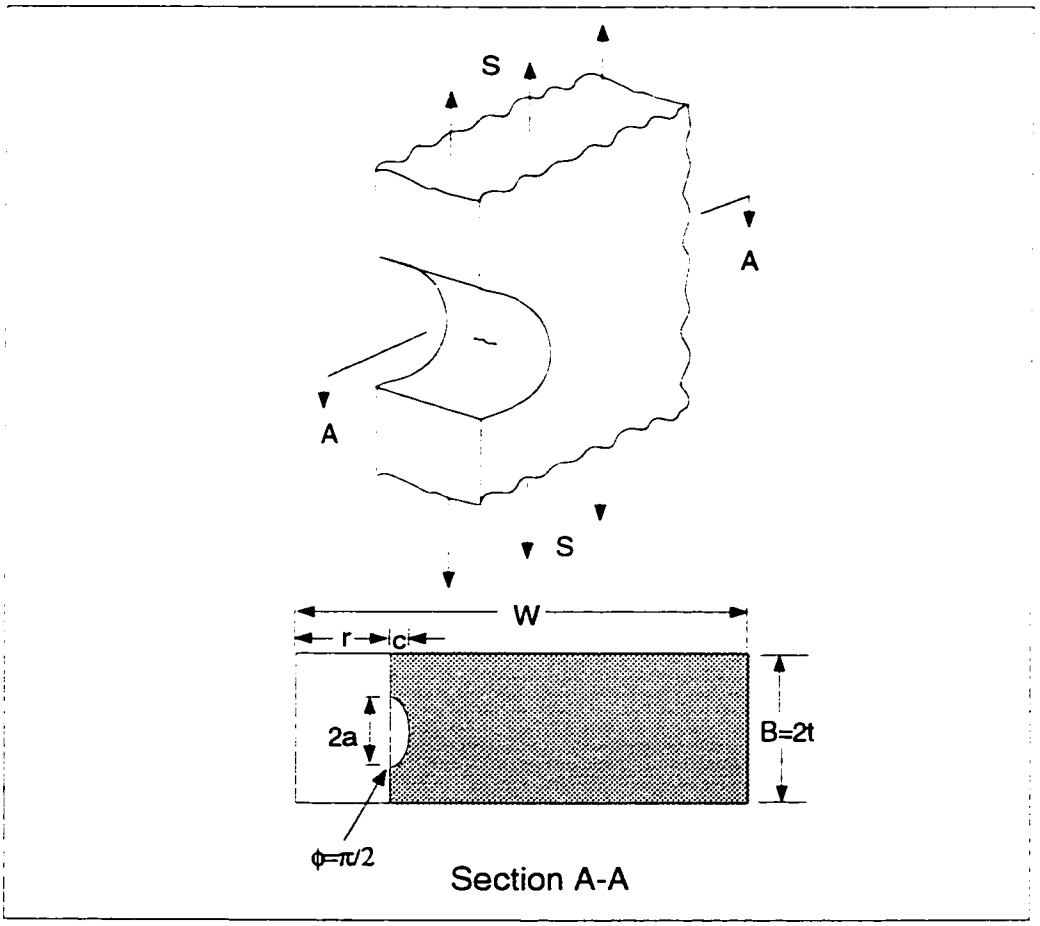

Figure 2.9 Surface crack at a notch [66]

The intensity factor solutions used in this investigation are strain-based intensity factor equations which are suitable for plastically strained short cracks and which

converge to the conventional linear elastic stress intensity for long cracks and elastic nominal stresses. This strain-based intensity factor, which includes a modification to describe the behavior of short cracks, replaces the conventional stress intensity factor which does not apply to small cracks. The strain-based K-solution used has the following form

$$\Delta K = F\Delta\varepsilon E Q_\varepsilon \sqrt{\pi l} \qquad 2.43$$

where
F is a geometric factor that accounts for crack front shape and finite specimen size, $\Delta\varepsilon$ is the local strain range, E is Young's Modulus, l is the crack length measured from the notch root and Q_ε is a surface strain concentration factor [73] that accounts for short crack behavior. The surface strain concentration factor can be expressed as [73]

$$Q_\varepsilon = \frac{\Delta\varepsilon}{\Delta e} = 1 + 5.3e^{-(\alpha l / D)} \qquad 2.44$$

where
D is the grain size in the crack growth direction, and α is a factor that accounts for the ease of cross slip in the material.

The surface strain concentration factor, Q_ε, decays rapidly with crack length and equation 2.43 converges to the long crack strain intensity factor equation which has the following form:

$$\Delta K = F\Delta\varepsilon E\sqrt{\pi l} \qquad 2.45$$

The effective strain intensity factor was calculated by replacing the total strain range $\Delta\varepsilon$ in equation 2.43 with the effective portion of the strain cycle. The steady state and built-up crack opening stress formulas, shown in section 2.2.3, were used to estimate the crack opening stress variation throughout the load history, as explained in chapter 5. Effective strain ranges were calculated using effective stress ranges and the elastic Young's Modulus if the local stresses and strains were completely elastic. For inelastic local stresses and strains, the crack opening strain was

calculated using the crack opening stress and the cyclic stress-strain curve. The effective strain was then obtained by subtracting the crack opening strain from the maximum strain. After substituting the effective strain range, $\Delta\varepsilon_{eff}$, in equation 2.43 it takes the following form:

$$\Delta K_{eff} = F\Delta\varepsilon_{eff} EQ_{\varepsilon}\sqrt{\pi l} \qquad 2.46$$

2.2.6 Shape Factor Estimates

The steady state shape for a single surface crack is a thumbnail shape with a geometrical shape factor of 0.72 [74]. This is typical at near endurance limit stress where only a single crack grows to cause failure. At high stress levels, multiple cracks are observed. They link up to form a dominant crack. As they link up, the shape of the crack elongates and the shape factor increases. The extreme shape factor for a straight through crack is 1.12 [75]. For this reason, F was assumed to have a value of 0.72 at low stress levels, near the fatigue limit, which increased linearly to 1.12 as the stress level reached twice the fatigue limit. For cracks in which the crack shape is known such as cracks from flaws at a notch root, the shape factor is calculated based on the crack length and depth.

2.2.7 Fatigue Life Prediction

The crack growth for a crack emanating from a flaw at a notch root, was calculated at the deepest point and on the surface until the crack reached the edges of the specimen. A fast crack growth was then assumed which drives the crack from a semi-elliptical to a through crack, i.e. No crack growth calculations were done and the crack was assumed to jump from a semi elliptical crack to a through crack. The crack growth stages for a crack around a flaw at the notch root, assumed in the model, are summarized in the following five stages, and are schematically shown in Figure 2.10:

1. Fast crack growth of the crack around the flaw to a semi-circular shape, i.e. No crack growth calculations were done and the crack around the flaw was assumed to jump to a semi-circular shape.

2. The growth of the semi-circular crack under the effect of the flaw and notch stress fields until the crack leaves the flaw stress field.
3. The growth of the crack under the effect of the notch stress field until the crack reaches the specimen edges. Note that in this case the crack growth rates in the depth and surface directions are different and that the crack assumes a semi-elliptical shape.
4. Fast crack growth from a semi-elliptical crack shape touching the specimen edges to a straight fronted through crack.
5. Growth of the through crack under the notch stress field until fracture.

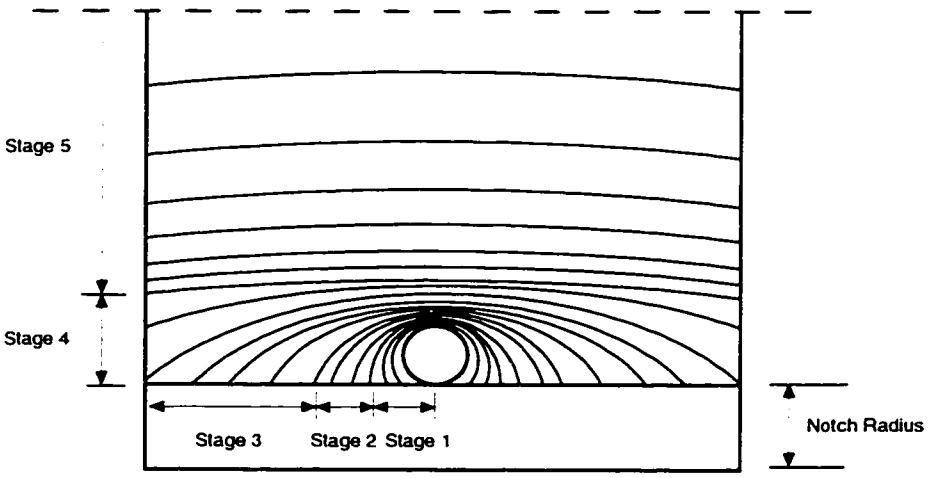

2.10 A schematic showing the crack growth stages for a flaw at notch root

Fatigue life prediction is handled by numerical integration along the reference closure-free crack growth curve between initial and final crack lengths l_0 and l_f as

$$N_f = \int_{l_i}^{l_f} \frac{da}{f(\Delta K_{eff})} \qquad 2.47$$

Basinski and Basinski [76] and Hunsche and Neumann [77] defined cracks as singularities in a crystal related to surface intrusions and extrusions deeper than 3μm developed in persistent slip bands. In this thesis, the value of l_i was assumed to be 3μm while l_f was determined by the onset of fast fracture. The integration was done every 30-50 cycles for the constant-amplitude loading, but the frequency of integration was increased to once every 10 cycles for variable-amplitude loading to allow accurate calculations of the effective stresses as the crack closure stress level built up, and was increased even more to a cycle-by-cycle calculation for service load histories.

2.3 Studies for a Flaw at a Distance from the Notch Root

It has been assumed in this chapter that the flaw is exactly at the notch root. Another case includes a flaw being at some distance from the notch root, but still affected by the notch stress field. Evidence for this has been observed on fracture surfaces of specimens. The following modifications in the crack growth stages are assumed in the model, and are schematically shown in Figure 2.11:

1. The growth of a crack around the flaw under the effect of the flaw and notch stress fields until the crack reaches the notch root edge.
2. Fast crack growth of the crack around the flaw to a semi-circular crack, i.e. No crack growth calculations were done and the crack around the flaw was assumed to jump to a semi-circular shape.
3. The growth of the crack under the effect of the notch stress field until the crack reaches the specimen edges. Note that in this case the crack growth rates in the depth and surface directions are different and the crack assumes a semi-elliptical shape.
4. Fast crack growth from a semi-elliptical crack shape touching the specimens edges to a straight fronted through crack.
5. Growth of the through crack under the notch stress field until fracture.

The same K-solution for a flaw at notch root is used, but in this case the crack in the depth direction is growing in two different directions. A crack growing away from the flaw and notch root on one side and a crack growing between the flaw and notch root on the other side.

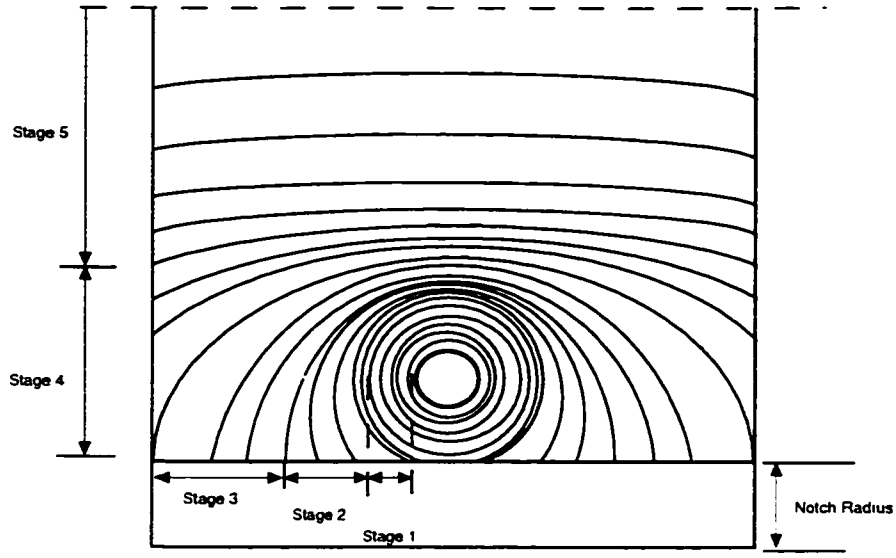

Figure 2.11 A schematic showing the crack growth stages for a flaw at a distance from the notch root

2.4. Summary

This chapter explained the fatigue crack growth model used to predict the fatigue life of smooth specimens, notched specimens, and notched specimens with a flaw at or near the notch root of a cast aluminum alloy. The fatigue crack growth model uses a fracture mechanics approach. It is based on an effective strain intensity factor, which includes a modification to describe the behavior of short cracks, elastic and plastic notch strain calculations based on Neuber's formula, and a reference crack growth rate curve obtained during closure-free crack growth. This chapter also described an approximate method for the calculation of the stress intensity factor solution for the case of a flaw at a notch root, using the available stress intensity factor solutions for individual flaws and notches.

CHAPTER 3

MATERIALS AND TEST TECHNIQUES

3.1 Materials

The materials used in this investigation are 206, 319, and 390 cast aluminum alloys in "high-gas" and "low-gas" conditions. The high-gas material had the number and size of the gas pores artificially increased while the low-gas material was cast in the normal manner. The material was supplied in the form of plates 6.35 mm thick in the as-cast and hipped conditions. Hipping is a process in which the cast material is subjected to a high pressure at high temperature and then slowly cooled down to eliminate internal flaws. The 319 cast aluminum alloy was the only material supplied in the hipped condition. The chemical composition and the mechanical properties of the materials are listed in Tables 3.1 and 3.2 to 3.5, respectively, and the monotonic and cyclic stress-strain curves are shown in Figures 3.1 to 3.4.

3.2 Specimens

3.2.1 Specimen Geometry and Preparation

All testing was carried out on flat specimens machined from the 6.35 mm thick plates of the material supplied. Flat smooth fatigue test specimens with dimensions of 12.7 mm(0.5") in width, 88.90 mm(3.5")in length, and 2.54 mm(0.1") or 3.556 mm(0.14") in thickness were used, as shown in Figure 3.5. Edge notched fatigue test specimens with dimensions of 25.4 mm(1.0")in width, 88.90 mm(3.5") in length, and 3.556 mm(0.14") in thickness were used for notched fatigue tests, and crack growth test specimens with dimensions of 44.45 mm(1.75") in width, and 2.54 mm(0.1") in thickness were used for stress intensity versus crack growth rate tests as shown in Figures 3.6 and 3.7, respectively.

The smooth and notched specimens were prepared in accordance with ASTM standard E606 for constant-amplitude low-cycle fatigue tests. The preparation included hand polishing of the gauge section in the loading axis direction with emery paper of grades 240, 400, 500, and 600. Final polishing was done for the crack growth test specimens using a metal polish which aided crack observations. In strain controlled tests an air-drying polyurethane (M-coat D from Micro-Measurement) was applied on the specimen edge or the location of the extensometer knife blades to decrease the possibility of a knife-edge failure and reduce slippage of the extensometer.

Table 3.1 Chemical composition (percentage by weight)

Alloy	Si	Cu	Cr	Mn	Mg	Fe	Ni
Al 206 (As-cast)	0.1	4.3	<0.01	0.37	0.26	0.03	<0.01
Al 319 (As-cast and Hipped)	5.9	3.4	0.07	0.38	0.25	0.91	0.07
Al 390 (As-cast)	17.3	4.8	<0.01	0.02	0.52	0.2	<0.01

Table 3.2 Mechanical properties of Al 206 (As-cast condition)

Mechanical properties	Units	Magnitude	
		High-gas	Low-gas
Modulus of Elasticity	MPa	67,000	67,000
Monotonic Tensile Yield Stress (0.2% offset)	MPa	264	243
Cyclic Yield Stress (0.2% offset)	MPa	315	315
Ultimate Tensile and Fracture Stress	MPa	332	314
Fracture Strain	%	3.34	3.8
Monotonic Strength Coefficient (K)	MPa	460	472
Monotonic Strain Hardening Exponent (n)		0.0874	0.1077

Table 3.3 Mechanical properties of Al 319 (As-cast condition)

Mechanical properties	Units	Magnitude	
		High-gas	Low-gas
Modulus of Elasticity	MPa	68,400	68,400
Monotonic Tensile Yield Stress (0.2% offset)	MPa	152	149
Cyclic Yield Stress (0.2% offset)	MPa	210	210
Ultimate Tensile and Fracture Stress	MPa	193	198
Fracture Strain	%	1.04	1.08
Monotonic Strength Coefficient (K)	MPa	480	495
Monotonic Strain Hardening Exponent (n)		0.1835	0.188

Table 3.4 Mechanical properties of Al 390 (As-cast condition)

Mechanical properties	Units	Magnitude	
		High-gas	Low-gas
Modulus of Elasticity	MPa	80,000	80,000
Monotonic Tensile Yield Stress (0.2% offset)	MPa	160	183
Cyclic Yield Stress (0.2% offset)	MPa	183	183
Ultimate Tensile and Fracture Stress	MPa	160	188
Fracture Strain	%	0.42	0.45
Monotonic Strength Coefficient (K)	MPa	649	782
Monotonic Strain Hardening Exponent (n)		0.2246	0.2314

Table 3.5 Mechanical properties of Al 319 (Hipped condition)

Mechanical properties	Units	Magnitude	
		High-gas	Low-gas
Modulus of Elasticity	MPa	68,400	68,400
Monotonic Tensile Yield Stress (0.2% offset)	MPa	162	149
Cyclic Yield Stress (0.2% offset)	MPa	240	240
Ultimate Tensile and Fracture Stress	MPa	232	227
Fracture Strain	%	1.65	2.31
Monotonic Strength Coefficient (K)	MPa	561	510
Monotonic Strain Hardening Exponent (n)		0.1991	0.2007

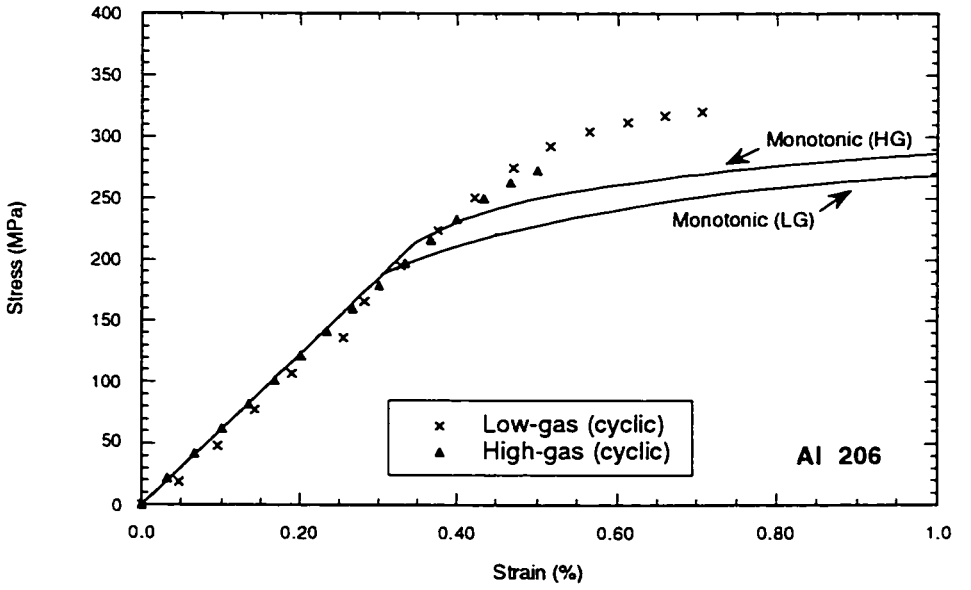

Figure 3.1 Monotonic and cyclic stress-strain curves for Al 206

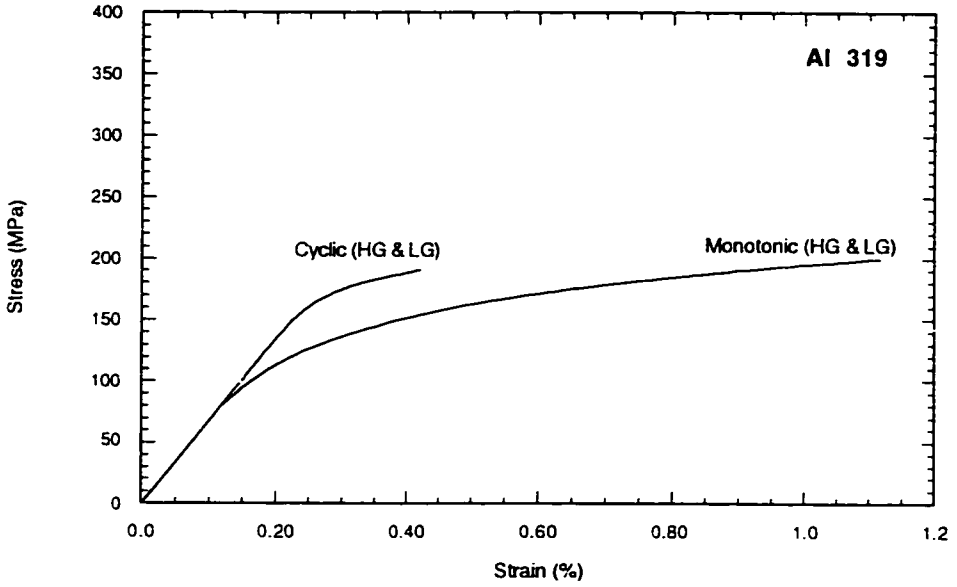

Figure 3.2 Monotonic and cyclic stress-strain curves for Al 319

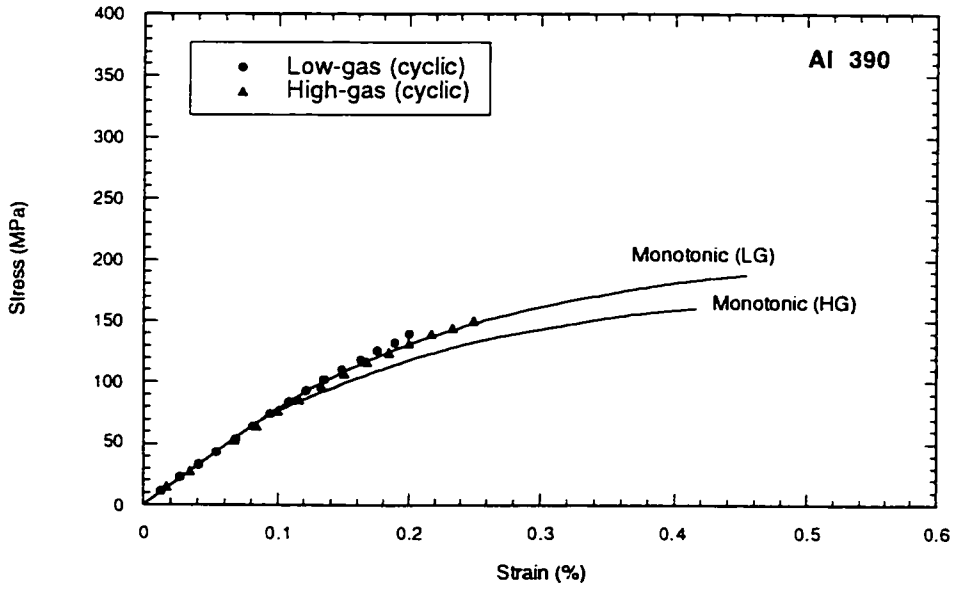

Figure 3.3 Monotonic and cyclic stress-strain curves for Al 390

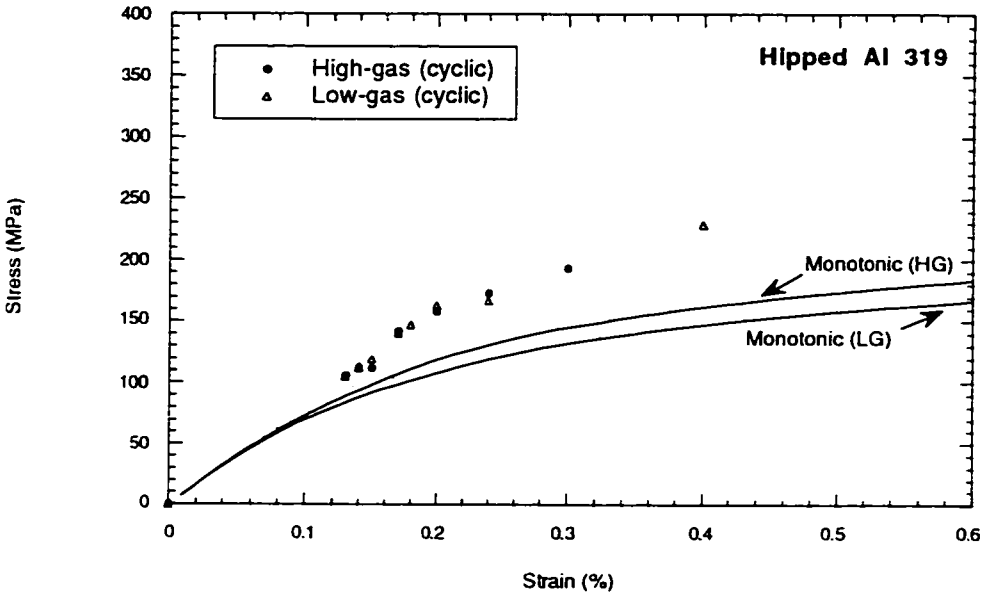

Figure 3.4 Monotonic and cyclic stress-strain curves for Hipped Al 319

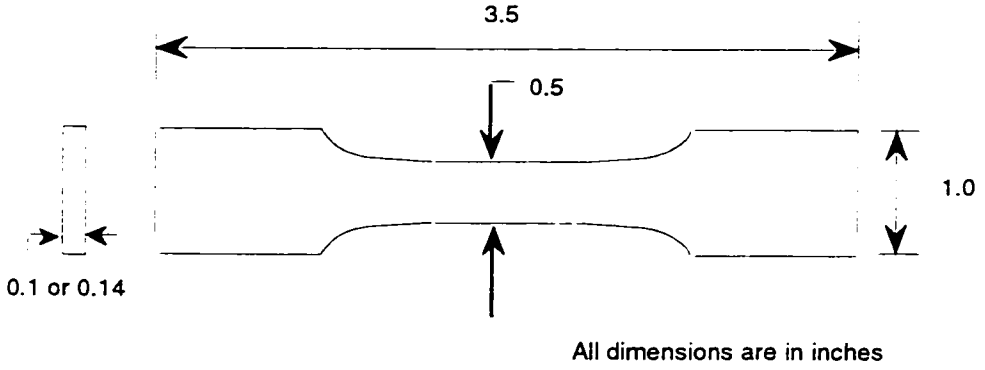

Figure 3.5 Smooth specimen geometry

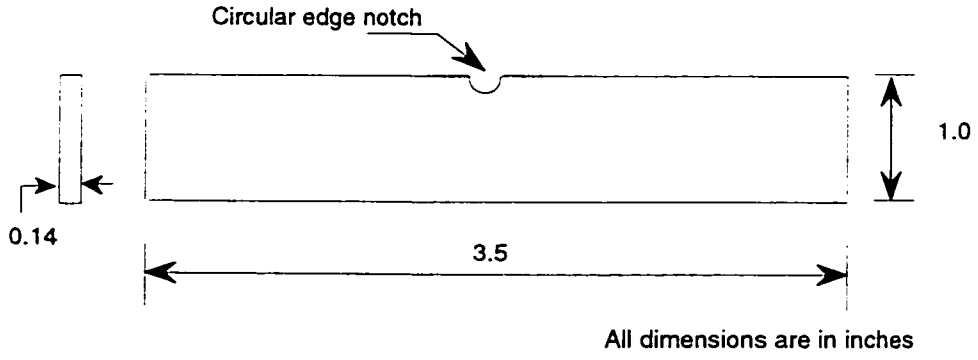

Figure 3.6 Notched specimen geometry

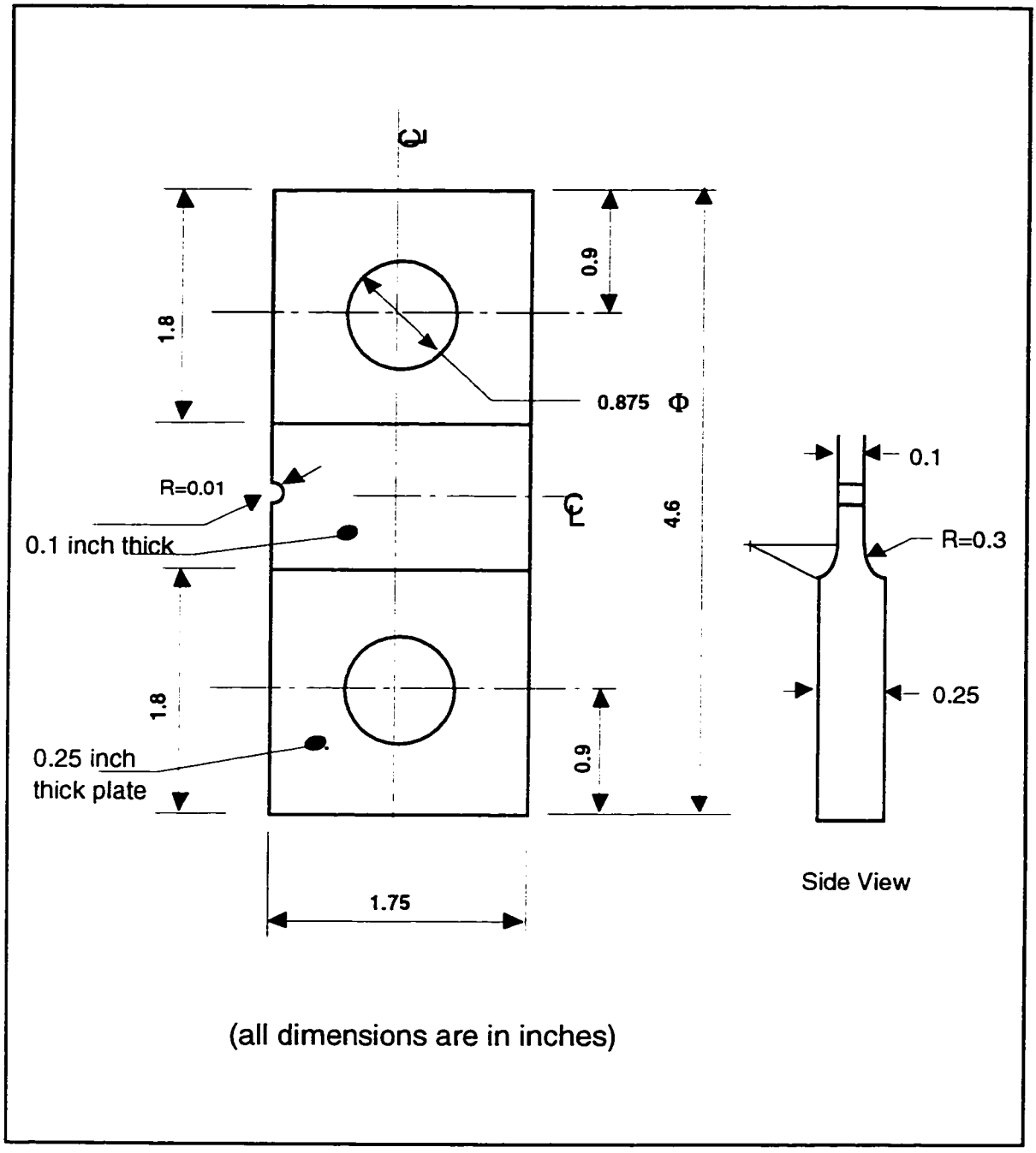

Figure 3.7 Crack growth rate specimen geometry

3.2.2 Specimen Gripping

The gripping assembly for flat specimens is shown in Figure 3.8. The specimen was inserted into the lower grip and secured by tightening a screw that moves the

clamping wedges and clamps the specimen with enough force to prevent slippage during the fatigue test. The other end of the specimen was then inserted into the upper grip and secured with another screw. The hydraulic actuator was raised until the lower grip was immersed in the attached pot containing liquid wood's metal, which was then frozen. This procedure ensures that the axis of the specimen is coincident with the loading axis of the testing frame, and that the gauge section of the specimen is not subjected to residual stresses during the assembly process. For strain controlled tests, an axial extensometer was mounted on the specimen gauge section and held in place by means of wire springs.

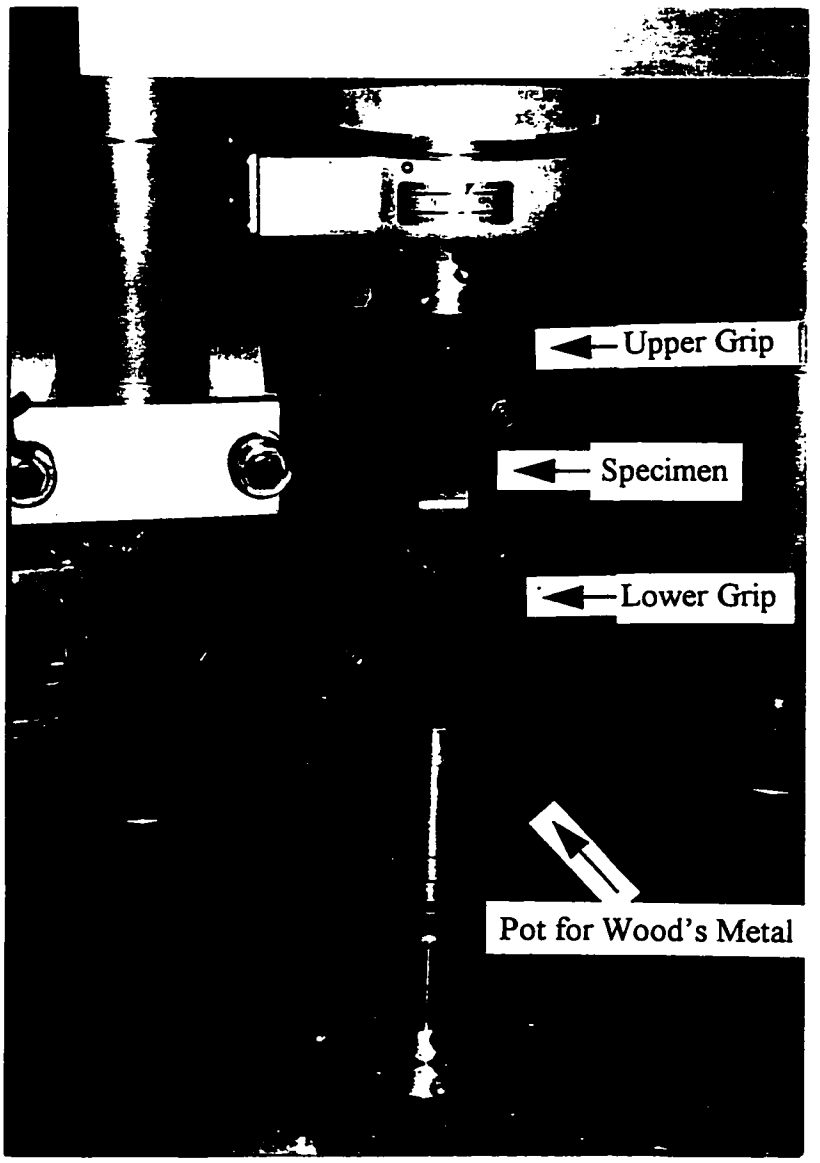

Figure 3.8 Gripping assembly for flat specimens

3.3 Experimental Program

3.3.1 Constant-amplitude Tests

Strain-life and stress-life constant-amplitude fatigue tests were conducted on the cast aluminum alloys at a stress ratio (minimum stress/maximum stress) of -1 (R=-1). The fatigue limit was taken as the stress level at which specimens did not fail after 10 million cycles.

3.3.2 Intermittent Underload Tests

Variable-amplitude strain-life and stress-life fatigue tests were also conducted. A block loading history was used consisting of an underload followed by small cycles which had the same maximum stress as the underload cycle. The underload cycle used is about the yield stress magnitude, and is chosen as the constant-amplitude stress level that would give a fatigue life of 10,000 cycles A schematic diagram for the block loading history is shown in Figure 3.9. The number of small cycles "N" was chosen so that the following conditions were fulfilled:

1- The damage due to the underloads (according to Miner) was not allowed to exceed 20%, .i.e. number of underloads in the expected life did not exceed 0.2 of the number of underloads only required to cause failure. This ensures a fatigue test in which most of the damage is done by the small cycles.

2- All small cycles between underloads were free of closure. This was achieved by choosing "N" so that the crack opening stress as it builds-up after underloads did not reach the minimum stress of the small cycles before the application of the next underload which reduced the crack opening stress. The value for "N" was based on a crack opening stress build-up model proposed by the present author[78] and fitted to test data for the present material[79]. The variable-amplitude strain-life curve is not an effective strain-life curve only over a small part of the curve. This part of the curve occurs when the small cycles approach the size of the large underloads. The small cycles in that case are not fully open and the crack opening stress approaches that of the large underloads.

3.3.3 Service Load History Tests

The stress history examined in this study is the torsion channel of the Society of Automotive Engineers (SAE) GKN Grapple-Skidder history, which is a good example of an actual measured service history. The history was supplied in the form of normalized sequential peak and valley points with a maximum value of 318 and a minimum value of -238 and contains 41124 reversals. The history is shown in Figure 3.10. The numbers were scaled up or down in magnitude to obtain different overall test stress levels. Each test level was denoted by the maximum absolute value of the stress range throughout the scaled history.

A total of 321 fatigue tests were conducted on smooth and notched specimens in this investigation under the different fatigue loading histories. A list of the number of fatigue tests conducted is given in Table 3.6.

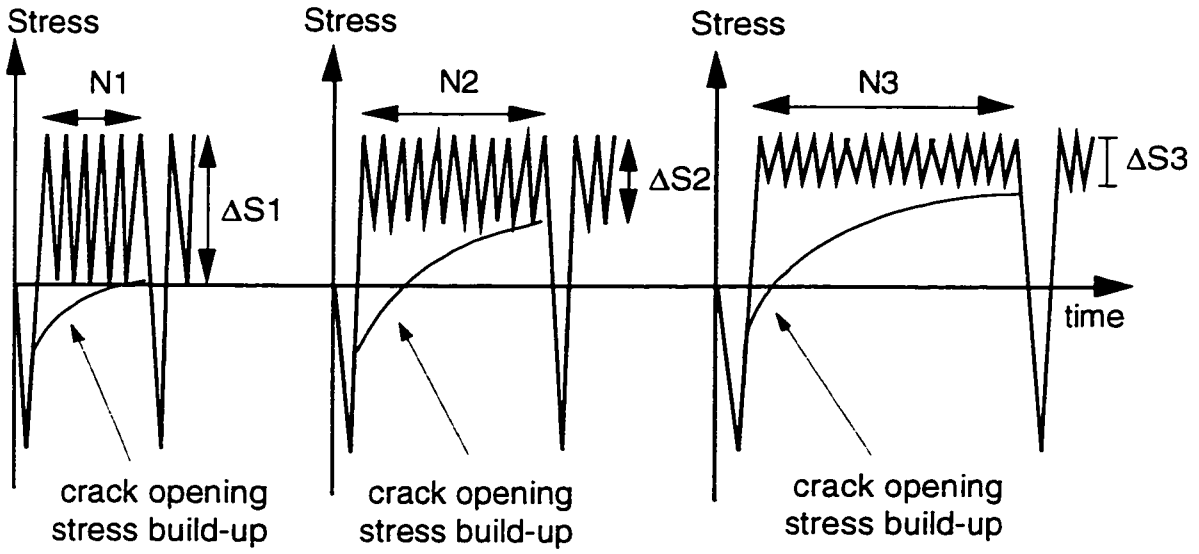

Figure 3.9 A schematic diagram for the block loading history

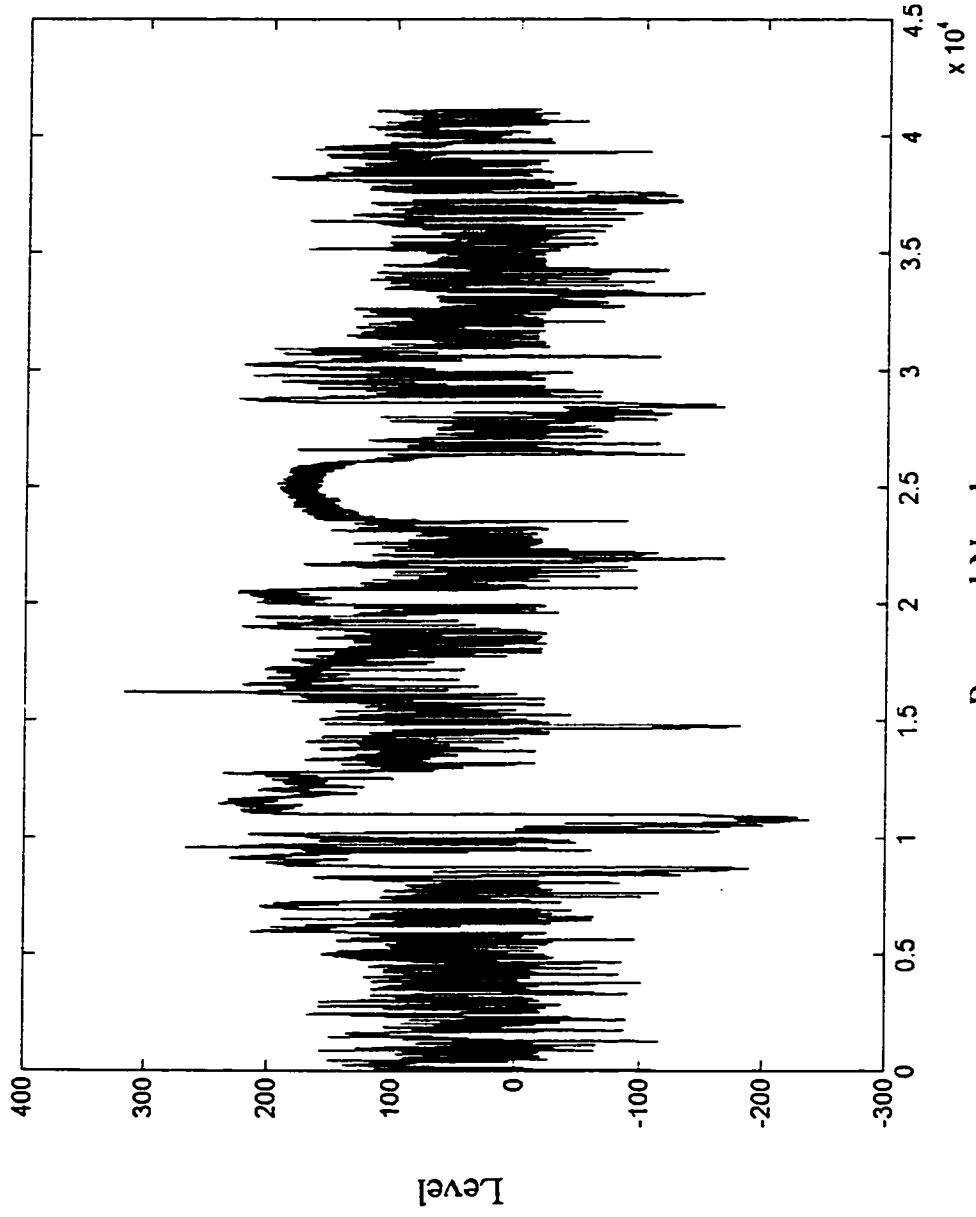

Figure 3.10 The torsion channel of the SAE GKN Grapple-Skidder History

Table 3.6 Number of fatigue tests conducted on smooth and notched specimens (HG: High-Gas, LG: Low-Gas)

Geometry	Smooth Specimens				Notched Specimens			
Condition	As-Cast		Hipped		As-Cast		Hipped	
	HG	LG	HG	LG	HG	LG	HG	LG
Constant-amplitude Loading	30	33	11	11	24	-	23	-
Variable-Amplitude Loading	33	28	13	13	29	-	18	-
Service Load History	7	-	7	-	14	-	27	-

3.4 Test Techniques

All tests were carried out in a laboratory environment at room temperature (23°c) using a uniaxial closed-loop servo-controlled electro-hydraulic testing machine. Calibration of the load cell was carried out before all tests in this investigation using a standardized calibration load cell. Extensometers used were calibrated periodically using a calibration instrument containing a dial gauge with a precision of 0.0001 inches.

3.4.1 Closure Free Crack Growth Rate Tests

Crack growth in terms of effective stress intensity was measured under constant- and variable-amplitude loading. A traveling microscope of 900X was mounted on the machine facing the specimen. A vernier with an accuracy of 0.0001 mm was attached to the microscope to measure changes in crack length. The variable-amplitude loading history was found to be a better and easier technique in producing the closure free crack growth data than the constant-amplitude loading technique. In the constant-amplitude loading technique, a K-decreasing procedure has to be used . During the K-decreasing phase the load has to be carefully reduced by 10% in each step. If the load drop is higher than 10%, the steady state crack opening stress will not be able to make the transition to the new crack opening

stress level and the crack will not grow. This might give an early fatigue threshold value. Also in the constant-amplitude technique, very high stress ratios might be needed in relatively brittle materials to obtain the closure free crack growth data. These brittle materials cannot withstand the high stresses when the crack growth length is not too long. Using the block loading history, the crack is ensured to be always fully open which prevents an artificially elevated fatigue threshold. Also in the variable-amplitude loading technique the low crack opening stress level, due to the underload cycle, allows the small stress cycles applied after the underload to be fully open at lower stress ratios than those applied when using the constant-amplitude loading technique. Both the constant- and variable-amplitude loading procedures are explained in detail in the following sections.

3.4.1.1 Constant-amplitude Loading Procedure

Under constant-amplitude loading, the combination of the stress ratio, R, and the maximum stress have to be high enough to ensure a fully open crack. However, the maximum stress must be kept below that causing failure by exceeding the fast fracture stress intensity factor, K_c. Stress ratios up to 0.85 were used in this investigation to obtain fully open crack growth curves.

A small notch of about 0.25 mm was introduced on one side of the specimen, at mid length as shown in Figure 3.7, to produce a stress raiser which served to localize the crack initiation site. This size was small enough that once initiated the crack rapidly grew out of the zone of influence of the notch. A K-decreasing procedure was used which minimized load interaction effects. During the K-decreasing phase the applied load was reduced by 10% in each step and the crack was allowed to grow at least five plastic zone sizes each step to allow the crack to grow out of the plastic zone of the previous higher load. This sequence was followed until no crack growth was detected after 3 million cycles. After the threshold stress intensity factor was determined a load increasing phase having a 10% load increase in each step was applied until a desired maximum crack growth rate was reached, such as 10^{-7} m/cycle.

3.4.1.2 Variable-amplitude Loading Procedure

A block loading history was also applied to obtain the closure free crack growth curve. Each block consisted of a underload followed by a number of small cycles having the same maximum stress as the underload. The small cycles minimum stress was changed to produce different ΔK values. A schematic for the block loading is shown in Figure 3.9

The procedure followed to obtain the crack growth rate of the small cycles was as follows:

1- The crack growth rate, $(da/dN)_t$, for the block loading history was determined.

2- The crack growth rate for the underload cycles alone was determined during the block test by inserting a group of underload cycles and measuring their growth rate, $(da/dN)_{U.L.}$, between measurements of block growth rates.

3- The crack growth rate for the small cycles in the block test, $(da/dN)_s$, was obtained by subtracting the growth per block due to the underload cycle, $(da/dN)_{U.L.}$, from the total growth per block, $(da/dN)_t$, and divided by the number of cycles in the block as follows:

$$(da/dN)_s = \frac{(N+1)(da/dN)_t - (da/dN)_{U.L.}}{N} \qquad 3.1$$

where N is the number of small cycles between underloads

The advantage of the variable-amplitude history over the constant-amplitude history is that we can use stress ratios which are not very high and still obtain fully open crack growth in which the whole stress cycle is effective. The application of the underload cycle in the variable-amplitude history decreases the crack opening stress to a low level and a large number of small cycles is required for it to return to its steady state level. If the frequency of the underloads is small enough, the crack opening stress is reduced by a new underload before it reaches the minimum stress of the small cycles and all the small cycles are fully open.

3.4.2 Crack Opening Stress Build-up Measurements

The program used to measure the crack opening stress build-up involved applying constant-amplitude small cycles until a steady-state crack opening stress was reached, then applying an underload cycle, followed by cycling at the initial test conditions until the crack opening stress level returned to the value it had prior to the underload cycle. A schematic for the program applied and the crack opening stress changes is shown in Figure 3.11

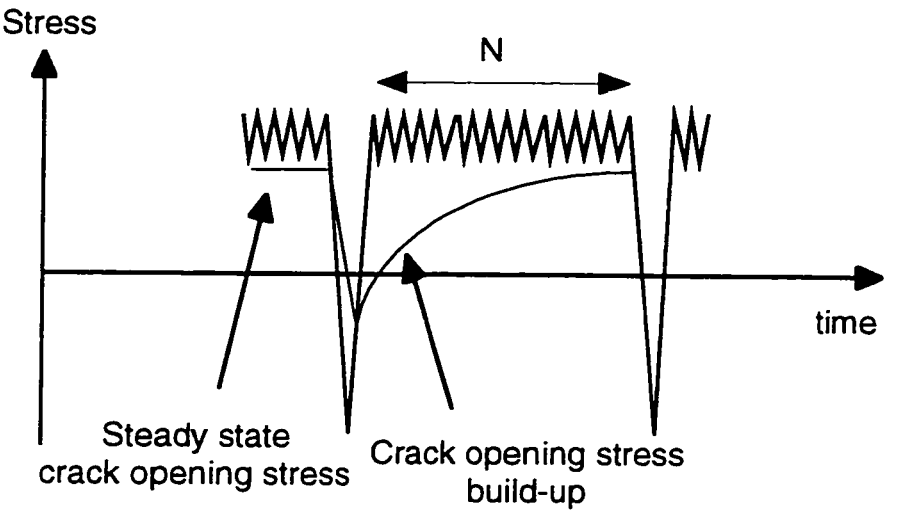

Figure 3.11 A schematic for the history used in the crack opening stress build-up measurements

The crack tip region was examined throughout a stress cycle using a 900x microscope at cycle numbers 1, 5, 10, 20, 50, 100, 200, 500, 1000, 2000, 5000,10000, 20000, and 50000 after the underload and the crack opening and crack closure stress levels were recorded. The procedure followed for measuring the crack opening stress was to stop the test at the maximum stress of the required cycle and then to drop the load while looking at the crack tip region until the crack surfaces starts to touch each other. If the crack opening stress is lower than the minimum stress of the stress cycle then the loading history is altered, so the test is continued without any measurements until the end of the block. Then the test is resumed by applying another block and is stopped at the maximum stress of the required stress cycle to record the crack opening stress reading. A set of readings was repeated five times for each small cycle stress level, and the average of the five readings at a given cycle number after the overload was taken as the crack opening

or crack closure stress level. The crack opening and crack closure stress levels are defined as the levels at which the crack surfaces just open or close, respectively, at a distance of 0.25 mm behind the crack tip.

3.4.3 Fatigue Tests

A digital process control computer was used to output constant-amplitude cycles, periodic underloads followed by constant-amplitude small cycles, and the variable-amplitude GKN Grapple-Skidder history in the form of a sinusoidal loading wave. Strain controlled fatigue tests were conducted at frequencies between 1 and 45 HZ, while load controlled fatigue tests were conducted at frequencies up to 150 HZ depending on the stress amplitude of the small cycles in the history using a FLEX control software [80]. Failure was defined as 10% load drop for strain controlled tests and full separation of the specimen for load controlled tests.

3.4.4 Ultra-Sonic Observations

One of the test series needed in this investigation was to study and test the fatigue behavior of specimens having natural flaws at the notch root. It was necessary to accurately locate large flaws, their size, and their depth below the surface of the cast plate so as to be able to cut the specimens and then machine the required notch size with the natural flaw located at the notch root. The cast plates were sent out to be examined using ultra-sonic waves. The X and Y coordinates of the plates' flaws, their size, and their depth from the plates surface were determined. Figure 3.12 shows a part of one of the plates after detecting the flaws using ultra-sonic waves.

3.4.5 Fractographic Observations

Fractography performed on the aluminum alloys, Al 206, Al 319, and Al 390 showed dendritic crystals in all of them, but the size and distribution of the dendrites varied from one material to the other. More dendrites were found in Al 319 and Al 390 than in Al 206. Defects in the cast aluminum alloys in the High-gas and Low-gas condition are shown in Figure 3.13.

Broken fatigue test specimens were examined under a microscope to identify the flaw shape, size, and location from the notch root. A camera was mounted on the microscope to capture the fracture surface with the flaws. A very fine ruler was photographed at the same magnification as the specimen photograph and used to measure the flaw size. In some cases a small digital vernier with a resolution of 0.0001 inches was used to measure the flaw size under the microscope. Fractographic observations, in this investigation, helped in determining the reason for some unusual fatigue test results as will be shown and explained in chapters 4 and 5.

Winspect Nondestructive Inspection Software

Licensed to Edward Ginzel, Materials Research Institute

Date : Sat Apr 01, 1995
Time : 18:07:40
Filename : C:\ZIPZONE\A1.SDT

HORIZONTAL AXIS (millimtrs)		VERTICAL AXIS (millimtrs)	
Start :	-140.621	Start :	-14.316
Length :	159.900	Length :	330.000
Resolution :	0.300 (533 pts.)	Resolution :	0.300 (1100 pts.)

Comment: Al plate "I" C-scan with ref. FBH at 0,0 (0.3mm pitch)

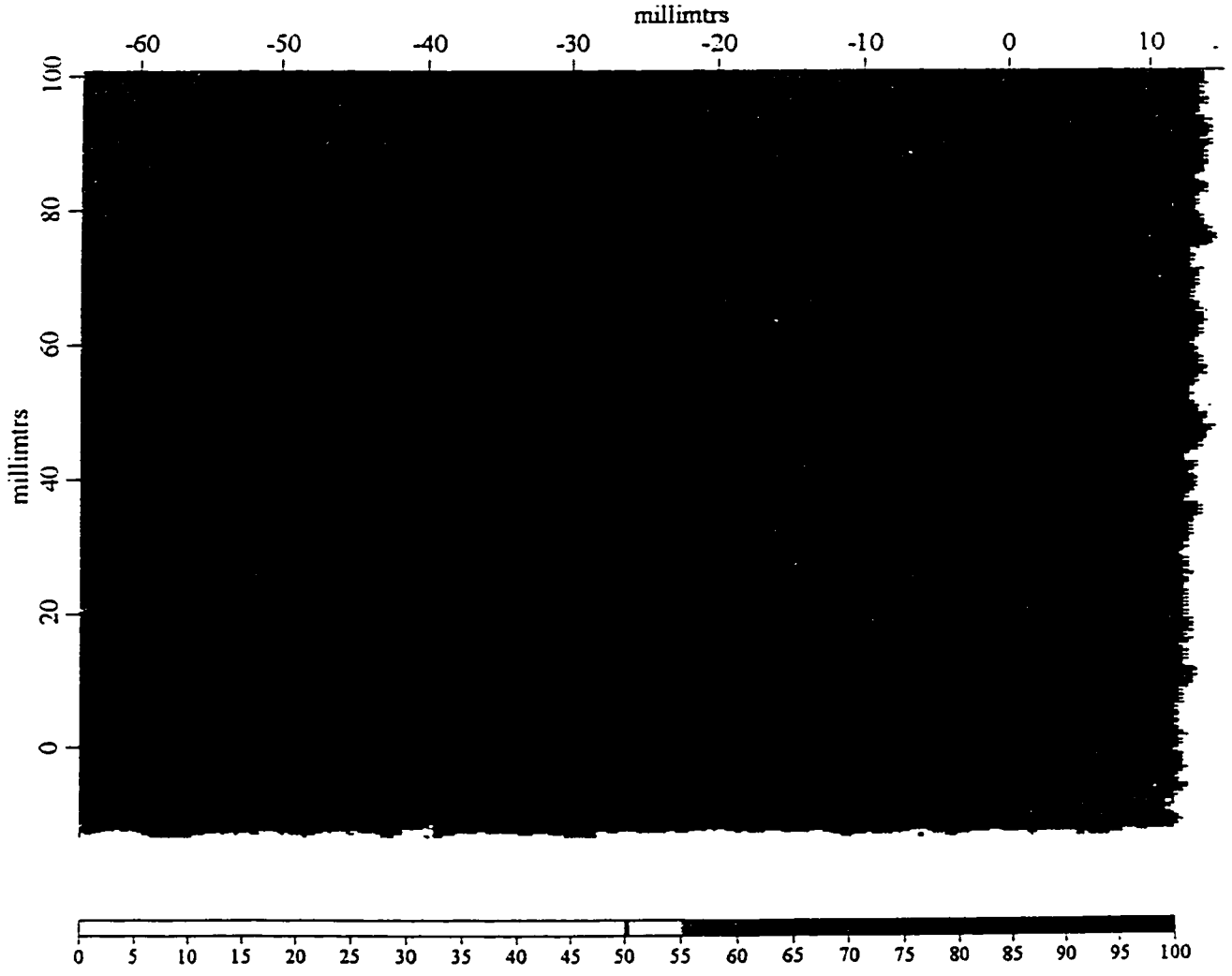

Figure 3.12 A picture of a cast plate after detecting the flaws using ultra-sonic waves

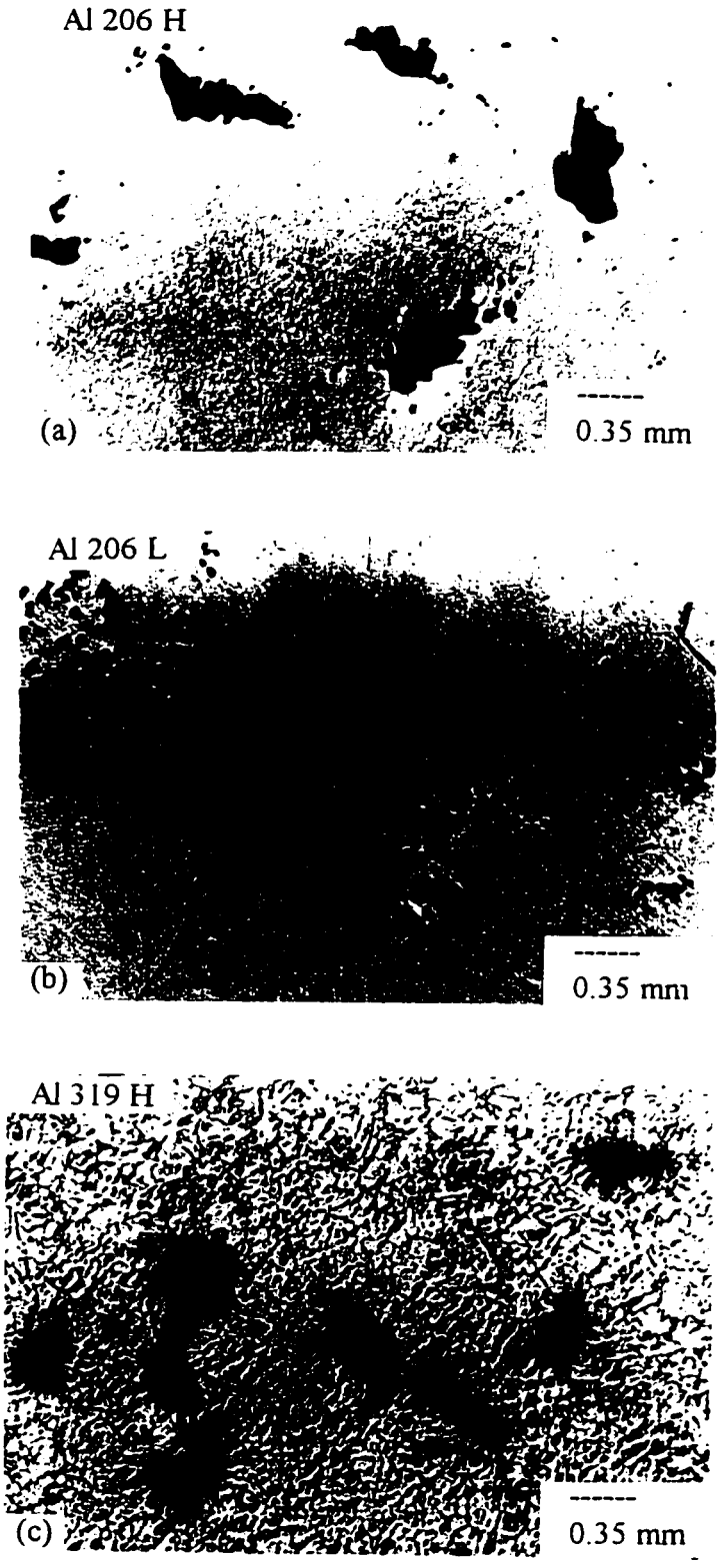

Figure 3.13 Defects in cast aluminum alloys
(a) Cast Al 206 High-Gas, (b) Cast Al 206 Low-Gas, (c) Cast Al 319 High-Gas

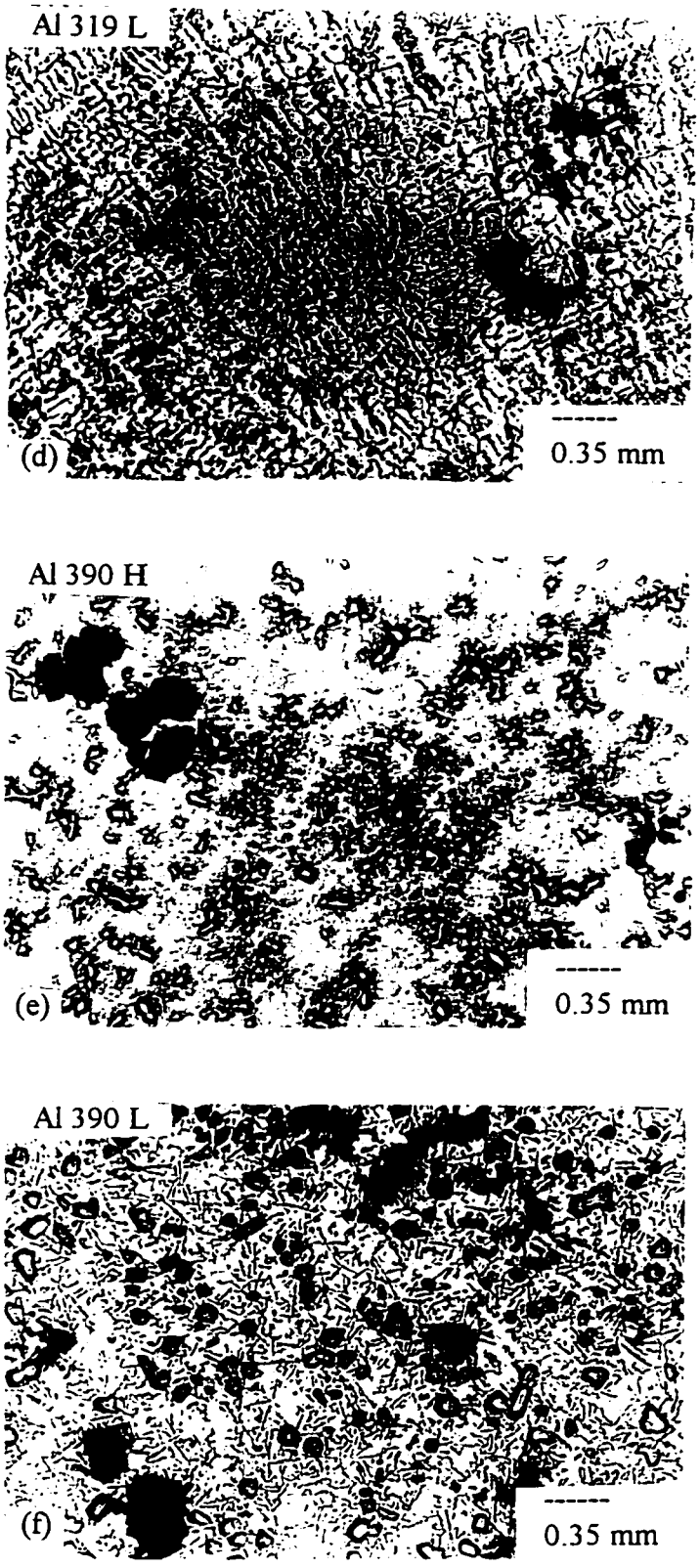

Figure 3.13 (Continued) Defects in cast aluminum alloys
(d) Cast Al 319 Low-Gas, (e) Cast Al 390 High-Gas, (f) Cast Al 390 Low-Gas

3.5 Summary

This chapter presented the materials used in this investigation and their mechanical properties. It also showed the different kinds of specimens used and their design together with the specimen preparation prior to testing and its gripping in the testing machine.

This chapter explained the three experimental programs used in this study. The first program was the constant-amplitude program, and the second was the intermittent underload program which consists of repeated blocks, with each block consisting of an underload followed by a number of constant-amplitude small cycles that varies depending on the stress or strain amplitude of the small cycles. The third program was using the GKN Grapple-Skidder history which consists of 41,124 reversals.

This chapter explained the different test techniques used in this investigation. They include a technique for producing effective stress intensity factor versus crack growth rate data using an underload block loading history rather than the conventional constant-amplitude history. Another technique was for measuring the crack opening stress build-up after the application of underloads using a high magnification power microscope,(900X). Procedures for fatigue tests under strain and load control, fractographic observations and ultra-sonic observations to detect the flaw location, and size were also presented.

CHAPTER 4

FATIGUE BEHAVIOR UNDER CONSTANT-AMPLITUDE AND INTERMITTENT UNDERLOAD HISTORIES

4.1 Introduction

In this chapter, fatigue test data obtained using smooth specimens and notched specimens with a flaw at the notch root under constant-amplitude and intermittent underload block loading histories are examined. The results show an improvement in smooth specimen fatigue strength, under constant-amplitude loading, as a result of the hipping process which decreased the flaw size. They also show the effect of the variation in flaw size and flaw position, in the notch root, on the fatigue life of notched specimens having small and large notch radii. The underloads, in the block loading history, followed by constant-amplitude smaller cycles, reduced the crack opening stress enough that the smaller constant-amplitude cycles became fully effective which reduced their effective fatigue life.

4.1.1 Load Histories

Constant- and variable -amplitude histories are used in this chapter. The constant-amplitude load history consisted of fully reversed loading or strains at a stress ratio of -1(R=-1). The variable-amplitude load history consisted of a series of repeated blocks, in which each block consisted of an underload followed by a number of small cycles which had the same maximum stress as the underload cycle (see section 3.3). A schematic diagram for the constant-amplitude and block loading histories used is shown in Figure 4.1.

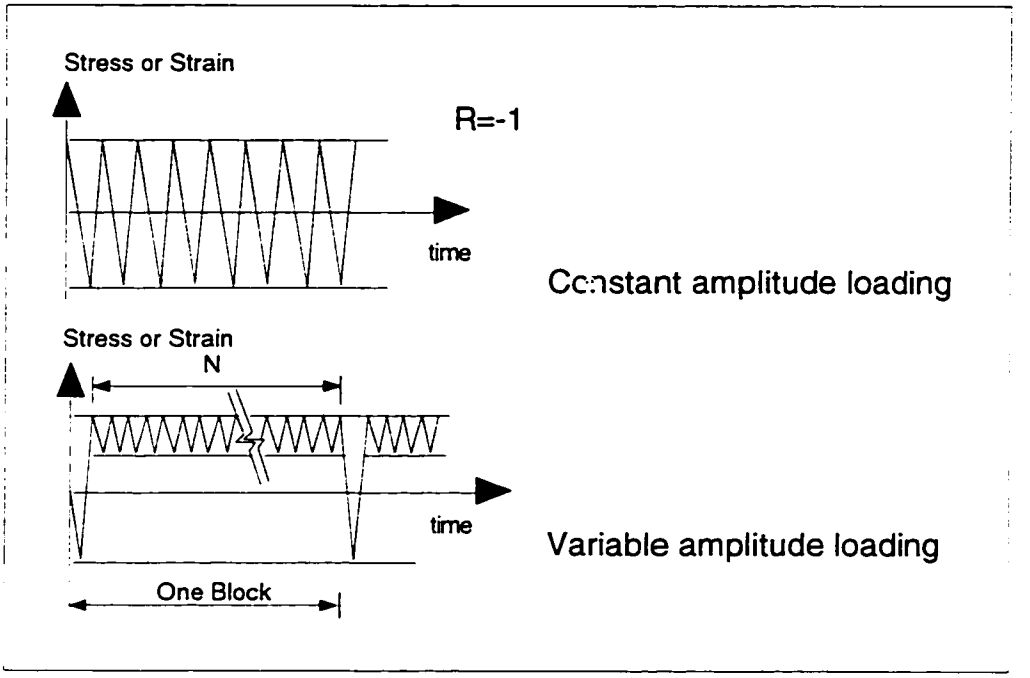

Figure 4.1 Constant- and variable-amplitude histories

4.1.2 Materials

Smooth specimens fatigue tests under constant- and variable-amplitude loading were done on the 206, 390, and 319 cast aluminum alloys in the as-cast condition and on the 319 cast aluminum alloy in the hipped condition. The notched specimen fatigue tests, under constant- and variable-amplitude loading, were conducted only on the high-gas 319 cast aluminum alloy in the as-cast and hipped condition.

4.1.3 Objective and Outline

It is generally accepted that the fatigue strength of materials containing defects or flaws is lower than that of a defect free material. If a defect is located at a stress concentration region, such as a notch root, an even lower fatigue strength might be expected. It is the objective of this chapter to determine the reductions in fatigue life caused by having a defect at a notch root under the application of constant- and variable-amplitude fatigue loads and to analytically predict those reductions. The following sections describe the smooth and notched specimen fatigue tests, a method for calculating an empirical model for crack opening stress build-up, and fatigue life predictions based on the proposed analytical model (chapter 2).

4.2 Fatigue Tests of Smooth Specimens

This section provides the smooth fatigue test data for the as-cast and hipped materials under constant- and variable-amplitude load histories.

4.2.1 As-Cast Fatigue Test Results

Strain-life constant-amplitude fatigue tests at R=-1 were conducted on the 206, 319 and 390 cast aluminum alloys in both the high-gas and low-gas conditions. Figures 4.2 to 4.6 show strain range versus number of cycles to failure data for the three materials.

Fatigue limit and fatigue test results under constant-amplitude loading are given in Tables 4.1 and 4.2. It can be seen that there was no significant difference in fatigue life between the high-and low-gas cast aluminum alloys except near the fatigue limit region, where the low-gas 319 aluminum alloy is superior to the high-gas material.

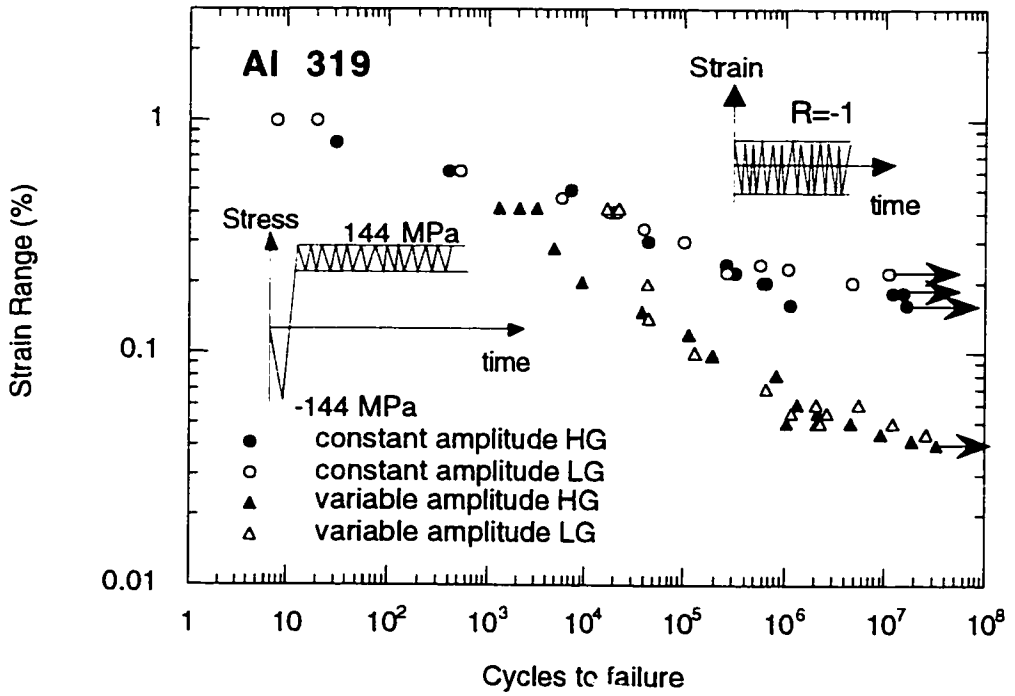

Figure 4.2 Constant- and variable-amplitude loading fatigue data for Al 319 alloy

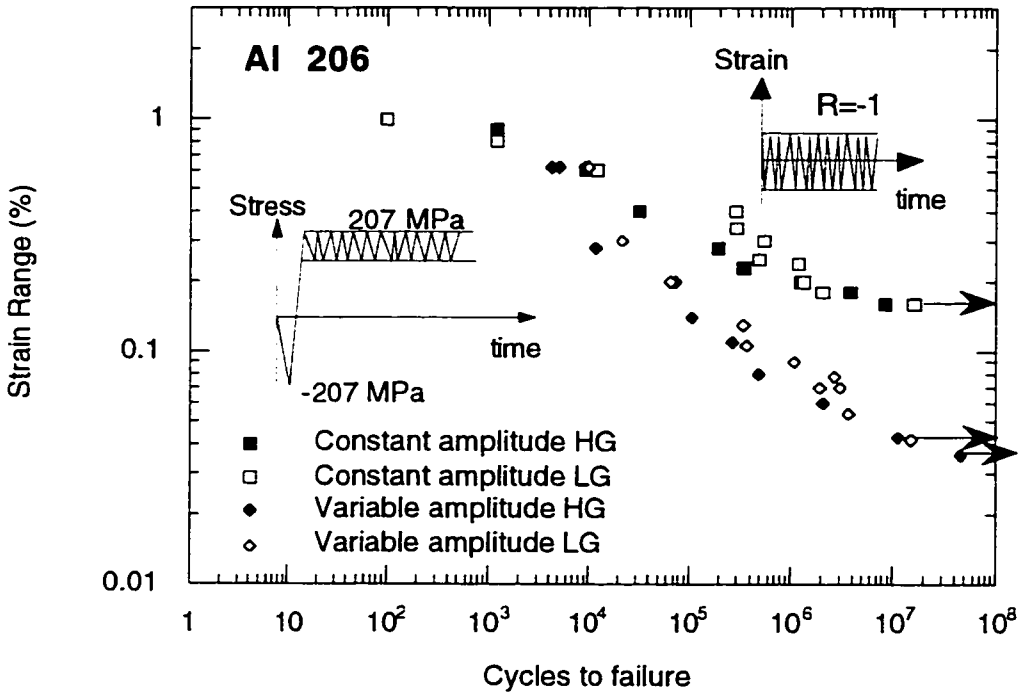

Figure 4.3 Constant- and variable-amplitude loading fatigue data for Al 206 alloy

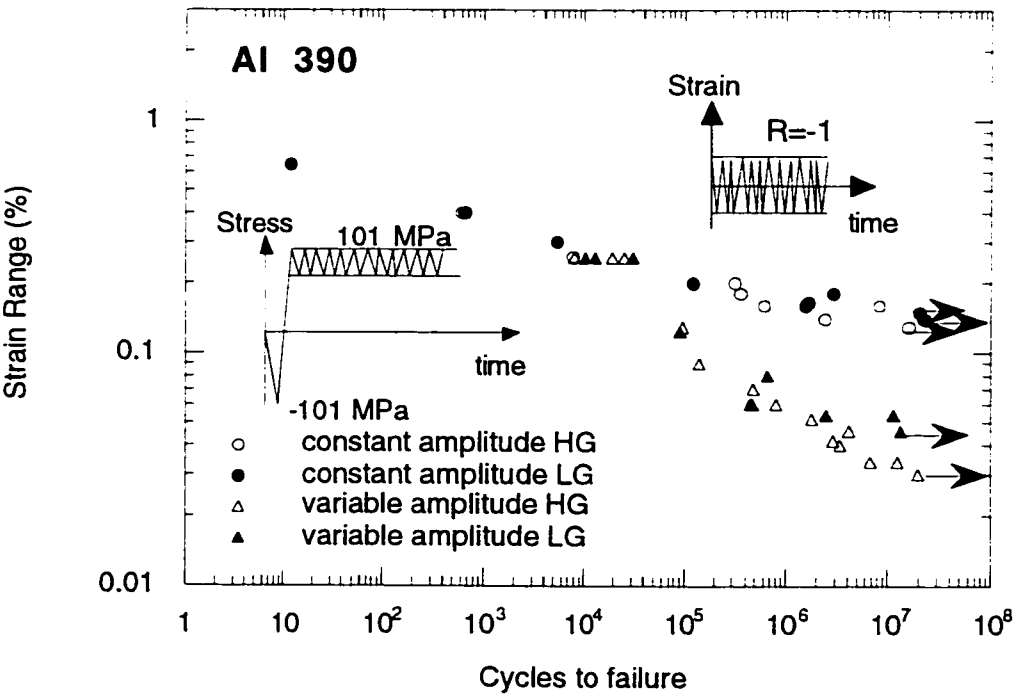

Figure 4.4 Constant- and variable-amplitude loading fatigue data for Al 390 alloy

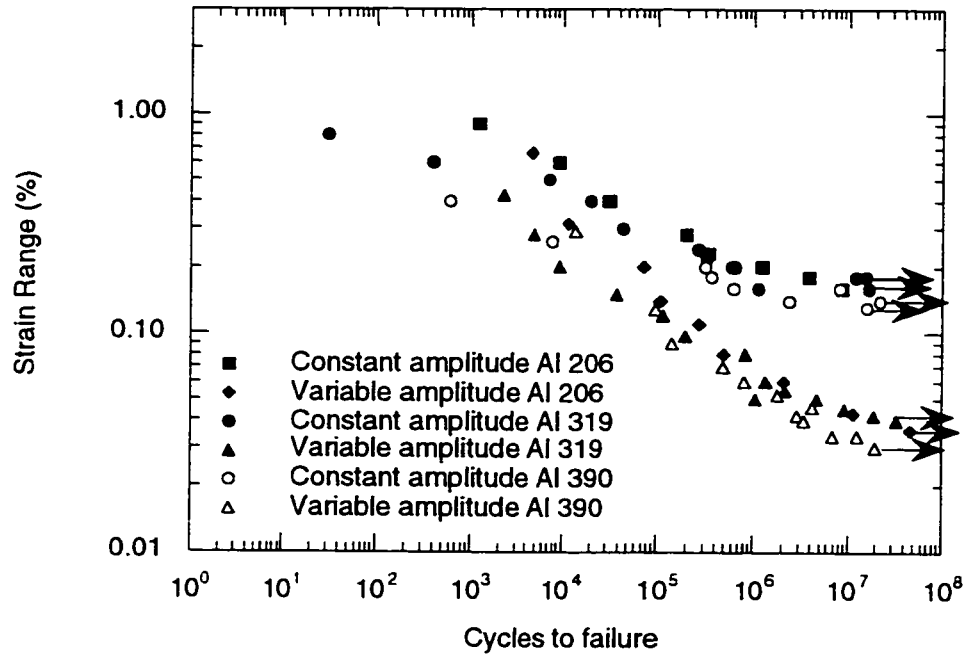

Figure 4.5 Constant- and variable-amplitude loading fatigue data for High-gas cast aluminum alloys

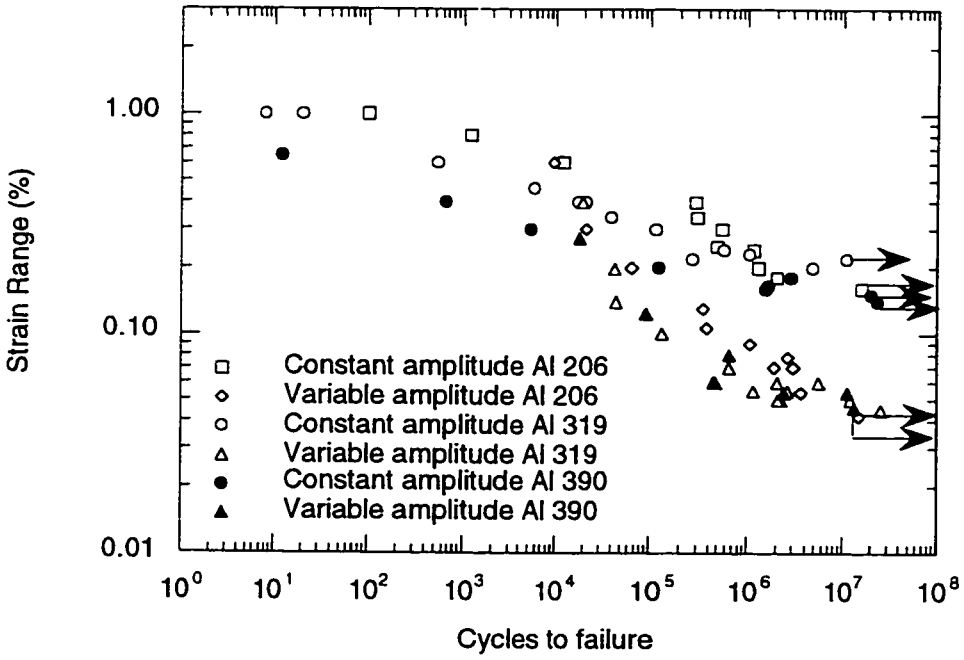

Figure 4.6 Constant- and variable-amplitude loading fatigue data for Low-gas cast aluminum alloys

Fatigue tests under variable-amplitude loading were conducted under load control. The fatigue test results are shown in Figures 4.2-4.6. The underload cycle used, for each material, is chosen as the corresponding constant-amplitude stress level that would give a fatigue life of about 10,000 cycles. The underload stress levels for the 319, 206, and 390 cast aluminum alloys were ±144 MPa, ±207 MPa, and ±101 MPa, respectively. Fatigue limit and fatigue test results are given in Tables 4.3 and 4.4. Results are plotted on axes of the strain range of the small cycles versus the equivalent number of small cycles to failure on a log scale. Miner's linear damage rule was used to calculate the equivalent number of small cycles to failure. The total damage is given by the sum of the underload damage, D_{ul}, and the small cycle damage, D_s:

$$D_{ul} + D_s = 1 \tag{4.1}$$

The damage caused by the underloads is calculated as the number of underloads in a test, N_{ul}, divided by the number of underload cycles to failure, N_{ful}, in a constant-amplitude loading history containing only underload cycles:

$$D_{ul} = \frac{N_{ul}}{N_{ful}} \tag{4.2}$$

Then an equivalent life for small cycles is obtained as

$$N_{fseq} = \frac{N_s}{D_s} \tag{4.3}$$

where N_s is the number of small cycles in a fatigue test, and D_s is the damage done by small cycles = 1- D_{ul}.

Combining Equations 4.1, 4.2, and 4.3 gives

$$N_{fseq} = \frac{N_s}{1 - D_{ul}} = \frac{N_s}{1 - \frac{N_{ul}}{N_{ful}}} \tag{4.4}$$

The underload block loading history used was the most damaging history possible for the applied stresses, as the crack was fully open throughout the small cycles. The underload strain-life curves shown in Figures 4.2-4.6, therefore, represent lower-bound strain-life curves for the three cast aluminum alloys. The reductions in fatigue strength caused by this history from the constant-amplitude fatigue strength are shown in Table 4.5.

Table 4.1 Fatigue limit stress and strain ranges under constant-amplitude loading

Fatigue limit	Al 206		Al 319		Al 390	
	High-Gas	Low-Gas	High-Gas	Low-Gas	High-Gas	Low-Gas
Strain range(%)	0.16	0.16	0.16	0.22	0.13	0.14
Stress range (MPa)	104.88	107.64	100.74	155.94	102.12	117.3

Table 4.2 Constant-amplitude fatigue life data for Al 206, Al 319, and Al 390

AL 206			
High-Gas		Low-Gas	
Strain range (%)	Cycles to failure	Strain range (%)	Cycles to failure
0.90	1,200	1.0	100
0.60	9,206	0.80	1,200
0.40	31,958	0.60	12,170
0.28	197,135	0.40	291,786
0.23	342,330	0.34	297,237
0.20	1,237,215	0.25	492,665
0.18	3,809,646	0.30	547,582
0.16	8,517,700	0.24	1,191,298
		0.20	1,328,995
		0.18	2,063,955
		0.16	16,032,035

Al 319			
High-Gas		Low-Gas	
Strain range (%)	Cycles to failure	Strain range (%)	Cycles to failure
0.80	31	1.0	8
0.60	401	1.0	20
0.50	7,137	0.60	531
0.40	20,000	0.46	5,816
0.30	44,319	0.40	17,708
0.24	263,147	0.40	21,268
0.22	320,829	0.34	39,855
0.20	601,932	0.30	101,913
0.20	644,011	0.22	267,497
0.16	1,126,063	0.24	568,773
0.18	12,057,416	0.23	1,075,283
0.18	15,455,960	0.20	4,770,570
0.16	16,563,501	0.22	11,000,000

Table 4.2 (Continued) Constant-amplitude fatigue life data for Al 206, Al 319, and Al 390

Al 390			
High-Gas		Low-Gas	
Strain range (%)	Cycles to failure	Strain range (%)	Cycles to failure
0.40	606	0.650	12
0.26	7,768	0.400	656
0.20	312,756	0.300	5,312
0.18	362,811	0.200	120,921
0.16	610,261	0.180	2,932,103
0.14	2,393,206	0.166	1,659,371
0.16	8,183,890	0.160	1,559,500
0.13	15,711,017	0.150	20,278,526
0.14	22,063,000	0.140	23,193,098

Table 4.3 Fatigue limit strain range under variable-amplitude loading

Fatigue limit	Al 206		Al 319		Al 390	
	High-Gas	Low-Gas	High-Gas	Low-Gas	High-Gas	Low-Gas
Strain range(%)	0.036	0.021	0.04	0.045	0.03	0.046

Table 4.4 Variable-amplitude fatigue life data for Al 206, Al 319, and Al 390

Al 206							
High-Gas				Low-Gas			
Strain amp. (%)	N	N_f (Cycles)	N_{fseq} (Cycles)	Strain amp. (%)	N	N_f (Cycles)	N_{fseq} (Cycles)
0.3140	10	10,186	11,581	0.1500	20	20,160	21,340
0.1000	45	2,217	2,191	0.1000	22	51,934	65,008
0.1000	40	53,464	72,665	0.0650	120	268,378	346,413
0.0700	50	74,256	106,290	0.0503	420	343,536	374,652
0.0550	260	220,283	268,474	0.0450	630	914,950	1,076,545
0.0400	600	414,088	485,838	0.0390	1050	2,109,357	2,666,284
0.0300	2100	1,724,920	2,096,595	0.0350	3900	2,820,423	3,050,029
0.0215	17300	9,913,472	11,316,084	0.0350	3900	1,824,670	1,917,848
0.0180	10000	23,107,311	46,220,002	0.0270	3900	3,343,157	3,670,894

Table 4.4 (Continued) Variable-amplitude fatigue life data for Al 206, Al 319 and Al 390

Al 319							
High-Gas				Low-Gas			
Strain amp. (%)	N	N_f (Cycles)	N_{fseq} (Cycles)	Strain amp. (%)	N	N_f (Cycles)	N_{fseq} (Cycles)
0.1400	12	4,404	4,805	0.0980	50	41,985	42,978
0.1000	40	8,692	9,384	0.0700	50	43,867	44,994
0.0750	50	29,020	38,391	0.0500	50	116,843	129,819
0.0600	200	89,878	112,281	0.0350	100	493,588	652,308
0.0485	890	175,526	192,562	0.0275	800	1,089,395	1,169,723
0.0400	700	535,744	819,912	0.0300	500	1,721,933	2,086,466
0.0250	9000	990,109	1,042,071	0.0250	800	1,851,119	2,097,661
0.0300	3850	1,152,352	1,333,827	0.0250	1000	2,040,028	2,276,002
0.0275	9000	1,943,183	2,154,358	0.0275	800	2,286,849	2,676,022
0.0250	9000	3,711,327	4,567,917	0.0300	100	1,454,571	5,517,887
0.0225	9000	6,229,589	9,090,747	0.0250	1000	7,477,471	12,112,919
0.0210	36000	15,179,469	18,779,023	0.0225	3000	17,804,152	25,588,181
0.0200	18000	17,907,258	32,675,590				

Al 390							
High-Gas				Low-Gas			
Strain amp. (%)	N	N_f (Cycles)	N_{fseq} (Cycles)	Strain amp. (%)	N	N_f (Cycles)	N_{fseq} (Cycles)
0.0645	25	77,658	95,200	0.062	10	66,417	90,494
0.0450	95	127,970	140,131	0.030	685	429,387	444,083
0.0350	155	394,064	478,902	0.030	685	453,211	469,660
0.0300	430	707,197	800,374	0.040	220	560,697	648,932
0.0260	600	1,472,822	1,786,473	0.027	680	2,045,953	2,448,461
0.0210	2900	2,689,536	2,881,662	0.027	680	5,899,725	11,275,043
0.0200	3500	3,168,532	3,389,306	0.023	1370	8,718,150	13,412,536
0.0230	1500	3,436,408	4,114,288				
0.0170	3500	5,938,502	6,765,662				
0.0170	3500	9,926,454	12,478,391				
0.0150	3500	13,911,304	19,502,362				

Table 4.5 Fatigue strength reductions due to variable-amplitude loading

Al 206		Al 319		Al 390	
High-Gas	Low-Gas	High-Gas	Low-Gas	High-Gas	Low-Gas
77%	87%	75%	79%	77%	66%

4.2.2 Fatigue Test Results for Hipped Material

Strain-life constant-amplitude fatigue tests at R=-1 were conducted on the hipped 319 aluminum alloy from both the high-gas and low-gas conditions. In Figures 4.7 and 4.8, which show strain range versus number of cycles to failure data, there is no significant difference in fatigue life between the high-gas and low-gas conditions. The fatigue limit strain range was 0.26% which is equivalent to a stress range of 180 MPa. The 0.26% constant-amplitude fatigue limit strain obtained represents an increase of about 62.5% in fatigue strength from the flawed (non hipped) high-gas Al 319 alloy. The fatigue test results under constant-amplitude loading are given in Table 4.6. Fatigue test results under variable-amplitude loading are shown in Figures 4.7 and 4.8. The underload cycle stress levels used were ±144 MPa. The constant-amplitude fatigue limit strain amplitude of smooth specimens was reduced by 85% for the high-gas metal and by 78% for the low-gas metal. The fatigue test results under variable-amplitude loading are given in Table 4.7.

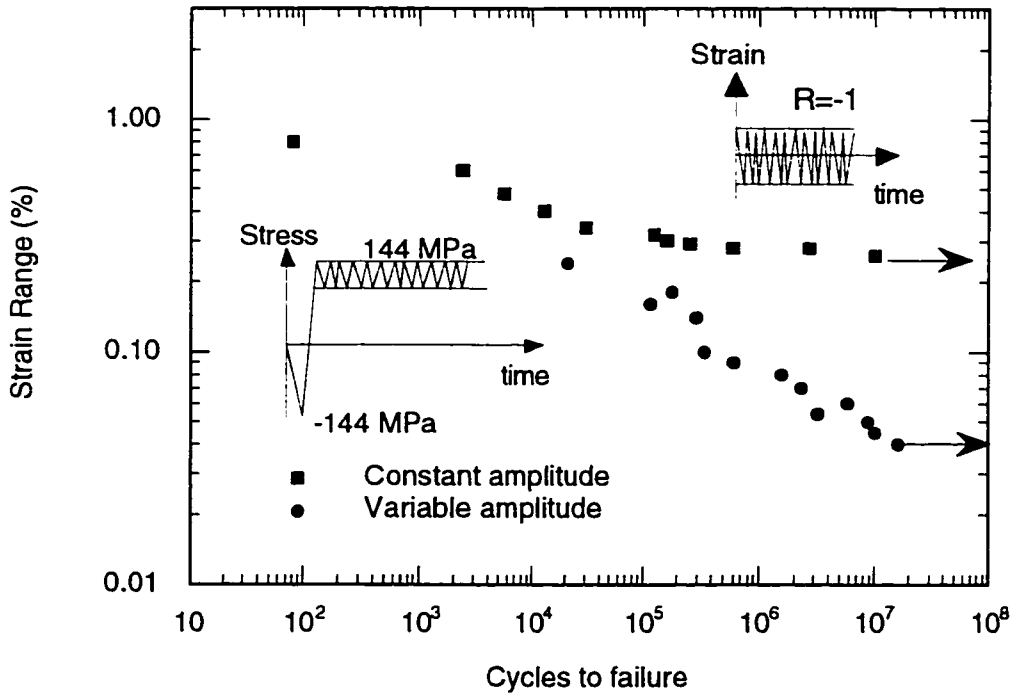

Figure 4.7 Constant- and variable-amplitude strain-life curves for Al 319 High-gas Hipped

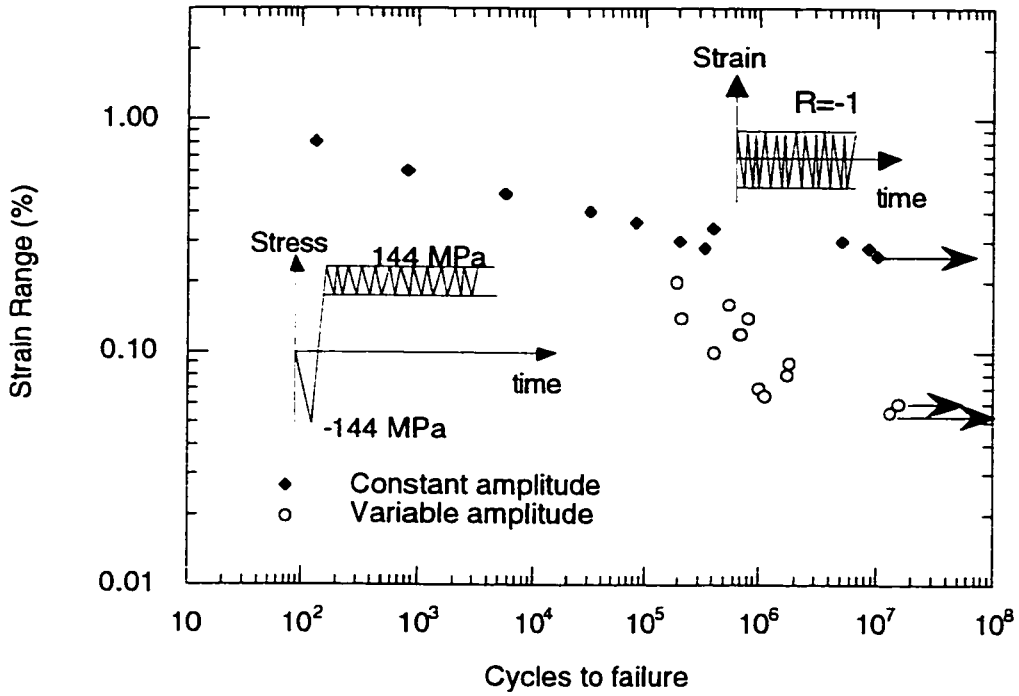

Figure 4.8 Constant- and variable-amplitude strain-life curves for Al 319 Low-gas Hipped

Table 4.6 Constant-amplitude fatigue life data for Hipped Al 319

High-Gas		Low-Gas	
Strain range (%)	Cycles to failure	Strain range (%)	Cycles to failure
0.400	81	0.40	132
0.300	2,383	0.30	832
0.240	5,618	0.24	5,677
0.200	12,797	0.20	31,587
0.170	31,073	0.18	83,169
0.160	124,415	0.17	397,941
0.150	162,507	0.15	5,119,476
0.145	258,190	0.15	202,997
0.140	601,484	0.14	336,361
0.140	2,682,867	0.14	8,611,743
0.130	10,050,000	0.13	10,132,000

Table 4.7 Variable amplitude fatigue life data for Hipped Al 319

High-Gas				Low-Gas			
Strain amp. (%)	N	N_f (Cycles)	N_{fseq} (Cycles)	Strain amp. (%)	N	N_f (Cycles)	N_{fseq} (Cycles)
0.12	195	20,801	20,866	0.1	150	184,592	190,732
0.09	950	178,035	180,483	0.08	600	537,184	551,852
0.08	825	114,460	115,558	0.07	432	207,425	210,132
0.07	430	280,581	294,911	0.07	650	780,633	810,138
0.05	703	334,402	346,793	0.06	750	651,869	669,340
0.045	805	582,781	616,586	0.06	750	681,039	700,157
0.04	970	1,395,701	1,570,471	0.05	800	367,364	372,267
0.035	1,180	1,992,240	2,292,736	0.05	800	403,546	409,555
0.03	1,472	4,432,560	5,797,842	0.045	805	1,680,132	1,796,432
0.027	1,715	2,955,989	3,201,520	0.04	800	1,606,748	1,713,552
0.025	3,000	7,195,886	8,851,345	0.035	1,000	969,459	999,062
0.0225	3,000	7,995,660	10,092,166	0.03	2,000	12,590,000	15,711,960
0.02	3,000	11,370,000	16,145,187	0.0275	2,000	10,950,000	13,237,213

4.2.3 Comparison of Cast and Hipped Fatigue Test Results

It is observed in Figures 4.9 and 4.10 that there is a significant improvement (62.5%) in fatigue strength from an as-cast condition to a hipped condition in constant-amplitude loading fatigue. However, that improvement is nearly eliminated under variable-amplitude loading. To understand this observation, the specimen fracture surfaces were examined under an optical microscope. It was found that the hipping process did not eliminate all flaws but there were still some very small shrinkage and gas pores. In an examination of the fracture surfaces of high-gas hipped specimens tested under constant-amplitude loading, six specimens out of eleven had small flaws on the fracture surface while for the low-gas hipped specimens only three out of eleven had small flaws on the fracture surface. In spite of the presence of small flaws, the fatigue life strength was significantly improved from the as-cast condition under constant-amplitude loading. An examination of the fracture surfaces of the hipped specimens tested under variable-amplitude loading found that nearly all the specimens had flaws on the fracture surface. So the 319 cast aluminum alloy, which showed improvement in fatigue strength from the as-cast to the hipped condition under constant-amplitude loading, did not show a significant improvement under variable-amplitude loading.

This behavior indicates a greater sensitivity of the 319 cast aluminum alloy to flaws or defects under variable-amplitude loading than under constant-amplitude loading. Indeed at long lives under variable-amplitude loading, very small flaws seem to be almost as damaging as large ones. Similar results were obtained for small notches in a 2024-T351 aluminum alloy under variable-amplitude loading by DuQuesnay *et al.*[81]. DuQuesnay *et al.* [81] showed that the notch size effect observed under constant-amplitude loading is reduced under variable-amplitude loading as shown in Figures 4.11 and 4.12.

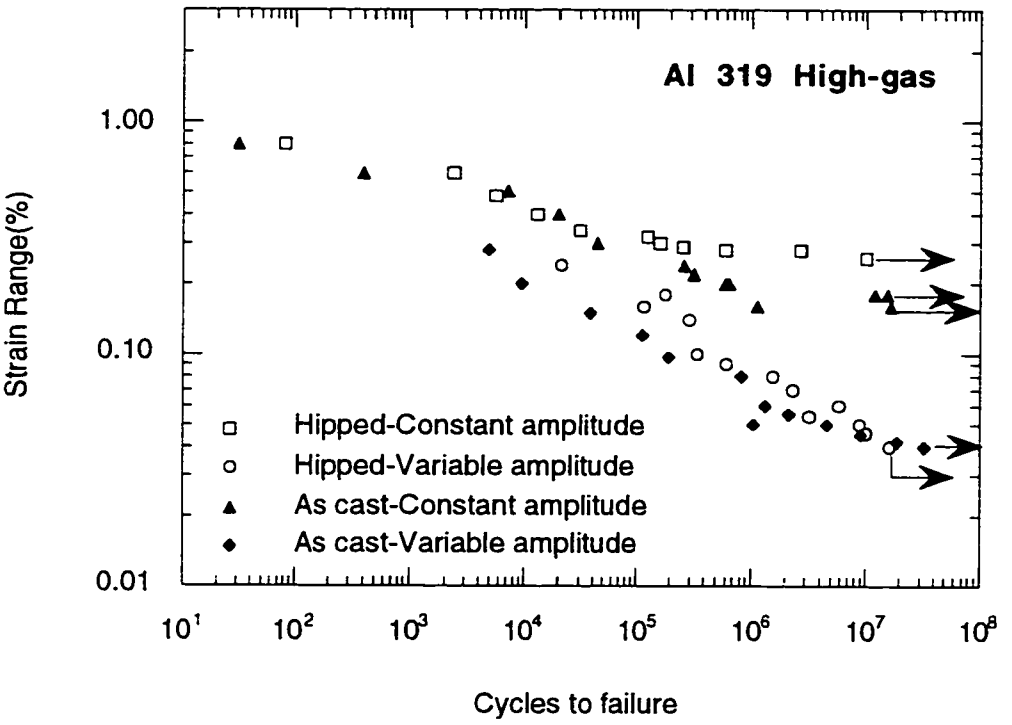

Figure 4.9 Experimental data for High-gas Hipped and cast Al 319 under constant and variable-amplitude loading

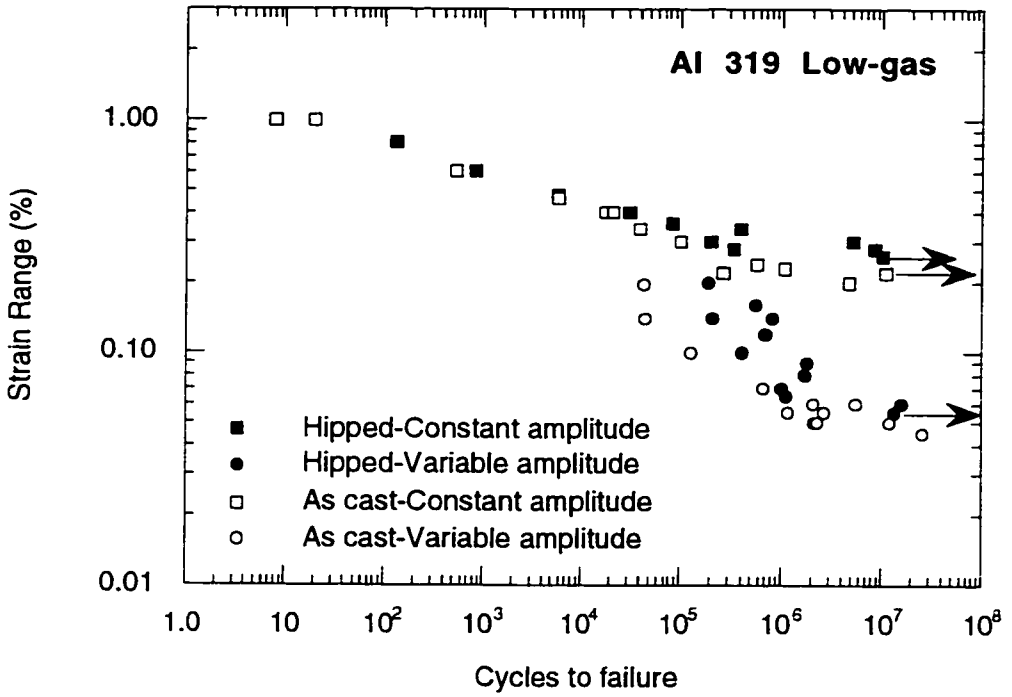

Figure 4.10 Experimental data for Low-gas Hipped and cast Al 319 under constant and variable-amplitude loading

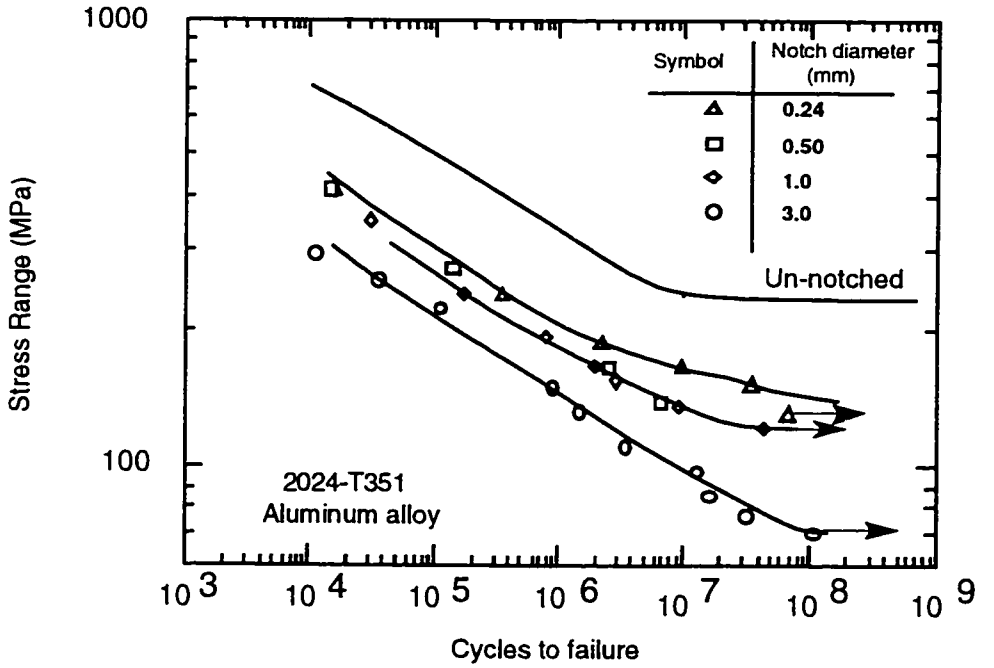

Figure 4.11 Fatigue notch size effect under constant-amplitude loading in 2024-T351 aluminum alloy [82]

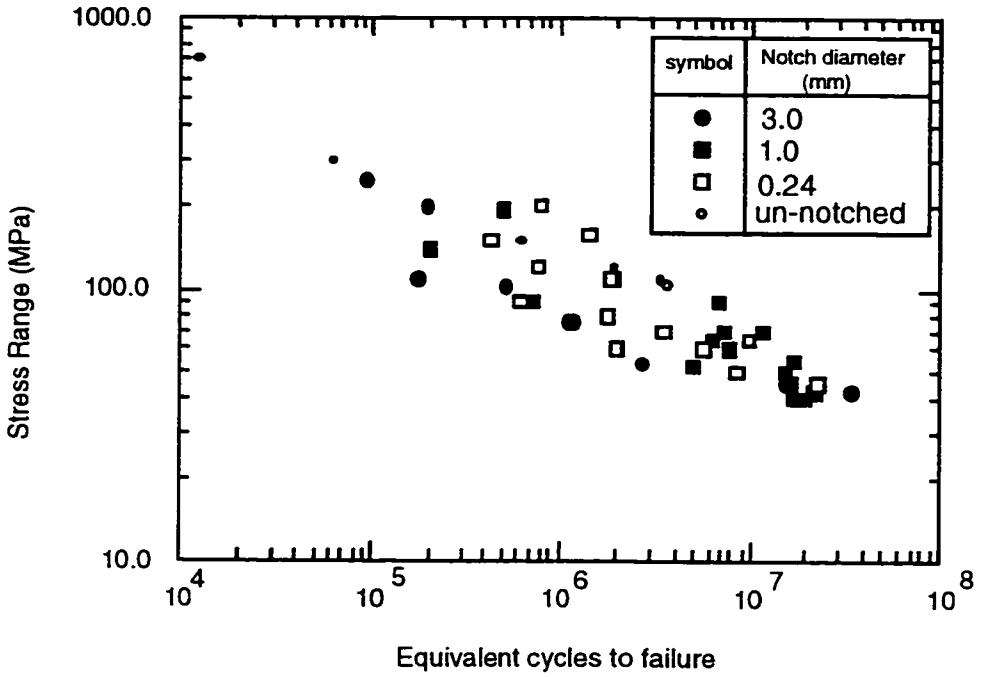

Figure 4.12 Stress versus equivalent life curves for center-notched specimens subjected to periodic overloads [81]

The $\Delta\sigma_{th}$ versus crack length curves (Kitagawa curve), for the material, for stress cycles with and without closure are shown schematically in Figure 4.13. The local notch stress versus crack length is shown on the same plot. The stress at which the notch stress lies completely above and just touches the kitagawa curve is the fatigue limit stress and the crack length at which the notch stress touches the kitagawa curve is the largest non-propagating crack length. The notch radius for which the fatigue notch factor (K_f) is less than the theoretical stress concentration factor is larger for constant-amplitude loading (curve with closure) than for variable-amplitude loading (intrinsic curve). Figure 4.14 shows a sketch of the relationship between the notch radius and K_f for constant and variable-amplitude loading. The Figure shows that as the notch radius increases the fatigue notch factor increases until it is equal to K_t where it stabilizes. Stabilization is reached at a smaller notch radius under variable-amplitude loading than under constant-amplitude loading. Flaws in smooth specimens are treated as notches [83], with a notch size equal to the flaw diameter. It is then expected that there is a certain flaw size at which the

fatigue notch factor is equal to K_t. This flaw size is expected to be smaller under variable-amplitude fatigue loading than under constant-amplitude fatigue loading.

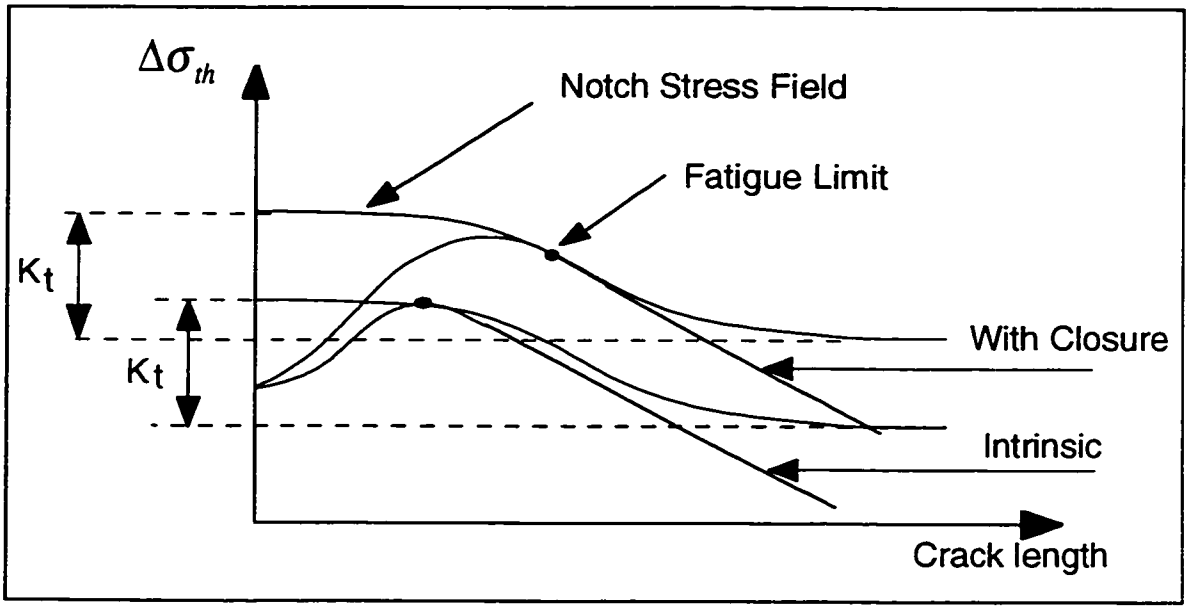

Figure 4.13 A schematic of intrinsic and with crack closure Kitagawa curves with the notch stress fields

This explains why having a smaller flaw size in the hipped than in the as-cast Al 319 showed an improvement in fatigue life under constant-amplitude loading but not under variable-amplitude loading.

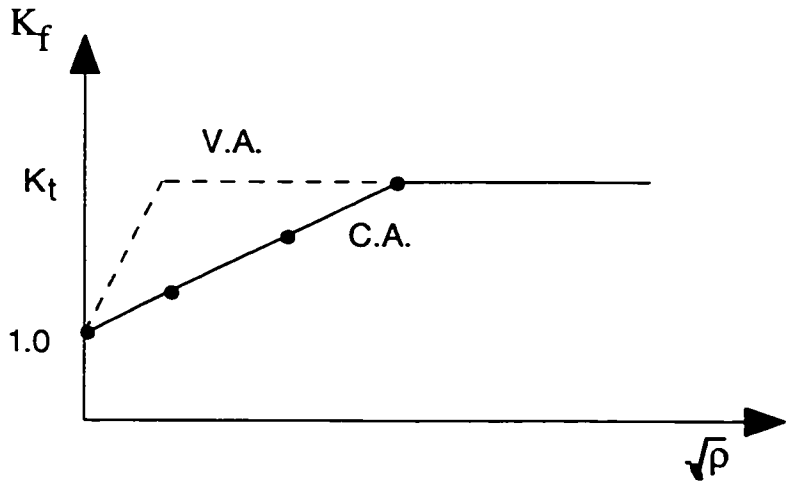

Figure 4.14 A schematic of the relation between the fatigue notch factor (K_f) and the square root of the notch radius of curvature ($\sqrt{\rho}$)

4.3 Detection of Natural Flaws

To study the effect of a flaw at a notch root on the fatigue behavior of notched specimens of the cast aluminum alloy material, specimens were prepared by two procedures:

Procedure 1- The cast aluminum alloy plates were examined by ultra-sonic waves to detect the location of the defects and their depth below the material surface. The notched specimens were then cut from the cast plate so that the natural flaw was at the notch root. When possible large flaws were used.

Procedure 2- Notched specimens were machined from the hipped cast aluminum alloy, which had only very small flaws, and a natural flaw was modeled as a drilled hole which was of the same size as the average flaw in the cast aluminum alloy, as shown in Figure 4.15. The hole was drilled at the notch root of the hipped aluminum alloy.

Both procedures for specimen preparation produced a notched cast aluminum specimen with a flaw at a notch root. However, there was some variation in the accuracy of positioning of the flaw at the notch root, which resulted in a variability in the fatigue results for natural flaws.

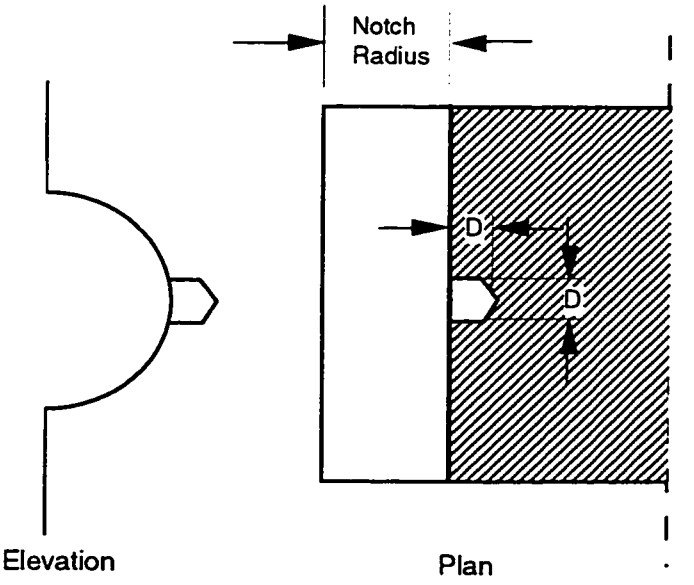

Figure 4.15 Position and shape of the artificial flaw

4.4 Notched Specimen Fatigue Tests

This section gives the notched fatigue test results for the as-cast and hipped materials under the constant- and variable-amplitude loading histories. The notches used were circular edge notches of 1.0 mm, 3.0 mm, and 6.0 mm in diameter with natural and artificial flaws at the notch roots.

4.4.1 Theoretical Stress Concentration

The theoretical surface stress concentration factor, K_t, and the stress field ahead of the notch for the three different notch sizes, has been calculated using finite element analysis. The ABAQUS [84] finite element analysis package was used to construct the finite element mesh and to perform the analysis. By symmetry, only one-half of the specimen was modeled. The finite element mesh used was very finely spaced in the vicinity of the notch as shown in Figure 4.16. Eight-noded plane strain elements were used in the mesh which consisted of 256 elements. The gripping of the specimen was modeled in the finite element code by preventing any rotation and displacement at the ends, except for the displacement in the loading direction which was allowed. The analysis gave gross stress concentration factors, K_{tg}, of 3.205, 3.109, and 3.011 for the 6.0 mm, 3.0 mm, and 1.0 mm diameter edge notches, respectively. The stress distribution ahead of the notch was also measured experimentally for the 6.0 mm diameter edge notch by gluing six strain gauges along the specimen width in front of the notch. The experimental stress field was compared with the finite element results and there was good agreement as shown in Figure 4.17.

The theoretical stress concentration factor for a flaw at the root of an edge notch was calculated using the available stress concentration factors of individual flaws and notches. The stress concentration factor for the case of a big notch size to flaw size ratio, $\frac{R}{r}$, at which the notch size is 20 times the flaw size, is taken as the multiplication of the stress concentration factor of a 12.0 mm diameter notch, K_{tg}=3.48 obtained using finite element analysis, by the stress concentration factor of a 0.6 mm diameter flaw, K_{tf}=2.03 [85], i.e. $K_t = K_{tg} \times K_{tf} = 3.48 \times 2.03 = 7.065$. The stress concentration factor for $\frac{R}{r}$=0, is taken as the stress concentration of the 0.6 mm diameter flaw. The stress concentration for $\frac{R}{r}$=1, is taken as the stress concentration of a deep notch having a depth equal to the sum of the edge notch

radius and the flaw diameter, K_t=3.75 [85]. The stress concentration factor in terms of the notch size to flaw size ratio $\frac{R}{r}$ is plotted in Figure 4.18.

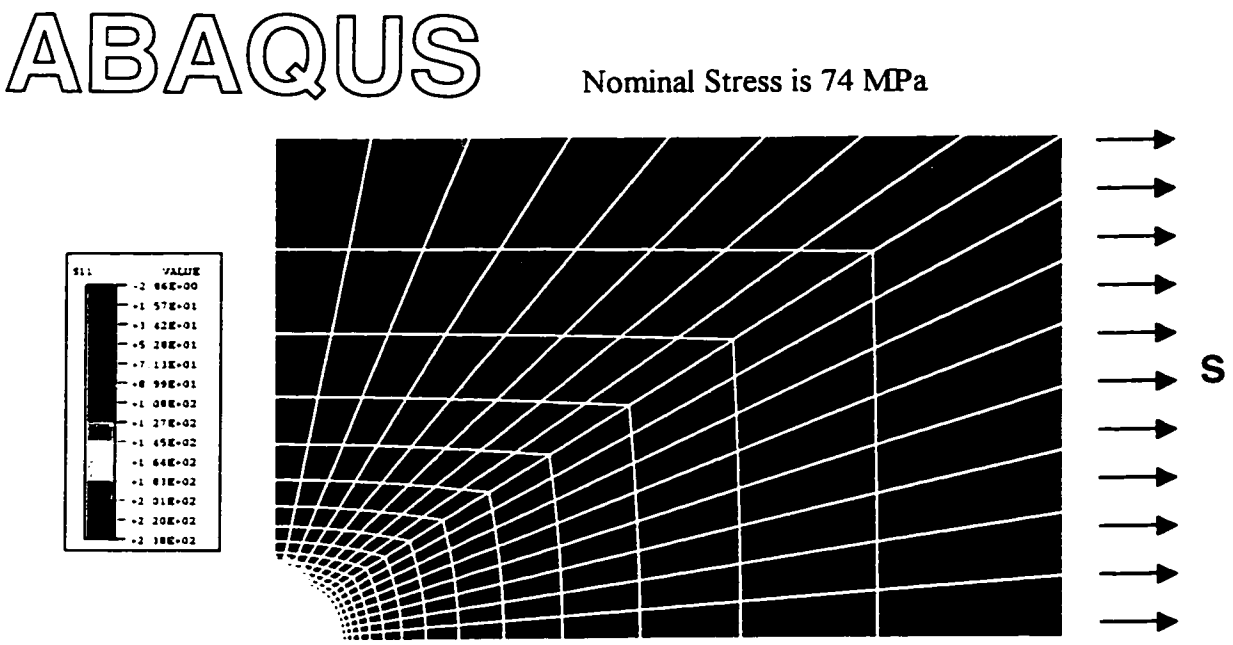

Figure 4.16 The finite element mesh in the vicinity of the 3.0 mm radius notch

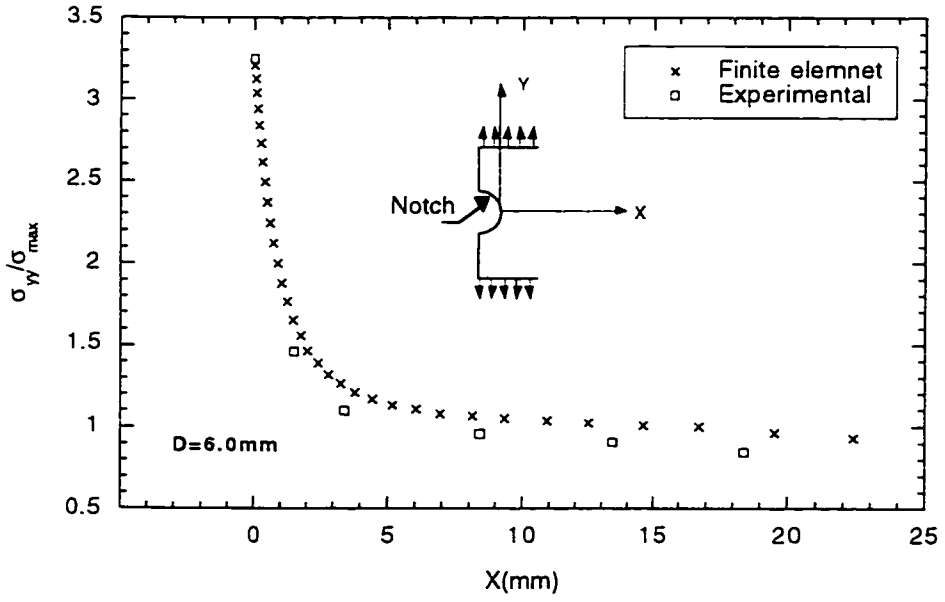

Figure 4.17. Experimental and finite element results for the stress field ahead of a 3.0mm radius edge notch

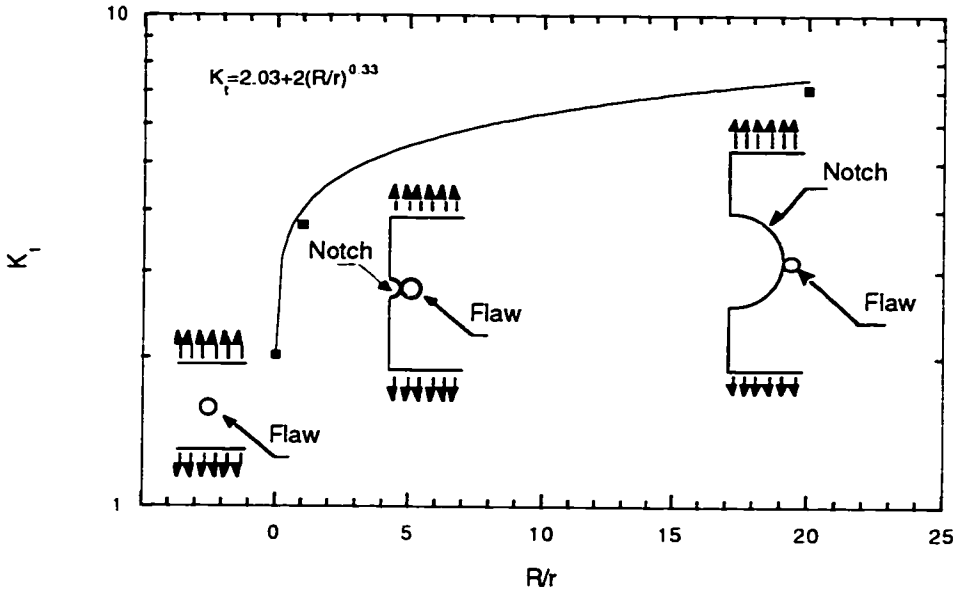

Figure 4.18 The relation between the notch size to flaw size ratio and the stress concentration factor K_t

Comparison between the notch stress field for uncracked specimens and the elastic stress concentration factor, K_p, for a crack emanating from an edge notch and for a crack emanating from a flaw in an edge notch root is shown in Appendix B.

4.4.2 Natural Flaw at a Notch Root

The notches used in this series of tests were circular edge notches of 1.0 mm, 3.0 mm, and 6.0 mm in diameter and the specimens were prepared according to the procedure explained in section 4.3. Stress-life constant-amplitude fatigue tests at R=-1 were conducted on the 319 cast aluminum alloy in the high-gas condition. The high-gas condition was used in this series of tests because the material has larger and more numerous gas pores than the metal in the low-gas condition. The larger and more numerous gas pores made it easier to detect a large flaw and locate it at the notch root. Figure 4.19 shows the fatigue data plotted in terms of the fatigue life versus the gross nominal stress range multiplied by the gross surface stress concentration factor, $K_{tg}\Delta S$, to account for the different K_{tg} values of the

three notch sizes. The fatigue limit and fatigue test results in terms of the nominal stresses applied on the notched specimens are given in Tables 4.8 and 4.9.

Variable-amplitude stress-life fatigue tests were also conducted. The underload cycle used, for each notch size, was chosen as the corresponding constant-amplitude stress level that would give a fatigue life of 10,000 cycles. The underload stress levels for the 1.0 mm, 3.0 mm, and 6.0 mm diameter notches were ±105 MPa, ±90 MPa, and ±70 MPa, respectively. The fatigue test results under variable-amplitude loading are shown in Figure 4.19. Results are plotted on axes of the equivalent number of small cycles to failure versus the nominal stress range multiplied by the gross surface stress concentration factor, $K_{tg}\Delta S$, on log scales. The fatigue limit and fatigue test results, in terms of the nominal stresses applied on the notched specimens, are given in Tables 4.10 and 4.11.

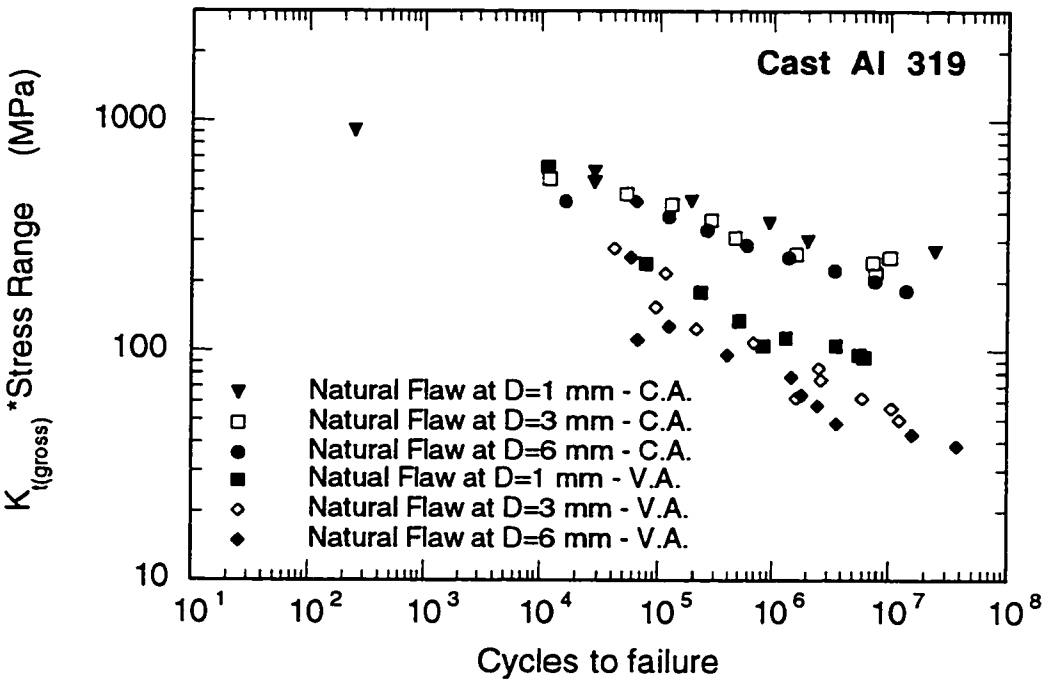

Figure 4.19 S-N curves for notched 319 cast aluminum alloy having natural flaw at notch root

After testing, the fracture surface of each specimen was examined under a 900X power optical microscope to locate the position of the flaw in the notch root. Figure 4.20 shows two cases in which the flaws were positioned accurately at the notch root and shows also a case in which the positioning of the flaw was less accurate as well as a case in which the size of the flaw was less than the largest average flaw size of 0.9 mm. This variation in size and location of the flaws resulted in a considerable range of scatter in the fatigue data as can be seen in Figure 4.19. From the fracture surface examinations, it was concluded that the average size of the flaws found at the notch roots of the specimens tested was about 0.6 mm in diameter.

Table 4.8 Fatigue limit stress range for notched as-cast Al 319 with natural flaw at notch root under constant-amplitude loading

Fatigue limit	Natural flaw at 1.0 mm diameter notch	Natural flaw at 3.0 mm diameter notch	Natural flaw at 6.0 mm diameter notch
Stress range (MPa)	90	82	57

Table 4.9 Constant-amplitude fatigue life data for notched as-cast Al 319 with natural flaw at notch root

Natural flaw at 1.0 mm diameter notch		Natural flaw at 3.0 mm diameter notch		Natural flaw at 6.0 mm diameter notch	
Stress range (MPa)	Cycles to failure	Stress range (MPa)	Cycles to failure	Stress range (MPa)	Cycles to failure
300	246	180	11,766	140	16,185
200	27,617	155	51,774	120	119,480
180	27,837	140	127,326	105	259,920
150	188,070	120	281,499	90	577,730
120	919,562	100	455,670	80	1,375,006
100	2,010,737	85	1,593,455	70	3,455,900
90	23,900,000	82	10,000,000	63	7,558,290
		78	7,234,866	57	13,628,480
		70	7,640,000		

Table 4.10 Fatigue limit stress range for notched as-cast Al 319 with natural flaw at notch root under variable-amplitude loading

Fatigue limit	Natural flaw at 1.0 mm diameter notch	Natural flaw at 3.0 mm diameter notch	Natural flaw at 6.0 mm diameter notch
Stress range (MPa)	32	18	12

Table 4.11 Variable-amplitude fatigue life data for notched as-cast Al 319 with natural flaw at notch root

Natural flaw at 1.0 mm diameter notch				Natural flaw at 3.0 mm diameter notch			
Stress range (MPa)	N	N_f (Cycles)	N_{fseq} (Cycles)	Stress range (MPa)	N	N_f (Cycles)	N_{fseq} (Cycles)
80	40	66,996	76,429	90	12	34,342	40,851
60	90	188,466	228,285	70	60	99,136	113,135
45	360	447,239	500,955	50	450	91,755	93,154
38	900	1,154,198	1,299,793	40	180	190,306	207,812
35	1,700	781,622	825,153	35	300	569,797	676,720
35	1,700	2,978,743	3,523,484	27	500	1,767,870	2,520,488
32	2,000	4,493,625	5,614,225	24	1,500	2,294,703	2,635,227
31	2,000	4,859,156	6,186,914	20	2,000	1,504,754	1,606,668
				20	2,000	4,756,178	5,957,144
				18	2,500	10,310,000	15,864,014
				16	2,500	12,100,000	20,541,715

Table 4.11 (continued) Variable-amplitude fatigue life data for notched as-cast Al 319 with natural flaw at notch root

Natural flaw at 6.0 mm diameter notch			
Stress range (MPa)	N	N_f (Cycles)	N_{fseq} (Cycles)
80	20	56,054	57,237
40	100	118,477	120,882
35	40	63,591	64,564
30	125	366,159	391,985
24	170	1,202,027	1,452,708
20	600	1,674,832	1,798,479
18	800	2,304,407	2,481,701
15	1,100	3,319,532	3,589,304
13.5	1,500	12,265,179	15,440,927
12	1,500	22,861,736	37,106,553

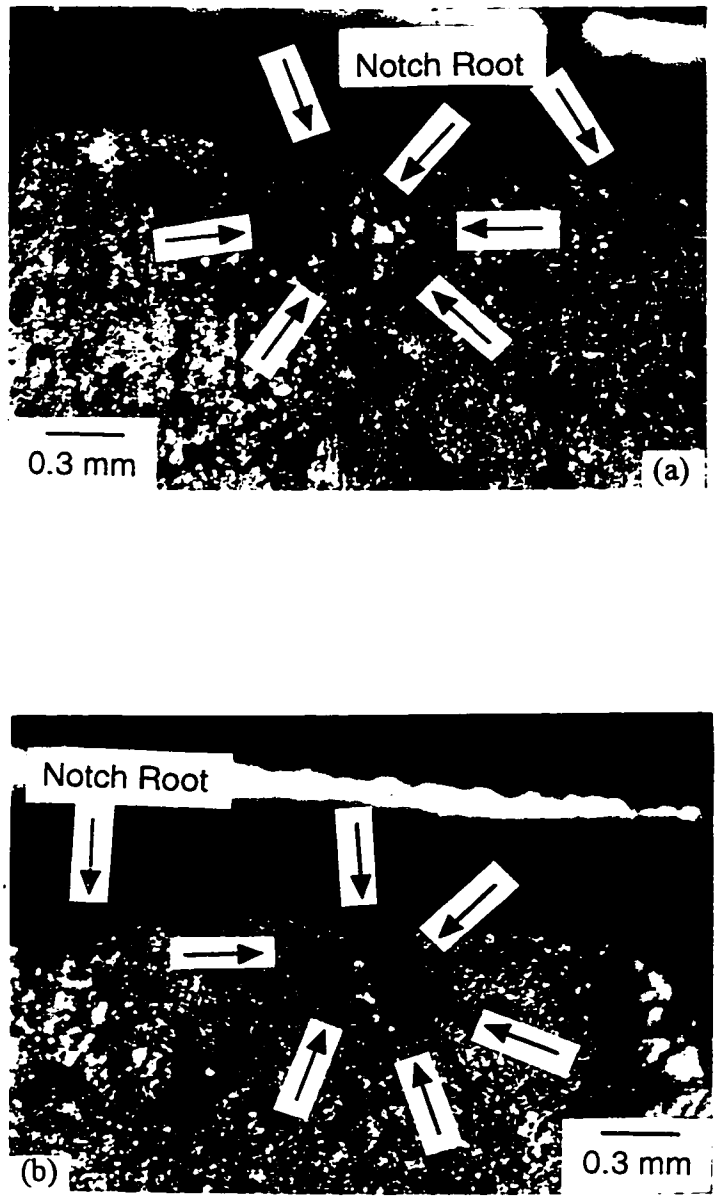

Figure 4.20 Pictures of the positions of a flaw at the notch root
(a) a case of a flaw positioned accurately at the notch root, (b) A case of a flaw positioned accurately at the notch root,

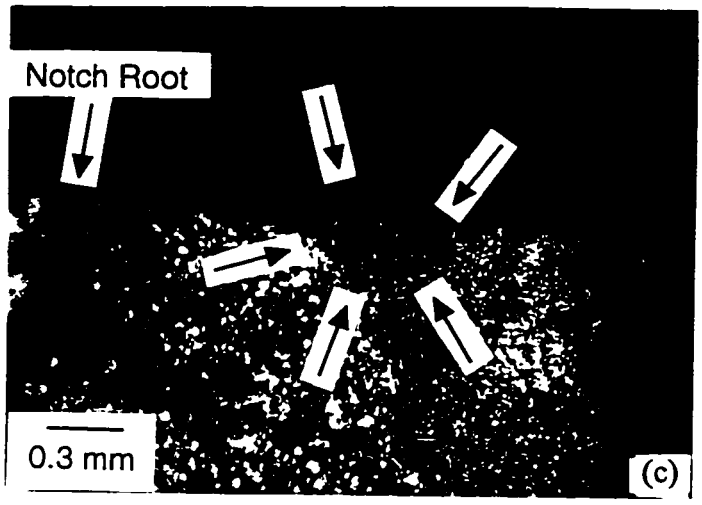

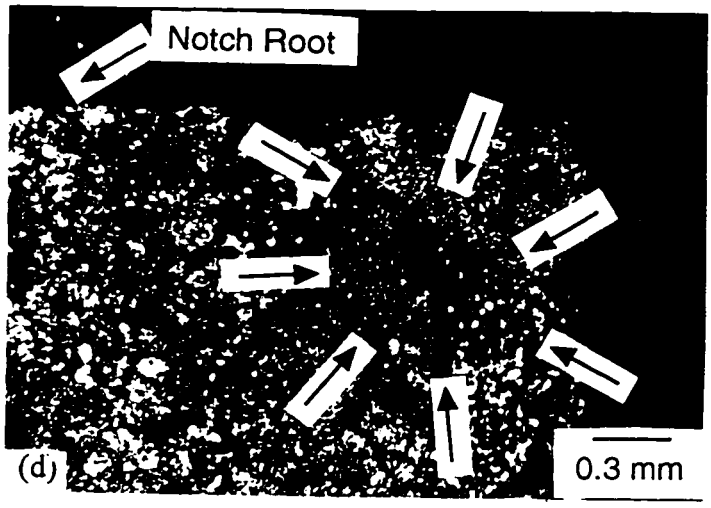

Figure 4.20 (continued) Pictures of the positions of a flaw at the notch root
(c) flaw at notch root, but flaw size is less than the largest average flaw at the specimen surface, (d) flaw is located away from the notch root

4.4.3 Artificial Flaw at a Notch Root

To model a natural flaw, a hole of 0.6 mm in diameter and 0.6 mm in depth was drilled at the notch root of the hipped 319 aluminum alloy. The notches used in this series of tests were circular edge notches 1.0 mm, 3.0 mm, and 6.0 mm in diameter and the specimens were prepared according to procedure 2 explained in section 4.3.

Stress-life constant-amplitude fatigue tests at R=-1 conducted on the hipped 319 aluminum alloy are plotted in terms of the fatigue life versus the gross nominal stress range multiplied by the gross surface stress concentration factor, $K_{tg}\Delta S$, and are shown in Figure 4.21. The fatigue limit and fatigue test results, in terms of the nominal stresses applied on the notched specimens, are given in Tables 4.12 and 4.13. Variable-amplitude fatigue tests were also conducted. The underload cycle used, for each notch size, is chosen as the corresponding constant-amplitude stress level that would give a fatigue life of 10,000 cycles. The underload stress levels for the 1.0 mm, 3.0 mm, and 6.0 mm diameter notches were ±130 MPa, ±105 MPa, and ±85 MPa, respectively. Figure 4.21 shows the equivalent number of small cycles to failure versus the nominal stress range multiplied by the gross surface stress concentration factor, $K_{tg}\Delta S$. The fatigue limit and fatigue test results, in terms of the nominal stresses applied on the notched specimens, are given in Tables 4.14 and 4.15. Again as in the smooth specimen tests, the underload block loading history used was the most damaging history possible for the applied stress, since the crack was fully open throughout the small cycles.

Table 4.12 Fatigue limit stress range for notched Hipped Al 319 with a 0.6 mm diameter drill at notch root under constant-amplitude loading

Fatigue limit	A 0.6 mm diameter drill at 1.0 mm diameter notch	A 0.6 mm diameter drill at 3.0 mm diameter notch	A 0.6 mm diameter drill at 6.0 mm diameter notch
Stress range (MPa)	117	90	80

Table 4.13 Constant-amplitude fatigue life data for notched Hipped Al 319 with a 0.6 mm diameter drill at notch root

A 0.6 mm diameter drill at 1.0 mm diameter notch		A 0.6 mm diameter drill at 3.0 mm diameter notch		A 0.6 mm diameter drill at 6.0 mm diameter notch	
Stress range (MPa)	Cycles to failure	Stress range (MPa)	Cycles to failure	Stress range (MPa)	Cycles to failure
260	10,449	300	47	200	428
220	159,864	220	1,366	180	44,452
220	60,193	210	17,754	170	23,823
180	184,452	190	153,558	120	527,907
150	1,103,050	180	259,498	95	1,429,508
130	5,015,400	150	192,972	86	1,870,573
117	6,338,160	130	1,493,723	80	11,555,068
		105	1,664,980		
		92	12,634,599		

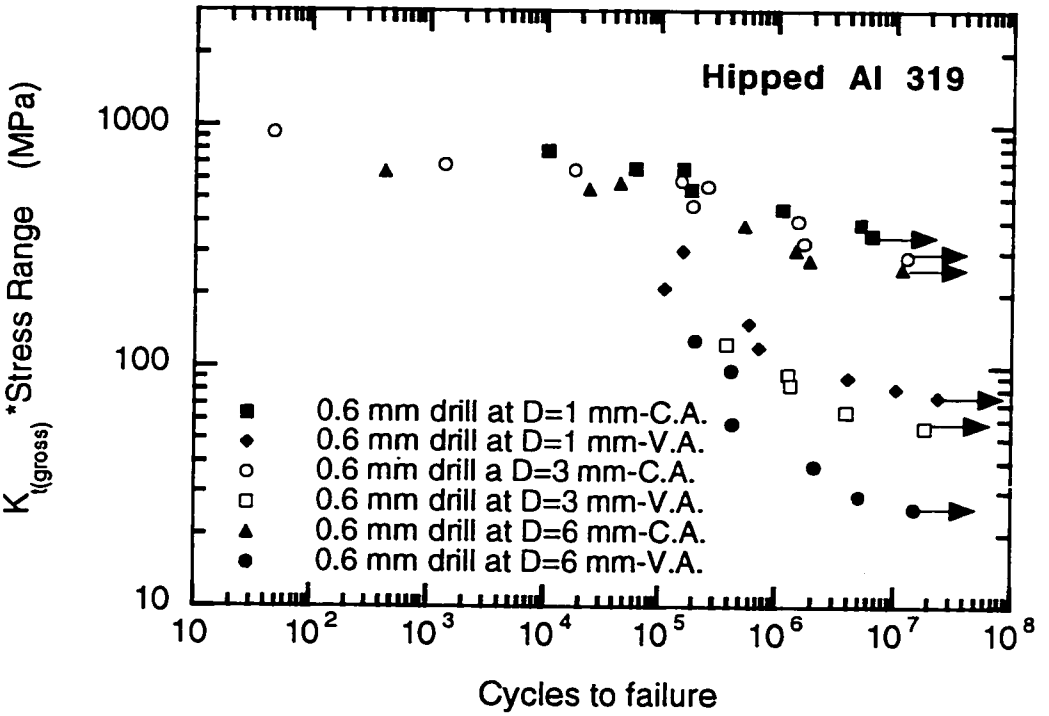

Figure 4.21 S-N curves for notched 319 Hipped aluminum alloy having a hole drilled at the notch root

Table 4.14 Fatigue limit stress range for notched Hipped Al 319 with a 0.6 mm diameter drill at notch root under variable-amplitude loading

Fatigue limit	A 0.6 mm diameter drill at 1.0 mm diameter notch	A 0.6 mm diameter drill at 3.0 mm diameter notch	A 0.6 mm diameter drill at 6.0 mm diameter notch
Stress range (MPa)	25	18	8

Table 4.15 Variable-amplitude fatigue life data for notched Hipped Al 319 with a 0.6 mm diameter drill at notch root

A 0.6 mm diameter drill at 1.0 mm diameter notch				A 0.6 mm diameter drill at 3.0 mm diameter notch			
Stress range (MPa)	N	N_f (Cycles)	N_{fseq} (Cycles)	Stress range (MPa)	N	N_f (Cycles)	N_{fseq} (Cycles)
100	50	124,603	159,436	40	150	334,490	379,612
70	200	104,178	109,069	30	1,000	1,177,179	1,259,373
50	330	498,830	581,120	27	1,500	1,258,970	1,320,457
40	850	662,200	714,587	21	1,500	3,390,772	3,882,347
30	2,500	3,431,380	3,948,437	18	1,800	11,785,744	18,651,665
27	3,500	8,041,904	10,304,546				
25	850	6,479,515	23,793,753				

A 0.6 mm diameter drill at 6.0 mm diameter notch			
Stress range (MPa)	N	N_f (Cycles)	N_{fseq} (Cycles)
40	70	185,399	205,287
30	350	397,500	415,916
18	600	416,545	428,272
12	700	1,859,053	2,088,895
9	1,000	4,096,098	4,940,246
7	1,800	13,000,000	18,641,007

4.4.4 Comparison of Fatigue Results for Natural and Artificial Flaws at a Notch Root

The ultimate strength of the as-cast 319 aluminum alloy in the high-gas condition is 193 MPa, but the hipped material, in the same condition, has an ultimate strength of 232 MPa. Since a material's fatigue limit varies with its ultimate strength, the constant-amplitude S-N curves of the three notch sizes examined having a 0.6 mm drill at the notch root were multiplied by the ratio of the hipped ultimate stress to the as-cast ultimate stress and then compared to the constant-amplitude S-N curves of the as-cast material having a natural flaw at the notch root. The comparison is shown in Figure 4.22. From the figure it can be seen that the data for natural and artificial flaws fall together for each notch size which suggests that a natural flaw in the as-cast 319 aluminum alloy can be modeled by an equivalent drilled hole of the same size.

The same procedure was applied to the fatigue test data for variable-amplitude loading and the results obtained are plotted in Figure 4.23. The figure shows that the 0.6 mm diameter drilled hole and the natural flaw did not give similar fatigue lives near the fatigue limit region. As shown in Figure 4.23 the difference between the natural and artificial flaw at the notch root results, in terms of fatigue limit stress ranges multiplied by the notch stress concentration factor, was highest for the 1.0 mm diameter notch, at 33 MPa, and lower for the 3.0 mm and 6.0 mm diameter notches, at 12 MPa and 17 MPa, respectively. An examination of the fracture surface of the broken specimens with natural flaws at their notch roots revealed that there was a variation in the sizes of the flaws that caused failure and in their location in the notch root. This variation explains the difference in fatigue limit between the as-cast and hipped specimens having a natural and an artificial flaw at the notch root, respectively. The difference between the fatigue limit for as-cast and hipped materials, due to the variation in flaw size and flaw location, is larger for small notches than for large notches. This difference is expected to be more pronounced for small notches than for large notches because notch stress fields decay more rapidly for small notches than for large notches, and a given variation in flaw size or distance from the notch root will cause a larger change in the combined notch-flaw stress field for a small notch than for a large notch.

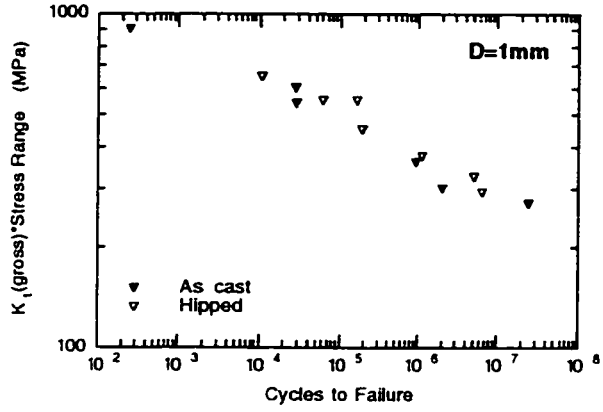

(a)

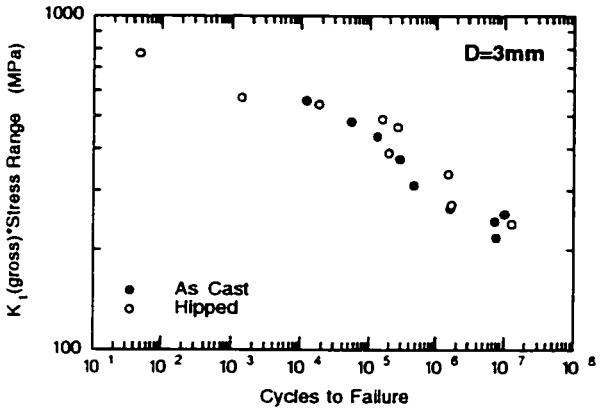

(b)

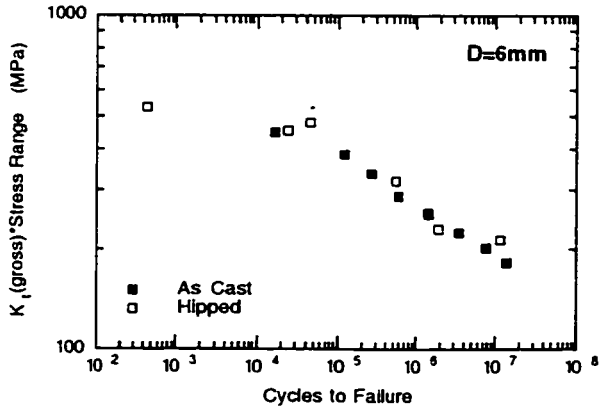

(c)

Figure 4.22 Comparison of constant-amplitude S-N curves for notched as-cast and hipped 319 aluminum with a flaw and a hole drilled at the notch root; (a) Notch diameter is 1 mm, (b) Notch diameter is 3 mm, (c) Notch diameter is 6 mm

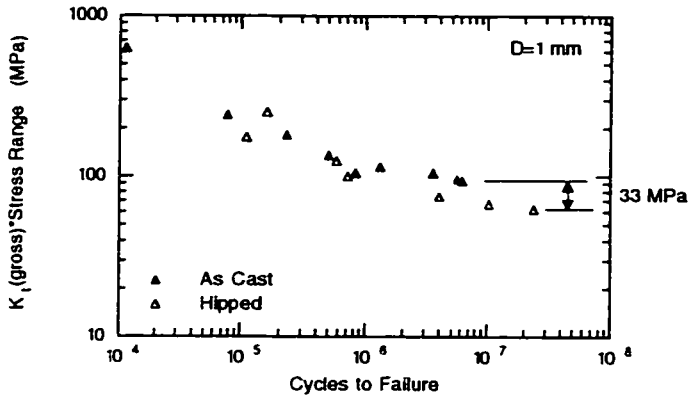

(a)

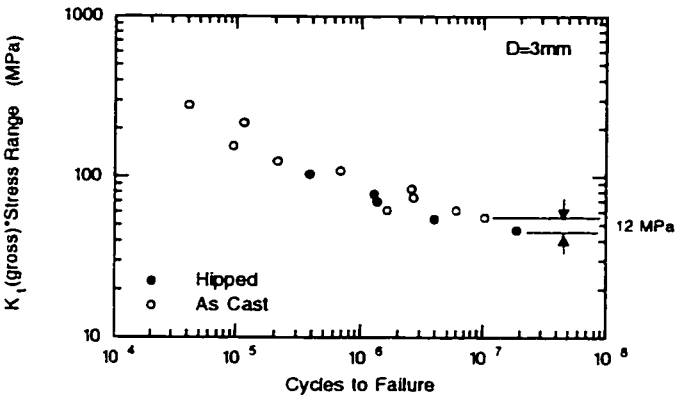

(b)

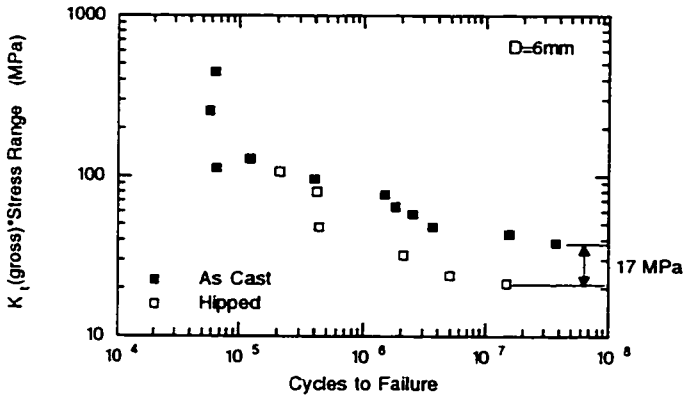

(c)

Figure 4.23 Comparison of variable-amplitude S-N curves for notched as-cast and hipped 319 aluminum with a flaw and a hole drilled at the notch root; (a) Notch diameter is 1 mm, (b) Notch diameter is 3 mm, (c) Notch diameter is 6 mm

The stress field ahead of the notch is increased if a flaw is introduced at the notch root. If the flaw dimensions are much smaller than the notch dimensions, the stress concentration factor, K_t, at the flaw is expected to be the product of the stress concentration factor of the notch, K_{tg}, and the stress concentration factor of the flaw, K_{tf}, i.e. $K_t = K_{tg} \times K_{tf}$, and the maximum decrease in the fatigue strength for a flaw at a notch root is expected to be equal to the smooth specimen fatigue limit divided by the factor ($K_{tg} \times K_{tf}$). The observed results under constant-amplitude loading showed that ratio of the fatigue limit stress range, caused by a 0.6 mm diameter drill at the notch root of 6 mm diameter, to that for smooth specimens is 3.3 which is higher than K_{tg}=3.205 and lower than the maximum theoretical value of K_t=3.205x2.03=6.50 for a small flaw at the root of a large notch. Fatigue limit data for notched specimens with flaws under variable-amplitude loading showed a decrease from the smooth specimen variable-amplitude fatigue limit of a factor of 4 for the 0.6 mm diameter drill at the root of a 6 mm diameter notch, which is again higher than the K_{tg} value of 3.205 and lower than the maximum theoretical value of K_t=6.50.

DuQuesnay *et al.* [81] studied the notch fatigue behavior of center notched 2024-T351 aluminum alloy specimens under variable-amplitude loading. The variable-amplitude loading sequence consisted of a periodic compression-tension overload of yield magnitude followed by smaller, high stress ratio cycles. They found that the notch size effect that is typically observed under constant-amplitude loading [82] is reduced under variable-amplitude loading as shown in Figures 4.11 and 4.12. A similar observation was made by MacDougall and Topper [86] for a SAE 1045 steel. In their results, as shown in Figure 4.24, there was no significant difference in the fatigue limit stress range for different center notch sizes tested under the same variable-amplitude loading. For the case of a constant flaw size at a notch root, a notch size effect was observed under both constant- and variable-amplitude loading. The fatigue test results of Figures 4.19 and 4.21 for constant- and variable-amplitude loading, respectively, show that as the size of a notch with a constant size flaw increases, the fatigue limit decreases. The fatigue strengths multiplied by K_{tg} for a 0.6 mm diameter hole drilled at the root of 1.0 mm , 3.0 mm, and 6.0 mm diameter notches, respectively, were 352 MPa, 280 MPa, and 256 MPa for constant-amplitude loading and 75 MPa, 57 MPa, and 25 MPa for variable-amplitude loading.

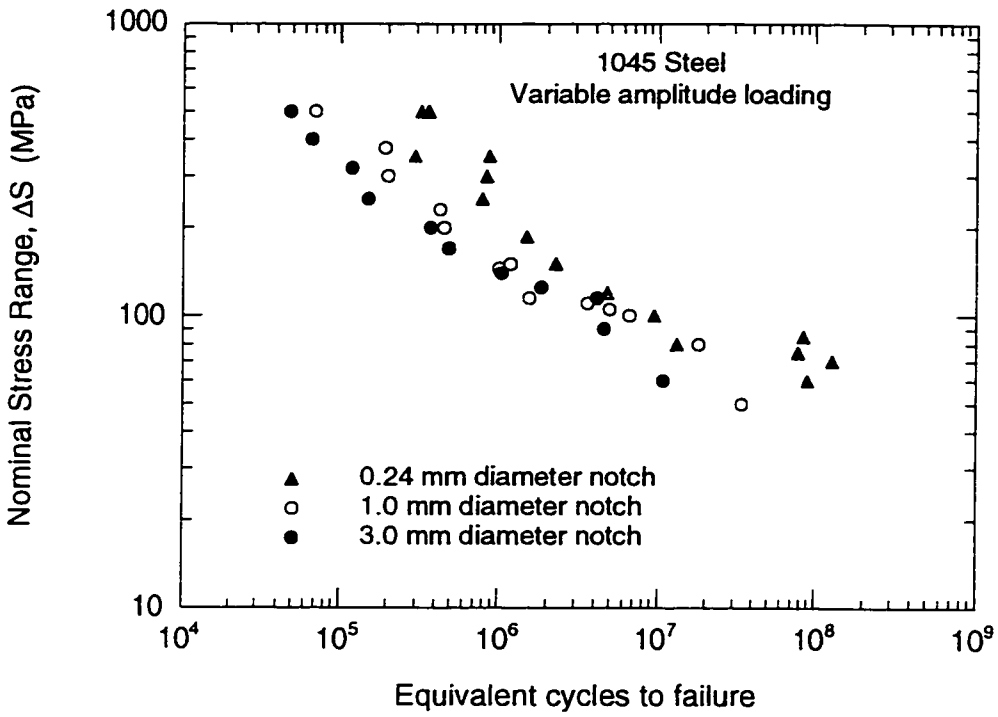

Figure 4.24 Notch size effect for 1045 steel specimens subjected to variable amplitude loading [86]

4.5 Constant- and Variable-amplitude Crack Opening Stress Measurements

4.5.1 Crack Opening Measurements After a 62 MPa to -124 MPa Underload

Figures 4.25, 4.26, 4.27, and 4.28 show crack opening stresses as a function of the number of cycles after an underload for the various stress ratios used. The underload stress cycle had a maximum stress (S_{max})of 62 MPa and a minimum, near yield, stress (S_{min}) of -124 MPa.

For the R=0.85 test, the maximum and minimum stress of the constant-amplitude cycles were 62 MPa and 53 MPa, respectively. The crack length when the measurements were made was 6.85 mm. Figure 4.25 shows that the crack opening stress level is a minimum immediately after the underload (23.84 MPa) and then increases in a roughly exponential manner until it reaches a steady state of 43.20

MPa after about 500 of the constant-amplitude small cycles. This steady state stress level is still below the minimum stress of 53 MPa for the small cycles and the crack is fully open during all of the small cycles.

For R=0.5 test data, shown in Figure 4.26, the maximum and minimum stresses of the constant-amplitude small cycles were 62 MPa and 31 MPa, respectively. The crack opening stress level again decreased to a minimum immediately after the underload. The crack opening stress increased from a post underload value of 21.4 MPa to a steady state stress level of 32.4 MPa. Again the increase is roughly exponential in form, but at this stress ratio the final steady state opening stress was higher than the minimum stress of the small cycles and consequently the last steady state small cycles were partly closed. The opening stress reached the level of the minimum stress at about cycle number 50 after the underload. Thus the first 50 cycles after the underload are fully open.

For the test at R=0, the minimum stress was zero and the maximum stress was 27.6 MPa. The crack opening stress changes after an underload are shown in Figure 4.27. Unlike the R=0.85 and R=0.5 tests, there is no period during which the stress cycles are fully open after the underload. The crack opening stress immediately after the underload is 5.56 MPa from which level it increases in an exponential manner to a steady state level of 20.7 MPa.

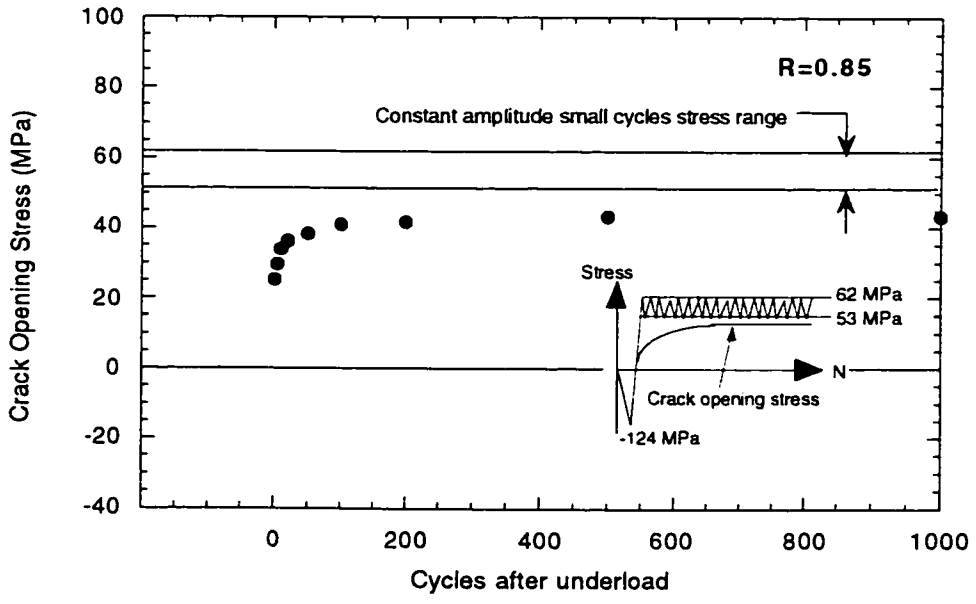

Figure 4.25 Crack opening stress build-up measurements for R=0.85

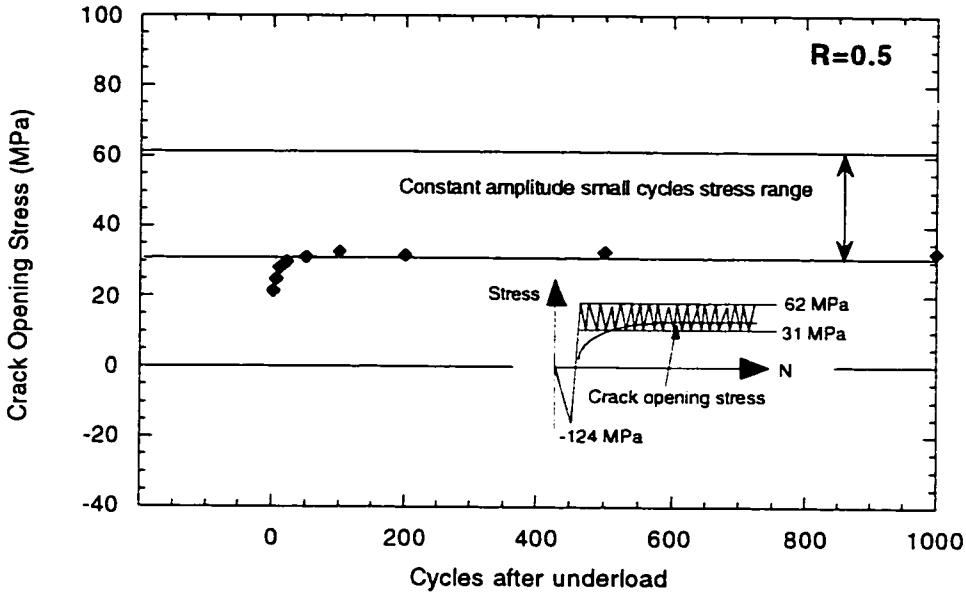

Figure 4.26 Crack opening stress build-up measurements for R=0.50

Finally for small cycles with R=-1, the minimum stress was -31 MPa and the maximum stress was 31 MPa. As shown in Figure 4.28, the crack opening stress after the underload was 5.86 MPa from which it increased to a steady state level of 13.8 MPa.

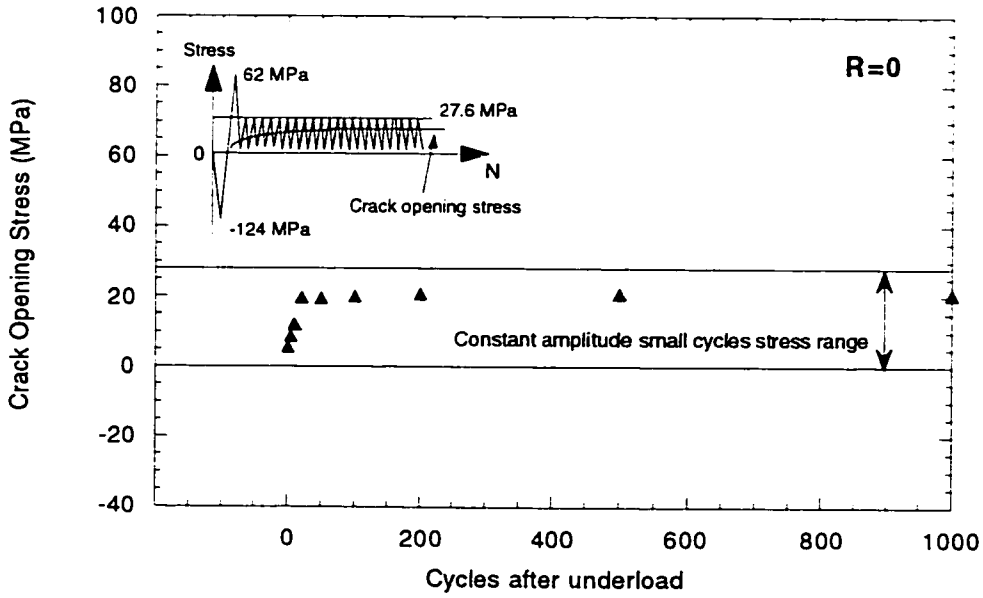

Figure 4.27 Crack opening stress build-up measurements for R=0

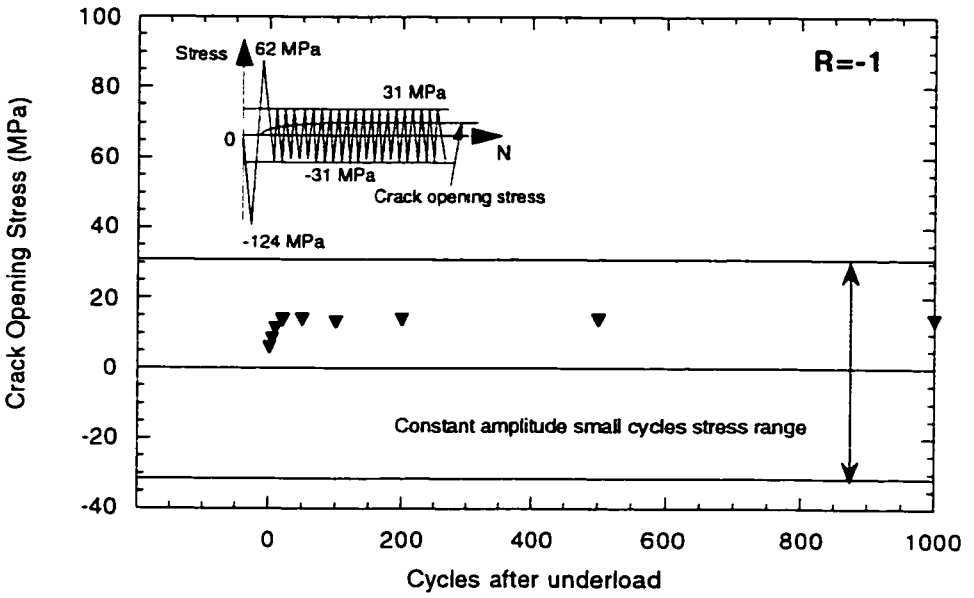

Figure 4.28 Crack opening stress build-up measurements for R=-1

4.5.2 Crack Opening Stress Measurements After a 62 MPa to -138 MPa Underload

Crack opening stress build-up measurements were made for another underload stress level. In this test, the underload applied was 138 MPa in compression and 62 MPa in tension followed by 50,000 constant-amplitude small cycles at an R-ratio of 0.90. The constant-amplitude small cycles had a maximum nominal stress of 62 MPa and a minimum nominal stress of 55.9 MPa. The crack opening stress level drops immediately after the underload to a stress level of +15.25 MPa and then increases until it reaches a steady state stress level of 38.64 MPa. The steady state stress level was reached after about 1000 constant-amplitude cycles following the underload.

Crack opening stress measurements show that the crack opening stress build-up trend is the same for different R ratios at an underload stress level of -124 MPa in compression and 62 MPa in tension. The crack opening stress is lowered by the underload and then builds-up after a slight delay, increasing in an exponential manner until it reaches a steady state level. When the underload compressive stress level is 138 MPa, but the maximum stress level is maintained at 62 MPa, the same

build-up trend is observed except that a larger number of cycles are needed for the crack opening stress to reach a steady state level.

4.5.3 Crack Opening Stress Build-up Formula

All crack opening stress measurements are plotted in terms of $(S_{op} - S_{opul})$ divided by $(S_{opss} - S_{opul})$ versus the number of cycles following the underload, N, normalized by the number of cycles at which this ratio reaches 80% of the steady state level, $N_{0.8}$, on a semi-log scale in Figure 4.29. The following equation gives a reasonably good fit to the data:

$$\frac{(S_{op} - S_{opul})}{(S_{opss} - S_{opul})} = 1 - \psi Exp(-b(N/N_{0.8})^a) \qquad 4.2$$

where

ψ, **b** and **a** are material constants.

S_{op} is the instantaneous crack opening stress

S_{opul} is the post-underload crack opening stress

S_{opss} is the steady state crack opening stress of the cycles following the underload

N is the number of cycles following the underload.

$N_{0.8}$ is the number of cycles following the underload at which the normalized closure stress increase, $(S_{op} - S_{opul})/(S_{opss} - S_{opul})$, reaches 80% of its steady state level and,

ψ, **b** and **a** are constants which are derived from curve fitting and have values of 1.9, 3.0 and 0.75, respectively.

Values of $N_{0.8}$ are plotted versus $(S_{opss} - S_{opul})$ on a log-log scale in Figure 4.30. A simple linear curve fit to the data is shown giving $N_{0.8}$ as

$$N_{0.8} = 1.158(S_{opss} - S_{opul})^{1.331} \qquad 4.3$$

The crack opening stress build-up formula can be used to calculate the crack opening stress of any cycle following an underload in variable-amplitude or service load histories.

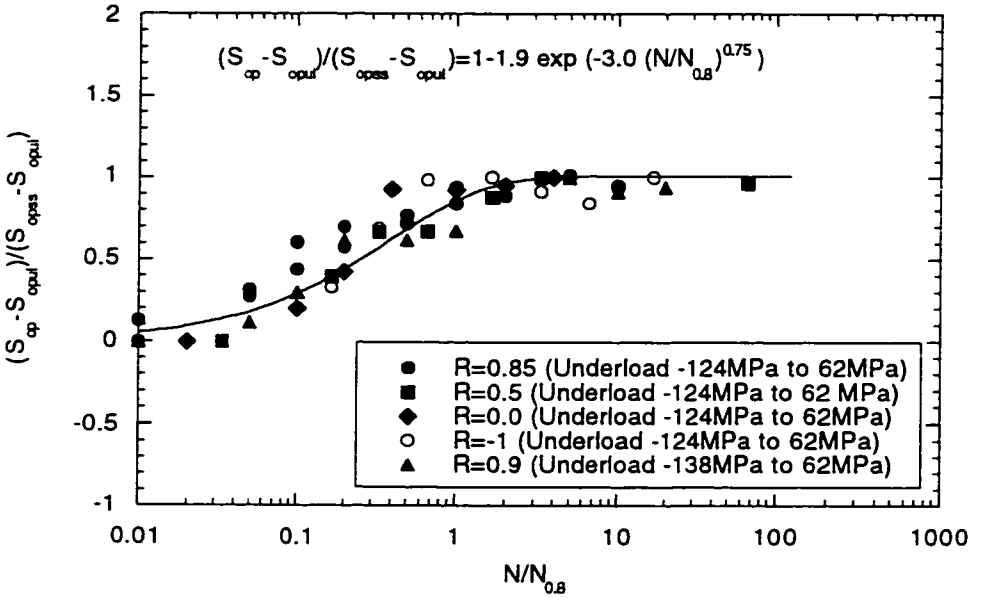

Figure 4.29 Normalized crack opening stress build-up data for Al 319

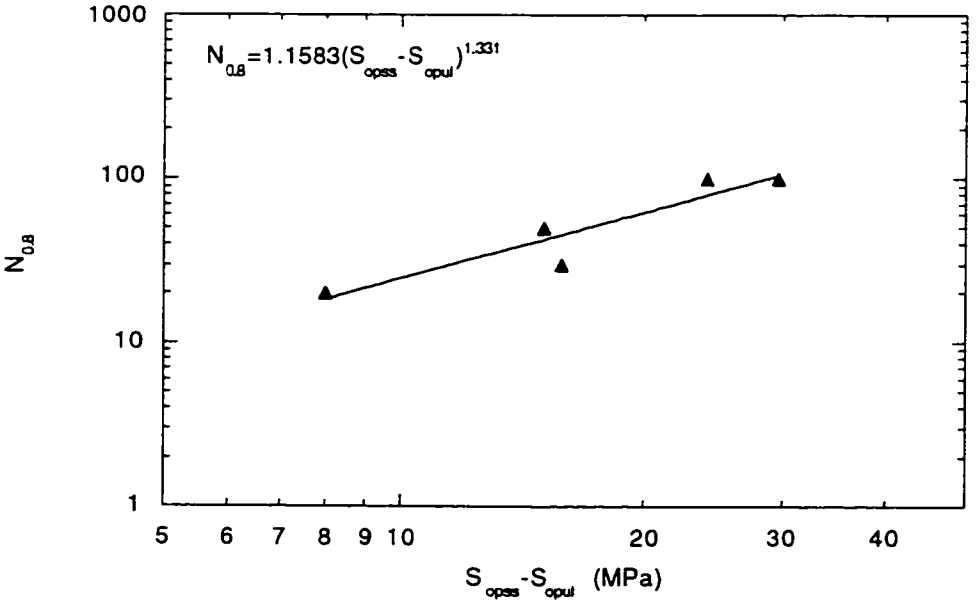

Figure 4.30 Relation between $N_{0.8}$ and $(S_{opss} - S_{opul})$ for cast Al 319

4.5.4 Steady State Crack Opening Stress Formula

An empirical model, proposed by DuQuesnay [68], for the steady state crack opening stress under constant-amplitude loading was used. The model, which has two experimentally determined constants θ and φ, takes the following form:

$$S_{op} = \theta\sigma_{max}\left[1-\left(\frac{\sigma_{max}}{\sigma_y}\right)^2\right]+\varphi\sigma_{min} \qquad 4.4$$

where σ_{max} and σ_{min} are the local maximum and minimum notch root stresses in notched specimens, or the nominal maximum and minimum stresses in smooth specimens, and σ_y is the cyclic yield stress. Crack opening stress measurements for the 319 cast aluminum alloy were made using a 900X microscope. Values of θ=0.55 and φ =0.2 were obtained. The values for θ and φ were used in the model to determine the steady state crack opening stresses for the cast aluminum alloy.

4.6 Crack Growth in Terms of Effective Stress Intensity

4.6.1 Crack Growth under Constant-amplitude Loading

All constant-amplitude crack growth curves in terms of the effective stress intensity are shown in Figures 4.31-4.33. Two R-ratios (R=0.7 and R=0.85) were used for cast Al 206 to obtain the crack growth rate in terms of effective stress intensity. Both R-ratios gave the same crack growth rate, which indicated that R=0.7 was enough to ensure a fully opened crack, as shown in Figure 4.31. The effective threshold stress intensity factor range obtained was 1.92 MPa$\sqrt{m}$. An R-ratio of 0.8 was used for cast Al 319 and cast Al 390. The crack opening stresses were checked for both materials and it was found that R=0.8 for Al 390 was enough to ensure a fully opened crack but was not high enough to ensure a fully opened crack for Al 319. The effective threshold stress intensity factor range obtained for Al 390 was 1.07 MPa $\sqrt{m}$. The effective threshold stress intensity factor range for Al 319 was obtained using the underload testing program which is explained in the following section.

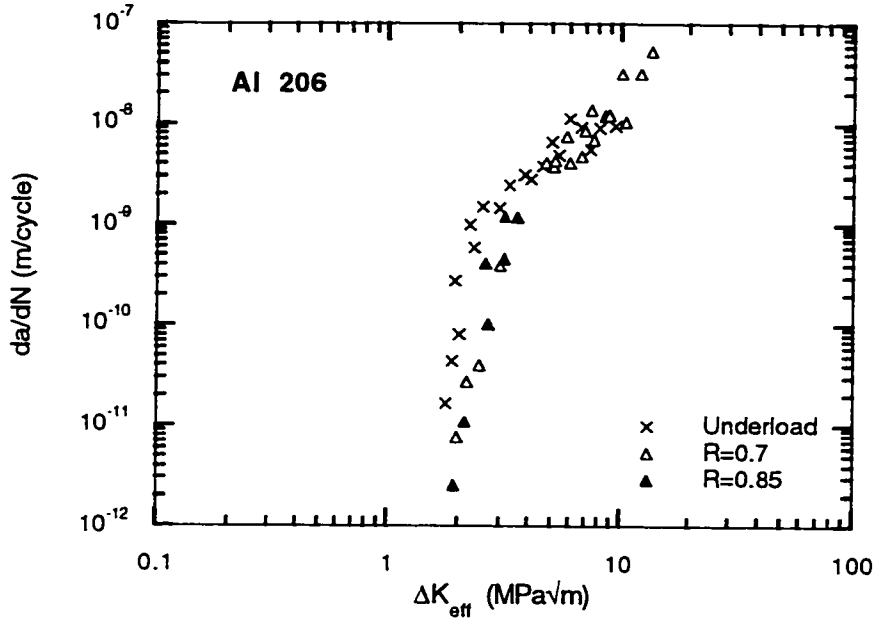

Figure 4.31 Constant- and variable-amplitude crack growth rate in terms of the effective stress intensity for Al 206

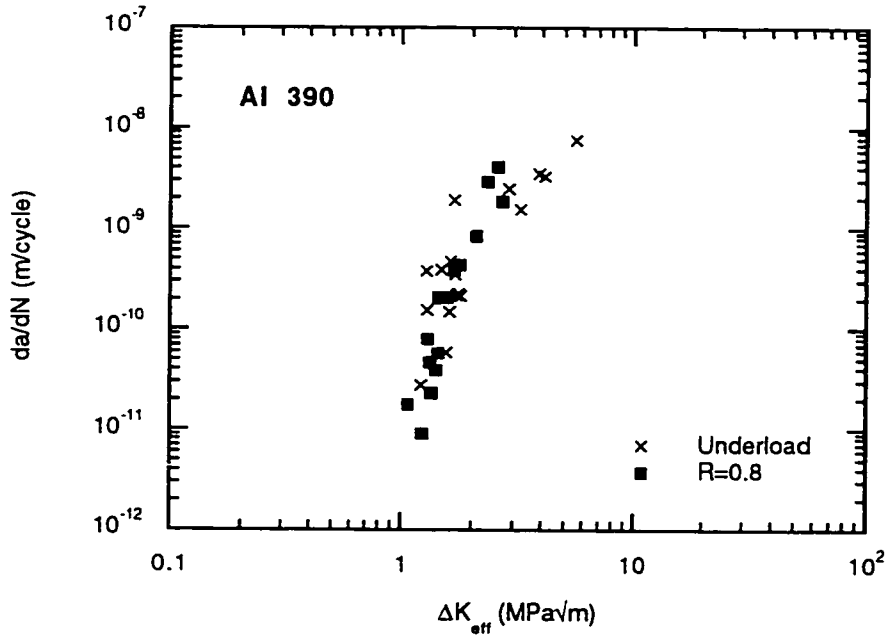

Figure 4.32 Constant- and variable-amplitude crack growth rate in terms of the effective stress intensity for Al 390

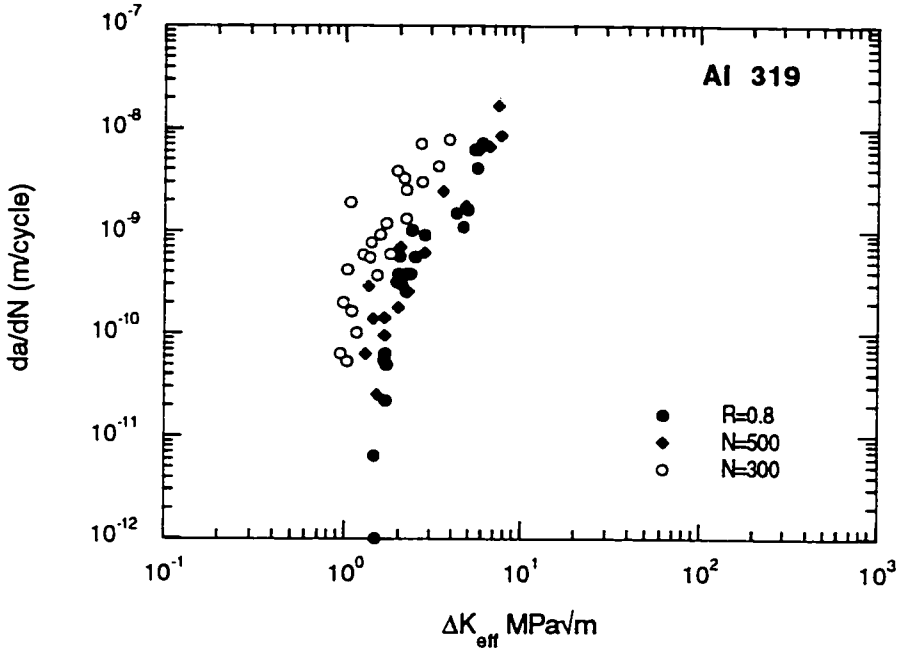

Figure 4.33 Constant- and variable-amplitude crack growth rate in terms of the effective stress intensity for Al 319

4.6.2 Crack Growth under Variable-amplitude Loading

The variable-amplitude loading testing procedure explained previously in section 3.4.1.2. was applied to obtain the effective stress intensity versus crack growth rate curves. A schematic for the block loading history applied is shown in Figure 3.9 (in chapter 3). The underload stress levels for Al 206 were -103.5 and +69.0 MPa and the number of small cycles, N, between underloads was 500. The maximum and minimum stresses of the underload and the number of small cycles were chosen so that underload crack growth represents only a small fraction of the total crack growth during a block loading history and does not exceed $5x10^{-10}$ m/cycle. The curve obtained for Al 206, as shown in Figure 4.31, was in good agreement with the R=0.7 and R=0.85 curves, and the effective threshold stress intensity factor range obtained using the variable-amplitude loading program was 1.73 MPa$\sqrt{m}$.

The underload stress levels for Al 390 were -103.5 MPa and +34.5 MPa and the number of cycles between underloads was 500. The curve obtained in Figure 4.32 was in good agreement with the R=0.8 curve. The crack opening stresses for small

cycles between underloads were checked and the measurements revealed that the small cycles were fully open. The effective stress intensity factor range obtained was 1.17 MPa$\sqrt{m}$.

Two tests were done for Al 319. The underload stress levels for both tests were -82.8 MPa and +41.4 MPa. The number of small cycles, N, between underloads was 500 for the first test and 300 for the second test. Crack opening stresses were checked for the first case and it revealed that some of the small cycles applied between undreloads, particularly those which are before the underload cycle, are not fully opened. The second case was then applied with N=300 to ensure fully opened cracks. The curves obtained are shown in Figure 4.33. The effective stress intensity factor range obtained was 0.98 MPa$\sqrt{m}$.

4.7 Fatigue Life Prediction

Fracture mechanics approaches used in fatigue life predictions of cast materials assume that a crack exists from the first load cycle. This crack can be as small as a slip band crack. Linear elastic fracture mechanics does not apply to these cracks, and other parameters such as the J-integral or a strain intensity factor must be used.

In this section the fatigue crack growth model presented in chapter (2) is used to analyse the effect of constant- and variable-amplitude loads on the fatigue crack growth of smooth specimens and of specimens with a flaw at a notch root. The significance of variations in the accuracy of positioning the flaw at the notch root are also examined.

4.7.1 Fatigue Life Prediction for Smooth Specimens

The inhomogeneities, flaws, in smooth specimens are modeled as semi-circular edge notches having radii similar to the flaw radius. The fatigue crack growth model, presented earlier in chapter 2 (Figure 2.1), requires the calibration of the ease of cross slip factor, α, in each material. The procedure followed for calibration was to choose a value for the coefficient (α/D), in equation 2.44, that forced the variable-amplitude loading fatigue life prediction line to agree with the defect-free material effective strain-life curve. This curve was constructed by multiplying the smooth specimens variable-amplitude results of the 206, 319 and 390 cast

aluminum alloys by the flaw stress concentration factor. Then the calibrated model was used to predict fatigue life of smooth specimens for constant-amplitude loading and of notched specimens for constant- and variable-amplitude loading. Figures 4.34-4.36 show the predicted fatigue lives compared with the experimental results for Al 206, Al 319, and Al 390 under constant- and variable-amplitude loading. Cycles to failure versus strain range curves are plotted for the constant-amplitude loading, while an equivalent number of small cycles to failure versus the strain range of the small cycles are plotted for the variable-amplitude loading. Figure 4.37 shows the prediction for the smooth hipped 319 aluminum alloy in the high-gas and low-gas conditions under constant- and variable-amplitude loading. Again the model prediction agreed well with the experimental results.

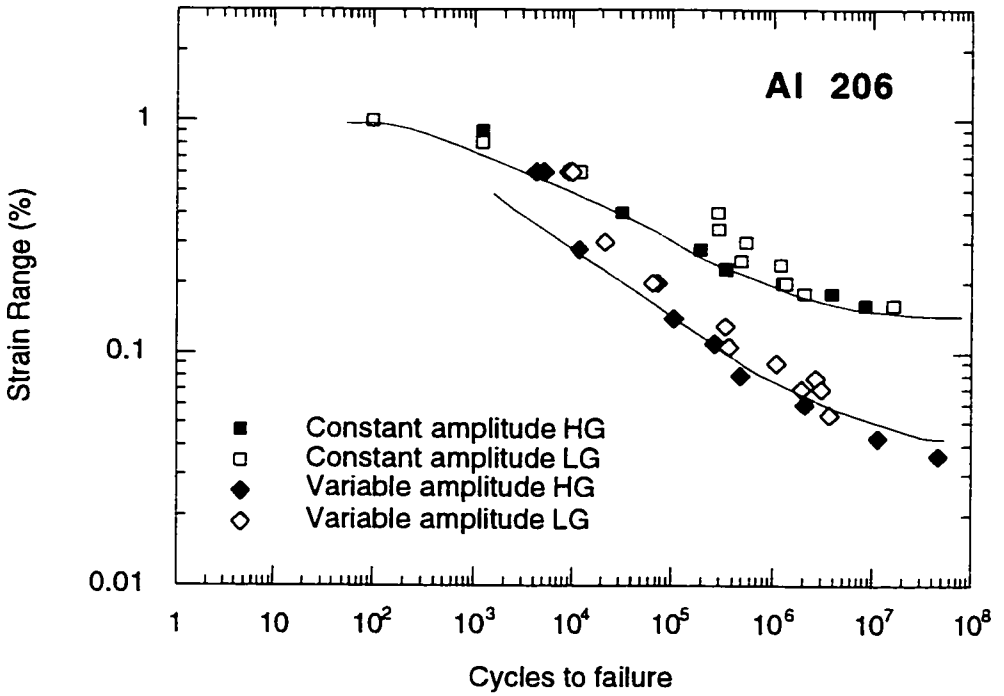

Figure 4.34 Constant- and variable-amplitude fatigue data and fatigue life prediction for Al 206

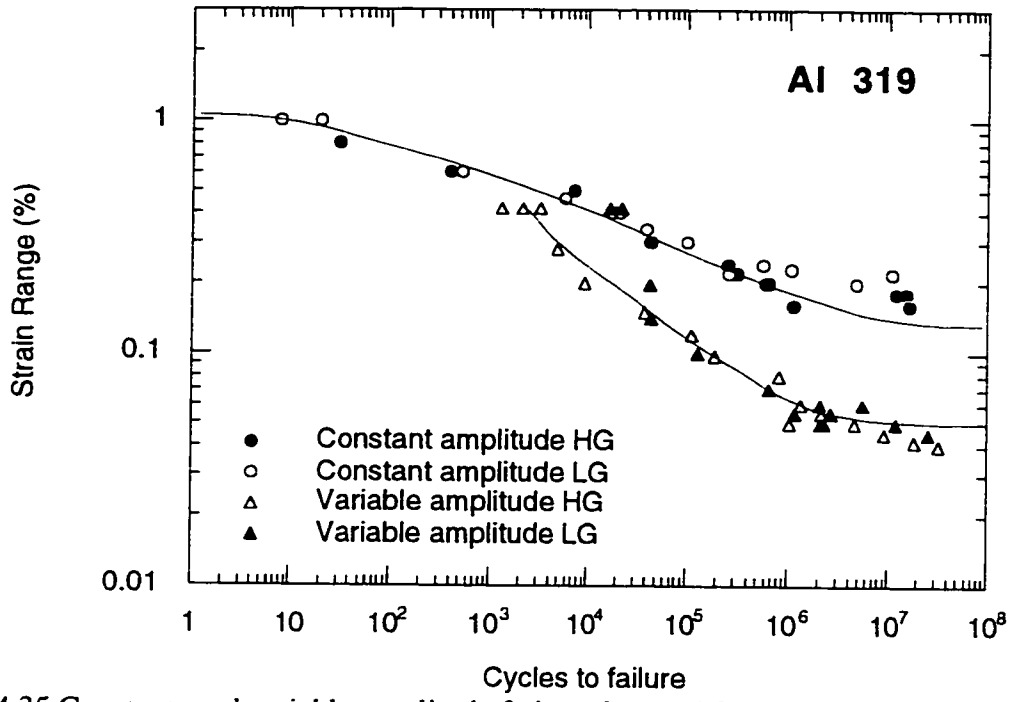

Figure 4.35 Constant- and variable-amplitude fatigue data and fatigue life prediction for Al 319

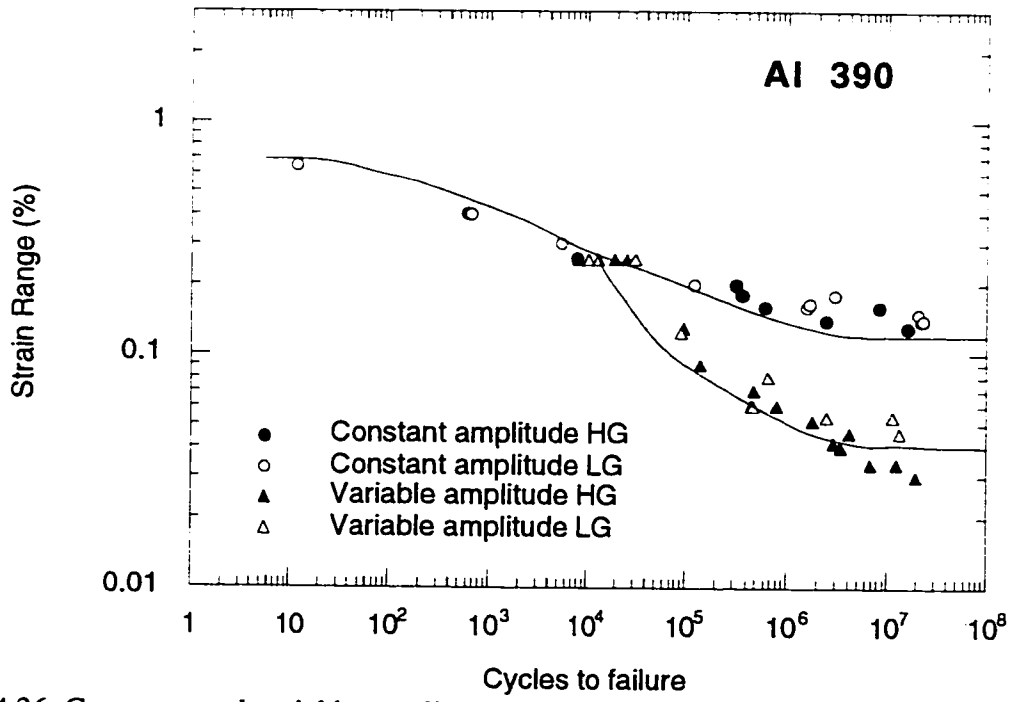

Figure 4.36 Constant- and variable-amplitude fatigue data and fatigue life prediction for Al 390

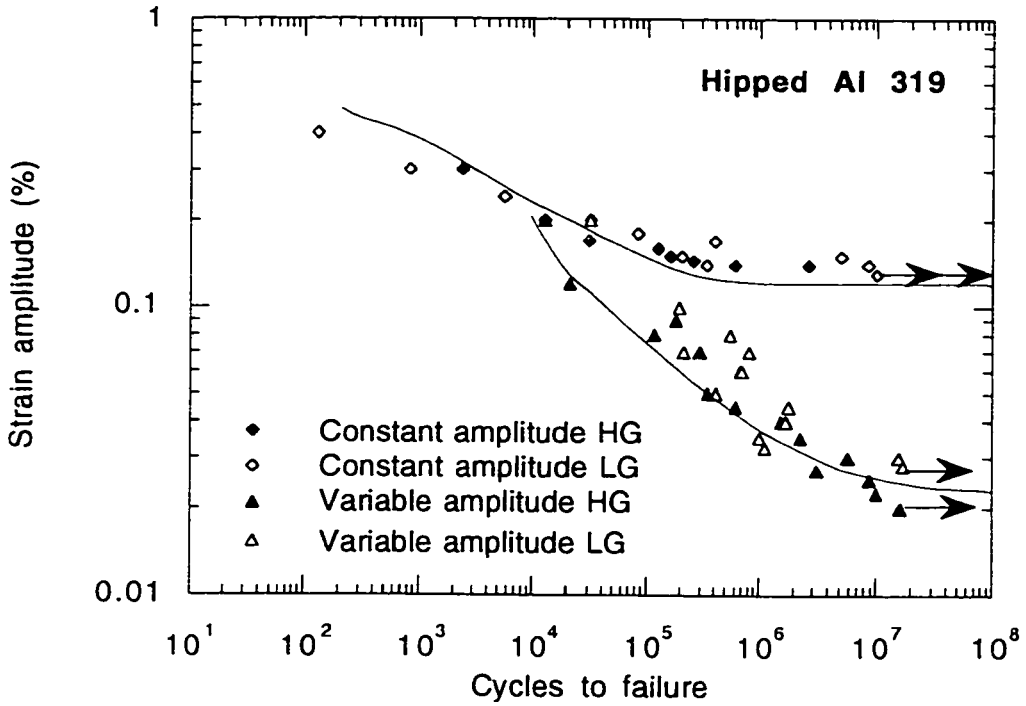

Figure 4.37 Constant- and variable-amplitude fatigue data and fatigue life prediction for Hipped Al 319

4.7.2 Fatigue Life Prediction for Specimens with a Flaw at a Notch Root

Flaws at notch roots are modeled by a spherical cavity having the same diameter as the natural flaw. The fatigue crack growth model for flaws at notch root, presented earlier in chapter (2), was used to predict the fatigue life for the as-cast Al 319 with a natural flaw at the notch roots and for the hipped Al 319 with a drilled hole at the notch roots of the 1.0 mm, 3.0 mm, and 6.0 mm diameter edge notches under constant- and variable-amplitude loading. The experimental fatigue life results for the as-cast and hipped Al 319 are compared with fatigue life predictions in Figures 4.38, 4.39 and 4.40 for constant-amplitude loading. The model predictions agree well with the experimental results.

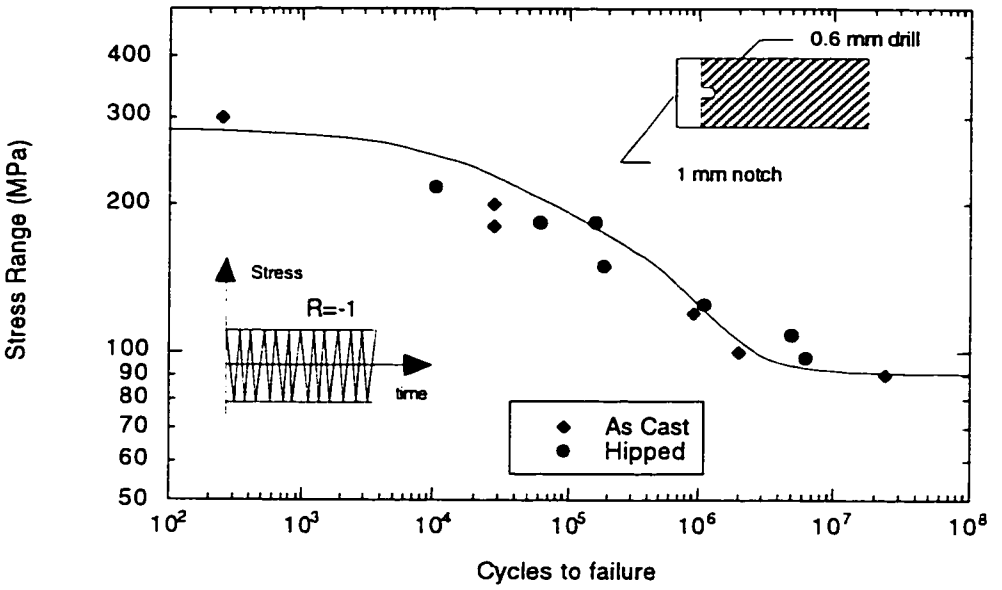

Figure 4.38 Constant-amplitude fatigue data and fatigue life prediction for 1.0 mm diameter notch with artificial and natural flaw at notch root

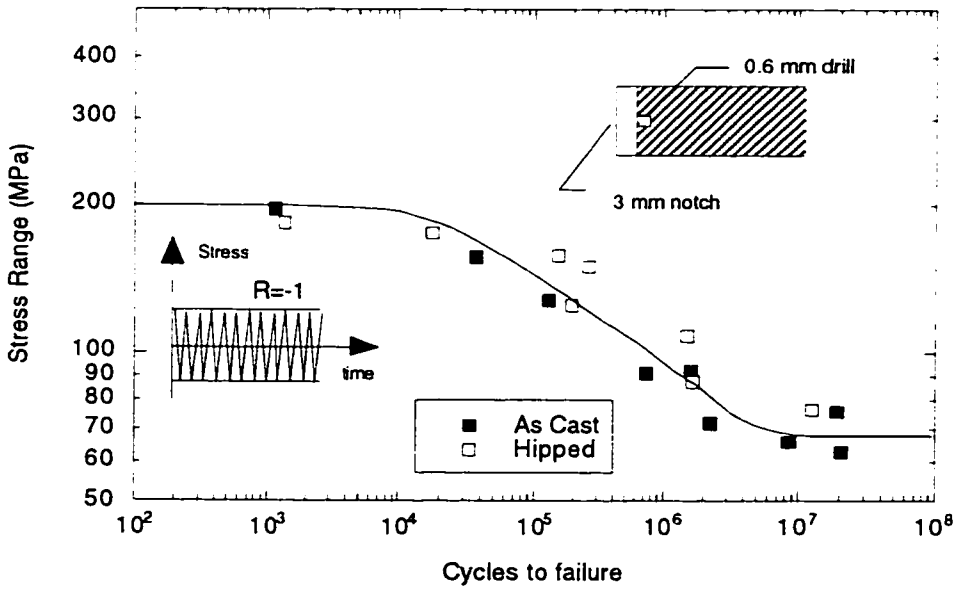

Figure 4.39 Constant-amplitude fatigue data and fatigue life prediction for 3.0 mm diameter notch with artificial and natural flaw at notch root

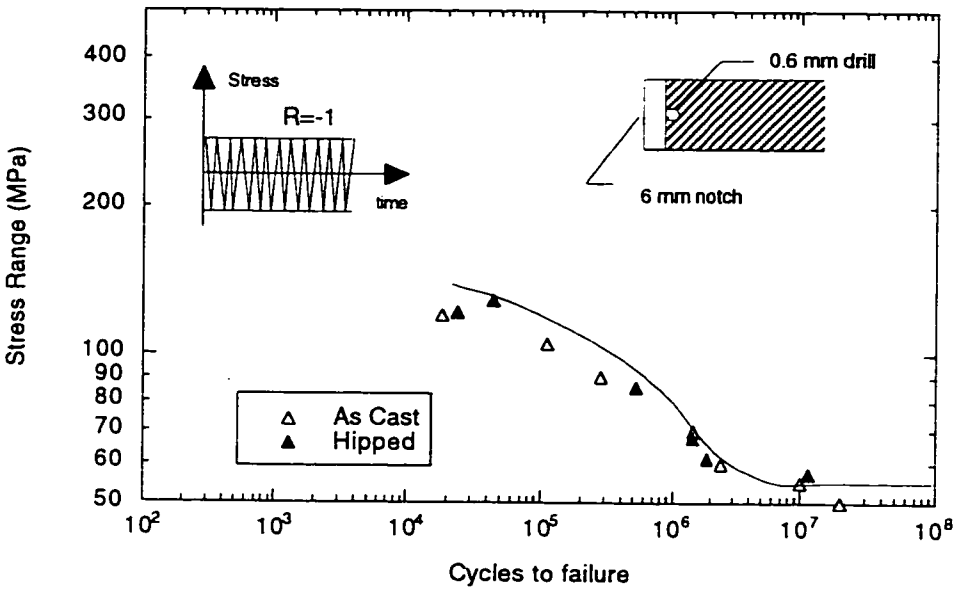

Figure 4.40 Constant-amplitude fatigue data and fatigue life prediction for 6.0 mm diameter notch with artificial and natural flaw at notch root

As mentioned before, the plates of the as-cast high-gas 319 cast aluminum alloy material were examined by ultra-sonic waves to detect the location of the defects and their depth below the material surface. Notched specimens were then cut from the cast plate so that the natural flaw was located at the notch root. There was some variation in the accuracy of positioning of the flaw at the notch root. This variation caused a deviation between fatigue results for the hipped Al 319 with a drilled hole at the notch root and the results for the as-cast Al 319 with a natural flaw at the notch root for variable-amplitude loading. The experimental fatigue life results for variable-amplitude loading for the hipped Al 319 are compared with fatigue life predictions in Figures 4.41, 4.42 and 4.43. The model was also used to predict a fatigue life band which covers the range of different flaw sizes and flaw locations in the notch root, found in the microscopic observations of the as-cast Al 319 fractured surfaces of the fatigued specimens. One limit was taken as a 0.6 mm flaw positioned accurately at the notch root, which was the most severe case observed, and the other limit was taken as a 0.4 mm flaw positioned 0.4 mm away from the notch root, which was the least severe case. Figures 4.44, 4.45, and 4.46 show the fatigue life prediction bands together with the cast Al 319 material fatigue test. Most of the data fall within the predicted fatigue life band.

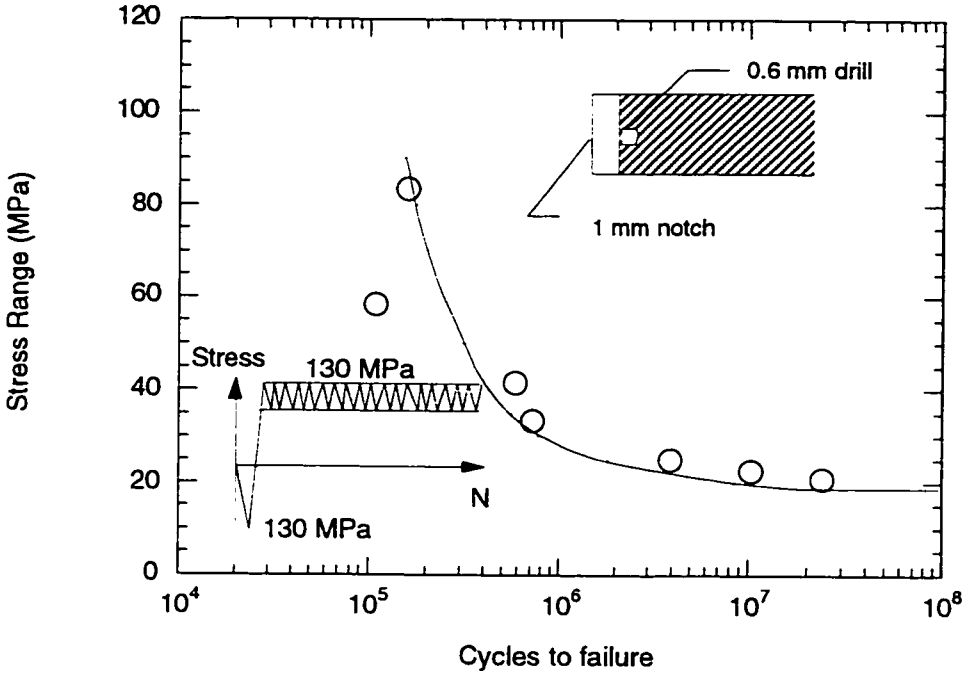

Figure 4.41 Variable-amplitude fatigue data and fatigue life prediction for 1.0 mm diameter notch with 0.6 mm drill at notch root

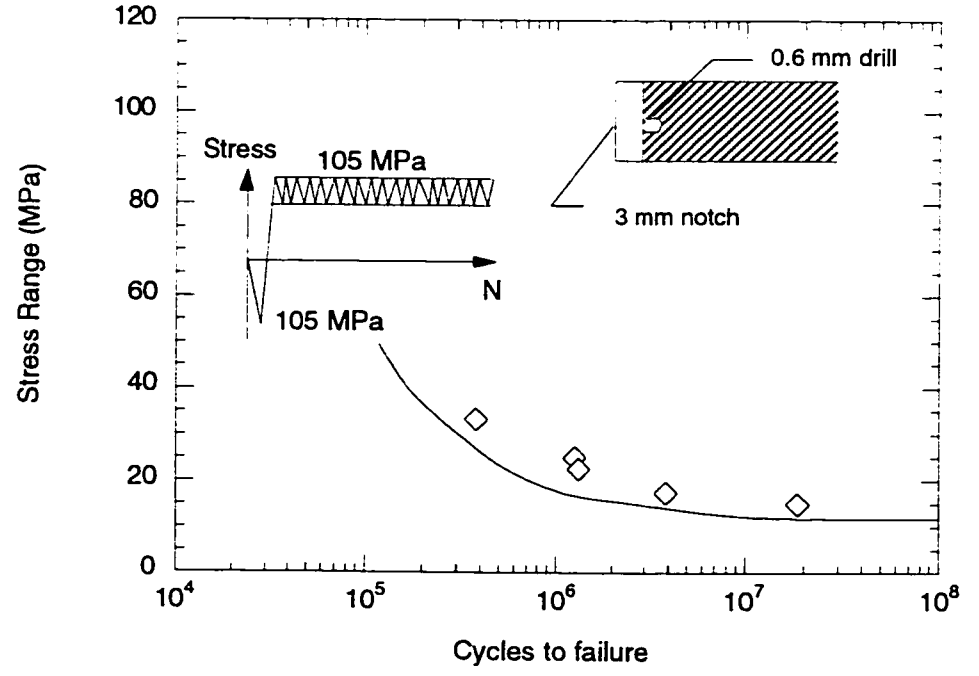

Figure 4.42 Variable-amplitude fatigue data and fatigue life prediction for 3.0 mm diameter notch with 0.6 mm drill at notch root

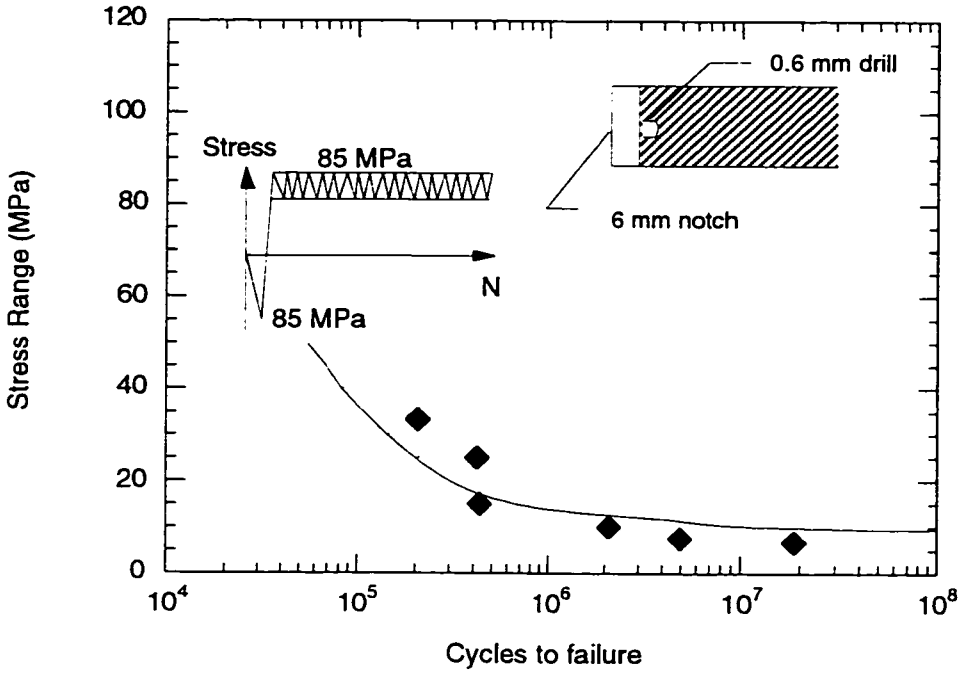

Figure 4.43 Variable-amplitude fatigue data and fatigue life prediction for 6.0 mm diameter notch with 0.6 mm drill at notch root

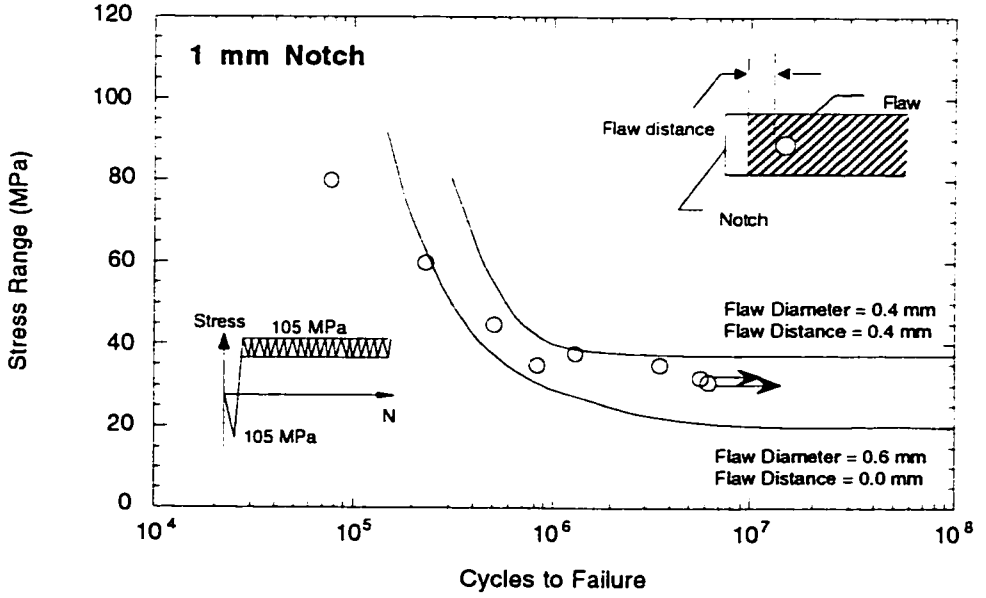

Figure 4.44 Variable-amplitude fatigue life data and fatigue life prediction for as-cast 319 aluminum with a flaw in a 1.0 mm diameter notch

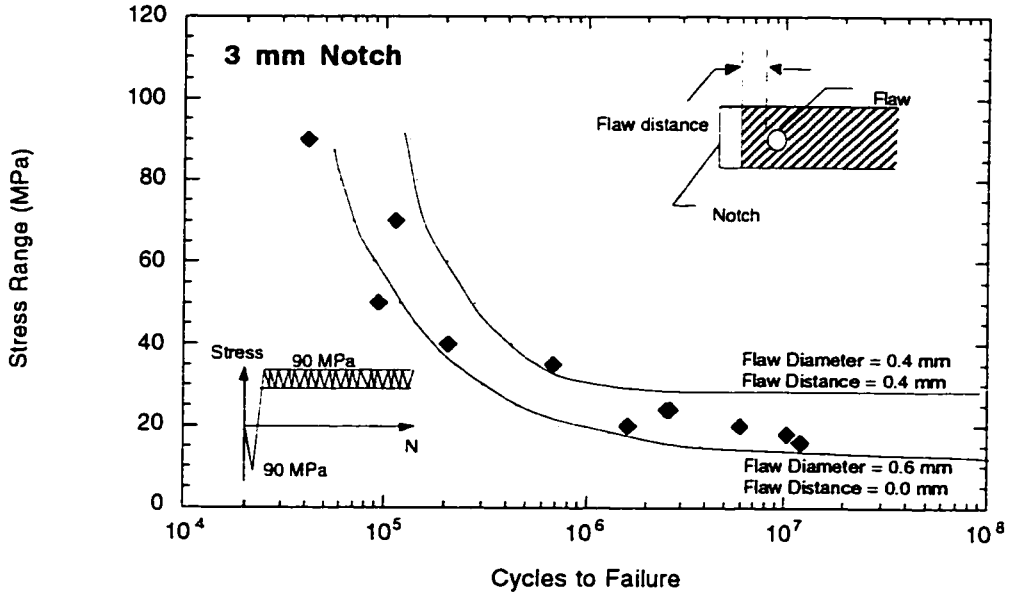

Figure 4.45 Variable-amplitude fatigue life data and fatigue life prediction for as-cast 319 aluminum with a flaw in a 3.0 mm diameter notch

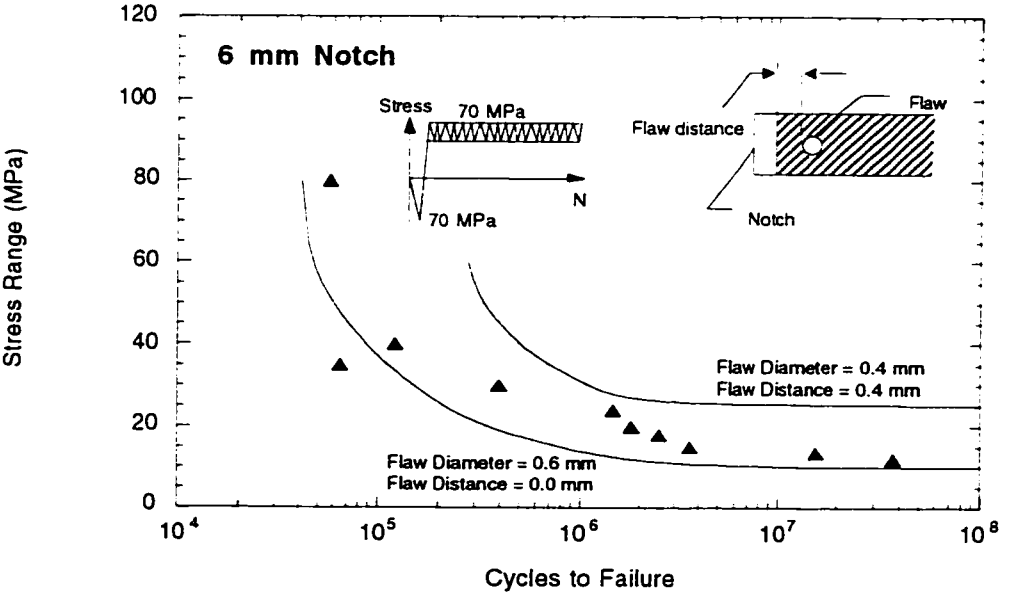

Figure 4.46 Variable-amplitude fatigue life data and fatigue life prediction for as-cast 319 aluminum with a flaw in a 6.0 mm diameter notch

4.8 Summary

This chapter described the experimental test results for cast aluminum 319, 390, and 206 materials in the as-cast and hipped conditions. The materials were tested under constant-amplitude and intermittent underload block loading histories. The specimens examined were smooth, notched, and notched with an artificial or natural flaw at notch root.

The smooth test results showed that a block loading history consisting of underloads followed by constant-amplitude smaller cycles reduced the crack opening stress so that the smaller constant-amplitude cycles were fully effective. The variable-amplitude loading history caused a fatigue strength reduction of 66-87% in the three alloys tested. The results also showed that the hipping process increased the fatigue strength by 62.5% for the high-gas 319 cast aluminum alloy and that the fatigue cracks in the three cast aluminum alloys initiated and propagated from casting pores.

The notched and notched with artificial or natural flaws at notch root results showed that natural flaws in the as-cast 319 aluminum alloy can be modeled by an equivalent drilled hole of the same size. It also showed that there is a notch size effect under constant- and variable-amplitude loading, and that the fatigue life of notched 319 cast aluminum specimens having a small notch radius is more affected by a given variation in flaw size and flaw position than specimens having a large notch radius.

This chapter also described the fatigue life prediction due to a crack growth analysis which was used to model the fatigue behavior of the cast aluminum material under constant- and variable-amplitude loading. The crack growth analysis based on an effective strain-based intensity factor, elastic and plastic notch strain calculations based on Neuber's formula, and a reference crack growth curve, obtained during closure-free crack growth, was able to model the observed fatigue behavior of the three cast aluminum alloys under constant- and variable-amplitude loading.

CHAPTER 5

CASTING DEFECTS AT A NOTCH ROOT AND THEIR ROLE IN THE FATIGUE BEHAVIOR OF CAST ALUMINUM UNDER SERVICE LOAD HISTORY

5.1 Introduction

In this chapter, fatigue test data obtained using an SAE service load history are examined. These data included fatigue tests of smooth specimens, notched specimens, and notched specimens with flaws or casting defects at the notch root. The results show that circular edge notches reduced the fatigue strength and a 0.6 mm diameter drilled hole at the notch root resulted in a further reduction. The region in which the casting defect is important and effective has been determined. The reductions in the constant-amplitude loading fatigue life caused by having a defect at a notch root, and the effect of the notch size on these reductions under the service load history were determined by fatigue tests. The results show that the fatigue strength of notched specimens decreased as the notch size increased.

Most conventional fatigue life predictions are made using constant-amplitude fully reversed strain-life data and mean stress correction factors. Recently predictions have been made using effective strain-life data and an assumed constant crack opening stress level equal to the crack opening stress following the largest range in the history. The former predictions tend to be unconservative and the latter tend to be conservative. In this chapter, fatigue life predictions for smooth specimens, notched specimen, and notched specimens with a flaw at notch root made using the strain-life, effective strain-life, and crack growth approaches are compared with fatigue test results. The fatigue life predictions results revealed that the strain-life approach for the smooth specimens, notched specimens, and notched specimens with a flaw at the notch root is unconservative although mean stresses have been

taken into account. The effective strain-life approach gives good predictions for smooth specimens and notched specimens, and gives conservative predictions for notched specimens with a flaw at the notch root. The crack growth approach gives good fatigue life predictions for all cases.

5.1.1 Loading History

The stress history examined in this study is the torsion channel of the Society of Automotive Engineers (SAE) GKN Grapple-Skidder history, which is shown in Figure 3.10 in chapter 3.

5.1.2 Materials Used

The Materials used in this part of the thesis are 319 cast aluminum alloys in the as-cast and hipped conditions. The high-gas as-cast 319 alloy had the number and size of the gas pores artificially increased, compared to material cast in the normal manner (low-gas). Only the material in the high-gas condition is used in this part of the thesis.

5.2 Smooth Specimen Fatigue Test Results

This section provides the smooth fatigue test data for the as-cast and hipped 319 cast aluminum alloy tested under the torsional channel of the SAE GKN Grapple-Skidder history.

5.2.1 As-Cast and Hipped Fatigue Results

Fatigue tests under the SAE GKN Grapple-Skidder stress history were conducted on the 319 cast aluminum alloy in the as-cast and hipped conditions. Figure 5.1 shows the maximum stress range in the applied history versus the number of blocks to failure on a semi-log scale. Fatigue test results are given in Table 5.1. The hipping process, which includes subjecting the cast material to a high pressure at a high temperature followed by slowly cooling it to eliminate flaws, improves the fatigue life of as-cast smooth specimens subjected to the service load history.

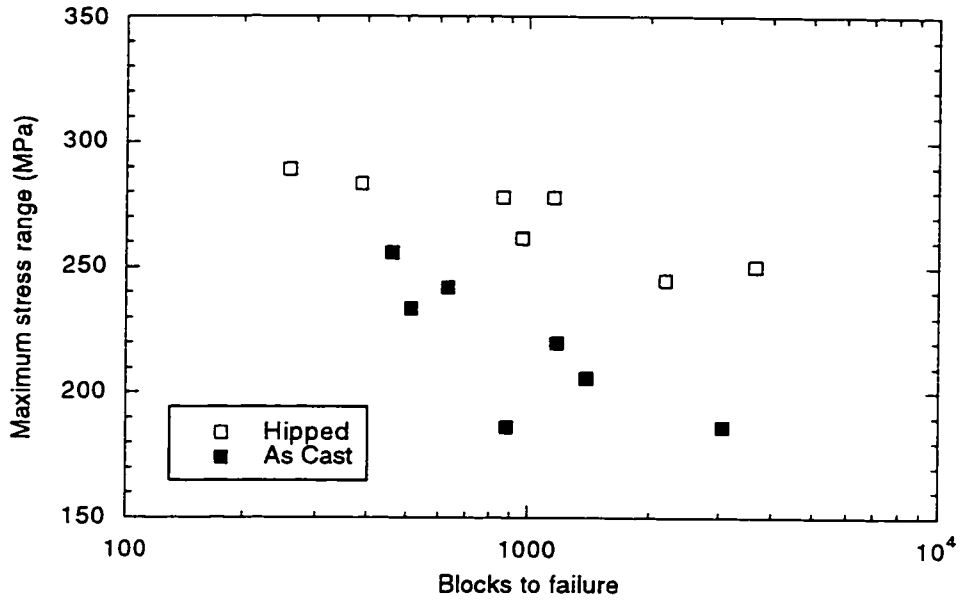

Figure 5.1 As-cast and hipped Al 319 fatigue test results for smooth specimens

Table 5.1 Smooth specimen fatigue life data for as-cast and Hipped Al 319

Al 319			
As-Cast		Hipped	
Maximum Stress Range (MPa)	Blocks to failure	Maximum Stress Range (MPa)	Blocks to failure
256	461	289	258
242	632	284	386
234	512	278	860
220	1,179	278	1,154
206	1,389	261	966
186	882	250	3,647
186	3,046	245	2,186

5.2.2 Comparison of Cast and Hipped Fatigue Test Results

After examining the fracture surfaces of the broken hipped smooth specimens, it was concluded that the average maximum size of flaws present in the cast Al 319

after hipping has decreased from 0.6 mm, for the unhipped condition, to 0.2 mm in diameter. The hipping process increased the constant-amplitude fatigue limit for the hipped aluminum alloy from a strain amplitude of 0.16% for the as-cast 319 aluminum alloy to a strain amplitude of 0.26%, as shown in chapter 4. The service load history fatigue test results of this part of the thesis, shown in Figure 5.1, also show an increase in fatigue resistance with hipping. For 1000 loading blocks (41,124,000 reversals) the maximum stress range has increased from about 230 MPa, for the as-cast samples, to about 270 MPa, for the hipped samples.

5.3 Notched Specimen Fatigue Test Results

This section provides notched fatigue test data for the as-cast and hipped 319 cast aluminum alloy tested using the torsional channel of the SAE GKN Grapple-Skidder history. Two groups of notched specimens were examined. The first group included 1.5 mm and 3.0 mm radius circular edge notched specimens, while the second group included notched specimens with circular edge notches of radii similar to those in the first group, but with a 0.6 mm diameter drill at the notch root. The 0.6 mm diameter drill was used to simulate the effect of a natural flaw existing at the notch root [64]. The first group was tested only in the hipped condition because the number and size of flaws are small compared to the as-cast condition, and there is a small probability of having a flaw at the notch root. The lack of a flaw was checked by examining the failed specimens fracture surface under the microscope after each test to confirm a failure due to the notch and not due to a flaw at the notch root. The second group was tested in the as-cast and in the hipped conditions.

5.3.1 Hipped Fatigue Results with no Flaw at the Notch Root

Fatigue tests under the SAE GKN Grapple-Skidder stress history were conducted on notched specimens in the hipped condition. Data of the maximum stress range in the applied service load history are plotted versus the number of blocks to failure on a semi-log scale for 3.0 mm and 1.5 mm circular edge notches in Figures 5.2 and 5.3, respectively. The fatigue test results are given in Table 5.2 for the 3.0 mm and 1.5 mm radius notches.

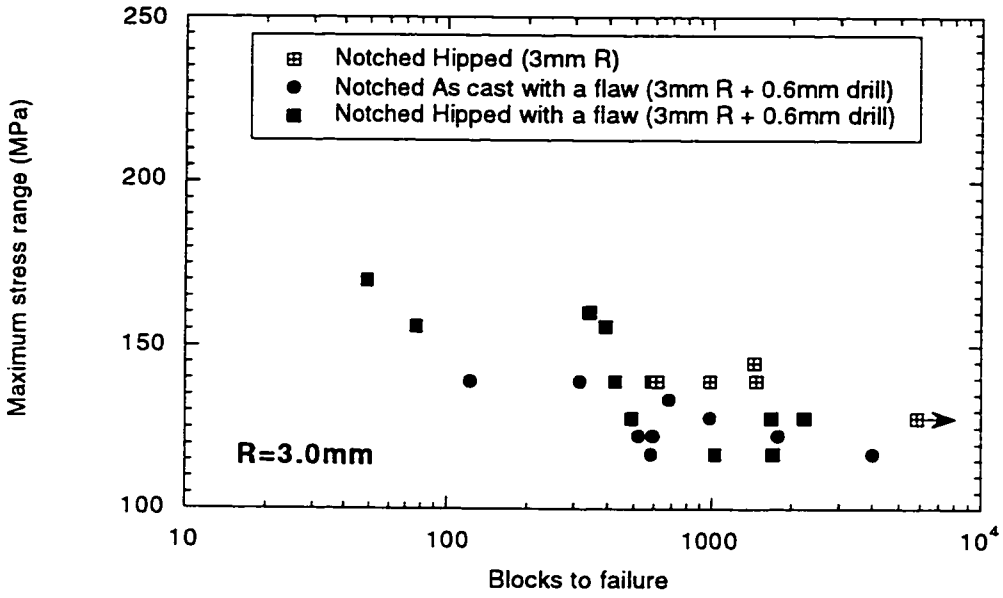

Figure 5.2 As-cast and Hipped Al 319 fatigue test results for 3.0 mm radius notched specimens

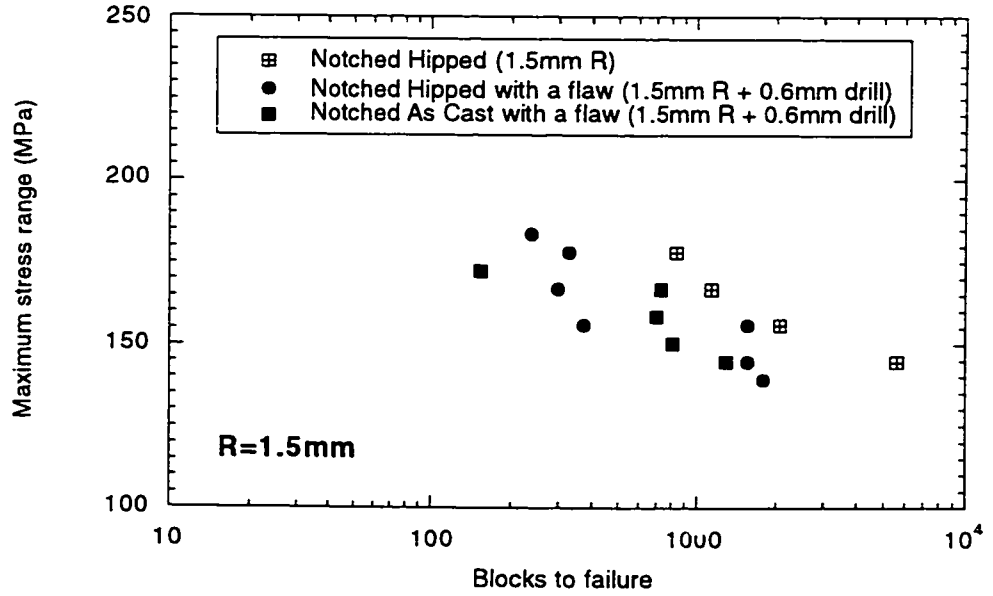

Figure 5.3 As-cast and Hipped Al 319 fatigue test results for 1.5 mm radius notched specimens

Table 5.2 Notched specimen fatigue life data for Hipped Al 319

Notched Hipped Al 319			
3.0 mm Radius Notch		1.5 mm Radius Notch	
Maximum stress range (MPa)	Blocks to failure	Maximum stress range (MPa)	Blocks to failure
145	1,443	178	836
139	1,475	167	1,145
139	610	156	2,077
139	980	145	5,623
128	5,800		

5.3.2 Hipped and As-Cast Fatigue Results with an Artificial Flaw at the Notch Root

Fatigue tests under the SAE GKN Grapple-Skidder history were conducted on notched specimens with a 0.6 mm drill at the notch root in the as-cast and hipped conditions. Figures 5.2 and 5.3 show these data points on a semi-log scale for 3.0 mm and 1.5 mm circular edge notches, respectively. The fatigue test results are given in Table 5.3 for the 3.0 mm and 1.5 mm radius notches. Figures 5.2 and 5.3 show that there is no significant difference in the fatigue life between the as-cast and hipped Al 319 notched specimens when an artificial flaw in the form of a drill having a diameter equal to that of the natural flaw size is machined at the notch root.

Table 5.3 Fatigue life data for as-cast and hipped Al 319 notched specimens with a flaw at notch root

3.0 mm Radius Notch with 0.6 mm Drill at Notch Root			
As-Cast		Hipped	
Maximum stress range (MPa)	Blocks to failure	Maximum stress range (MPa)	Blocks to failure
139	313	170	49
133	678	160	340
128	977	156	76
122	1,773	156	390
122	519	139	424
122	589	139	585
117	582	128	490
117	3,972	128	1,674
117	3,972	128	2,223
		117	1,025
		117	1,691

Table 5.3(continued) Fatigue life data for as-cast and hipped Al 319 notched specimens with a flaw at notch root

1.5 mm Radius Notch with 0.6 mm Drill at Notch Root			
As-Cast		Hipped	
Maximum stress range (MPa)	Blocks to failure	Maximum stress range (MPa)	Blocks to failure
172	154	183	237
167	730	178	329
158	697	167	298
150	806	156	1,564
145	1,300	156	372
		145	1,561
		139	1,792

5.3.3 Comparison of Smooth and Notched Fatigue Test Results

The Fatigue test results for the following: (a) smooth specimens in the as-cast and hipped conditions, (b) notched specimens in the hipped condition, and (c) notched specimens with a flaw at the notch root in the as-cast and hipped conditions are all plotted in Figures 5.4 and 5.5 for 3.0 mm and 1.5 mm radius notches, respectively. The fatigue test results show that the fatigue strength, at 1000 blocks of fatigue life, is reduced by a factor of 1.57 by the 3.0 mm notch and 1.22 by the 1.5 mm notch compared to the unnotched hipped metal. The introduction of the 0.6 mm diameter drilled flaw into the two notch roots increases the reduction to a factor of 1.83 for the 3.0 mm notch and 1.46 for the 1.5 mm notch

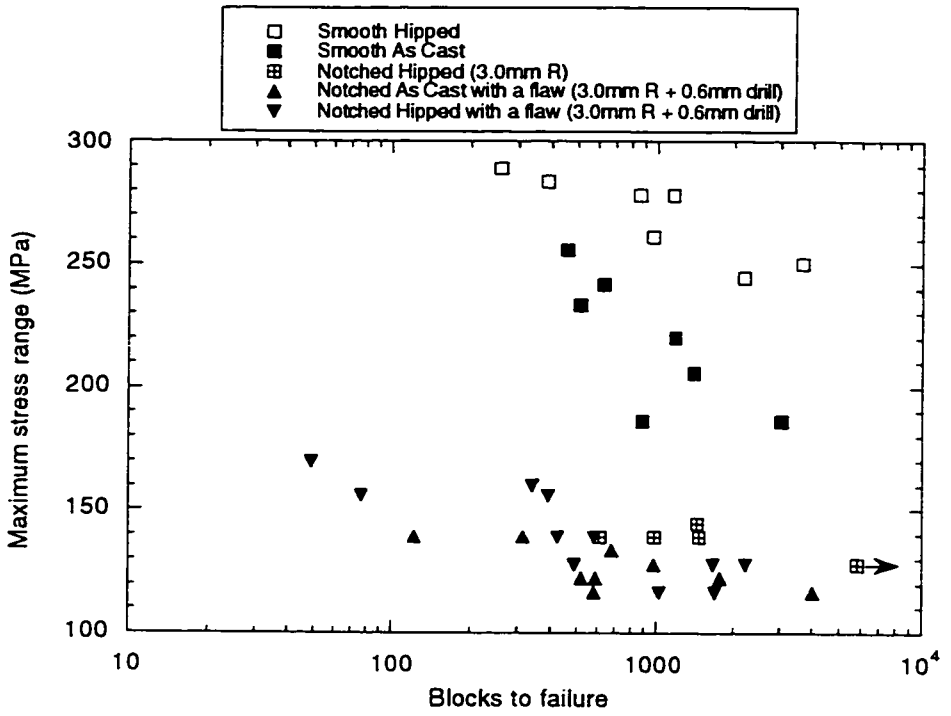

Figure 5.4 As-cast and Hipped Al 319 fatigue test results for smooth and 3.0 mm radius notched specimens

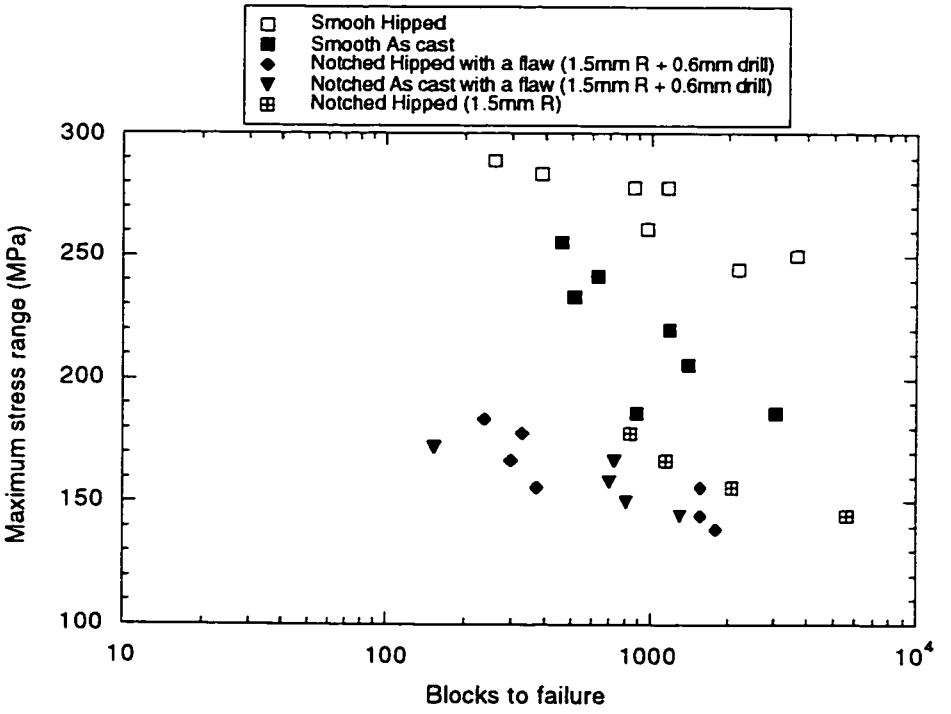

Figure 5.5 As-cast and Hipped Al 319 fatigue test results for smooth and 1.5 mm radius notched specimens

5.4 Fatigue Life Prediction Using the Crack Growth Model

The crack growth model presented in chapter 2 was used to predict the fatigue life of smooth specimens, notched specimens, and notched specimens with a flaw at their notch roots. The model follows the service load history reversal by reversal and calculates the local stresses and strains continuously updating the crack length and the concentration factor, K_p. A rainflow cycle counting technique was used to count closed stress-strain loops and to determine the maximum and minimum stresses in each loop.

This section presents the method used to calculate the variations in the crack opening stress levels during the service load history. It also presents the fatigue life predictions compared with the experimental data.

5.4.1 Crack Opening Stress Variation

The crack opening stress level during loading with the torsional channel of the SAE GKN Grapple-Skidder history was not constant, but varied, decreasing after large loads and increasing again during the intervening smaller load cycles. The crack opening stress at the end of the current cycle is calculated, based on the crack opening stress of the previous cycle, Figure 5.6, and the changes during the cycle. The following cases were considered:

1. If the crack opening stress after the previous cycle is higher than the new cycle, the current crack opening stress is dropped to the crack opening stress of the new cycle, calculated using equation 4.4, (Figure 5.6-(a)). This assumption is based on crack opening stress measurements [80] which showed that the crack opening stress drops immediately after the application of a large overload or underload. However, using equation 4.4, cycles with a low maximum stress would give low opening stress values even though the compressive peak was not low enough to decrease the crack opening stress. To circumvent this problem, the crack opening stress for cycles with a maximum stress less than the average of the tensile peaks in the history was calculated using a maximum stress equal to the average of the tensile peaks, Fig. 5.6-(b).

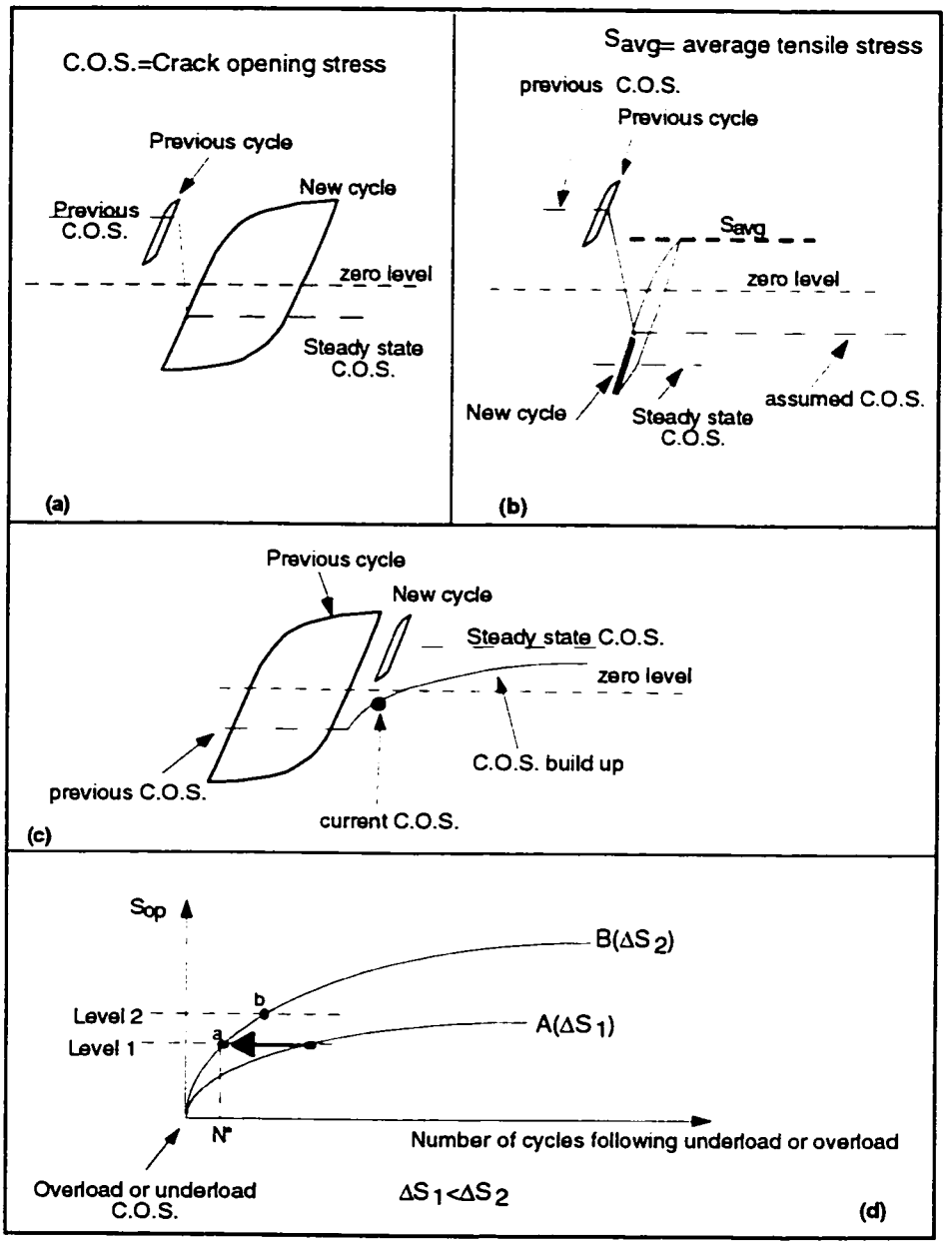

Figure 5.6 Cases of crack opening stress changes during the SAE GKN Grapple-Skidder history

2. If the crack opening stress after the previous cycle is lower than the crack opening stress of the new cycle, Figure 5.6-(c), the incremental increase in crack opening stress during the current cycle is calculated using the crack opening stress build-up formulas, equations 4.2 and 4.3. The increase in the crack opening stress per cycle was calculated as follows:

   a- Assume the previous crack opening stress is at level 1 on the crack opening stress build-up curve A, as shown in Figure 5.6-(d). The crack opening stress during the current cycle will follow the crack opening stress build -up curve for that cycle, curve B. In moving from curve A to curve B we maintain the same crack opening stress level. An equivalent number of cycles following the underload, N*, which gives a crack opening stress on curve B equal to the crack opening stress level of the previous cycle is first calculated (point a).

   b- The equivalent number of cycles, N*, is then updated by increasing it by one cycle, and the new crack opening stress, level 2 at point b, is calculated.

5.4.2 Fatigue Life Prediction for Smooth Specimens

Figure 5.7 shows the fatigue life prediction curves for the smooth as-cast and hipped Al 319 specimens plotted with the experimental data on a semi-log scale. Casting flaws in the as-cast and hipped materials were modeled as circular notches having the same diameter as the flaws. The notches were assumed to be edge notches, which represent the flaw location with the most detrimental effect on fatigue life. The notch diameter used in predicting the as-cast and hipped materials fatigue life was 0.6 mm and 0.2 mm, respectively. The experimental data points agree well with the predicted fatigue life.

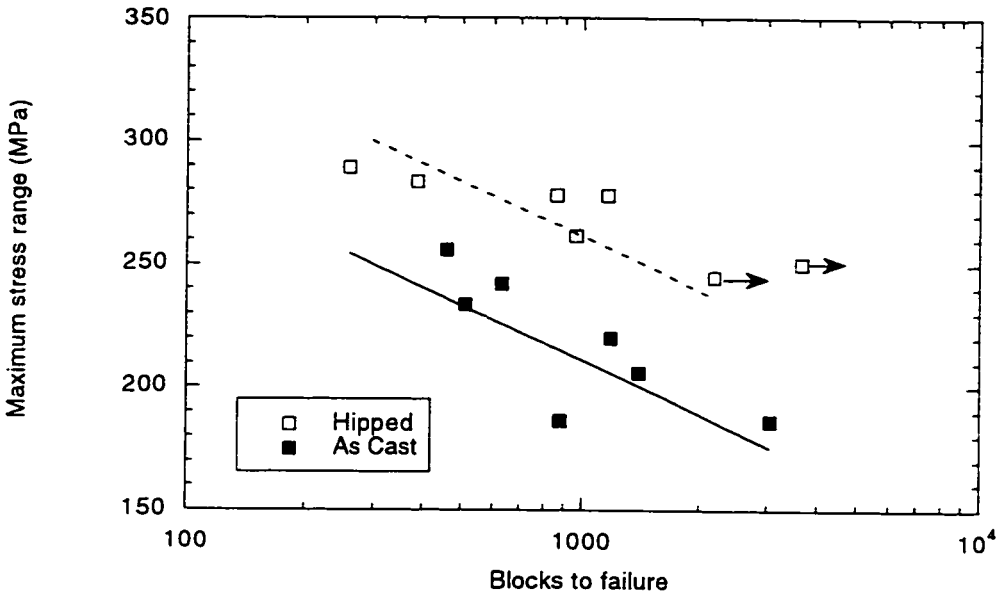

Figure 5.7 Fatigue life prediction curves for smooth as-cast and Hipped Al 319

5.4.3 Fatigue Life Prediction for Notched Specimens with and without a Flaw at the Notch Root

Figures 5.8 and 5.9 show the fatigue life prediction curves for notched specimens having 3.0 mm and 1.5 mm radius notches with and without a 0.6 mm diameter hole at the notch root, respectively, together with the corresponding experimental data. In both Figures, most of the experimental data lie close to the predicted fatigue life.

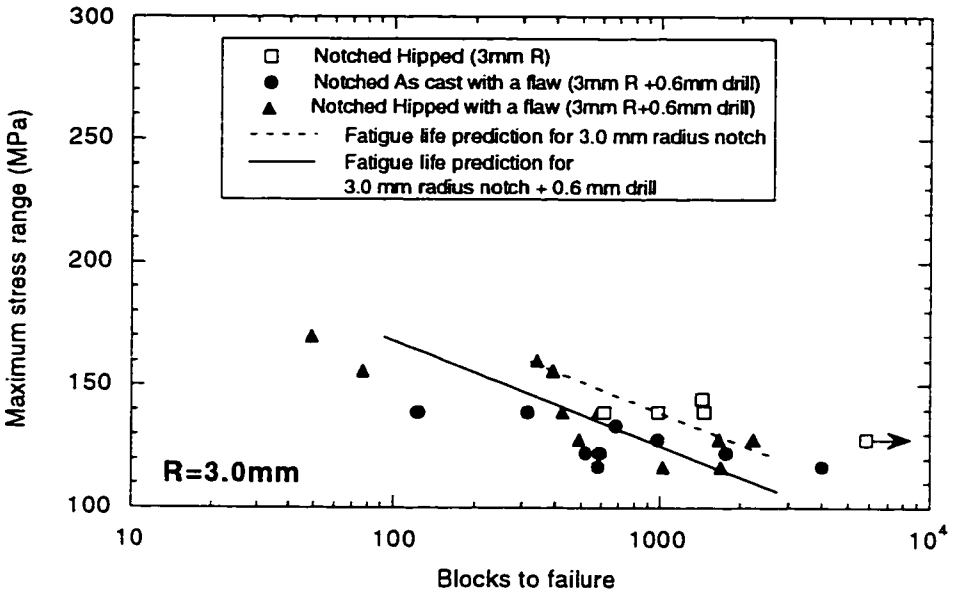

Figure 5.8 Fatigue life prediction curves for 3.0 mm radius notched specimens

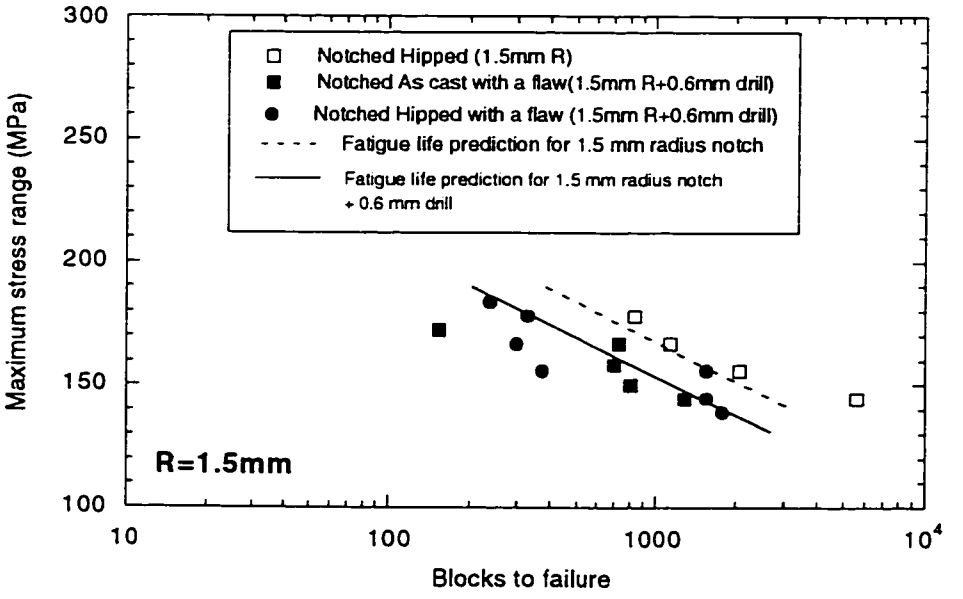

Figure 5.9 Fatigue life prediction curves for 1.5 mm radius notched specimens

5.5 The Effect of a Flaw at a Notch Root on Fatigue Life

The variations with length of the elastic stress concentration factor, K_p, for a crack emanating from a 3.0 mm radius notch and for a crack emanating from a 0.6 mm flaw at the root of the 3.0 mm radius notch are shown in Figure 5.10. The elastic stress concentration factor decreases from an initial maximum value of K_t to a value of 1.0 as the crack passes outside the stress field of the notch. It can be seen in Figure 5.10 that the defect causes a concentration factor that is greater than the elastic stress concentration factor due to the notch stress field only over the length l_2. The difference in fatigue life between a notched specimen and a notched specimen with a flaw at notch root is the difference between the number of cycles required to grow an initial $3\mu m$ crack to a length of l_1 under the notch stress field, and the number of cycles required to grow an initial $3\mu m$ crack, from the flaw depth, to a length of L_2, under the notch and flaw stress fields. l_1 and l_2 are 0.945 mm and 0.345 mm for the 3.0 mm radius edge notch with a 0.6 mm diameter flaw at the notch root and 0.886 and 0.286 for the 1.5 mm radius edge notch with a 0.6 mm diameter flaw at the notch root.

The difference in fatigue life between the notched specimens with and without a flaw at the notch root were calculated from the experimental results given in Figures 5.2 and 5.3 at different stress levels. The calculation showed that the fatigue lives of the 3.0 mm and 1.5 mm radius notched specimens with a 0.6 mm diameter flaw at the notch root were 40% and 38% shorter than the notched specimen fatigue lives, respectively. The percentage of the life of a notched specimens required to propagate a crack to a length of l_1, under a maximum stress range of 173 MPa for a 3 mm notch and 148 MPa for a 1.5 mm notch, were calculated using the crack growth model and were 62% and 40%, respectively. The percentage reduction in number of cycles to propagate a crack to a total depth of l_1 from the notch root due to a flaw at notch root, under a maximum stress range of 173 MPa for a 3 mm notch and 148 MPa for a 1.5 mm notch, was also calculated using the crack growth model, and was 70% and 78% for the 3.0 and 1.5 mm radius notches, respectively.

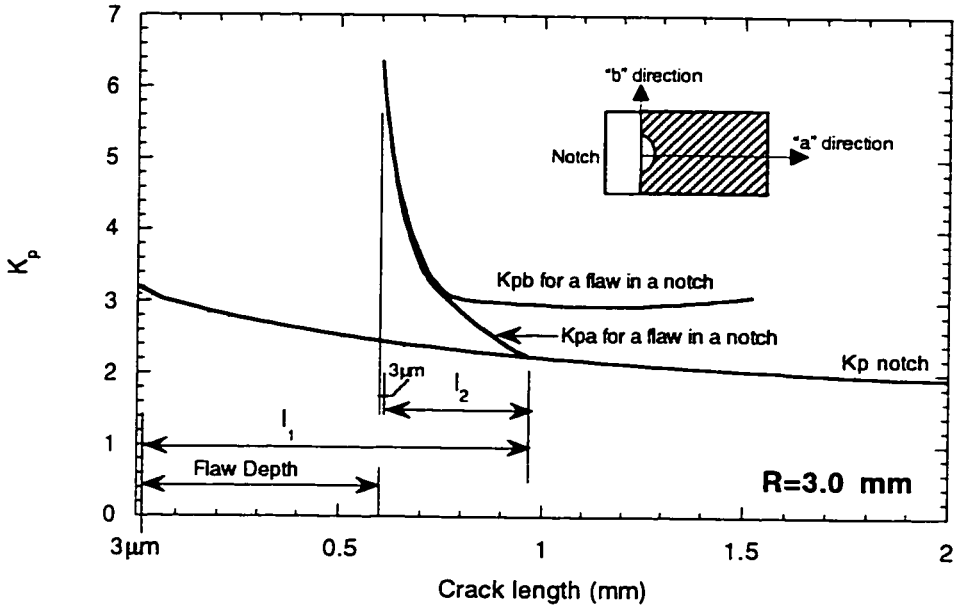

Figure 5.10 The elastic stress concentration factor, K_p, for a crack emanating from a notch and from a flaw at notch root for a 3.0 mm radius notch

5.6 Fatigue Life Prediction using the Local Strain-Life Approach

In this section, conventional fatigue life prediction methods based on the local strain-life approach are explained. The local strain-life approach has gained acceptance as a useful method of evaluating the fatigue life of a notched component. Both the American society for testing and material (ASTM) and the society of Automotive engineers (SAE) have recommended procedures and approaches for conducting strain-controlled tests and using these data to predict fatigue lives [87-91].

Fatigue life predictions may be made using the strain-life approach with the following information:

1- Material properties obtained from strain controlled fatigue tests which include
   a- Strain-life data.
   b- cyclic stress-strain data.
2- Stress-strain history at the critical location.
3- Techniques for identifying damaging events (e.g. cycle counting techniques).

4- Methods to incorporate mean stress and sequence effects.
5- A damage summation technique

In constant-amplitude fatigue, the effect of a notch on the fatigue strength of notched components is less than that suggested by the theoretical surface stress concentration factor, K_t, for notched components with small notch radii. Topper and El-Haddad [63] classified notches into two types, blunt notches and sharp notches depending on the behavior of the threshold stress with crack length. They specified a critical notch root radius, ρ_{cr}, which separates blunt notches from sharp notches derived in terms of the material constant ℓ_o, given by

$$\rho_{cr} = 4\ell_o \qquad 5.1$$

where ℓ_o is a material constant given by

$$\ell_o = \frac{1}{\pi}\left(\frac{\Delta K_{th}}{F\Delta\sigma_e}\right)^2 \qquad 5.2$$

where ΔK_{th} is the threshold stress intensity
$\Delta\sigma_e$ is the fatigue limit stress range
F is the shape factor for an edge crack.

For blunt notches, the fatigue notch factor is equal to K_t while for sharp notches it is given by

$$K_f = \frac{1}{F}\left[1 + \frac{K_t - 1}{2\sqrt{\ell_o/\rho}}\right] \qquad \rho < 4\ell_o \qquad 5.3$$

where ρ is the notch root radius.

The local strain-life approach has been used to predict fatigue life for a flaw at a notch root in two ways. The first way was by using constant-amplitude, fully reversed strain-life data and correcting for mean stress (the local strain-life method), while the second way was by using effective strain-life data and a crack opening stress estimate (the effective strain-life method). Both calculations are explained in the following sections.

5.6.1 The Local Strain-Life Method

Fatigue life predictions using the strain-life approach include using the following:
1- The constant-amplitude strain-life curve, but in the present case because the strain-life data for smooth specimens, even the hipped material, included a strength reduction due to casting defects, an estimated constant-amplitude strain-life curve, shown in Figure 5.11, was constructed from the 3.0 mm notched specimen fatigue data by multiplying the strains at a given life in the elastic region by the notch stress concentration factor, K_t, and by using Neuber's formula for the strains in the plastic region.

2- The theoretical stress concentration factor, K_t. A constant-amplitude fatigue ℓ_o value of 0.305 mm was calculated from equation 5.2 using a constant-amplitude threshold stress intensity factor of 6.5 $MPa\sqrt{m}$ [59] and a constant-amplitude fatigue limit stress range of 210 MPa obtained from the constructed strain-life curve. The value of ℓ_o via equation 5.1 showed that notched specimens will act as blunt notches while notched specimens with a flaw at the notch root will behave as sharp notches. The gross stress concentration factors for the notched specimens are 3.205 and 3.109 for the 3.0 mm and 1.5 mm radius edge notches, and 6.305 and 5.432 for 0.6 mm diameter flaws at the notch roots of the 3.0 mm and 1.5 mm radius edge notches, respectively. In the fatigue life prediction using the strain-life approach, the stress concentration factor, K_t, was used for notched specimens and the fatigue notch factor, K_f, for the notched specimens with a 0.6 mm diameter flaw at the notch root. The fatigue notch factors calculated from equation 5.3 were 3.69 and 3.19 for the 3.0 mm and 1.5 mm radius notches with a flaw at the notch root, respectively.

3- The Smith Watson Topper mean stress correction. This correction accounts for the mean stress by assuming the value of $\sqrt{\sigma_{max}\Delta\varepsilon}$ to be constant for all mean stress levels at a given fatigue life. The fatigue life corresponding to each closed loop in the service load history was obtained and the damage was then calculated as $1/N_f$. Miner's linear damage rule was then used for damage summation.

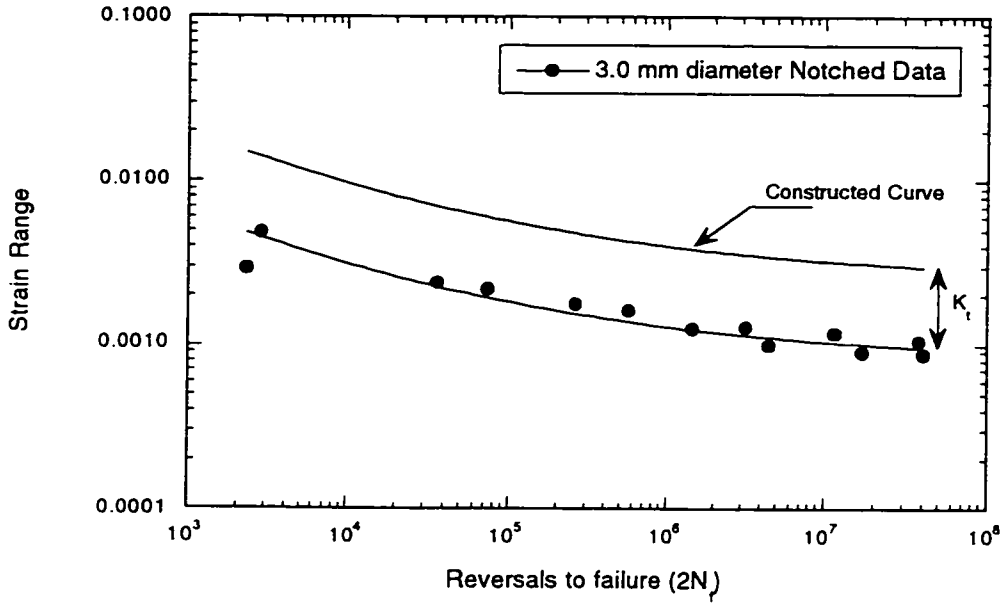

Figure 5.11 Constructed fully reversed strain-life data for 319 cast aluminum alloy

5.6.2 The Effective Strain-Life Method

Fatigue life predictions using the effective strain-life approach included using the following:

1- The effective strain-life data. An effective strain-life curve, shown in Figure 5.12, was estimated from the smooth specimen hipped Al 319 effective strain-life data because in the present case the smooth specimen effective strain-life data included a strength reduction due to casting defects. The estimated effective strain-life curve was constructed by multiplying the effective elastic strains at a given fatigue life by the stress concentration factor, K_t, for the defects and using Neuber's formula for strains in the plastic region. The effective strain-life curve was fitted to [92]

$$\Delta\varepsilon_{eff} = \Delta\varepsilon^{*} + A(2N_f)^{B} \qquad 5.4$$

where $\Delta\varepsilon_{eff}$ is the total effective strain range

$\Delta\varepsilon^{*}$ is the intrinsic strain range and is equal to 0.00102

A and B are material constants and are equal to 0.0299 and -0.26, respectively.

2- The theoretical stress concentration factor, K_t, for notched specimens, and the fatigue notch factor, K_f, for notched specimens with a flaw at the notch root. An ℓ_o value of 0.078 mm was calculated from equation 5.2 using an effective threshold stress intensity factor of 0.98 $MPa\sqrt{m}$ and an effective fatigue limit stress range of 62.3 MPa obtained from the effective strain-life curve. The fatigue notch factors of the 3.0 mm and 1.5 mm radius edge notched specimens with a 0.6 mm diameter flaw at the notch root, calculated from equation 5.3, were 6.17 and 5.34, respectively

3- A crack opening stress estimate which was calculated using equations 4.2, 4.3, and 4.4 (given in chapter 4) for variable amplitude loading.

Equation 5.4 was solved for life to failure, N_f, and the damage due to each closed loop in the service load history was calculated as $1/N_f$. Miner's linear damage rule was then used for damage summation.

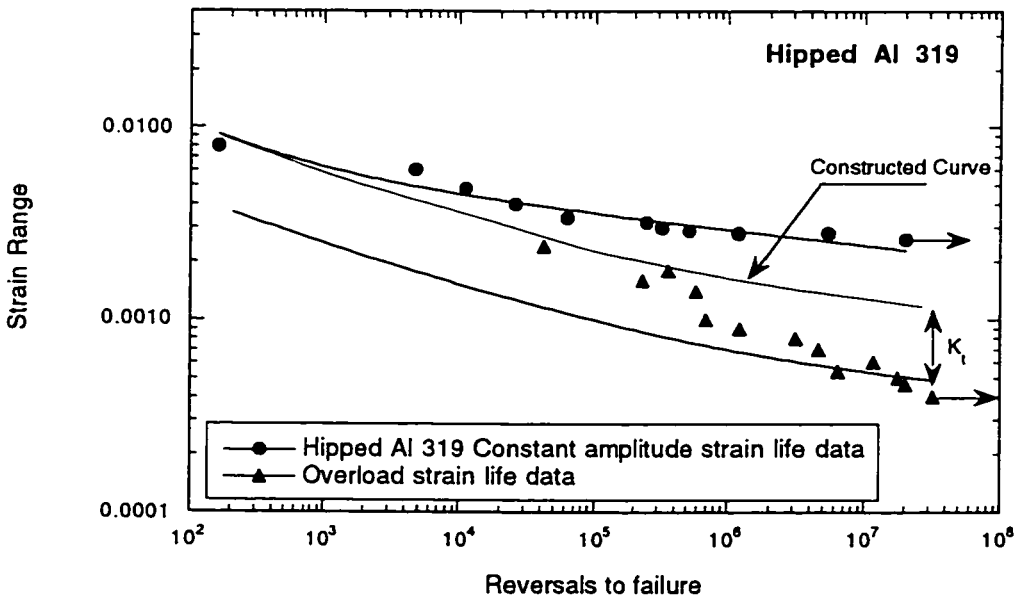

Figure 5.12 Constructed effective strain-life data for 319 cast aluminum alloy

5.6.3 Comparison of the Prediction of the Crack Growth Model, the Local Strain-Life Method and the Effective Strain-Life Method with the Fatigue Test Data

The fatigue life predictions for the smooth, notched, and notched with a flaw at notch root specimens using the strain-life, effective strain-life, and crack growth analyses are plotted together with the fatigue test data in Figures 5.13 to 5.17. The local strain-life method for the smooth specimens, notched specimens, and notched specimens with a flaw at the notch root is unconservative although mean stresses have been taken into account. This is expected because underloads in the service load history decrease the crack opening stress to a lower level than that which occurs in the constant-amplitude reference tests. Effective strain-life predictions which account for the lowering of crack opening stress due to large strain cycles give good predictions for smooth and blunt notched specimens. They are quite conservative for the specimens with flaws in the notch roots.

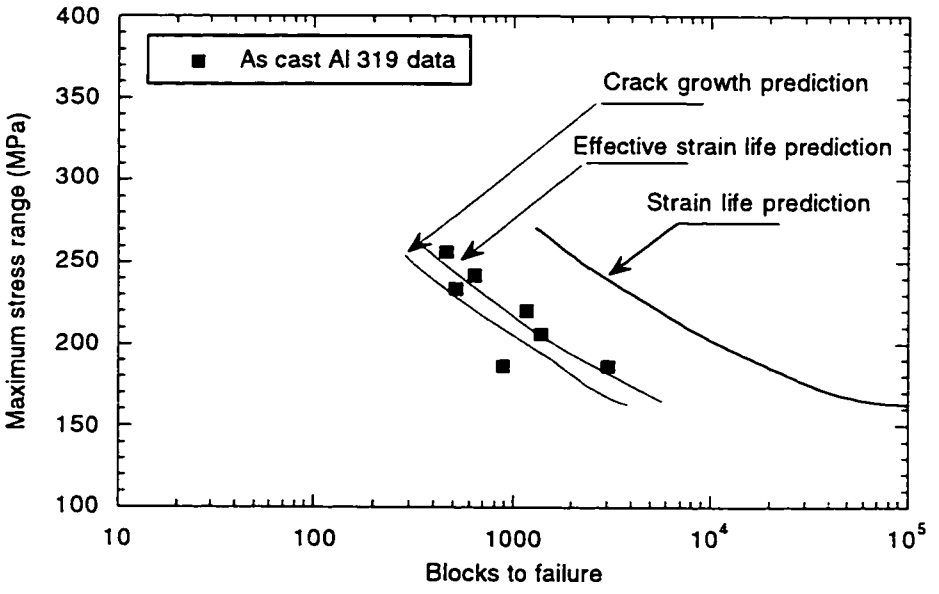

Figure 5.13 Fatigue life prediction for smooth as-cast specimens using strain-life, effective strain-life and crack growth approaches

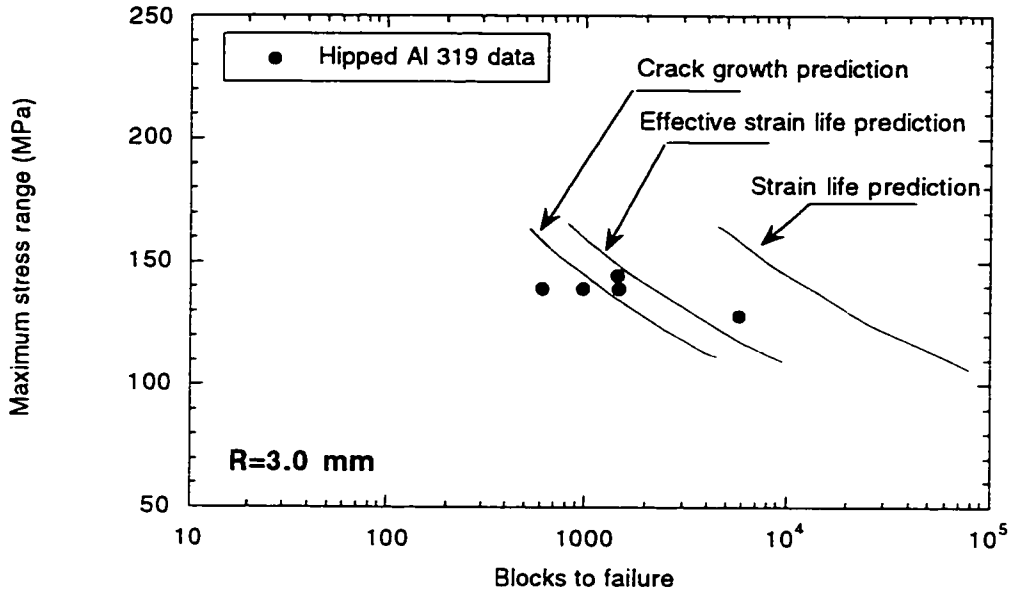

Figure 5.14 Fatigue life prediction for 3.0 mm notched hipped specimens using strain-life, effective strain-life and crack growth approaches

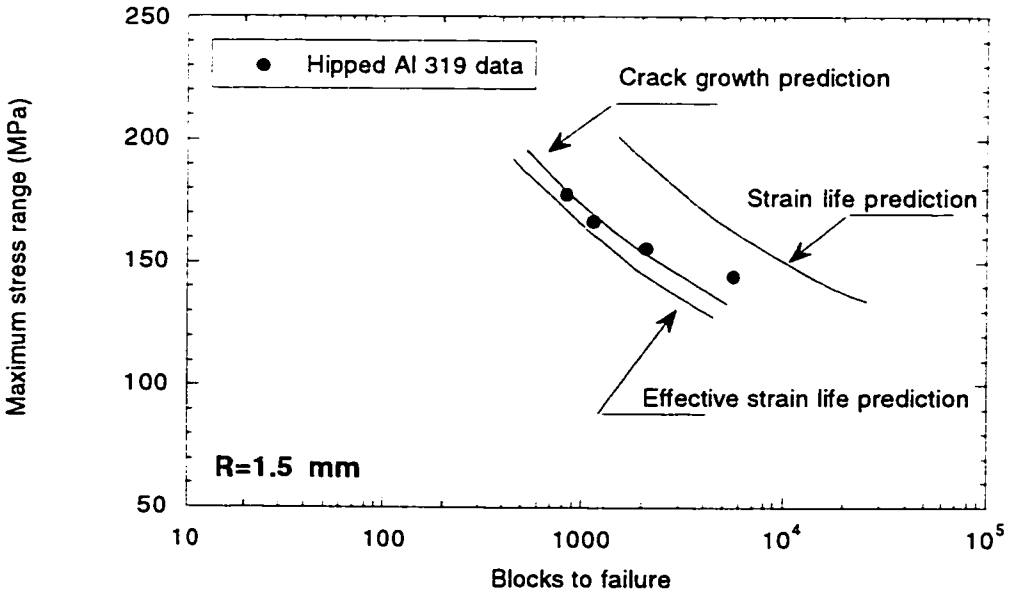

Figure 5.15 Fatigue life prediction for 1.5 mm notched Hipped specimens using strain-life, effective strain-life and crack growth approaches

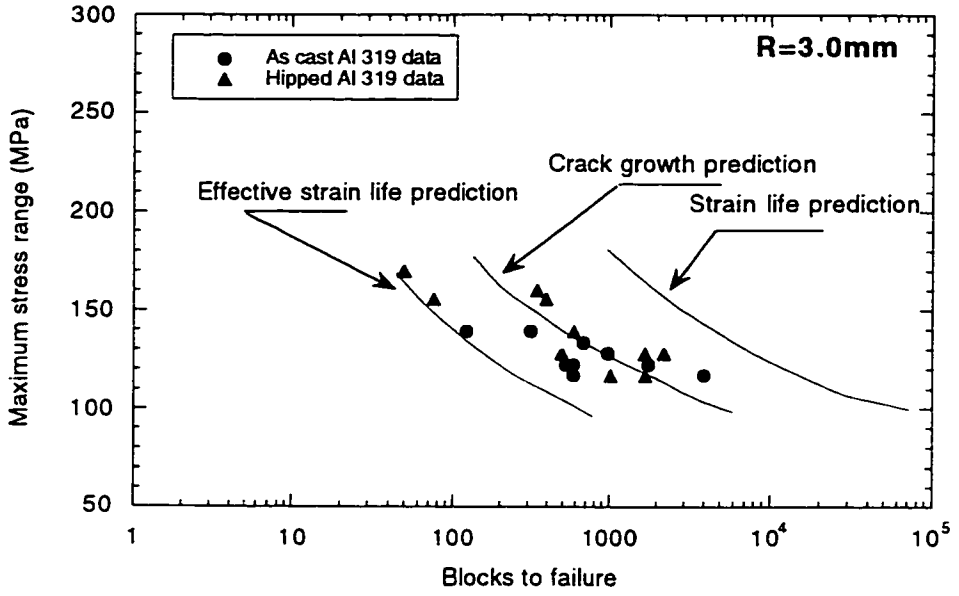

Figure 5.16 Fatigue life prediction for 3.0 mm notched specimens with 0.6 mm drill at notch root using strain-life, effective strain-life and crack growth approaches

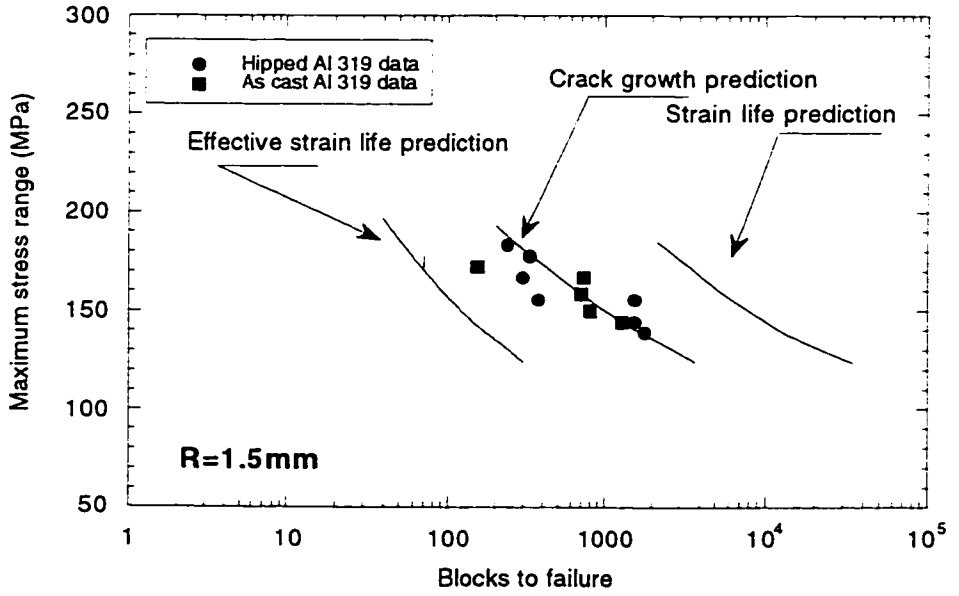

Figure 5.17 Fatigue life prediction for 1.5 mm notched specimens with 0.6 mm drill at notch root using strain-life, effective strain-life and crack growth approaches

Here the rapid decrease in stress concentration with crack length makes the use of a concentration factor based on the notch root unduly conservative. The crack growth calculations which account for the crack opening stress changes due to large strain cycles and the decrease in concentration factor as the crack advances give good predictions for all of the specimen geometries.

5.6.4 An Estimated Constant Crack Opening Stress Level

Tensile overloads, and compressive underloads of yield stress magnitude during fatigue loading drastically reduce crack closure stresses. Crack closure stresses then increase to a steady state level during a large number of smaller cycles as shown previously in section 4.5. The crack growth rate is accelerated during this period of reduced crack closure. In the absence of sufficient experimental data to calibrate a model describing the variation in crack opening stress or finite element results, an assumption has sometimes been made that the crack opening stress throughout fatigue loading remains at the level it would have following the largest cycle in the history. DuQuesnay *et al.*[93] used this assumption in predicting fatigue lives for smooth specimens of 1045 Steel subjected to the Log-Skidder and Grapple-Skidder histories, and for smooth specimens of 2024-T351 aluminum alloy subjected to the Log-Skidder history. Their predictions tended to be conservative. Fatigue life prediction were made in this study for the 319 cast aluminum smooth and notched specimens under the SAE GKN Grapple-Skidder service load history using this assumption. They were also conservative as shown in Figures 5.18 to 5.20. The fatigue life predictions for the notched 319 cast aluminum material with flaws at the notch root which were already conservative using the effective strain-life approach became even more conservative as shown in Figures 5.21 and 5.22. DuQuesnay *et al.*'s [93] fatigue life prediction for smooth specimens, while conservative, were reasonable for the histories examined; however, the present fatigue life predictions for smooth specimens were more conservative than DuQuesnay's. This can be attributed to the material used and its crack opening stress build-up behavior. For the materials used by DuQuesnay *et al.*, the crack opening stress requires many cycles after the application of an underload or an overload to build-up to the steady state level [79], while the 319 cast aluminum material used in this study requires fewer cycles to reach the steady state crack opening stress [64]. Therefore, fatigue life predictions using the minimum crack opening stress in the history are more conservative in the present material with its faster crack opening stress build-up.

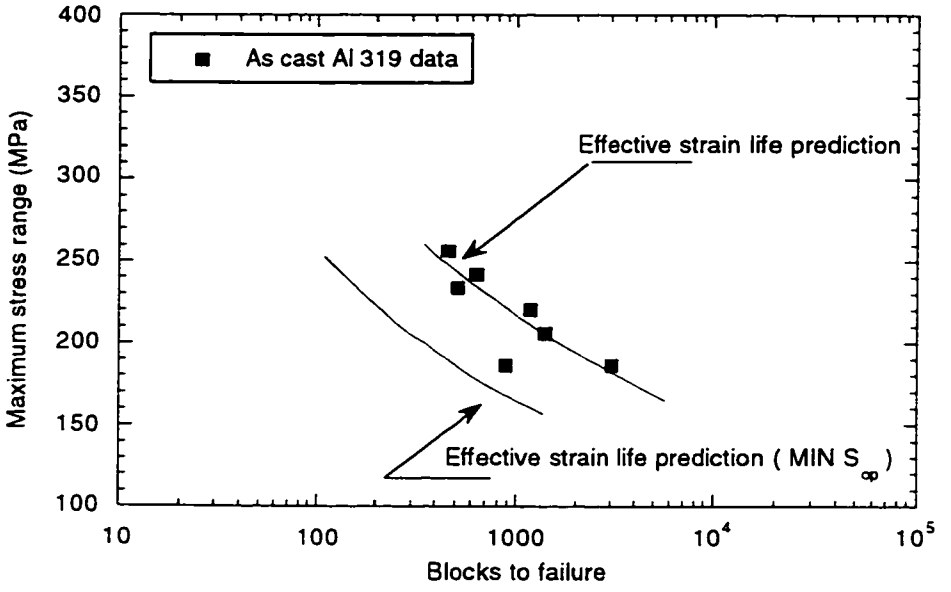

Figure 5.18 Fatigue life prediction for smooth as-cast specimens using the effective strain-life approach and an assumed crack opening stress equal to that following the largest cycle in the load history

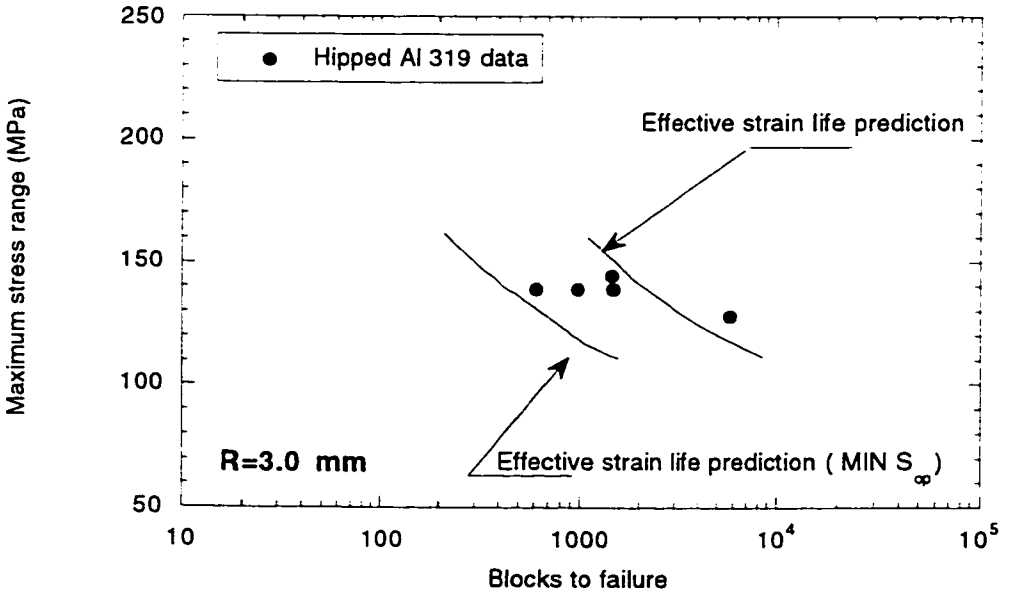

Figure 5.19 Fatigue life prediction for 3.0 mm notched Hipped specimens using the effective strain-life approach and an assumed crack opening stress equal to that following the largest cycle in the load history

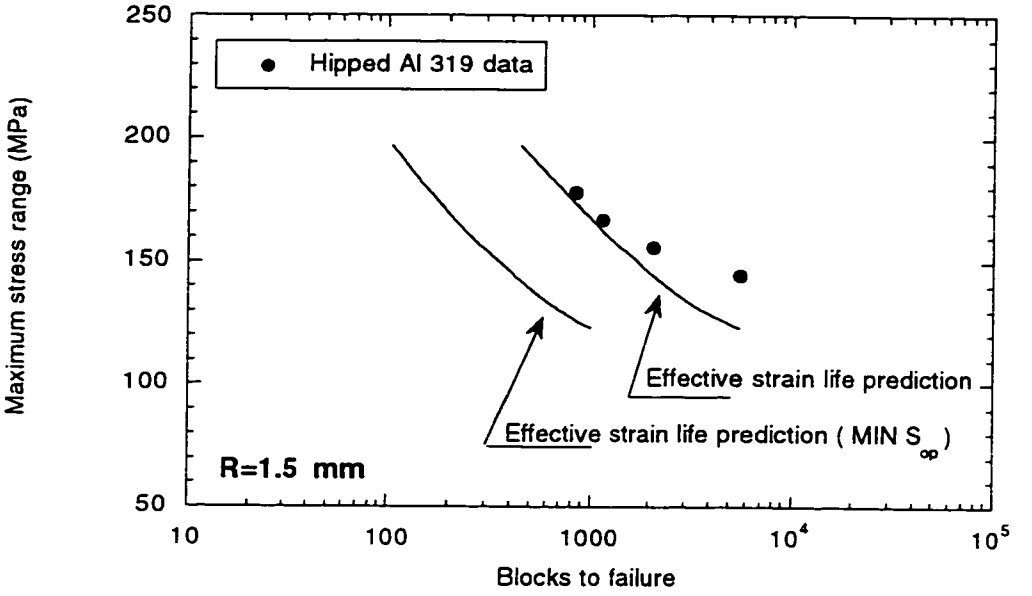

Figure 5.20 Fatigue life prediction for 1.5 mm notched hipped specimens using the effective strain-life approach and an assumed crack opening stress equal to that following the largest cycle in the load history

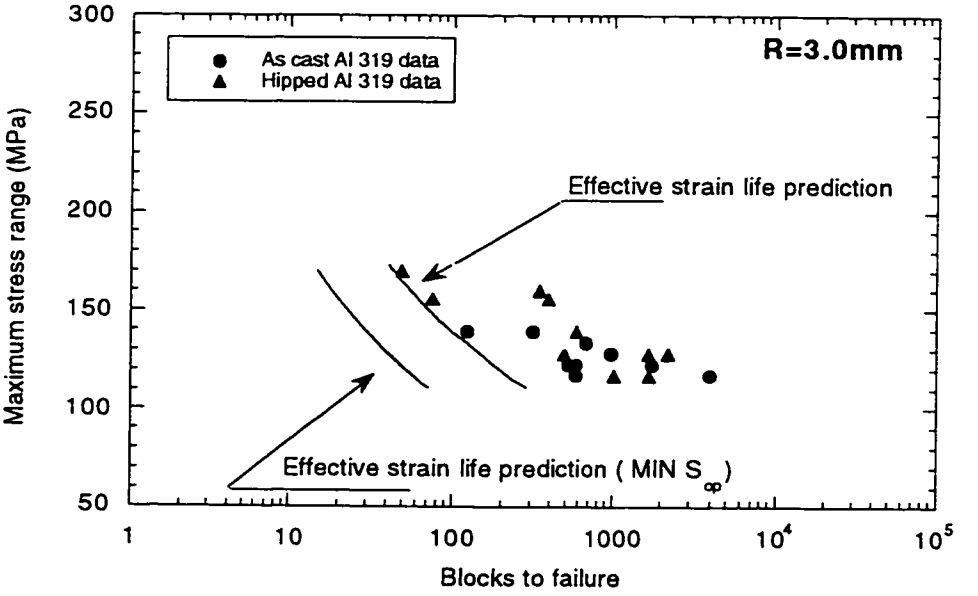

Figure 5.21 Fatigue life prediction for 3.0 mm notched specimens with 0.6 mm drill at notch root using the effective strain-life approach and an assumed crack opening stress equal to that following the largest cycle in the load history

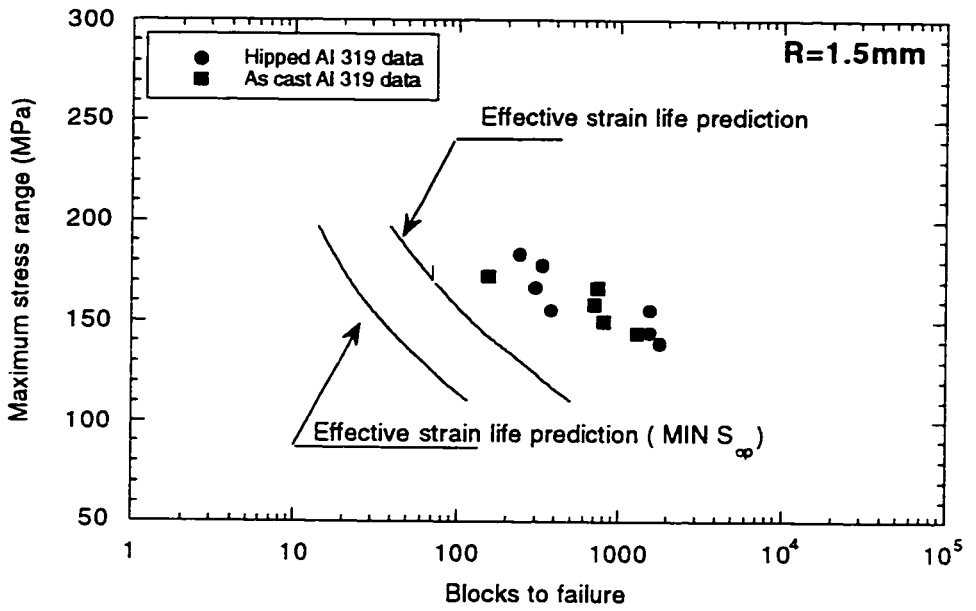

Figure 5.22 Fatigue life prediction for 1.5 mm notched specimens with 0.6 mm drill at notch root using the effective strain-life approach and an assumed crack opening stress equal to that following the largest cycle in the load history

The procedure followed for obtaining the frequency of the cycle in the load history that had a crack opening stress, which when used as a constant level gives the correct fatigue life for a given load level, was as follows:

a- The rainflow cycle counting technique was used to reduce the service load history to closed stress-strain loops and the maximum, minimum, and mean stresses in each loop were determined.

b- The steady state crack opening stress levels for all stress cycles were calculated using equation 4.4. The crack opening stress for cycles with a maximum stress less than the average of the tensile peaks in the history was calculated using a maximum stress equal to the average of the tensile peaks.

c- The steady state crack opening stress levels were arranged in an ascending order, starting with the most severe cycle which has the lowest crack opening stress. This arrangement represents the distribution of the SAE service load history in terms of the severity of the stress cycles in decreasing the crack opening stress.

d- A load cycle corresponding to a given frequency of occurrence in the crack opening stress ascending order arrangement is chosen, and the crack growth model is run using a constant crack opening stress equal to the crack opening stress due to the chosen load cycle. Its value is updated each block as the elastic stress concentration factor, K_p, decreases with crack length. By trial and error a load level is found that gives the observed fatigue life.

The cycle number corresponding to the average constant crack opening stress level which gives a fatigue life that matches the experimental values for the 1.5 mm and 3.0 mm radius notches was 1028 for both notch sizes and its frequency of occurrence is one in 20. This implies that for the SAE GKN service load history, the fatigue life of notched specimens having a 0.6 mm diameter flaw at the notch root can be predicted using a constant crack opening stress level equal to the steady state crack opening stress of a cycle which occurs once every 20 cycles in the history, without the need to follow the changes in the crack opening stress. Further investigation of other load histories is necessary to determine if this frequency is sensitive to variations in load history. Also it is expected that it will vary somewhat with material. If a conservative level can be established for a class of metals, the extensive testing required to establish variations in crack closure may not be necessary for design.

5.7 Summary

This chapter described the fatigue test results for cast aluminum 319 in the as-cast and hipped conditions. The materials were tested under the torsional channel of the SAE GKN Grapple-Skidder history. The specimens examined were smooth specimens, notched specimens, and notched specimens with an artificial flaw at the notch root.

The smooth specimens test results showed that the hipping process improved the fatigue life of the 319 cast aluminum alloy. For 1000 blocks of fatigue life, the maximum stress range has improved from 230 MPa to 270 MPa. The notched specimens and the notched specimens with an artificial flaw at the notch root test results showed that the fatigue lives of the 3.0 mm and 1.5 mm radius notched

specimens with a 0.6 mm diameter flaw at the notch root were 40% and 38% shorter than the notched specimen fatigue lives, respectively.

This chapter also described fatigue life predictions for smooth specimens, notched specimens, and notched specimens with a flaw at the notch root subjected to the SAE GKN Grapple-Skidder history made using strain-life, effective strain-life and crack growth models. The strain-life approach using constant-amplitude data gave unconservative fatigue life predictions for smooth specimens, notched specimens and notched specimens with a flaw at the notch root. The effective strain-life approach using effective strain-life data gave good predictions for smooth and blunt notched specimens, but was quite conservative for the specimens with flaws in the notch roots. The crack growth calculations which account for the crack opening stress changes due to large strain cycles and the decrease in concentration factor as the crack advances give good predictions for all of the specimen geometries. The conventional methods for fatigue life prediction using the fatigue notch factor, K_f, do not account for the decrease in concentration factor as the crack advances and can not describe the fatigue behavior of notches with high K_t values that decay rapidly, such as a notch root with a flaw at the notch root.

CHAPTER 6

CONCLUSIONS

Smooth specimens, notched specimens and notched specimens with flaws at the notch root made of three cast aluminum materials, namely Al 319, Al 390 and Al 206, were fatigue tested in this investigation under three types of loading histories. These histories included a constant-amplitude loading history, an intermittent underload block loading history and a SAE service load history. The fatigue test results revealed that the casting defects are the main sites for fatigue crack initiation and propagation. The block loading history consisting of underloads followed by constant-amplitude smaller cycles reduced the crack opening stress so that the smaller constant-amplitude cycles were fully effective. This loading history caused a fatigue strength reduction of 66-87% in the three aluminum alloys. The results also revealed that there is a fatigue strength reduction due to a notch and there is a further reduction due to a flaw at the notch root.

The hipping process applied to the 319 cast aluminum alloy, which included subjecting the material to a high pressure at high temperature and then slowly cooling it, decreased the size of the flaw in the material from 0.6 mm to 0.2 mm in diameter and increased the constant-amplitude fatigue strength by 62.5%.

A notch size effect was observed under constant- and variable-amplitude loading for a 0.6 mm diameter flaw at the notch root. For the hipped material under constant-amplitude loading, the fatigue limit multiplied by the gross stress concentration factor decreased from 352 MPa to 256 MPa as the notch size increased from 1 mm to 6 mm in diameter. The corresponding values for variable-amplitude fatigue were from 75 MPa to 25 MPa.

The fatigue lives of the 1.5 mm and 3.0 mm radius notched specimens subjected to the SAE service load history were decreased by 38% and 40%, respectively, due to a flaw of 0.6 mm diameter at the notch root.

A crack growth analysis using an effective strain intensity factor, notch strain calculations based on Neuber's formula, and a reference crack growth curve obtained during closure-free crack growth was able to model the fatigue behavior of the three cast aluminum materials tested in this investigation under the three types of loading histories. The model predictions were in good agreement with the experimental data.

Natural flaws in the as-cast 319 aluminum alloy can be modeled by an equivalent drilled hole of the same size.

The crack growth model was used to analyse the effect of variations in the flaw size and flaw position in the notch root. The model results suggested that the fatigue limit varies more for a given variation in the flaw size and flaw position for notched specimens having a small notch radius than for specimens having large notch radius. The model results were in good agreement with the experimental data.

The percentage of the fatigue life of 1.5 mm and 3.0 mm radius edge notched specimens spent in growing a crack to a total length l_1 from the notch root at which notched specimens with or without a flaw have the same elastic stress concentration factor K_p, was calculated using the crack growth model. The results indicated that the fatigue lives of the 3.0 mm and 1.5 mm radius notched specimens with a 0.6 mm diameter flaw at the notch root were 40% and 38% shorter than the notched specimen fatigue lives, respectively. The percentage of the life of a notched specimens required to propagate a crack to a length of l_1, under a maximum stress range of 173 MPa for a 3 mm notch and 148 MPa for a 1.5 mm notch, were calculated using the crack growth model and were 62% and 40%, respectively. The percentage reduction in number of cycles to propagate a crack to a total depth of l_1 from the notch root due to a flaw at notch root, under a maximum stress range of

173 MPa for a 3 mm notch and 148 MPa for a 1.5 mm notch, was also calculated using the crack growth model, and was 70% and 78% for the 3.0 and 1.5 mm notches, respectively.

Fatigue life predictions for smooth, notched and notched specimens with a flaw at the notch root subjected to the SAE GKN Grapple-Skidder history made using strain-life, effective strain-life and crack growth models were compared. The local strain approach using constant-amplitude data gave unconservative fatigue life predictions for smooth specimens, notched specimens and notched specimens with a flaw at the notch root. The local strain approach using effective strain-life data gave good predictions for smooth and blunt notched specimens, but was quite conservative for the specimens with flaws in the notch roots. The conventional methods for fatigue life prediction using the fatigue notch factor, K_f, do not account for the decrease in concentration factor as the crack advances and cannot describe the fatigue behavior of notches with high K_t values that decay rapidly such as a notch root with a flaw at the notch root.

In the absence of sufficient experimental data or finite element results to calibrate a model describing the variation in crack opening stress, a conservative assumption has sometimes been made that the crack opening stress throughout fatigue loading remains at the level it would have following the largest cycle. This assumption, while shown in earlier studies to be conservative, was reasonable for the materials and histories examined. It was shown to be more conservative for the cast aluminum material used in this study because of the crack opening stress which requires fewer cycles to reach the steady state crack opening stress than that for the materials studied earlier (1045 Steel and 2024-T351 aluminum). The analytical crack growth model was used to determine the frequency of the cycle in the SAE GKN Grapple-Skidder history that had a crack opening stress, which when used as a constant level gives the correct fatigue life.

APPENDIX A

Weight function for the deepest point "A" of a semi-elliptical surface crack

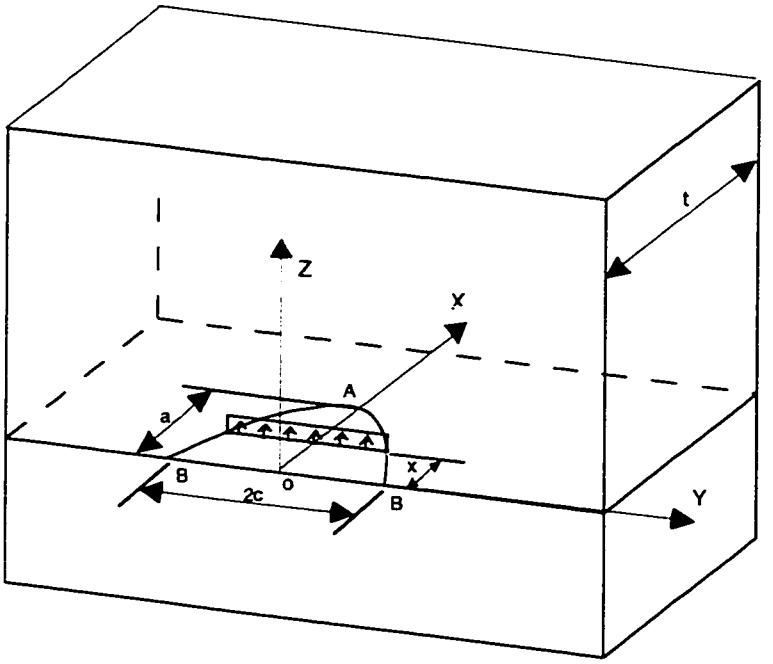

$$m_A = \frac{2}{\sqrt{2\,\pi\,(a - x)}}\ \{\ 1 + M_{1A}\,(1 - \frac{x}{a}\ )^{1/2} + M_{2A}\,(1 - \frac{x}{a}\ ) + M_{3A}\,(1 - \frac{x}{a}\ )^{3/2}\ \}$$

where

$$M_{1A} = \frac{\pi}{\sqrt{2Q}}\,(4Y_o - 6Y_1)\ - \frac{24}{5}$$

$$M_{2A} = 3$$

$$M_{3A} = 2\,(\ \frac{\pi}{\sqrt{2Q}}\ Y_o - M_{1A} - 4\ )$$

$$Y_o\ = B_o + B_1\,(\ \frac{a}{t}\ )^2 + B_2\,(\ \frac{a}{t}\ )^4$$

$B_o = 1.10190 - 0.019863\ (a/c) - 0.043588\ (a/c)^2$

$B_1 = 4.32489 - 14.9372\ (a/c) + 19.4389\ (a/c)^2 - 8.52318\ (a/c)^3$

$B_2 = -3.03329 + 9.96083\ (a/c) - 12.582\ (a/c)^2 + 5.3462\ (a/c)^3$

$$Y_1 = A_o + A_1\,(\ \frac{a}{t}\ )^2 + A_2\,(\ \frac{a}{t}\ )^4$$

$A_o = 0.546128 - 0.114206\ (a/c) - 0.046523\ (a/c)^2$

$A_1 = 3.022 - 10.8679\ (a/c) + 14.94\ (a/c)^2 - 6.8537\ (a/c)^3$

$A_2 = -2.28655 + 7.88771\ (a/c) - 11.0675\ (a/c)^2 + 5.16354\ (a/c)^3$

$$Q = 1 + 1.464\ (a/c)^{1.65} \qquad \text{for } 0 \le a/c \le 1$$

APPENDIX B

The elastic stress concentration factor, K_p, describes the crack tip stress field for a crack emanating from a notch or for a crack emanating from a flaw in a notch. The finite element results, describing the notch stress field for uncracked specimens, were plotted together with the elastic stress concentration factor, K_p, distribution for comparison. K_p for a crack emanating from a notch was calculated based on the equation proposed by Topper and El-Haddad [63] given by equation 2.19 for short cracks and by $\sqrt{\frac{l+c}{l}}$ for long cracks, where l is the crack length measured from the edge of the notch and c is the notch radius. K_p for a crack emanating from a flaw in a notch root was calculated based on the approximation made in this study given by equations 2.20 to 2.42. The non uniform stress σ for the notch stress field in equation 2.20 was replaced by the uniform stress σ_{uf} shown in Figure 2.7. The uncracked specimen local stress, σ_{yy}, was normalized by the maximum local stress, σ_{max}, and plotted versus the distance from the notch root, X, normalized by the notch radius of curvature, ρ, as shown in Figures B1, B2, and B3 for the 1.0 mm, 3.0 mm, and 6.0 mm diameter notches, respectively. The elastic stress concentration factor, K_p, for a crack emanating from a notch was normalized by the theoretical surface stress concentration factor, K_t, and plotted versus the crack length measured from the notch root, l, normalized by the notch radius of curvature, ρ, as shown in Figures B1, B2, and B3 for the 1.0 mm, 3.0 mm, and 6.0 mm diameter notches, respectively. Figures B1, B2, and B3 show that the elastic stress concentration factor solution, K_p, is very close to the stress field distribution and consequently, the stress field distribution can be used instead of K_p without significant errors.

Results shown in Figures B1, B2, and B3 were all plotted together, in Figure B4, with the normalized solution of the elastic stress concentration factor, K_p, for a crack emanating from a 0.6 mm diameter flaw at the notch root of the three notch diameters used; 1.0 mm, 3.0 mm, and 6.0 mm. The Figure shows that as the flaw size increases with respect to the notch size the theoretical surface stress concentration for a flaw in a notch, represented by the ratio $\frac{K_p}{K_t}$ at a crack length equals the flaw depth, decreases until it is expected to reach the theoretical surface stress concentration value of a flaw.

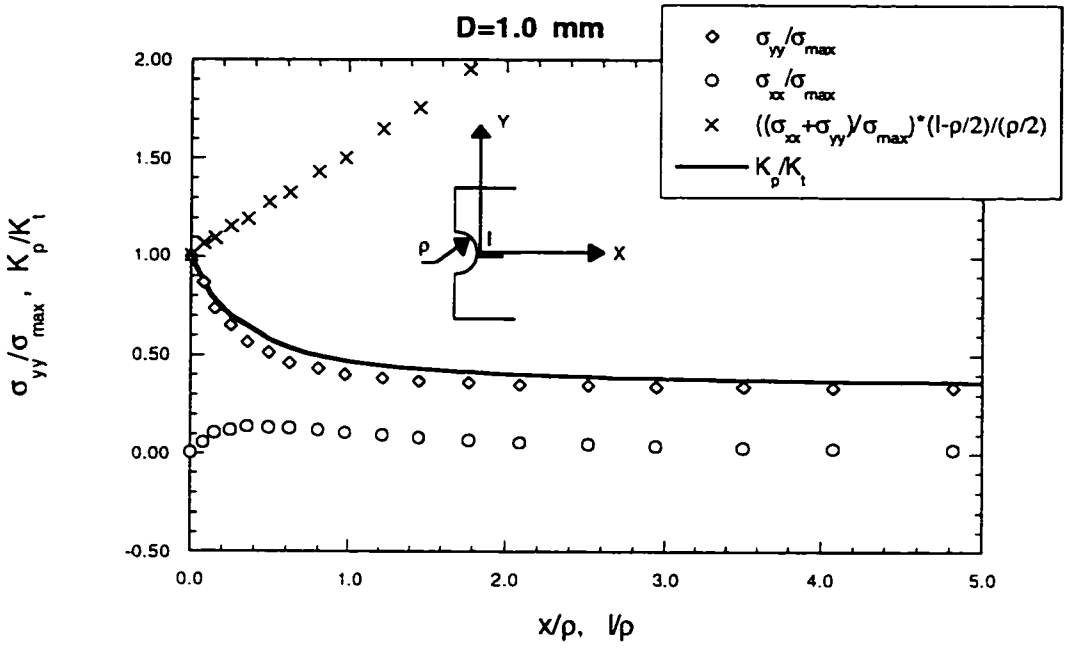

Figure B1 Normalized notch stress filed and elastic stress concentration factor distributions for 1.0 mm diameter notch

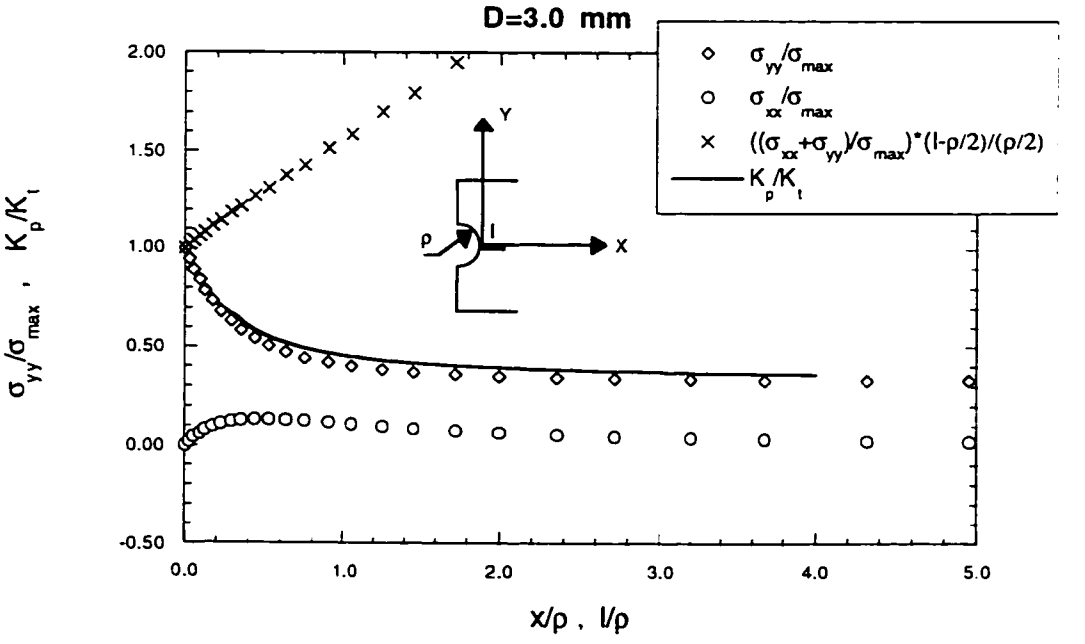

Figure B2 Normalized notch stress filed and elastic stress concentration factor distributions for 3.0 mm diameter notch

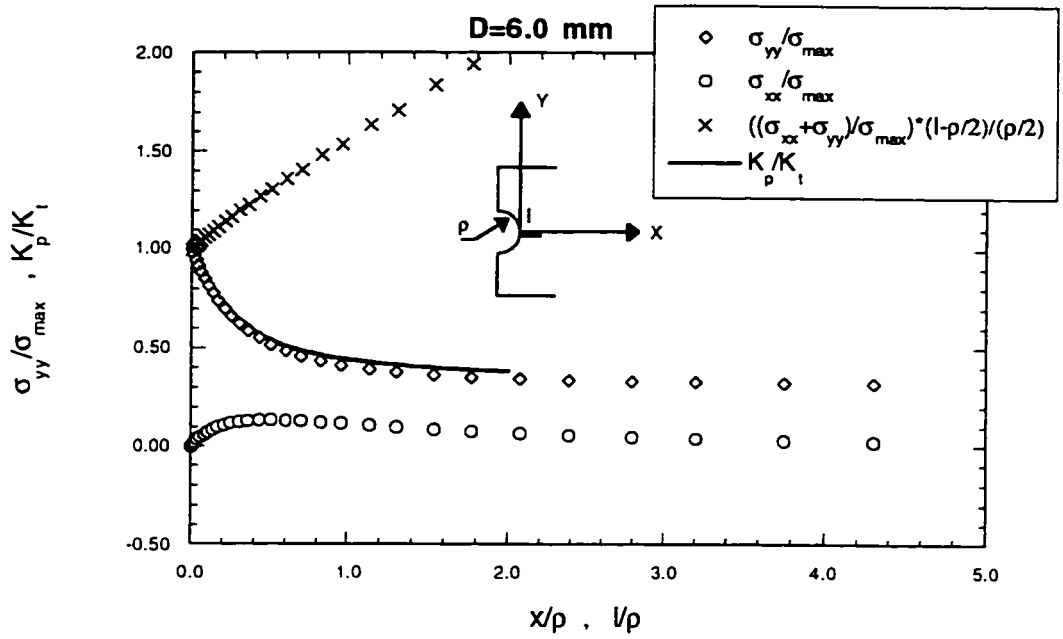

Figure B3 Normalized notch stress filed and elastic stress concentration factor distributions for 6.0 mm diameter notch

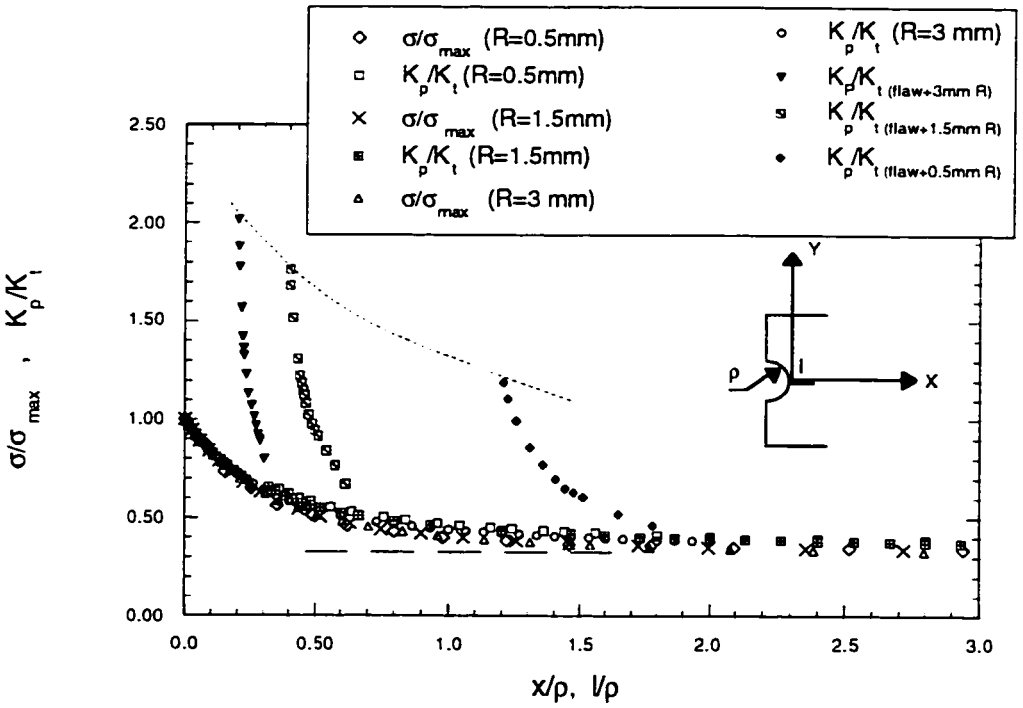

Figure B4 Normalized notch stress filed and elastic stress concentration factor distributions for 1.0 mm, 3.0 mm, and 6.0 mm diameter notches

REFERENCES

[1] Turkdogan, E.T. and Grange, R.A. (May 1970). "Microsegregation in steel," JISI, Vol. 208, Part 5, pp. 482-494.

[2] Paris, P.C. and Erdogan, F. (1963). "A critical analysis of crack propagation laws," ASME Journal of Basic Engineering, Vol. D85, pp. 528-534.

[3] De Kazinczy, F. (1966). "Influence of metallurgical defect size on the fatigue properties of cast steel,"JernKont. Ann., Vol. 150, No. 7, pp. 493-506.

[4] De Kazinczy, F. (Jan. 1969). "Size effect on fatigue of cast steels," JISI, pp. 40-43.

[5] De Kazinczy, F. (Nov. 1969). "Effect of grain-boundary precipitates on the endurance limit of cast steel," JISI, pp. 1454-1456.

[6] De Kazinczy, F. (1970). "Fatigue properties of a marine diesel engine crank throw forging," Europian shipbuilding journal of the ship technical society, Vol. 19, No. 1, pp. 9-12.

[7] De Kazinczy, F. (Sept. 1970). "Effect of small defects on the fatigue properties of medium strength cast steels," JISI, pp. 851-855.

[8] De Kazinczy, F. (April 1971). "Fatigue strength across healed hot tears in castings," JISI, pp. 310-312.

[9] Mitchell, M.R. (June 1975). "Review of the mechanical properties of cast steels with emphasis on fatigue behavior and the influence of microdiscontinuities," FCP report No. 15, College of Engineering, Urbana, Illinois.

[10] Evans, E.B., Elbert, L.J. and Briggs, C.W. (1956). "Fatigue properties of cast and comparable wrought steels," ASTM proc., Vol. 56, pp. 1-32.

[11] Briggs, C.W., Wallace, J.F.Vishnevisky, C. and Bertolino, N.F. (August 1967). "The effects of survace descontinuities on the fatigue properties of cast steel sections," ASME No. 67-WA/MET-17.

[12] Mitchell, M.R. (Dec. 1974). "Effect of graphite morphology, matrix hardness and structure on the fatigue resistance of gray cast iron," FCP report No. 14, College of Engineering, Illinois.

[13] Heuler, P, Berger, C. and Motz, J. (1992). "Fatigue behavior of steel castings near-surface defects," Fatigue Fract. Engng. Mater. Struct. Vol. 16, No. 1, pp. 115-136.

[14] Güngör, S. and Edwards, L. (1993). "Effect of surface texture on fatigue life in a squeeze-cast 6082 aluminum alloy," Fatigue Fract. Engng. Mater. Struct. Vol. 16, No. 4, pp. 391-403.

[15] Couper, M.J., Nesson, A.E. and Griffiths, J.R. (1990). "Casting defects and the fatigue behavior of an aluminum casting alloy," Fatigue Fract. Engng. Mater. Struct. Vol. 13, No. 3, pp. 213-227.

[16] DuQuesnay, D.L., Yu ,M.T., Topper, T.H. and Dabell, B.J. (1992). "Fatigue evaluation of a nodular cast iron component," SAE international congress and exposition, Detroit, Michigan, Feb. 24-28, SAE technical paper series no. 920669.

[17] Sonsino, C.M. and Ziese, J. (1993). "Fatigue strength and applications of cast aluminum alloys with different degrees of porosity," Int. J. Fatigue, Vol. 15, No. 2, pp. 75-84.

[18] Stanzl-Tschegg, S.E., Mayer, H.R., Tscheg, E.K. and Beste, A. (1993). "In-service loading of AlSi11 aluminum cast alloy in the very high cycle regime," Int. J. Fatugue, Vol. 15, No. 4, pp. 311-316.

[19] Liu, C.D., Bassim, M.N. and Lawrence, S.St. (1993). "Evaluation of fatigue-crack initiation at inclusions in fully pearlitic steels," Materials Science and Engineering, A167, pp. 107-113.

[20] Khalifa, T.A. (1989). "Fatigue crack initaition associated with inclusions in a low carbon steel," Journal of Materials Science Letters, Vol.8, pp. 427-429.

[21] Skallerud, B., Iveland, T. and Härkegård, G. (1993). "Fatigue life assessment of aluminum alloys with casting defects," Engineering Fracture Mechanics, Vol. 44, No. 6, pp. 857-874.

[22] Pearson, S. (1975). "Initiation of fatigue cracks in commercial aluminum alloys and the subsequent propagation of very short cracks," Engineering Fracture Mechanics, Vol. 7, pp. 235-47.

[23] Lankford, J. (1982). "The growth of small fatigue cracks in 7075-T6 aluminum," Fatigue of Engineering Materials and Structures, Vol. 5, pp. 233-48.

[24] Tanaka, K., Hojo, M. and Nakai, Y. (1983). "Crack initiation and early propagation in 3% silicon iron," In Fatigue Mechanisms: Advances in quantative measurement of fatigue damage, special technical publication 811, pp. 207-32, philadaelphia: American Society for Testing and Materials.

[25] El-Haddad, M.H., Smith, K.N. and Topper, T.H. (19790. "A strain based intensity factor solution for short fatigue cracks initiating from notches," Fracture mechanics, ASTM STP 677, C.W. Smith, Ed., American Society for Testing and Materials, pp. 274-289.

[26] Sehitoglu, H. (1985). "Characterization of crack closure," Fracture mechanics: Sixteenth symposium, ASTM STP 868, M.F. Kanninen and A.T. Hopper, Eds., American Society for Testing and Materials, pp. 361-380.

[27] Smith, R. A. and Miller, K. J. (1978). International Journal of Mechanical Engineering Science, Vol. 20, pp.201-206.

[28] Hammunda, H. M. and Miller, K. J. (1979). In Elastic Plastic Fracture, ASTM STP 668, American Society for Testing and Materials, pp.703-719.

[29] Gerard, D.A. and Koss, D.A. (1991). "The influence of porosity on short fatigue crack growth at large strain amplitudes," Int. J. fatigue, Vol. 13, No. 4, pp. 345-352.

[30] Takeshi Ogawa and Hideo Kobayashi (1987). "Near-threshold fatigue crack growth and crack closure in a nodular cast iron," Fatigue Fract. Engng. Mater. Struct., Vol. 10, No. 4, pp. 273-280.

[31] Tokaji, K., Ogawa, T. and Shamoto, K. (July 1994). "Fatigue crack propagation in spheroidal-graphite cast irons with different microstructures," Int. J. fatigue , Vol. 16, pp. 344-350.

[32] Murakami, Y. and Endo, T. (Jan. 1980). "Effects of small defects on fatigue strength of metals," Int. J. Fatigue, Vol. 2, pp. 23-30.

[33] Murakami, Y. and Endo, T. (1983). "Quantitative evaluation of fatigue strength of metals containing various small defcts or cracks," Engineering Fracture Mechanics, Vol. 17, No. 1, pp. 1-15.

[34] Gilchrist, M.D. and Smith, R.A. (1991). "Finite element modelling of fatigue crack shapes," Fatigue Fract. Engng. Mater. Struct., Vol. 14, No. 6, pp. 617-626.

[35] Springfield, C.W. and Jung, H.Y. (1988). "Investigation of stress concentration factor - Stress intensity factor interaction for flaws in fillited rods," Engineering Fracture Mechanics, Vol. 31, No. 1, pp. 135-144.

[36] Nord, K. (May 1983). "Three dimensional fracture analysis by quadratic isoparametric finite elements," M.S.E. thesis, The University of Alabama in Huntsville.

[37] Shivakumar, K.N. and Neuman Jr., J.C. (1991). "Stress intensity factor for large aspect ratio surface and corner cracks at a semi-circular notch in a tension specimen," Engineering Fracture Mechanics, Vol. 38, No. 6, pp. 467-473.

[38] Sato, T. and Shimada, H. (1988). "Evaluation of fatigue crack initiation life from a notch," Int. J. fatigue, Vol. 10, No. 4, pp. 243-247.

[39] Bannantine, J. A., Comer, J. J. and Handrock, J. L. (eds.) (1990). "Fundamentals of Metal Fatigue Analysis," by Prentice-Hall, Inc., A Divison of Simon & Shuster, Englewood Cliffs, New Jersy 07632.

[40] Taylor, D. (1986). "The Behavior of Short Fatigue Cracks, E.G.F. 1," Mechanical Engineering Publications, London, 479-490, K.J. Miller and E.R. de los Rios (Eds.)

[41] Kendall, J.M., M.N. James and J.F. Knott (1986). "The Behavior of Short Fatigue Cracks, E.G.F. 1," Mechanical Engineering Publications, London, 241-258, K.J. Miller and E.R. de los Rios (Eds.)

[42] Blom,A. F., A. Headland, W. Zhao, A. Fathulla, B. Weiss and R. Stickler (1986). "The Behavior of Short Fatigue Cracks, E.G.F. 1," Mechanical Engineering Publications, London, 37-66, K.J. Miller and E.R. de los Rios (Eds.)

[43] Topper, T.H. and M.H. El-Haddad (1979). The Canadian Metallurgical Quarterly, Vol. 18, pp. 207-213.

[44] Soniak, F. and L. Remi (1986). "The Behavior of Short Fatigue Cracks, E.G.F. 1," Mechanical Engineering Publications, London, 479-490, K.J. Miller and E.R. de los Rios (Eds.)

[45] Topper, T.H., M.T. Yu and D.L. DuQuesnay (1987). "Mechanisms and mechanics of fatigue crack initiation and growth," Proceedings of the international symposium on fracture mechanics, Edited by W.R. Tyson and B. Mukherjee, Vol. 6, pp. 81-94, Winnipeg.

[46] Tokaji, K., T. Ogawa and Y. Harada (1986). Fatigue Fract. Engng. Mater. Struct., Vol. 9, No. 3, pp. 205-217.

[47] El-Haddad, M.H., Smith, K.N., and Topper, T.H. (1979). "Fatigue crack propagation of short fatigue cracks," J. Engng. Mater. Technology, ASME, Vol. 10, pp. 42-46.

[48] H. Tada, P.C. Paris and G.R. Irwin (1973). "The Stress Analysis of Cracks Handbook", Del Research corporation, Hellertown, Pa.

[49] D.P. Rooke, and d.J. Cartwright (1975). "Compendium of Stress Intensity Factors", H.M. Stationery Office, London.

[50] G.C.M. Sih (1973). "Handbook of Stress Intensity Factors", Lehigh University, Bethlehem, Pa.

[51] W. Elber (1971). "The significance of fatigue crack closure," In Damage Tolerence in Aircraft Structures, ASTM STP 486, American Society for Testing and Materials, Philadelphia, pp. 230-242.

[52] Zhu, C. (1994). "A model for small fatigue crack growth," Fatigue Fract. Engng. Mater. Struct., Vol. 17, No. 1, pp. 69-75.

[53] Zuyu Sun, De los Rios, E.R. and Miller, K.J. (1991). "Modelling small fatigue cracks interacting with grain boundaries," Fatigue Fract. Engng. Mater. Struct., Vol. 14, pp. 277-29.

[54] Nicholls, D.J. and Martin, J.W. (1991). "A comparison of small fatigue crack growth, low cycle fatigue and long fatigue crack growth in Al-Li alloys," Fatigue Fract. Engng. Mater. Struct., Vol. 14, pp. 185-192.

[55] Hobson, P.D. (1982). "The formulation of a crack growth equation for short cracks," Fatigue Fract. Engng. Mater. Struct., Vol. 5, pp. 323-327.

[56] Chan, K.S. and Lankford, J. (1983). "A crack tip strain model for the growth of small fatigue cracks," Scripta Met., vol. 17, pp. 529-532.

[57] El Haddad, M.H., Topper, T.H. and Topper, T.N. (April 1981). "Fatigue life predictions of smooth and notched specimens based on fracture mechanics," Journal of Engineering Materials and Technology, Vol. 103, pp. 91-96.

[58] Gerald, J. and Menegazzi, A. (1994). "A fatigue crack propagation model under variable amplitude loading," Automation in fatigue and facture: Testing and analysis, ASTM STP 1231, C. Amzallag, Ed., American Society for Testing and Materials, Philadelphia, pp. 334-352.

[59] Ting, J.C. and Lawrence, Jr., F.V. (1993). "Modelling the long-life fatigue behavior of a cast aluminum alloy," Fatigue Fract. Engng. Mater. Struct., Vol. 16, No. 6, pp. 631-647.

[60] Dowling, N.E., "Fatigue at notches and the local strain and fracture mechanics approaches," Fracture mechanics ASTM STP 677 (edited by C. W. Smith), pp. 247-273, American Society for Testing and Materials.

[61] Dowling, N.E. (ed.) (1993). "Mechanical Behavior of Materials," by Prentice-Hall, Inc., A Divison of Simon & Shuster, Englewood Cliffs, New Jersy 07632.

[62] Larsson, M., Melander, A. and Nordgren, A. (March 1993). "Effect of inclusions on fatigue behavior of hardened spring steel," Materials Science and Technology, Vol. 9, pp. 235-245.

[63] Topper, T.H. and El Haddad, M.H. (June 1981). "Fatigue strength prediction of notches based on fracture mechanics," Proceedings of the international symposium on fatigue thresholds, Stockholm, Sweden, pp. 777-798.

[64] Dabayeh, A.A., Berube, A.J. and Topper, T.H. (1988). "An experimental study of the effect of a flaw at a notch root on the fatigue life of cast Al 319," Accepted for publication in the International Journal of Fatigue.

[65] Murakami, Y., Norikura, T. and Yasuda, T. (1982). "Stress intensity factors for a penny-shaped crack emanating from an ellipsoidal cavity," Trans. Japan Soc. Mech. Engrs., Vol. 48, No. 436, pp. 1558-1565.

[66] Newman, J.C., Jr. (1992). "Fracture mechanics parameters for small fatigue cracks," ASTM STP 1149, pp. 6-33.

[67] American Society for Testing and Materials (1986). Annual Book of ASTM Standards, Section 3: Metals Test Methods and Analytical Procedures, Vol. 03.01- Metals- Mechanical Testing; Elevated and Low-Temperature Tests, ASTM, Philadelphia, pp. 836-848.

[68] Duquesnay, D.L. (1991). "Fatigue Damage Accumulation in Metals Subjected to High Mean Stress and Overload Cycles," Ph.D. Thesis, University of Waterloo, Waterloo, Ontario, Canada.

[69] Dabayeh, A. (1994). "Changes in Crack Opening Stress after Overloads in a 2024-T351 Aluminum Alloy," M.A.Sc. thesis, University of Waterloo, Waterloo, Ontario, Canada.

[70] Yu, M.T., Topper, T.H. and Au, P. (1984). "The effects of stress ratio, compressive load and underloads on the threshold behavior of a 2024-T351 aluminum alloy," Proceedings of the 2nd international conference on fatigue and fatigue thresholds held at the university of Birmingham, UK., 3-7 September, pp. 179-190.

[71] Smith, R.A. and Cooper, J.F. (1989). Int. J. Press. Vess. Piping, Vol. 36, pp. 315.

[72] Soboyeji, W.O., Kishimoto, K., Smith, R.A. and Knott, J.F. (1989). Fatigue Fract. Engng. Mater. Struct., Vol. 12, pp. 167.

[73] Abdel-Raouf, H., Topper, T.H. and Plumtree, A. (1991). "A short fatigue crack model based on the nature of the free surface and its microstructure," Scr. Met. Mat., Vol. 25, pp. 597-602.

[74] Nisitani, H. and Chen, D.H. (1984). "Stress intensity factors for semi-elliptical surface cracks in a shaft under tension," Trans. Jap. Soc. Mech. Engrs., No. 50, pp. 1077-1082.

[75] Gross, G. and Srawley, J.E. (1964). "Stress Intensity Factors for a Single Notch Tension Specimen by Boundary Collocation of a Stress Function," NASA TN D-2395.

[76] Basinski, Z.S. and Basinski, S.J. (1985). "Low amplitude fatigue of copper single crystals," Acta Metall., Vol. 33, pp. 1307.

[77] Hunsche, A. and Neumann, P. (1986). "Quantitative measurement of persistent slip band profiles and crack initiation," Acta Metall., Vol. 34, pp. 207.

[78] Dabayeh, A.A. and Topper, T.H. (1995). "Changes in crack opening stress after underloads and overloads in 2024-T351 aluminum alloy," Int. J. Fatigue, Vol. 17, No. 4, pp. 261-269.

[79] Dabayeh, A.A., MacDougall, C, and Topper, T.H. (1996). "Crack opening stress reductions due to underloads and overloads in 2024-T351 aluminum and SAE 1045 Ssel," Proceedings of the Sixth International Fatigue Congres, Vol. I, pp.589-594.

[80] Pompetzki, M.A., Saper, R.A. and Topper, T.H. (1988). "Software for high frequency control of variable amplitude fatigue tests," Can. Metall. Q 252, pp. 181-194.

[81] DuQuesnay, D.L., MacDougall, C., Dabayeh, A. and Topper, T.H. (1995). "Notch fatigue behaviour as influenced by periodic overloads," Int. J. Fatigue , Vol. 17, No. 2, pp. 91.

[82] Duquesnay, D.L. (1986). "A Short Crack Fracture Mechanics Analysis of Notch-Size Effects in Fatigue, " M.A.Sc. Thesis, University of Waterloo, Waterloo, Ontario, Canada.

[83] Dabayeh, A.A., Xu, R.X., Du, B.P. and Topper, T.H. (1996). "Fatigue of cast aluminum alloys under constant and variable amplitude loading," Int. J. Fatigue, Vo. 18, No. 2, pp. 95-104.

[84] ABAQUS User's Manual (1995). (Hibbitt, Karlsson and sprenson Inc., Providence, RI, USA).

[85] Pilkey, W.D. (ed.) (1997). "Peterson's Stress Concentration Factors", By John Wiley & Sons Inc., Second Edition.

[86] MacDougall, C. and Topper, T.H. (1997). "The influence of variable amplitude loading on crack closure and notch fatigue behavior," Int. J. Fatigue, Vol. 19, No. 5, pp.389-400.

[87] American Society for Testing and Materials (1969). Manual on Low Cycle Fatigue Testing, ASTM STP 465, ASTM, Philadelphia.

[88] American Society for Testing and Materials (1980). ASTM Standard E606-80, Annual Book of ASTM Standards, ASTM, Philadelphia.

[89] Graham, J.A. (ed.) (1968). SAE Fatigue Desigh Handbook, Vol. 4, Society of Automotive Engineers, Warrendale, Pa.

[90] Wetzel, R.M. (ed.) (1977). Fatigue Under Complex Loading: Analysis and Experiments, Advances in engineering, Vol. 6, Society of Automotive Engineers, Warrendale, Pa.

[91] Morrow, J. and Socie, D.F. (1981). "The Evaluation of Fatigue Crack Initiation Life Prediction Methods," In Materials, Experimentation and Design infatigue, F. Sherratt and J. B. Sturgeon (eds.), Westbury House, Warwick, England, pp. 3.

[92] DuQuesnay, D.L., Topper, T.H., Yu, M.T. and Pompetzki, M.A. (1992). "The effective mean stress range as a mean stress parameter," Int. J. Fatigue, Vol. 14, No. 1, pp. 45-50.

[93] DuQuesnay, D.L., Pompetzki, M.A. and Topper, T.H. (1993). "Fatigue life predictions for variable amplitude strain histories," SAE transactions, Vol. 5, Also also appears in SAE special publication SP-1009 as SAE Technical Paper 930400.

IMAGE EVALUATION
TEST TARGET (QA-3)

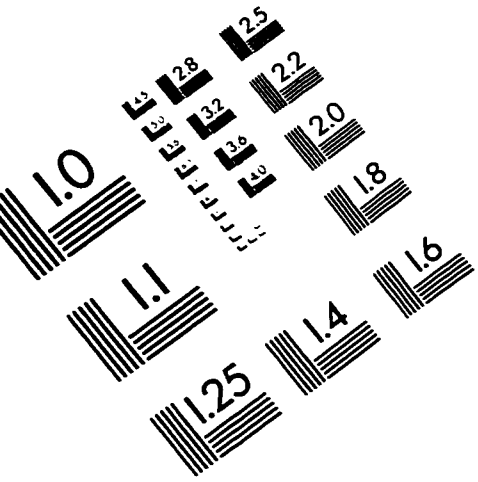

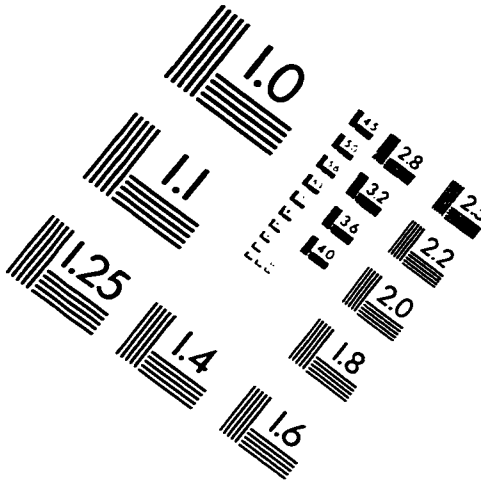

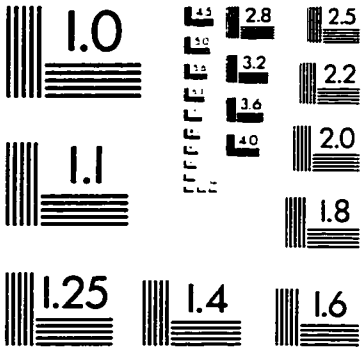

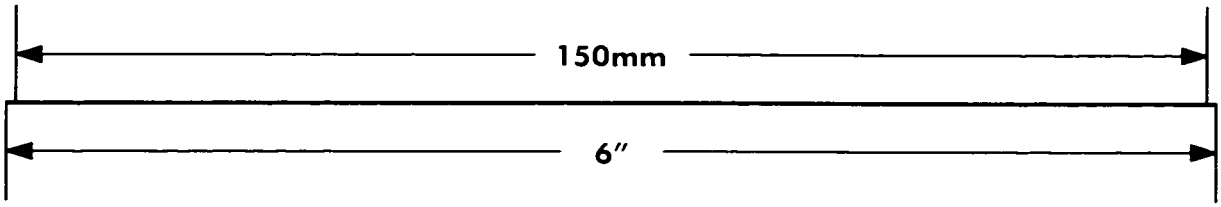

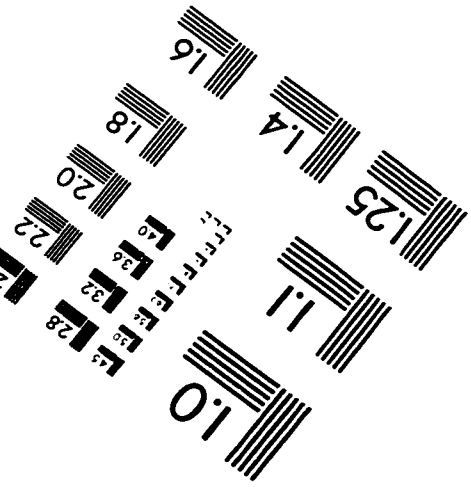

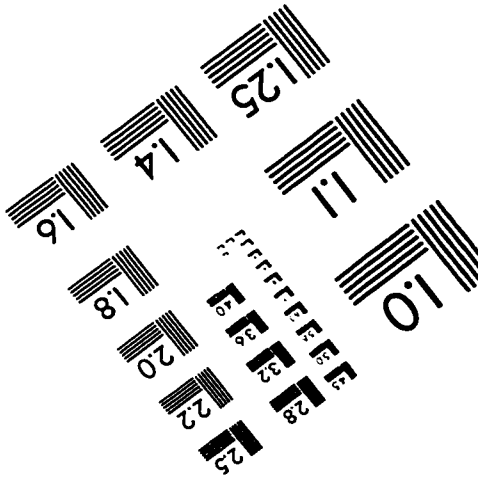

APPLIED IMAGE, Inc
1653 East Main Street
Rochester, NY 14609 USA
Phone: 716/482-0300
Fax: 716/288-5989

© 1993, Applied Image, Inc., All Rights Reserved